SIMULATIONS OF ADSORPTIONS AND PHASE TRANSITIONS

by

Wei Shi

BS, Coal Coking Chemical Engineering, East China University of Science and Technology, 1993

MA, Chemical Engineering, East China University of Science and Technology, 1996

Submitted to the Graduate Faculty of

the School of Engineering in partial fulfillment

of the requirements for the degree of

Doctor of Philosophy

University of Pittsburgh

2003

UNIVERSITY OF PITTSBURGH

SCHOOL OF ENGINEERING

This dissertation was presented

by

Wei Shi

It was defended on

May 5, 2003

and approved by

J. Karl Johnson, Associate Professor, Chemical and Petroleum Engineering Department

Bradley C. Bockrath, Ph.D, National Energy Technology Laboratory

Robert M. Enick, Professor, Chemical and Petroleum Engineering Department

Gerald D. Holder, Professor, Chemical and Petroleum Engineering Department

Eric Borguet, Associate Professor, Chemistry Department

Dissertation Director: J. Karl Johnson, Associate Professor, Chemical and Petroleum Engineering

ABSTRACT

SIMULATIONS OF ADSORPTION AND PHASE TRANSITIONS

Wei Shi, PhD

University of Pittsburgh, 2003

The objective of this thesis is to develop simulation tools that will allow us to study many phenomena from a molecular level. The topics covered in this thesis include bulk phase transitions, phase transitions in adsorbed fluids, and the application of single-walled carbon nanotubes as a gas storage media.

Multiple histogram reweighting and mixed-field finite-size scaling techniques have been developed to calculate the phase diagram for classical and quantum fluids in bulk and adsorbed phases. We show, for the first time, that capillary condensation shows a crossover of the effective exponent for the width of the coexistence curve from 2-D Ising-like (1/8) farther away from the critical point to mean-field (1/2) near the critical point. The first prewetting transitions clearly observed from simulation of quantum fluids are presented. The experimental wetting temperature of 19.1 K is reproduced from the simulation with a modified potential. Hydrogen adsorbing on a 15 Å thick film of Rb on Au gives a wetting temperature of about 1 K less than H_2 on pure Rb. This prediction should be observable from experiments.

Hydrogen adsorption onto single walled carbon nanotube bundles has been performed from computer simulations and compared with the experiments. We study the effect of CO_2 oxidation of the nanotubes on adsorption. Isotherms computed with a standard graphitic potential give remarkably good agreement with the experimentally measured isotherms before activation with

CO_2. The effect of activation is modeled by independently increasing the nanotube spacing and the solid-fluid interaction potential. It is found that only a combination of increased nanotube spacing and increased solid-fluid potential gives rough agreement with experiments.

Gases such as CH_4, Xe, and Ar have been studied on both the homogeneous (same tube diameter) and heterogeneous (different tube diameters) closed single-walled carbon nanotube bundles constructed from the basin-hopping method. Experimental gas adsorption data on SWNT bundles have previously been analyzed in terms of an over-simplified model of homogeneous nanotubes packed into perfect arrays. This analysis has led to the general conclusion that gases do not adsorb inside interstitial channels of homogeneous nanotube bundles. Our analysis overturns the current paradigm of gas adsorption on SWNTs by showing that adsorption inside interstices of heterogeneous SWNT bundles is vitally important to accurately describing these materials.

TABLE OF CONTENTS

Page

ABSTRACT . . . . . **iii**

ACKNOWLEDGMENTS . . . . . **viii**

LIST OF TABLES . . . . . **ix**

LIST OF FIGURES . . . . . **x**

1.0 OVERVIEW **1**

2.0 HISTOGRAM REWEIGHTING AND FINITE-SIZE SCALING STUDY . **6**

2.1 INTRODUCTION 6

2.2 THEORY 9

2.2.1 Histogram reweighting 9

2.2.2 Finite-size scaling 15

2.3 SIMULATION DETAILS 19

2.3.1 Vapor-liquid equilibrium 20

2.3.2 Finite-size scaling 20

2.4 RESULTS AND DISCUSSION 21

2.4.1 The LRC fluid 21

2.4.2 The TR and TS fluids 23

2.4.3 Summary of critical constants 24

2.5 CONCLUSIONS 25

3.0 PHASE TRANSITIONS OF ADSORBED FLUIDS 36

3.1 INTRODUCTION 36

3.2 THEORY AND METHODS 39

3.3 CAPILLARY CONDENSATION 41

3.4 PREWETTING 47

3.5 LAYERING TRANSITION 58

3.6 CONCLUSION 61

4.0 MULTIPLE HISTOGRAM REWEIGHTING FOR QUANTUM 65

4.1 INTRODUCTION 65

4.2 THEORY 66

4.3 SIMULATION DETAILS 69

4.4 RESULTS 70

4.5 CONCLUSIONS 79

5.0 WETTING TRANSITIONS OF HYDROGEN AND DEUTERIUM 80

5.1 INTRODUCTION 80

5.2 THEORY AND SIMULATION DETAILS 81

5.3 RESULTS 83

5.4 DISCUSSION AND CONCLUSION 87

6.0 CHEMICAL ACTIVATION OF CARBON NANOTUBES 89

6.1 INTRODUCTION 89

6.2 EXPERIMENTAL METHODS 91

6.3 SIMULATION METHODS 97

6.4 RESULTS AND DISCUSSION 100

6.5 SIMULATION RESULTS 109

6.6 CONCLUSIONS 113

7.0 GAS INTO INTERSTITIAL 115

7.1 INTRODUCTION 115

7.2 SIMULATION DETAILS 116

7.3 RESULTS 118

7.4 CONCLUSIONS 125

8.0 ADSORPTION ONTO CLOSED NANOTUBE BUNDLES 126

8.1 INTRODUCTION 126

8.2 THEORETICAL CALCULATIONS 127

8.3 RESULTS 130

8.3.1 Results for CH_4 133

8.3.2 Results for Ar 140

8.3.3 Results for Xe 140

8.4 CONCLUSION 146

9.0 FUTURE WORK 147

9.1 FUTURE WORK 147

BIBLIOGRAPHY 149

ACKNOWLEDGMENTS

I am very thankful to my advisor, Dr. J. Karl Johnson, for training, mentoring, and providing opportunities to me during the past four and some years. His inspiration, encouragement, and wise and thoughtful discourses have laid the foundation for my Ph.D. thesis. His constructive criticism "learning more makes one better" will forever guide me through my life. I am also very grateful for his kindness beyond my research. During the past years, I have not only learned a lot from him, but also built a family. I also appreciate Dr. Bradley C. Bockrath for his advice of part of work. I am also grateful to Dr. Milton W. Cole for his input to part of this thesis. I would like to thank National Energy Technology Laboratory and National Science Foundation for support of this work. I thank Dr. Robert M. Enick, Dr. Gerald D. Holder, and Dr. Eric Borguet for serving on this Ph.D. committee. I am indebted to the support and encouragement lent by my colleagues, and friends. Lastly but not least important, I would like to thank for my wife, Hua Ruan, for her invaluable support of my research. This thesis is the best gift to my wife and my baby little girl, Sophia.

LIST OF TABLES

Table No. Page

2.1 Saturation densities computed from the EOS and Hill's method 21

2.2 Comparison between Hill's method and the equal area construction. 22

2.3 Critical properties of the LJ fluids 24

3.1 Ratios of the grand canonical partition function 64

3.2 Reduced wetting temperature and prewetting critical temperature 64

5.1 Well depths, wetting temperatures, and prewetting critical points 83

6.1 Classes of nanotube bundles 98

LIST OF FIGURES

Figure No. — Page

2.1 The μ^*–ρ^* isotherms for LRC at $T^* = 1.15$ 12

2.2 The μ^*–ρ^* isotherms for LRC at $T^* = 1.27$ 13

2.3 Hill's method for calculation of the saturation chemical potential 14

2.4 The apparent $T_c^*(L)$, plotted as a function of $L^{-(\theta+1)/\nu}$ 27

2.5 The apparent $(\beta\mu)_c(L)$, plotted as a function of $L^{-(\theta+1)/\nu}$ 28

2.6 Isotherms for two temperatures and two different system sizes 28

2.7 Coexistence densities for LRC 29

2.8 The phase diagram for the LRC fluid with a cutoff of 5.0σ 30

2.9 A plot of T^*–μ^* at coexistence for $r_c^* = 2.5$ and 5.0 31

2.10 The density versus chemical potential isotherms 32

2.11 The phase diagrams for the TR and TS fluids with $r_c^* = 2.5$ 33

2.12 The phase diagrams for the TR and TS fluids with a cutoff of $r_c^* = 3.5$ 34

2.13 The phase diagrams for the LRC and TR fluids with $r_c^* = 5.0$ 35

3.1 Isotherms for $T^* = 0.7$ and 0.6 43

3.2 The T^*–ρ^* phase diagram for capillary condensation 45

3.3 Scaled width of the coexistence data 46

3.4 Isotherms for $T^* = 0.83$, 0.88 and 1.0 49

3.5 Density probability distribution at $T^* = 0.83$ and $\mu^* = -3.801$ 50

3.6 Local density profiles at $T^* = 0.83$ 51

3.7 Local density profiles at $T^* = 0.88$ 52

3.8 A plot of $\Delta\mu^* = \mu_{sat}^* - \mu_{pw}^*$ as a function of temperature 53

3.9 The temperature–density phase diagram 55

3.10 The ratio of the prewetting transition pressure to the saturation pressure 56

3.11 The density probability distributions at $T^* = 0.92$ 57

3.12 The $T = 100$ K isotherm for propane 59

3.13 The $T = 110$ K isotherm for propane 60

4.1 The T–ρ phase diagram for the TR H_2 71

4.2 The T–ρ phase diagram of long range corrected H_2 72

4.3 The density distribution for D_2 at 33 K 73

4.4 The T–μ/T phase diagrams of the TR and LRC H_2 74

4.5 The T–ρ phase diagram of LRC D_2 75

4.6 The isotherms for the 9-3 potential of H_2/Rb 77

4.7 The number density distribution at 30 K for H_2/Rb 78

5.1 The original CCZ and the 9-3 potentials 82

5.2 The local density profiles for the original CCZ 84

6.1 Block diagram of the Rupprecht and Patashnick TEOM 1500 93

6.2 Adsorption isotherms for hydrogen 96

6.3 Sample nanotube bundle used in the molecular simulation 99

6.4 Mass versus time from the experiment 101

6.5 Hydrogen isotherms 103

6.6 Comparison of adsorption isotherms of hydrogen 105

6.7 Isotherms comparison between simulations and experiment before activation. 110

6.8 Isotherms with increased nanotube spacing and solid-fluid adsorption potential. . . . 112

7.1 Sample of heterogeneous and homogeneous bundles 117

7.2 Isosteric heats of adsorption for CH_4 from simulations and experiment 119

7.3 Experimental and simulated q_{st} for Ar on SWNT bundles 122

7.4 Xenon q_{st} from experiments and simulations 124

8.1 Figure for two heterogeneous bundles both with 45 tubes 132

8.2 Isotherms from simulations and experiments for CH_4 at 159.88 K 133

8.3 The temperature effect on isosteric heat for CH_4 135

8.4 The bundle effect on isosteric heat of adsorption for CH_4 137

8.5 The isosteric heats at 159.88 K for CH_4 138

8.6 The isotherms at 159.88 K for CH_4 139

8.7 The bundle effect on isosteric heat for Ar 141

8.8 Isotherms at 250 K for Xe 142

8.9 Isotherms at 150 K for Xe 143

8.10 The temperature effect on isosteric heat for Xe 145

1.0 OVERVIEW

The equilibrium thermophysical properties and phase behavior of pure fluids and their mixtures is of central importance to many technological and scientific fields, for example, in designing separation processes for the chemicals, petroleum, pharmaceutical, and many other industries. Understanding the metabolism in living systems also requires a knowledge of the equilibrium properties of fluids. Numerous experiments have been performed to map out various phase transitions and obtain parameters for empirically or theoretically based models. However, experimental measurements are very time consuming and expensive. Empirical models are only valid over the range of conditions for which experimental data have been used for obtaining the model parameters. Even theoretically based models have limited predictive abilities for conditions and systems different from the ones for which they were designed[1]. I still remember the painful experience I went through when I tried to design a distillation tower during a undergraduate class. There were so many equations and parameters I had to choose with caution in order to obtain an accurate design.

Molecular-based simulations are an increasing important alternative to experimental measurements and theoretical techniques for obtaining properties of fluids and materials. By comparing the simulations with the experiments, the accuracy of the interaction potentials between particles can be assessed. Once the interaction potential is known, the properties at *any* condition can in principle be obtained through simulations. Using the same interaction potential as used in a theory, the accuracy of the theory can be evaluated. The power of the simulations lies in the ability to predict properties at any set of conditions, which can be verified from experiments. In the past few decades molecular simulation techniques have become powerful tools for studying phase transitions in fluids and solids, for predicting thermodynamics and transport properties of fluids, for aiding the interpretation of experimental measurements, for design of new materials, and for directing experimental studies.

Several books and review articles on the subject of simulation methods have appeared in recent years[2–6]. Readers seeking a more thorough discussion of the methodological aspects pertaining to a

particular simulation technique are therefore referred to the respective works described in the books and the review articles. We here present a simple review of several important methods. Monte Carlo methods or molecular dynamics methods are available to calculate the equilibrium properties of materials. Monte Carlo methods are based on generating a chain of configurations in phase space in terms of Boltzmann distribution. Some properties, such as pressure, enthalpy, etc. can be calculated as the ensemble average of the configuration chain. Compared with Monte Carlo methods, molecular dynamics methods generate the configuration chain by solving Newton's equations of motion with some kinds of numerical method. Dynamical properties, such as transport coefficients, which can not be obtained through Monte Carlo methods, can be obtained through molecular dynamics. Monte Carlo methods have proved to be more efficient than molecular dynamics for studying phase transitions although molecular dynamics is useful for obtaining the interfacial properties[7].

Many kinds of Monte Carlo methods have been used to calculate phase transitions. These methods can be divided into two categories, namely direct and indirect. By in direct, we mean that the phase transition can be directly identified from a single simulation. This includes Gibbs Ensemble Mote Carlo (GEMC)[8,9], etc. Gibbs ensemble has been widely used for simulation of fluid-phase equilibrium. GEMC is performed by carrying out a simulation simultaneously in two or more boxes at the same temperature. Each box represents distinct phases that coexist at a phase transition. The conditions for phase equilibrium, namely equality of pressure, temperature, and chemical potential of each component, are satisfied by exchanges of volume and the particles between the boxes. Chemical potential does not need to be calculated since the equality in chemical potential is implicitly satisfied by exchange of the particles. However, molecules must be transfered from one box to another. Hence, this method is not efficient at high densities, or as the complexity of the structure of the molecules increases. This problem can be partially alleviated with the configurational bias method[10]. GEMC is less accurate than the multiple histogram reweighting technique described below[11–13]. By indirect, we mean that the phase transitions can not be identified directly from the simulations. Data are collected during the simulation and post-processing of the data is performed to compute the phase equilibrium. Indirect methods include the NPT plus test particle method[14],

Grand canonical Monte Carlo, semigrand ensemble[15], the Gibbs-Duhem integration method[16,17], multiple histogram reweighting, etc. Grand canonical Monte Carlo method is widely used in the construction of isotherms of adsorption. Particles have to be deleted or created in the box during the simulation. This method will encounter the same problem as the GEMC does. The semigrand method is especially useful for studying mixtures. However, this technique is only efficient when the components under study are similar in both size and shape since the successful identity exchange in the simulation will be very low if the components are very dissimilar. The NPT plus test particle method is based on calculations of the chemical potentials for a number of state points. A phase coexistence point is determined at the intersection of the vapor and liquid branches of the chemical potential versus pressure diagram. Obviously, it requires many calculation to get one point of equilibrium. The Gibbs-Duhem integration is performed by numerically calculating a differential equation from a series of simulations. An Initial condition (one equilibrium point) is needed. One drawback of this method is that the error in the numerical integration may accumulate and propagate. The basic idea of histogram reweighting is that the microcanonical partition function is independent of temperature, chemical potential, etc. A global microcanonical partition function can be constructed from histograms in terms of the energy and number of particles collected during simulations at a series of different conditions. The phase diagram can then be obtained using the equal area criterion for the distribution curve of number of particles for the vapor and liquid sides. By combining with mixed-field finite size scaling, the critical point can be accurately identified. Overlap in the energy and particle number distributions between two neighboring state points are required in multiple histogram reweighting. Hence, enough points have to be run before multiple histogram reweighting can be used. This problem may be alleviated by using parallel tempering [18]. Many methods have been developed to model polymeric molecules. The expanded ensemble method is such an example[5]. The basic idea of the expanded ensemble is similar to parallel tempering. Both these two methods construct a series of different states. There are two main kinds of difference between these two methods:

1. The expanded ensemble is commonly used in canonical ensemble to measure the chemical potential of polymeric molecules. Hence, all the states must be the same temperature and volume. The parallel tempering method is widely used in the Grand canonical ensemble. The only constraint is that all the states must have the same volume.

2. Prefactor weights are needed for all states in the expanded ensemble to assure that all the states are visited with approximately the same frequency. An iterative process is used to obtain these weights. All the prefactor weights are set to unity in the parallel tempering method. Hence, it is more difficult to implement the expanded ensemble method than to use the parallel tempering method.

All of the methods mentioned above are intrinsically subject to finite size effects. This problem becomes more serious near the critical point. When the state point is close to the critical point, the long range fluctuations are suppressed by the finite size of the simulation box. Mixed-field finite size scaling has been developed[19,20] to calculate the critical parameters for an infinite system from the apparent critical parameters for finite sized systems.

Adsorption is another very important topic, governing processes such as water purification, gas separation, pollution prevention, and heterogeneous catalysis. Recently, hydrogen adsorption onto carbon nanotubes has attracted much attention[21–27]. Interest in hydrogen as a fuel has grown dramatically since 1990[21] due to the fact that hydrogen is non-polluting, forming water as a harmless combustion byproduct. There are currently four methods of storing H_2. These are: (1) compression, (2) liquefaction, (3) metal hydrides and (4) adsorption. None of these methods are currently suitable for on-board storage for fuel cell vehicles because none meets the DOE volumetric and gravimetric targets. Carbon nanotube based materials have been proposed as effective hydrogen sorbents because of their large theoretical surface areas and binding energies.

Many experiments for hydrogen adsorption onto carbon nanotube bundles have been performed. Claims of high values of hydrogen adsorption have been made in reports of investigations at low

temperature,[22] room temperature[23,24] and even higher temperatures[28]. Other experimental studies have found very limited uptake of hydrogen[25–27]. The reason for the difference is still unknown. These variations in the experiments may be in part due to differences in the way the SWNT samples were prepared or pretreated. To accurately understand the adsorption sites in the nanotube bundles is fundamental for the carbon nanotubes to be optimized as adsorbents. Many experiments to identify the adsorption sites onto single-walled carbon nanotubes (SWNTs)[29–43] have been performed. It is interesting to note that many researchers are still arguing whether or not gases can penetrate into the interstitial region of the nanotube bundles.

Molecular simulations can help resolve the above questions about adsorption onto carbon nanotubes. By comparing simulations with experiments, we can deduce the molecular level phenomena that give rise to experimentally observed quantities. This is one of the main objectives we will address in this thesis.

This thesis is composed of eight main chapters aside from this introduction. Chapter 2 is related to the histogram reweighting and finite size scaling techniques used to study the effects of different potentials, such as truncated and long-range corrected potentials on the vapor-liquid phase diagram. This problem is important to know since in the adsorption study, the truncated potential is always used. Chapter 2 has been published in *Fluid Phase Equilibria*[44]. Chapter 3 deals with the extension of multiple histogram reweighting to phase transitions in adsorption. This material has been published in *Molecular Physics*[45]. Chapters 4 and 5 deal with the phase transition of path integral fluids and the wetting of these fluids on metals. Chapter 6 presents experimental and simulation studies on H_2 adsorption on SWNTs. The experimental work was performed at NETL by Smith and coworkers. This material has been published in *the Journal Physical Chemistry B*[46]. Chapters 7 and 8 present simulations on adsorption of various gases on closed nanotube bundles. Chapter 7 has been submitted to *Physical Review Letters*[47]. Chapter 9 presents suggestions for future work.

2.0 HISTOGRAM REWEIGHTING AND FINITE-SIZE SCALING STUDY OF THE LENNARD-JONES FLUIDS [1]

2.1 Introduction

The Lennard-Jones (LJ) potential has been one of the most widely used functions for approximating the physics of simple nonpolar molecules. Both theory and simulations have been used to compute the properties of the LJ fluid and solid. The popularity of the LJ model is due more to its convenient mathematical form than to its accuracy in representing the properties of real fluids. For example, it is known that the LJ potential cannot be used to accurately represent the Ar potential energy surface.[48]

The full LJ potential is given by

$$\phi(r) = 4\epsilon \left[\left(\frac{\sigma}{r}\right)^{12} - \left(\frac{\sigma}{r}\right)^{6} \right], \tag{2-1}$$

where ϵ is the well depth of the potential and σ is the diameter of the atom, or the location at which the potential crosses zero, and r is the center to center distance between the LJ atoms. In computer simulations and many theories it is common to approximate thermodynamic (infinitely large) systems with finite-size systems that employ periodic boundary conditions. The LJ potential is often said to be short-ranged because the attractive tail decays as r^{-6}. However, for any finite system size the potential is not rigorously zero at a distance of half the box length where the potential is typically truncated. There are basically three approaches for dealing with the long-range tail of the LJ potential. The first option is to truncate the potential and add an approximate correction term for the tail.[2] This is the long-range corrected (LRC) fluid model that is commonly used for studies involving isotropic fluids and solids.

[1] This chapter is reprinted from reference [44]

The second option is to truncate the potential at some distance, r_c, and ignore the tail corrections. This is the truncated model (TR),

$$\phi_{\rm TR}(r) = \begin{cases} \phi(r) & r \le r_c \\ 0 & r > r_c \end{cases} . \tag{2-2}$$

Molecular simulation studies of anisotropic or inhomogeneous systems, such as simulations of adsorption, interfaces, and surface tension typically use this method, although methods have recently been developed to include tail corrections for surface tension calculations.[49,50]

The third possibility is to use a truncated and shifted potential that goes smoothly to zero at some finite value of r. This method is often used in molecular dynamics studies. The truncated and shifted (TS) potential is given by

$$\phi_{\rm TS}(r) = \begin{cases} \phi(r) - \phi(r_c) & r \le r_c \\ 0 & r > r_c \end{cases} . \tag{2-3}$$

A shifted-force potential has been developed for MD simulations,[51] but we will not consider that potential in this work. All three of these potentials (LRC, TR, TS) are used in both theoretical and simulation studies of fluids. It is therefore important to understand the phase behavior and the critical parameters of each of these fluids. A knowledge of how the properties change with the value of the cutoff is needed for comparing with experimental results or extrapolating to the full potential case.

In this paper we present a study of the critical parameters and phase diagrams of the LRC, TR, and TS LJ fluids as a function of the potential cutoff distance. Mixed-field finite-size scaling[19,20] is used to obtain estimates of the critical constants for each of the three potential models in the thermodynamic limit. Multiple histogram reweighting[11–13] is used to compute the phase diagrams. The multiple histogram reweighting technique is more precise and more efficient for computing phase diagrams than the widely used Gibbs Ensemble method.[8,9]

Mon and Binder proposed a way to calculate the critical temperature of infinite systems from a series of apparent critical temperatures using a classical power law. The critical temperature for the 2-D lattice gas was obtained.[52] Panagiotopoulos[53] obtained values of the reduced critical

temperature, T_c^*, and reduced critical density, ρ_c^*, for the LJ truncated potential by fitting the coexistence data estimated from Gibbs Ensemble Monte Carlo at sub-critical temperatures to the Ising-like scaling law. In keeping with common practice, we define the reduced temperature as $T^* = kT/\epsilon$, where k is the Boltzmann constant and T is the absolute temperature. The reduced density is defined as $\rho^* = N\sigma^3/V$, where N is the number of atoms and V is the total volume. Panagiotopoulos observed crossover from mean field to Ising-like behavior for 2-D, but not 3-D fluids. The disadvantage of this approach is that there is no rigorous way of deciding how many data near the critical point should be discarded from the parameter fitting to the scaling law. Smit [54] calculated the critical point for the LRC and TS potentials by fitting coexistence data from Gibbs ensemble simulations to the scaling law and the law of rectilinear diameters. His results were $T_c^* = 1.316(6)$, $\rho_c^* = 0.304(6)$ for the LRC potential and $T_c^* = 1.085(5)$, $\rho_c^* = 0.317(6)$ for the TS potential with $r_c = 2.5\sigma$, where the number in parentheses represents the uncertainty in the last digit. Lotfi *et al.* used the NPT plus test particle method to predict $T_c^* = 1.310$, $\rho_c^* = 0.314$ for the LRC fluid by correlating the resulting bubble and dew densities.[14] Caillol[55] performed a finite-size scaling study for the LRC potential in the grand canonical ensemble with hyper-spherical boundary conditions. Results from the predictions were $T_c^* = 1.326(2)$ and $\rho_c^* = 0.316(2)$.

Wilding[19,20] used finite-size scaling to estimate the critical constants in the thermodynamic limit. The critical temperature, chemical potential, and the field-mixing parameter can be tuned to satisfy the universal ordering operator distribution, $\tilde{p}^*_{\mathcal{M}}(x)$, assuming that the LJ fluid belongs to the same universality class as the Ising model. Apparent critical constants for a series of different system sizes were determined. The apparent critical constants are system size dependent due to corrections to scaling, energy operator asymmetry, and field mixing.[20,56] The critical parameters at infinite volume can be obtained by extrapolating finite volume values to infinite volume using the proper scaling coordinates.

Wilding used the histogram reweighting technique to facilitate the prediction of critical constants and calculation of vapor-liquid equilibrium (VLE). The histogram reweighting technique was introduced by Ferrenberg and Swendsen.[11–13] The essence of the method is that a single simulation

can give information about the properties of nearby state points. They developed a method of combining histograms from multiple simulations to greatly improve the statistics and extend the range of applicability of the method. This histogram reweighting method has been used to compute the phase diagrams and free energies of various fluids, but without applying finite-size scaling corrections.[57–60] Wilding[20] combined multiple histogram reweighting with mixed-field finite-size scaling to compute the critical constants for the TR LJ fluid truncated at $r_c = 2.5\sigma$. His results were $T_c^* = 1.1876(3)$ and $\rho_c^* = 0.3197(4)$. Potoff and coworkers[56,61,62] also applied the same techniques to the LRC fluid and to LJ mixtures. They obtained $T_c^* = 1.3120(7)$, $\rho_c^* = 0.316(1)$ for the LRC fluid. The same methods have been applied to critical phenomena in polymer blends.[5,63–66]

We note that Yan and de Pablo have developed a method they call hyper-parallel tempering for computing phase transitions.[18] This method can also be combined with mixed-field finite-size scaling to compute critical properties extrapolated to the thermodynamic limit. The advantage of hyper-parallel tempering is that it is much more efficient at exploring phase-space than other methods.

2.2 Theory

In this section we provide a brief overview of the multiple histogram reweighting and the mixed-field finite-size scaling methods and describe the use of the two methods to compute vapor liquid equilibrium phase diagrams.

2.2.1 Histogram Reweighting

We have collected histogram data for fluctuations in energy and particle number from grand canonical Monte Carlo (GCMC) simulations. As the GCMC simulation proceeds, the potential energy and the number of particles are recorded in a two-dimensional histogram $H(U_N, N)$, where

U_N is the configurational energy of the N particle system. The grand partition function can be written as

$$\begin{aligned} \Xi(\mu, V, T) &= \sum_N \sum_{U_N} \exp[N\beta\mu - \beta U_N]\Omega(N, V, U_N) \\ &= \sum_N \sum_{U_N} CH(U_N, N), \end{aligned} \tag{2-4}$$

where $\beta = 1/kT$, $\Omega(N, V, U_N)$ is the microcanonical partition function, and C is a simulation-specific constant. The probability of observing the system in a given state point is

$$\begin{aligned} P(U_N, N; \beta, \mu) &= \frac{H(U_N, N)}{\mathcal{N}} \\ &= \frac{\exp[(N\beta\mu) - \beta U_N]\Omega(N, V, U_N)}{\Xi(\mu, V, T)}, \end{aligned} \tag{2-5}$$

where $\mathcal{N}$ is defined as $\mathcal{N} = \sum_N \sum_{U_N} H(U_N, N)$. In this work we use a modified chemical potential μ defined by

$$\mu = \mu^f - kT \ln \Lambda^3, \tag{2-6}$$

where μ^f is the full chemical potential and Λ is the thermal de Broglie wavelength. Note that $\Omega(N, V, U_N)$ is independent of T and μ, so that simulations at different values of T, μ, but the same V all provide estimates of the same Ω. Ferrenberg and Swendsen[12,13] proposed a method for combining multiple histograms in a way that minimizes the global error in the estimate of $\Omega(N, V, U_N)$. Using this procedure, one can show that the normalized joint probability distribution is given by

$$P(U_N, N; \beta, \mu) = \frac{\sum_{j=1}^{K} H_j(N, U_N) \exp(-\beta U_N + \beta\mu N)}{\sum_{j=1}^{K} \mathcal{N}_j \exp(-\beta_j U_N + \beta_j \mu_j N)\Xi(\mu, T, V)/\Xi(\mu_j, T_j, V)}, \tag{2-7}$$

where K is the number of histograms combined. The above equation assumes that the histogram data are collected from configurations that are essentially uncorrelated from one another. This means that $g_n = 1$ in Eq. (3) of ref.[12]. If we set $\beta = \beta_i$ and $\mu = \mu_i$ in Eq. (2-7) where i denotes one of the K state points then we can sum Eq. (2-7) over all U_N and N to obtain

$$1 = \sum_N \sum_{U_N} \frac{\sum_{j=1}^{K} H_j(N, U_N) \exp(-\beta_i U_N + \beta_i \mu_i N)}{\sum_{j=1}^{K} \mathcal{N}_j \exp(-\beta_j U_N + \beta_j \mu_j N)\Xi(\mu_i, T_i, V)/\Xi(\mu_j, T_j, V)}. \tag{2-8}$$

Equation (2-8) can be used to estimate a value for each of the $K-1$ independent ratios, Ξ_i/Ξ_j, where $\Xi_j = \Xi(\mu_j, T_j, V)$. There are K equations given by Eq. (2-8), one for each of the K state points. The values of Ξ_i/Ξ_j are obtained from a least squares fit. Values for each of the Ξ_js may be estimated by arbitrarily specifying the value of Ξ at one of the K state points, then all the other Ξ_js can be calculated from Eq. (2-8). Note that values of Ξ so calculated can only be determined to within a multiplicative constant. The ensemble average of some property X at μ, V and T is given by

$$\begin{aligned} \langle X \rangle_{\mu,V,T} &= \sum_N \sum_{U_N} P(U_N, N; \beta, \mu) X(N, V, U_N) \\ &= \frac{\sum_N \sum_{U_N} X(N, V, U_N) \Omega(N, V, U_N) \exp(-\beta U_N + \beta \mu N)}{\sum_N \sum_{U_N} \Omega(N, V, U_N) \exp(-\beta U_N + \beta \mu N)}, \end{aligned} \tag{2-9}$$

where

$$\Omega(N, V, U_N) = \frac{\sum_{j=1}^{K} H_j(N, U_N)}{\sum_{j=1}^{K} \mathcal{N}_j \exp(-\beta_j U_N + \beta_j \mu_j N)/\Xi(\mu_j, T_j, V)}. \tag{2-10}$$

The pressure is given by

$$PV = kT \ln \Xi, \tag{2-11}$$

where Ξ can be obtained from Eq. (2-8) once all the Ξ_js are known. Vapor-liquid equilibrium can then be determined by solving Eq. (2-11) for the chemical potential that gives the same pressure for both phases at the same T. This can be accomplished by combining a limited number of histograms on each side of the phase diagram to form separate equations of state for the vapor and liquid branches. Several state points from the vapor side are combined to form an expression for Ξ^V for the vapor according to Eq. (2-8). Likewise, Ξ^L for the liquid branch is obtained by combining liquid and liquid-like state points. If the volume is constant for all the simulations then the equality of coexisting pressures implies the coexistence chemical potential, μ^{sat}, can be obtained by adjusting μ so that

$$\Xi^L(\mu^{\text{sat}}, T, V) = \Xi^V(\mu^{\text{sat}}, T, V), \tag{2-12}$$

One can only determine the ratio of partition functions at two different states from Eq. (2-8). The absolute value of the partition function can be computed by extrapolation to low density.[56]

However, the absolute value is not needed for computing VLE as long as the expressions for Ξ on each side of the phase envelop are referenced to the same arbitrary constant. In this case the constant in Eq. (2-8) can be eliminated from Eq. (2-12). Hence, we use the least squares solution to Eq. (2-8) for all K state points, referenced to a single constant, as the solutions for Ξ^L and Ξ^V. The values of $\langle N \rangle$ for each phase can be obtained from Eq. (2-9). The coexistence density is given by $\langle N \rangle / V$. We designate this method for computing coexistence value of μ and ρ as the EOS method, because we utilize the equation of state (EOS) through Eq. (2-11). We believe this to be the first time that this method has been used. There is some ambiguity as to how many state points to include in the expressions for Ξ^L and Ξ^V. Clearly, including all K state points would give a single isotherm with only trivial solutions to Eq. (2-12). The EOS method is shown graphically in Figs. 2.1 and 2.2 for the LRC fluid with a total of 14 state points. The solid lines

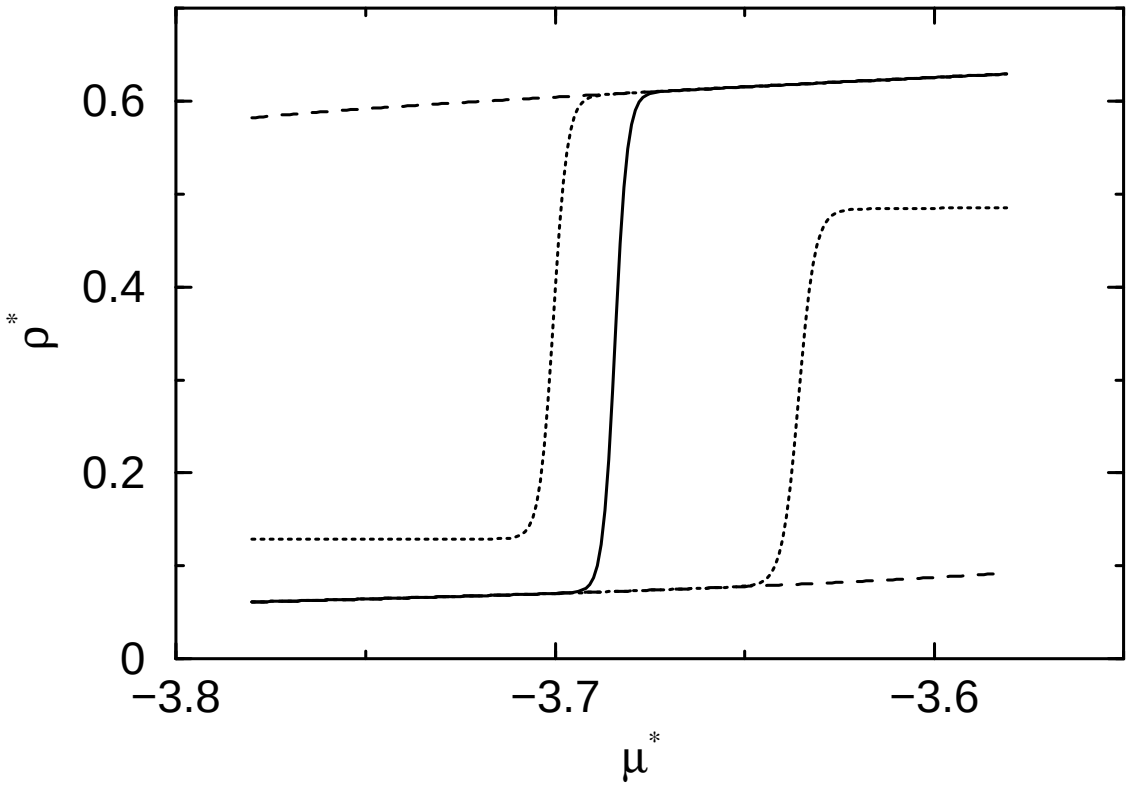

Figure 2.1: The μ^*–ρ^* isotherms for the LRC fluid with $r_c^* = 2.5$ and $V^* = 1331$ at $T^* = 1.15$. The solid line is computed from multiple histogram reweighting of all 14 state points. The dotted lines are vapor (lower) and liquid (upper) isotherms constructed from nine state points in each phase, and containing four common state points. The dashed lines are vapor (lower) and liquid (upper) isotherms constructed from four state points in each branch.

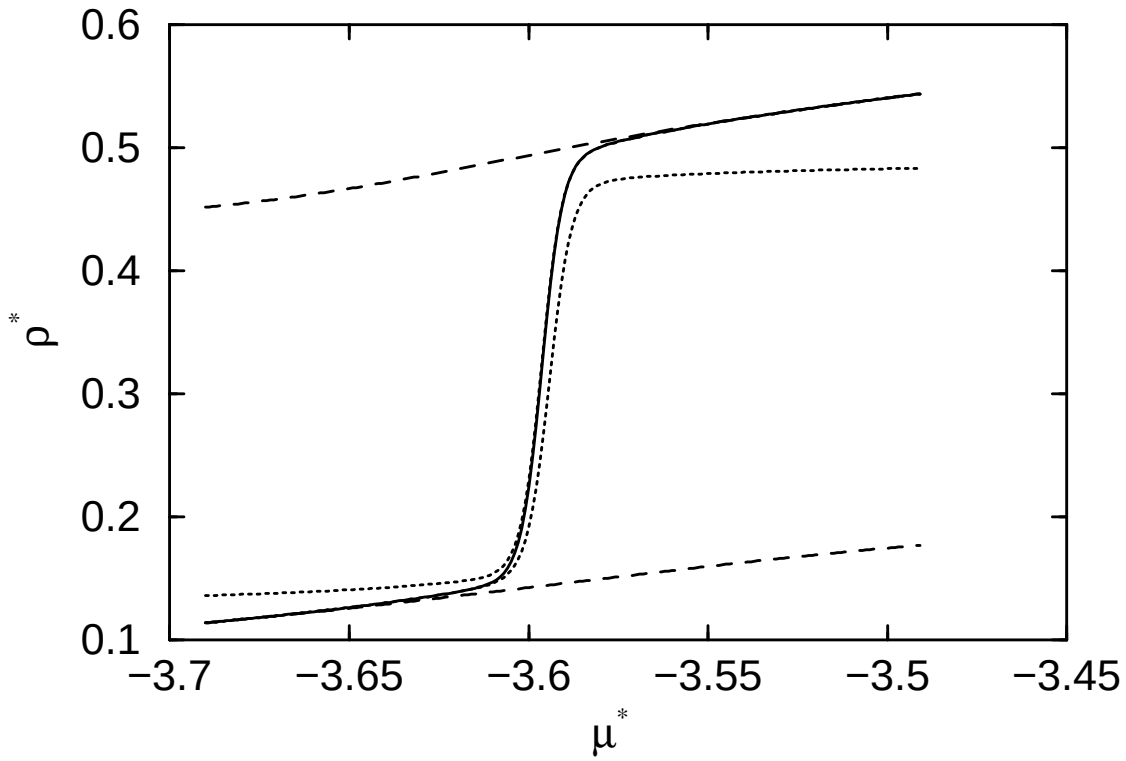

Figure 2.2: The μ^*–ρ^* isotherms for the LRC fluid with $r_c^* = 2.5$ and $V^* = 1331$ at $T^* = 1.27$. The lines are the same as in Figure 2.1.

in these figures are isotherms generated by combining all 14 state points. The dashed lines are obtained by combining four state points on each side of the phase diagram for Ξ^L and Ξ^V. The dotted lines are the results of combining nine state points, including four common points, in the expressions for Ξ^L and Ξ^V. For $T^* = 1.15$ (Figure 2.1) there are no differences in the coexistence properties computed from either the four or nine histogram expressions. At the higher temperature of $T^* = 1.27$ (Figure 2.2) the four histogram expressions yield accurate saturated densities, while the expressions constructed from nine histograms give unreasonable densities, although the value of $\mu^{\rm sat}$ is still accurate. The validity of the EOS method relies on an accurate extrapolation of the densities into the beginning of the metastable region for both the liquid and vapor branches. This is also a requirement of Hill's method for computing phase transitions for small systems.[67] In all calculations of the EOS method we have used four state points each to construct Ξ^L and Ξ^V because this number of state points was found to give reliable extrapolation to the metastable region for all cases.

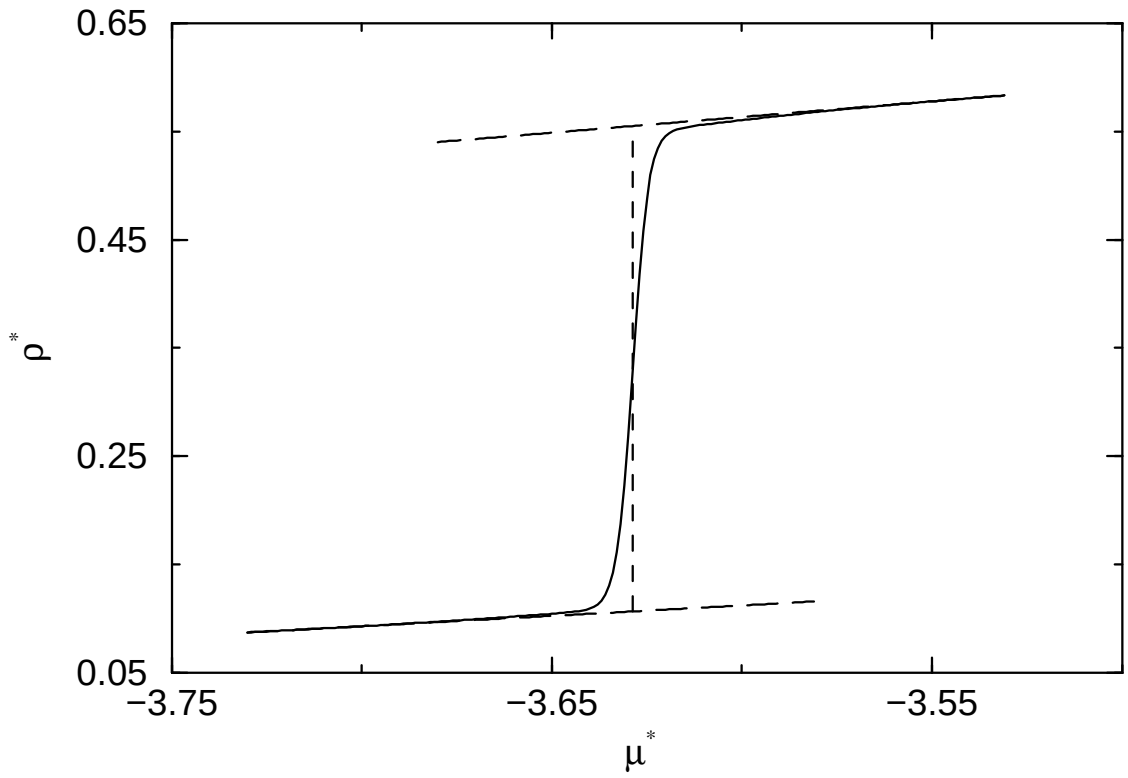

Figure 2.3: Hill's method for calculation of the saturation chemical potential. The solid line is the μ^*–ρ^* isotherm computed from multiple histogram reweighting. The long dashed lines are linear extrapolations of the liquid and vapor branches, and the short dashed line is the value of the chemical potential at saturation. The short dashed line is bisected by the μ^*–ρ^* isotherm. This isotherm is for the LRC fluid with $r_c^* = 2.5$, $V^* = 1331$ and $T^* = 1.22$.

We have also used Hill's method[67] combined with the density distribution to calculate VLE. The two requirements for the validity of Hill's method are that the system is not too small and that the temperature is not too close to criticality. There does not appear to be any quantitative measure for these requirements. The procedure for finding the coexistent chemical potential in our implementation of Hill's method goes as follows. The μ–ρ isotherm near the transition region from vapor to liquid is first plotted. Linear extrapolation approximation of both the vapor and liquid branches is then performed. A vertical line is drawn that connects the extrapolated isotherms such that this line is bisected by the μ–ρ isotherm. In other words, the μ–ρ isotherm computed from multiple histogram reweighting passes through the midpoint of the vertical line. See Figure 2.3 for an example of this procedure. The value of the chemical potential that defines this vertical line is the coexistence chemical potential. If the exact extrapolation into the metastable region were known

then Hill's method would yield the coexistence densities. Since we use linear extrapolation we need to use a more accurate method to compute the densities. We therefore compute the density distribution at the chemical potential obtained from Hill's method. The number distribution, $P(N) = \sum_{U_N} P(U_N, N; \beta, \mu)$, gives two distinct peaks, corresponding to the liquid and vapor states at subcritical temperatures. We have found that chemical potentials from Hill's method produce curves with approximately equal area under each peak, as required for equilibrium from the equal area criterion.[5] The agreement between Hill's method and the equal area construction will be explored in more detail in Sec. 2.4. The coexistence densities are the weight averaged densities in each of the two regions. The position of each of the peaks also gives estimates of the coexistence densities. The procedure for calculating the coexistence chemical potential in Hill's method can be automated by fitting lines to the liquid and vapor branches in the linear region of the curve. A one dimensional search is performed to find the vertical line whose mid-point is intersected by the μ–ρ curve.

As stated above, we use linear extrapolation from the liquid and vapor branches into the metastable region. This gives very accurate estimates of μ^{sat}, although the extrapolation is not accurate at higher temperatures. An accurate extrapolation into the metastable region can be obtained by using the EOS method described above. Using Ξ^L and Ξ^V to extrapolate into the metastable region with Hill's method is essentially a graphical implementation of the EOS method.

2.2.2 Finite-Size Scaling

The finite-size scaling technique (FSS) holds that the coarse-grained properties of systems near the critical point are universal. A prerequisite for universality is that the system size L, where L is the box length, must be sufficiently large. The properties depend on the specific combination of L and the scaling field, which measures the deviations from criticality. At criticality, the joint

distribution $p_L(\mathcal{M},\mathcal{E})$ exhibits scaling behavior of the form

$$p_L(\mathcal{M},\mathcal{E}) \simeq \Lambda^+_{\mathcal{M}}\Lambda^+_{\mathcal{E}}\tilde{p}^{\star}_{\mathcal{M},\mathcal{E}}(\Lambda^+_{\mathcal{M}}\delta\mathcal{M},\Lambda^+_{\mathcal{E}}\delta\mathcal{E}). \tag{2-13}$$

Near criticality,

$$p_L(\mathcal{M},\mathcal{E}) \simeq \Lambda^+_{\mathcal{M}}\Lambda^+_{\mathcal{E}}\tilde{p}^{*}_{\mathcal{M},\mathcal{E}}(\Lambda^+_{\mathcal{M}}\delta\mathcal{M},\Lambda^+_{\mathcal{E}}\delta\mathcal{E},\Lambda_{\mathcal{M}}h,\Lambda_{\mathcal{E}}\tau), \tag{2-14}$$

where τ and h are used to describe how far away the state point is from criticality. We introduce Eq. (2-14) because the universal distribution function $\tilde{p}^{*}_{\mathcal{M}}(x)$ is obtained from the integration of Eq. (2-14) with respect to energy $\mathcal{E}$ and then by setting $h = 0$ and $\tau = 0$ at criticality. The parameters in Eq. (2-13) and (2-14) are defined in the following equations,

$$\Lambda_{\mathcal{E}} = a_{\mathcal{E}}L^{1/\nu}, \tag{2-15}$$

$$\Lambda_{\mathcal{M}} = a_{\mathcal{M}}L^{d-\beta/\nu}, \tag{2-16}$$

$$\Lambda_{\mathcal{M}}\Lambda^+_{\mathcal{M}} = \Lambda_{\mathcal{E}}\Lambda^+_{\mathcal{E}} = L^d, \tag{2-17}$$

$$\delta\mathcal{M} \equiv \mathcal{M} - \langle\mathcal{M}\rangle_c, \tag{2-18}$$

$$\delta\mathcal{E} \equiv \mathcal{E} - \langle\mathcal{E}\rangle_c, \tag{2-19}$$

$$\mathcal{M} = \frac{\rho^* - su^*}{1-sr}, \tag{2-20}$$

$$\mathcal{E} = \frac{u^* - r\rho^*}{1-sr}, \tag{2-21}$$

where s and r are the mixed-field parameters, $u^* = U_N/(\epsilon V^*)$, where $V^* = V/\sigma^3$, d, β and ν are universal constants and $a_{\mathcal{M}}$ and $a_{\mathcal{E}}$ are system related constants. Equation (2-13) is only valid in the limit of large L. For small system sizes, one must consider L-dependent corrections to scaling.

This means that the apparent critical constants for small systems are L-dependent. The infinite volume critical constants can be extrapolated from results of finite systems plotted against the appropriate coordinate.[19,20] For example, the critical temperature scaling law is

$$T_c^*(\infty) - T_c^*(L) \propto L^{-(\theta+1)/\nu}, \tag{2-22}$$

where $T_c^*(\infty)$ is the reduced critical temperature in the thermodynamic limit, while, $T_c^*(L)$ is the reduced apparent critical temperature for the system size with box length of L, and θ is a universal constant.

Several histogram reweighting simulations near the critical point must be performed and combined in order to compute the apparent critical temperature with sufficient accuracy. This means that we must have an initial estimate for the critical point before collecting the histograms. This can be accomplished by performing histogram collection simulations over a range of temperatures and chemical potentials in order to estimate the phase diagram from either Hill's method or the EOS method. The coexistence data away from the critical region are then fitted to the Ising form power law to obtain estimates for T_c and ρ_c. The power law expression is given by

$$\rho_\pm^* - \rho_c^* = a|T^* - T_c^*| \pm b|T^* - T_c^*|^\beta, \tag{2-23}$$

where ρ_+ is the liquid density and ρ_- is the vapor density, and β is the critical exponent. Values of the parameters a, b, T_c^*, and ρ_c^* are adjusted simultaneously to obtain the best fit to the data. An estimate of μ_c is then obtained from Hill's method by constructing the μ–ρ isotherm for the estimated T_c with multiple histogram reweighting from Eq. (2-9). Two other temperatures, one on either side of the estimated critical temperature, are chosen and the corresponding coexistence chemical potentials are computed from Hill's method for those temperatures. Although Hill's method is not strictly valid near the critical point, it is used to provide an estimate of the coexistence chemical potential. Our calculations show that this estimate is quite close to the infinite volume critical chemical potential. Histograms are collected at each of these three state points. The histograms are then combined according to Eq. (2-8) and an estimate of the global microcanonical

partition function is obtained from Eq. (2-10). The probability distribution of $\mathcal{M}$ is mapped onto x, where

$$x = \frac{\mathcal{M} - \langle \mathcal{M} \rangle}{\sqrt{\langle \mathcal{M}^2 \rangle - \langle \mathcal{M} \rangle^2}}. \tag{2-24}$$

This definition results in x having unit variance. The apparent critical constants are obtained by adjusting T_c, μ_c and s such that $p_L(x)$ collapses onto the universal distribution $\tilde{p}^*_{\mathcal{M}}(x)$. We have used the BFGS method[68] to find the optimal values of the critical constants. It is important to have good initial guesses for T_c, μ_c and s to ensure the convergence of the method. The process for finding T_c, μ_c and s is outlined as follows:

1. An initial guess for $T_c(L)$ is taken from the fit to the power law.

2. An initial guess for $\mu_c(L)$ is found by iteration starting from the value of $\mu_c(L)$ from Hill's method. The probability $P(U_N, N; \beta, \mu)$ is computed from Eq. (2-7), with the values of $\Xi(\mu_j, T_j, V)$ calculated from Eq. (2-8) using the three histograms collected at the state points identified above. The normalized probability $P(N)$ is obtained from $P(U_N, N; \beta, \mu)$ with $P(N) = \sum_{U_N} P(U_N, N; \beta, \mu)$. The density distribution, $P(\rho) = P(N)$, is plotted and the chemical potential is adjusted by trial and error until a double-peaked distribution with approximately equal peak heights is obtained.[20]

3. An initial guess for s is chosen, keeping $r = -1.0$. The values of $\mathcal{M}$ are computed from Eq. (2-20) for all non-zero values of $P(U_N, N; \beta, \mu)$. A table containing $\mathcal{M}$ and $P(U_N, N; \beta, \mu)$ sorted by $\mathcal{M}$ is created and the minimum and maximum values of $\mathcal{M}$ corresponding to non-zero probability are identified. The probability of $\mathcal{M}$, $P(\mathcal{M})$, is computed by summing $P(U_N, N)$ over all values of (U_N, N) corresponding to the same (discrete) value of $\mathcal{M}$. In our calculations, we divide the range of $\mathcal{M}$ into 90 intervals with the interval width given by

$$\Delta\mathcal{M} = \frac{(\mathcal{M}_{\max} - \mathcal{M}_{\min})}{90}, \tag{2-25}$$

where $\mathcal{M}_{\max}$ and $\mathcal{M}_{\min}$ are the maximum and minimum values of $\mathcal{M}$ corresponding to nonzero values of $P(\mathcal{M})$. The density distribution of x, $p_L(x)$, is obtained through

$$p_L(x) = \frac{P(\mathcal{M})}{\Delta\mathcal{M}} \sqrt{\langle \mathcal{M}^2 \rangle - \langle \mathcal{M} \rangle^2}. \tag{2-26}$$

The value of s is tuned until $p_L(x)$ is qualitatively (visually) similar to the universal distribution $\tilde{p}^*_{\mathcal{M}}(x)$. We have found that the value of s is typically close to -0.035.

4. If $p_L(x)$ does not qualitatively collapse onto $\tilde{p}^*_{\mathcal{M}}(x)$ in Step 3 then one chooses a new initial guess for $T_c(L)$ and returns to Step 2.

5. The initial guesses for $T_c(L)$, $\mu_c(L)$ and s from the above steps are input to the BFGS method and the output values are taken as the best estimates for the system size dependent critical parameters. The objective function used in the BFGS method is the sum of the square of the difference between $p_L(x)$ and $\tilde{p}^*_{\mathcal{M}}(x)$ on the 91 discrete points defined by $\Delta\mathcal{M}$.

2.3 Simulation Details

We have performed separate sets of GCMC histogram simulations for estimating the saturated liquid and vapor densities and for computing the apparent critical constants. A single Monte Carlo (MC) move consisted of either an attempt to displace, create, or destroy an atom. The probability of making a displacement was set to 0.5, and the probability of attempting to create or destroy an atom was set to 0.25. The displacement acceptance ratio was adjusted during equilibration to be close to 0.4.

2.3.1 Vapor-Liquid Equilibrium

The VLE calculations for the LRC fluid were performed for values of the reduced cutoff, $r_c^* = r_c/\sigma$, of 2.5 and 5.0. Reduced volumes, $V^* = V/\sigma^3$, of 270, 540, and 1331 were used. Vapor-liquid equilibrium densities were computed for the $r_c^* = 5.0$ LRC fluid for $V^* = 1331$. Cutoff values of 2.5, 3.5, and 5.0 were used for the TR fluid. The volumes used in the simulations were 729, 729, and 1331, respectively. Vapor-liquid equilibrium for the TS fluid was computed for $r_c^* = 2.5$ and 3.5, with $V^* = 729$ in both cases. In all the simulations for VLE calculations the systems were equilibrated for at least 5×10^6 MC moves, and data collection was carried out for 5×10^6 MC moves. Production runs were divided into 10 subblocks for estimation of the variance.

2.3.2 Finite-Size Scaling

The simulations for use in FSS calculations required much longer runs to collect histograms of the accuracy required by the FSS method. The production runs lasted a total of 10^8 to 10^9 MC moves, depending on the system size. A linked cell neighbor list was used for simulations of the larger systems ($L > 3r_c$). The cell lists were regenerated only after successful deletion steps. For displacements and creation steps the lists were directly updated rather than being regenerated. The reduced volumes used for simulations of the TR fluid with a cutoff of 2.5σ are $V^* = 422$, 729, 1000, 1331, 1953 and 3375. Two independent sets of simulations were performed for each volume, giving two independent estimates of the apparent critical properties. The standard deviations (error bars in Figs. 2.4 and 2.5) were estimated from the two independent estimates of the critical properties.

The uncertainty in the intercept (i.e., T_c or $(\beta\mu)_c$) was computed from the uncertainty in the individual values of the data as described in[69]. The critical density and standard deviation at the thermodynamic limit was simply taken as the average of the apparent critical densities because the apparent critical density was essentially independent of system size.

Table 2.1: Saturation densities computed from the EOS and Hill's method (see text for details). Data are for the LRC fluid with $r_c^* = 2.5$ and $V^* = 1331$. The percent difference is calculated relative to Hill's method. The percent average absolute deviation is denoted as %AAD. The uncertainties of the coexistence densities from the EOS method are estimated from three sets of independent calculations for a smaller system size ($V^* = 270$).

T^*	ρ_v^*			ρ_l^*		
	EOS	Hill's Method	% difference	EOS	Hill's Method	% difference
1.15	0.0726(4)	0.0726	0	0.608(3)	0.608	0
1.16	0.0769(4)	0.0769	0	0.601(3)	0.601	0
1.17	0.0816(5)	0.0816	0	0.594(3)	0.594	0
1.18	0.0866(5)	0.0866	0	0.587(4)	0.587	0
1.19	0.0920(6)	0.0920	0	0.578(4)	0.578	0
1.20	0.0978(9)	0.0978	0	0.569(4)	0.569	0
1.21	0.1039(9)	0.104	0.1	0.559(5)	0.559	0
1.22	0.110(1)	0.111	0.9	0.548(6)	0.548	0
1.23	0.117(2)	0.118	0.8	0.537(7)	0.537	0
1.2405	0.124(3)	0.126	1.6	0.526(8)	0.525	0.2
1.25	0.131(5)	0.134	2.2	0.516(10)	0.515	0.2
1.2603	0.138(6)	0.143	3.5	0.505(13)	0.502	0.6
1.27	0.144(9)	0.153	5.9	0.496(16)	0.488	1.6
%AAD			1.2			0.2

The volume sizes for the TR and TS fluids with cutoffs of 3.5 σ were 729, 1405, 2000, and 2800. The volumes for the TR and LRC fluids with cutoffs of 5.0 σ were chosen to be 1331, 1953, and 3375. For the TS fluid with a cutoff of 2.5 σ the volumes were 729, 1000, 1331, 1953, and 3375. For the LRC fluid with a cutoff of 2.5 σ the volumes were 729, 1000, 1331, and 1953.

2.4 Results and Discussion

2.4.1 the LRC Fluid

The results of VLE calculations from the EOS method and Hill's method are shown in Table 2.1. The data are for $V^* = 1331$. The EOS partition functions were constructed by combining four state points in each phase. The saturated densities computed from these two methods are in excellent agreement. The error estimates for the EOS method were computed from the standard deviations

Table 2.2: Comparison between the reduced saturation chemical potentials $\mu^{\mathrm{sat}*}$ and densities computed from Hill's method and the equal area construction. The state points are for the LRC fluid with a cutoff of 2.5 σ and reduced volume of 1331.

T^*	$\mu^{\mathrm{sat}*}$		ρ_v^*		ρ_l^*	
	Hill's Method	Equal Area	Hill's Method	Equal Area	Hill's Method	Equal Area
1.15	−3.684358	−3.684357	0.072569	0.072569	0.607689	0.607689
1.18	−3.659204	−3.659207	0.086633	0.086632	0.586739	0.586738
1.23	−3.621868	−3.621879	0.117536	0.117532	0.536940	0.536933

from three independent sets of simulations at a smaller volume ($V^* = 270$). This assumes that the error in the EOS method is roughly constant in going from $V^* = 270$ to 1331.

We calculated the saturation chemical potential μ^{sat} from the equal area construction using the bisection method for three different temperatures. We started the iteration with an initial guess for μ^{sat} from Hill's method (truncated to four decimal places). The values of μ^{sat} from Hill's method and the equal area construction are compared in Table 2.2.

The bisection method typically converged to five decimal places within ten iterations. We have also computed the saturation densities from the value of μ^{sat} from both Hill's method (combined with the density distribution) and the equal area construction. The results are shown in Table 2.2. The difference between the saturated densities from the two methods is smaller than the statistical uncertainty in the data. Hence, we choose to use Hill's method because it has the advantage of giving good estimates even for small systems fairly near the critical point where the density distributions overlap and the equal area construction is difficult to implement.

Several μ^*–ρ^* isotherms for the LRC fluid with $r_c^* = 2.5$ are plotted in Figure 2.6, where $\mu^* = \mu/\epsilon$. Results for two different temperatures, $T^* = 1.16$ and 1.25, and volumes $V^* = 270$ and 540 are presented. The effect of volume on the equilibrium chemical potential was found to be very small at both temperatures. For a temperature of $T^* = 1.16$, $V^* = 270$ gave a saturation chemical potential of $\mu^* = -3.6735$, while $V^* = 540$ resulted in $\mu^* = -3.6736$. For $T^* = 1.25$, the values of μ^* at saturation are −3.6074 and −3.6070 for $V^* = 270$ and 540, respectively.

We have estimated the critical constants by fitting the coexistence data for $V^* = 1331$ at low temperature (1.15–1.26) to the power law using the 3-D Ising critical exponent $\beta = 0.3258$ (This

β is not to be confused with the reciprocal temperature, as in Eq. (2-4)). This gave $T_c^* = 1.3119$, $\rho_c^* = 0.316$. Finite-size scaling was then used to calculate the critical constants using this estimated T_c^* as an initial guess. The results are $T_c^*(\infty) = 1.3241(9)$, $\rho_c^*(\infty) = 0.3165(7)$. The coexistence densities were calculated from Hill's method. We have used $T_c^*(\infty)$ and $\rho_c^*(\infty)$ in conjunction with the power law expression of Eq. (2-23) to correlate the VLE surface treating a and b as the only adjustable parameters. In this paper, data from the six lowest temperatures were used to fit the values of a and b in each case. The phase diagram generated from Eq. (2-23) for the LRC fluid with $r_c^* = 2.5$ is shown in Figure (2.7). The effect of changing the cutoff from 2.5σ to 5.0σ on the coexistence properties of the LRC fluid is shown in Figs. 2.8-2.9. From Figure (2.8) we see that the coexistence densities for $r_c^* = 2.5$ and $r_c^* = 5.0$ at $V^* = 1331$ are in very close agreement over the entire temperature range. Figures 2.10 and 2.9 demonstrate that there is a systematic difference in the values of the the saturation chemical potentials for the LRC fluids with $r_c^* = 2.5$ and 5.0, both at $V^* = 1331$. The values of μ^* at saturation are uniformly higher for $r_c^* = 5.0$ compared with $r_c^* = 2.5$ over the entire temperature range. The average shift is about 0.0043. The reason for this is not apparent.

2.4.2 the TR and TS Fluids

We have performed detailed calculations of the TR fluid with a cutoff of 2.5σ. The results are shown in Figs. 2.4 and 2.5. The extrapolated value of $T_c^*(\infty)$ is 1.1879(4) and $(\beta\mu)_c(\infty)$ is $-2.777(1)$. These values are in excellent agreement with $T_c^*(\infty) = 1.1876(3)$ and $(\beta\mu)_c(\infty) = -2.778(2)$ from Wilding.[20] We have found that $\rho_c^*(L)$ varies weakly with system size. The arithmetic average of $\rho_c^*(L)$ was used to approximate $\rho_c^*(\infty)$, giving a value of 0.3201, which is very close to 0.3197(4) from Wilding.[20] The field mixing parameter s was around -0.035, which is reasonably close to Wilding's value of -0.0275, converted to the reduced units used in this paper.

The phase diagrams for the TR and TS fluids with $r_c^* = 2.5$ were generated in the same way as for the LRC fluid and are plotted in Figure 2.11. The phase diagrams for the TR and TS fluids

Table 2.3: Critical properties of the LJ fluids considered in this work. Critical constants estimated from the power law, Eq. (2-23), are denoted by PL. Finite-size scaling was used to compute the properties denoted by FSS.

Type	$T_c^*(\infty)$	$\rho_c^*(\infty)$	Source
LRC 2.5	1.3241(9)	0.3165(7)	this work [FSS]
LRC 5.0	1.3145(2)	0.316(1)	this work [FSS]
LRC	1.3120(7)	0.316(1)	Potoff *et al.* [FSS][56]
LRC	1.326(2)	0.316(2)	Caillol[55]
LRC	1.310	0.314	Lotfi[14]
LRC	1.316(6)	0.304(6)	Smit[54]
TR 2.5	1.1879(4)	0.3201(4)	this work [FSS]
	1.2073	0.3203	this work [PL]
	1.186(2)	0.316(3)	Potoff *et al.* [56]
	1.1876(3)	0.3197(4)	Wilding[20]
TR 3.5	1.2647(4)	0.3164(4)	this work [FSS]
	1.2694	0.3170	this work [PL]
TR 5.0	1.2963(1)	0.3161(8)	this work [FSS]
	1.2991	0.3177	this work [PL]
TS 2.5	1.0795(2)	0.3211(5)	this work [FSS]
	1.085(5)	0.317(6)	Smit[54]
TS 3.5	1.2211(9)	0.3183(5)	this work [FSS]
	1.2345	0.3153	this work [PL]

with $r_c^* = 3.5$ are plotted in Figure 2.12.

2.4.3 Summary of Critical Constants

Values of $T_c^*(\infty)$ and $\rho_c^*(\infty)$ from this work and previous simulations are summarized in Table 2.3.

The critical temperature for the TR fluid is about 10% larger than that for the TS fluid when both have $r_c^* = 2.5$. When r_c^* is increased to 3.5 the difference in critical temperature is reduced to 3.6%. We are specifically interested in comparing the properties of the LRC fluid with the truncated fluid. The reason for our interest is that in many simulations of inhomogeneous fluids (e.g., adsorption) the TR fluid is used as an approximation to the LRC fluid since it is more difficult to apply the long range corrections for an inhomogeneous fluid. One would therefore like to know what value of the cut off would give a phase diagram that is "similar" to that of the LRC fluid.

We compare the LRC and TR fluid, both with $r_c^* = 5.0$. The critical temperature for the LRC fluid is 1.3145(2) while that for the TR fluid is 1.2963(1). This is a decrease of 1.4% in T_c^*. The phase diagrams for these two fluids are plotted in Figure 2.13. The average absolute deviation in the coexistence densities between the LRC and TR fluids is about 0.8% and 1% for the vapor and liquid, respectively (using the LRC fluid as the reference). These are the magnitudes of the errors one would expect to incur by using the TR, $r_c^* = 5.0$ fluid to represent the LRC fluid.

The value of $T_c^*(\infty)$ for the LRC fluid with a cutoff of 5.0σ is closer to that reported by Potoff [56] than for 2.5σ. In Potoff's calculation, the cutoff distance is not actually fixed, but increases with the system size. Hence, we expect the larger cutoff to be in better agreement with Potoff's calculation. The value of $T_c^*(\infty)$ for the LRC fluid with a cutoff of 2.5σ is about 0.7% larger than that for 5.0σ and they are both close to Smit's calculation given the range of uncertainties. [54]

The critical constants for the TR fluid with a cutoff of 2.5σ are in excellent agreement with those from Wilding. [20] They are also consistent with those from Potoff. [56] The estimate of critical constants for TS fluid with a cutoff of 2.5σ is close to Smit's results. [54]

Predictions of T_c^* from the power law (Eq. (2-23)) are different from those using FSS. The power law critical temperatures are uniformly higher than the values of T_c^* from FSS. The difference is less than 2% in each case (see Table 2.3). The FSS method is more accurate, but the scaling law can provide estimation of the critical point around which histograms are collected when FSS is used to calculate the critical constants for infinite volume.

2.5 Conclusions

We have developed a new method for computing VLE from multiple histogram reweighting. We call this the EOS method because the expressions for the equation of state are constructed separately for the liquid and vapor branches from the histograms. We have used the EOS approach,

Hill's method, and equal area construction to compute VLE. All three methods are in very good agreement.

The difference in $T_c^*(\infty)$ between the TR and TS fluids decreases from 10% to 3.6% as the cutoff distance increases from 2.5σ to 3.5σ. The critical temperature for the LRC fluid is 1.4% larger than $T_c^*(\infty)$ for the TR potential with $r_c^* = 5.0$. The absolute average deviations in the saturation densities for the LRC and TR fluids with cutoffs of 5.0σ are 0.8% and 1% for the vapor and liquid, respectively. This indicates that the TR fluid with $r_c^* = 5.0$ is a reasonable approximation to the LRC fluid, giving quantitative agreement within a few percent at temperatures well below the critical point.

It is commonly assumed that the properties of the LRC fluid are not sensitive to the value of the cutoff for $r_c^* \geq 2.5$. This appears to be true for saturated vapor and liquid densities. However, the values of μ at vapor-liquid coexistence for the LRC fluid are systematically shifted to larger values as the reduced cutoff distance increases from 2.5 to 5.0. The reason for the shift in μ^{sat} with r_c^* is not known. The infinite volume critical temperature for $r_c^* = 2.5$ is about 0.7% larger than that for $r_c^* = 5.0$.

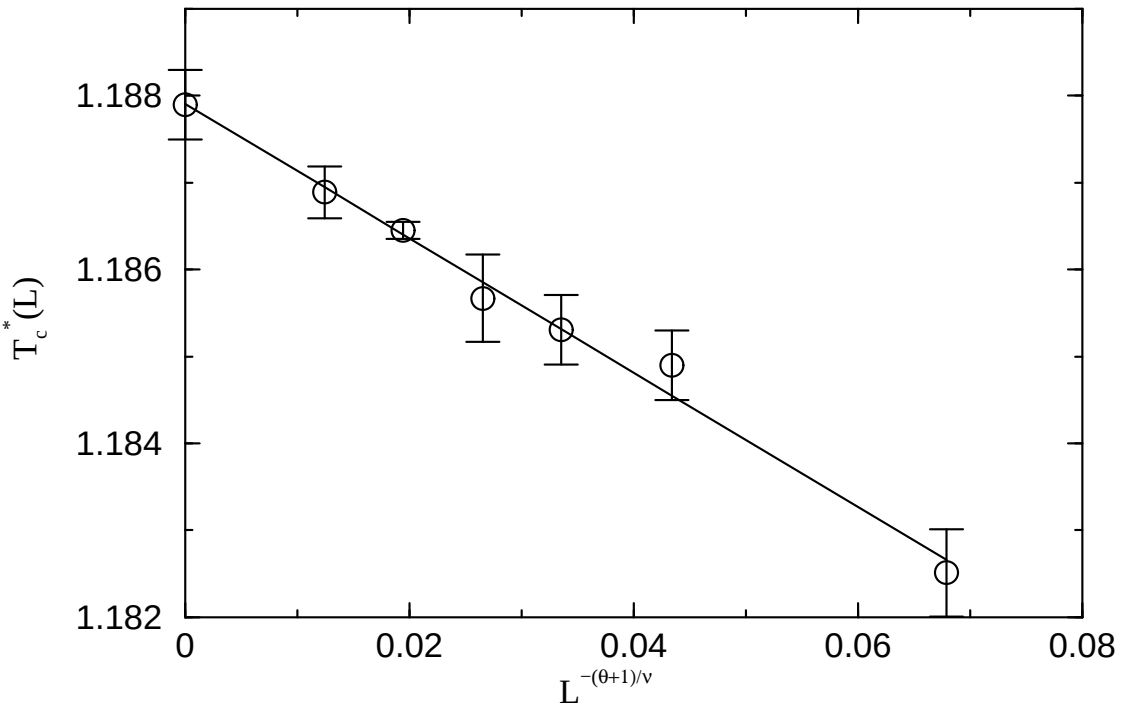

Figure 2.4: The apparent $T_c^*(L)$, plotted as a function of $L^{-(\theta+1)/\nu}$, with $\theta = 0.54$ and $\nu = 0.629$. The estimated value of $T_c^*(\infty)$ from extrapolation to infinite volume of the least squares fit to the data yields 1.1879(4).

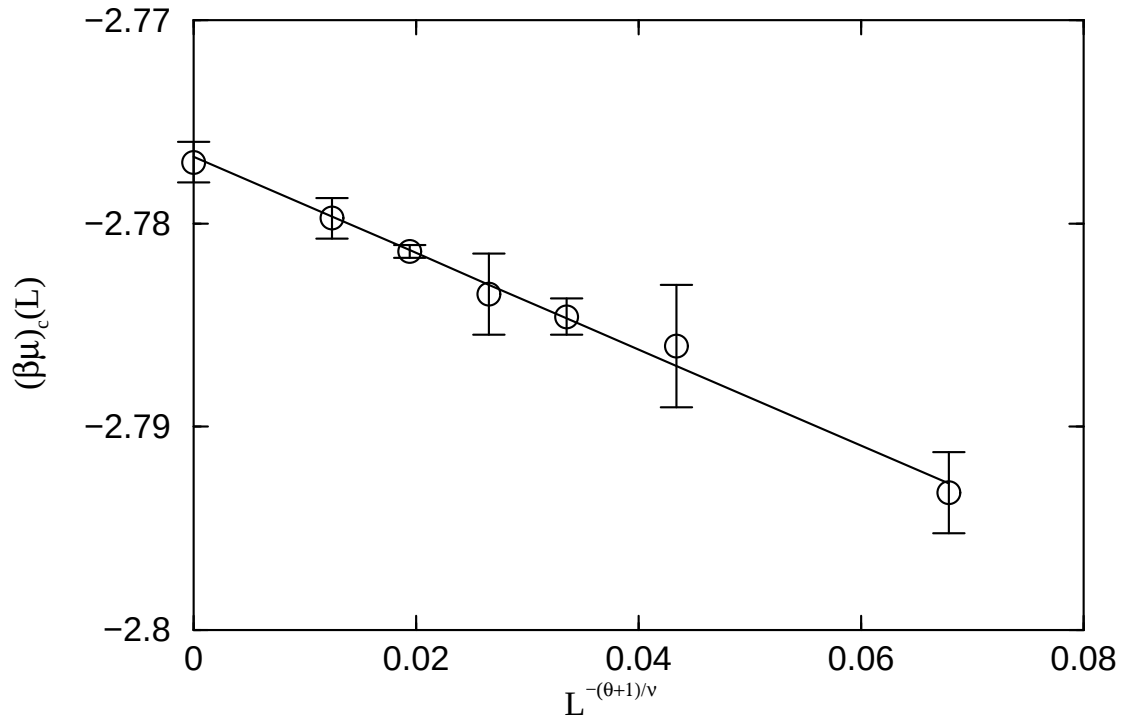

Figure 2.5: The apparent $(\beta\mu)_c(L)$, plotted as a function of $L^{-(\theta+1)/\nu}$ as in Figure 2.4. The estimated value of $(\beta\mu)_c(\infty)$ is $-2.777(1)$

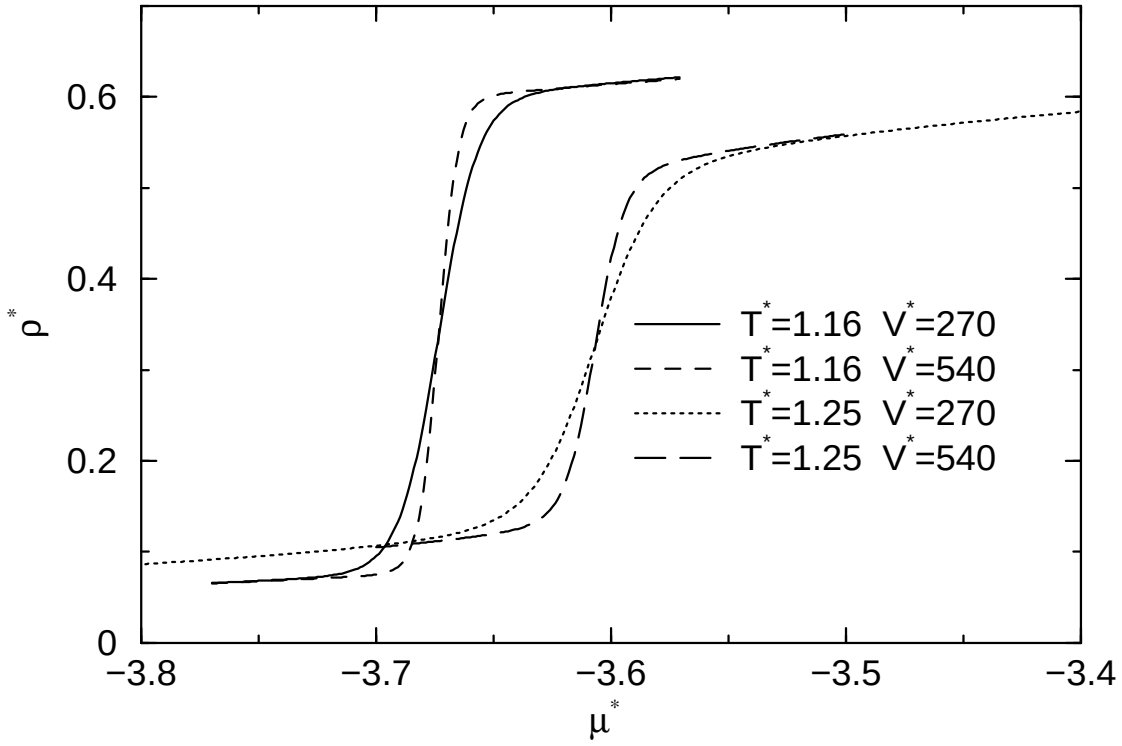

Figure 2.6: Isotherms for two temperatures and two different system sizes for the LRC fluid with a cutoff of 2.5σ.

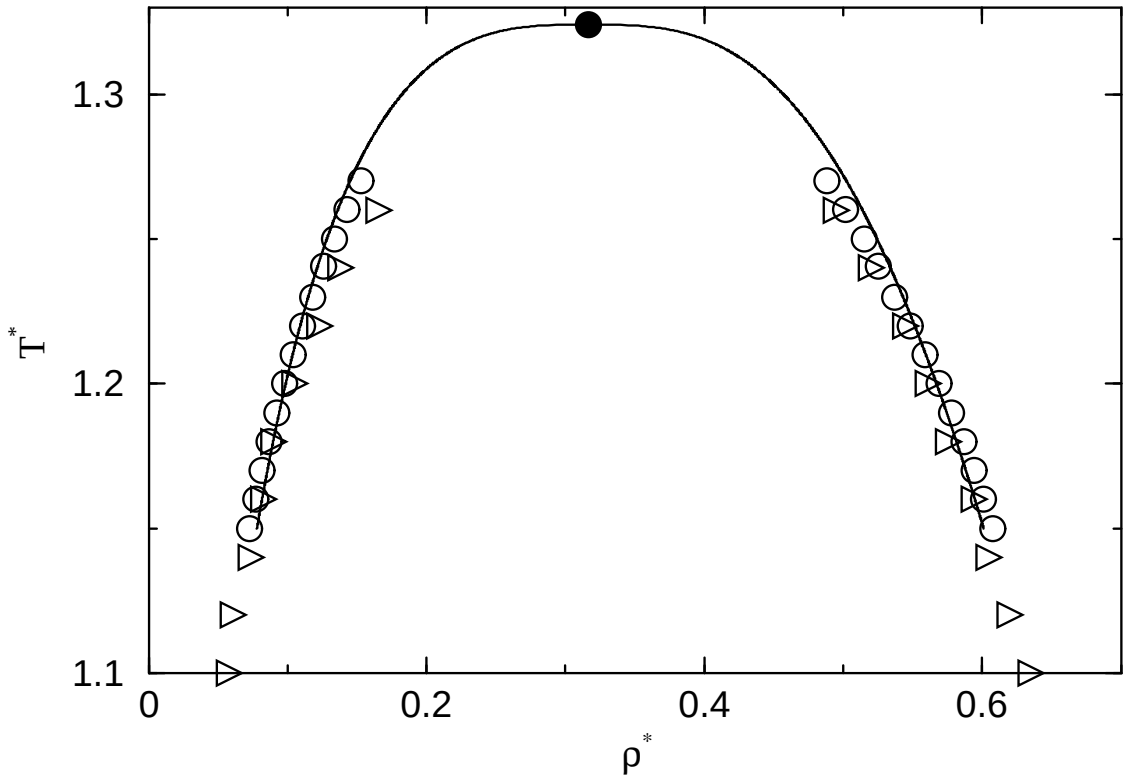

Figure 2.7: Coexistence densities for the LRC fluid with a cutoff of 2.5σ and a volume of $V^* = 1331$. The line is a fit to Eq. (2-23) using the critical point and the coexistence densities in the range $1.15 \leq T \leq 1.20$. The filled circle is the critical point extrapolated from finite-size scaling. The coexistence densities were obtained from Hill's method. Also shown ($\triangleright$) are the results of Conrad and de Pablo for the LRC fluid.[60]

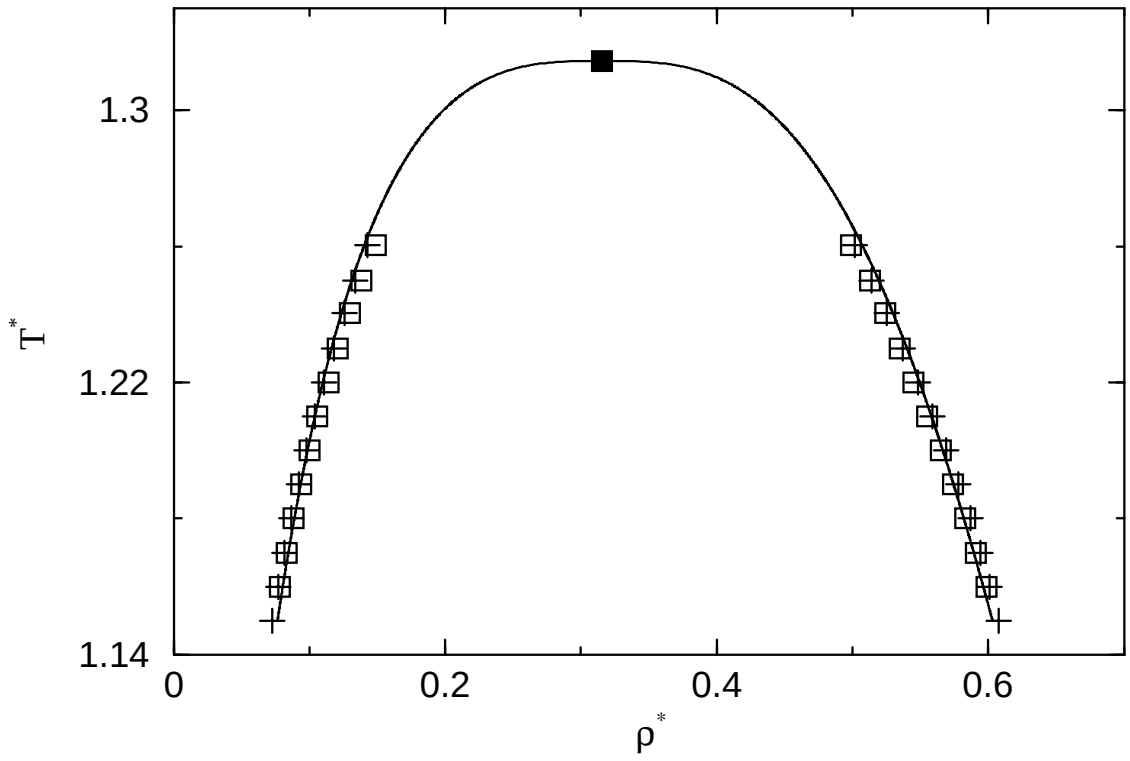

Figure 2.8: The phase diagram for the LRC fluid with a cutoff of 5.0σ (squares). The finite-size corrected critical point for $r_c^* = 5.0$ is shown as the filled square. The line is a fit to Eq. (2-23) using the critical point and the coexistence densities in the range $1.16 \leq T \leq 1.21$. The coexistence densities for $r_c^* = 2.5\sigma$ (pluses) are also included. The system volume was $V^* = 1331$ in both cases.

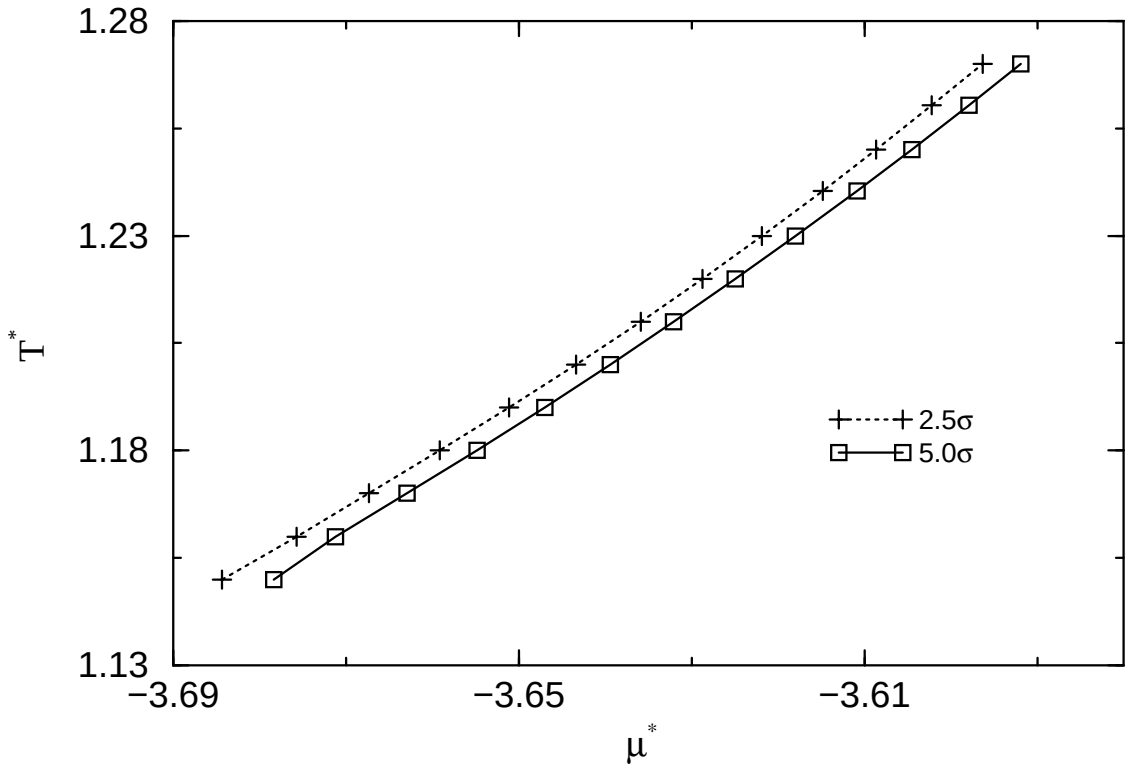

Figure 2.9: A plot of T^*–μ^* at coexistence for $r_c^* = 2.5$ (pluses) and 5.0 (squares), both at $V^* = 1331$. The lines are drawn as a guide to the eye. The value of $\mu^{\rm sat}$ increases with increasing cutoff.

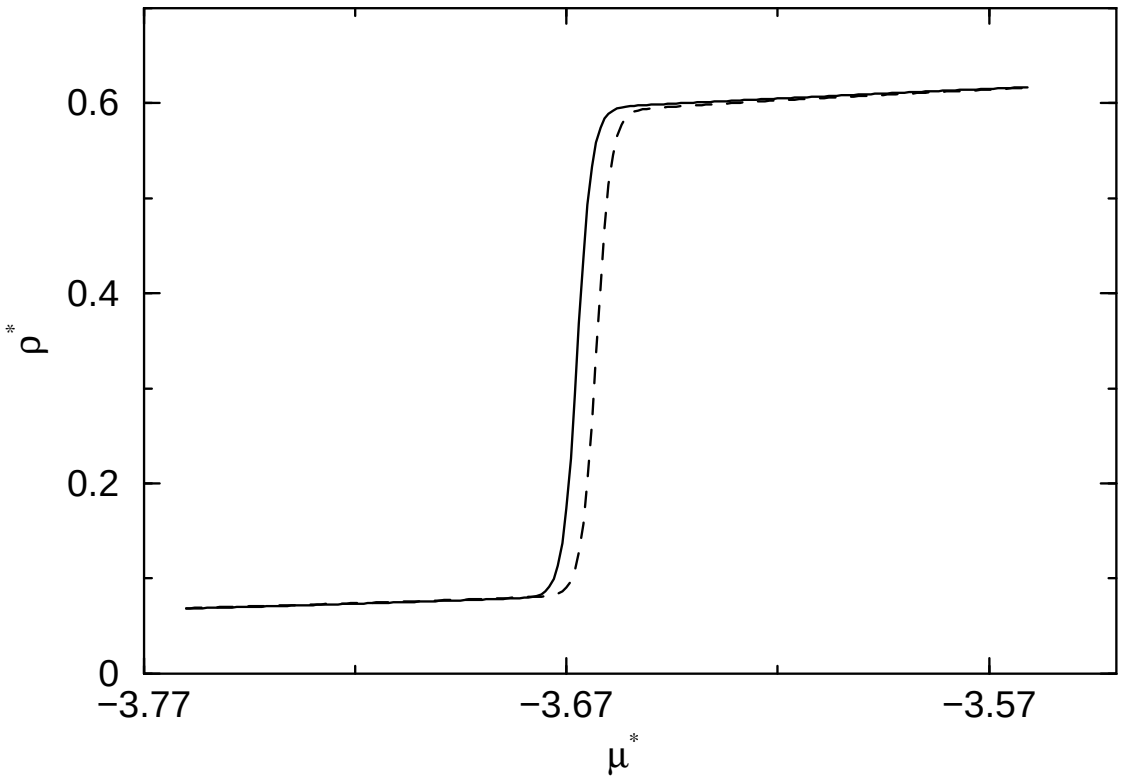

Figure 2.10: The density versus chemical potential isotherms for $r_c^* = 2.5$ (solid line) and 5.0 (dashed line), both for $V^* = 1331$, and $T^* = 1.17$.

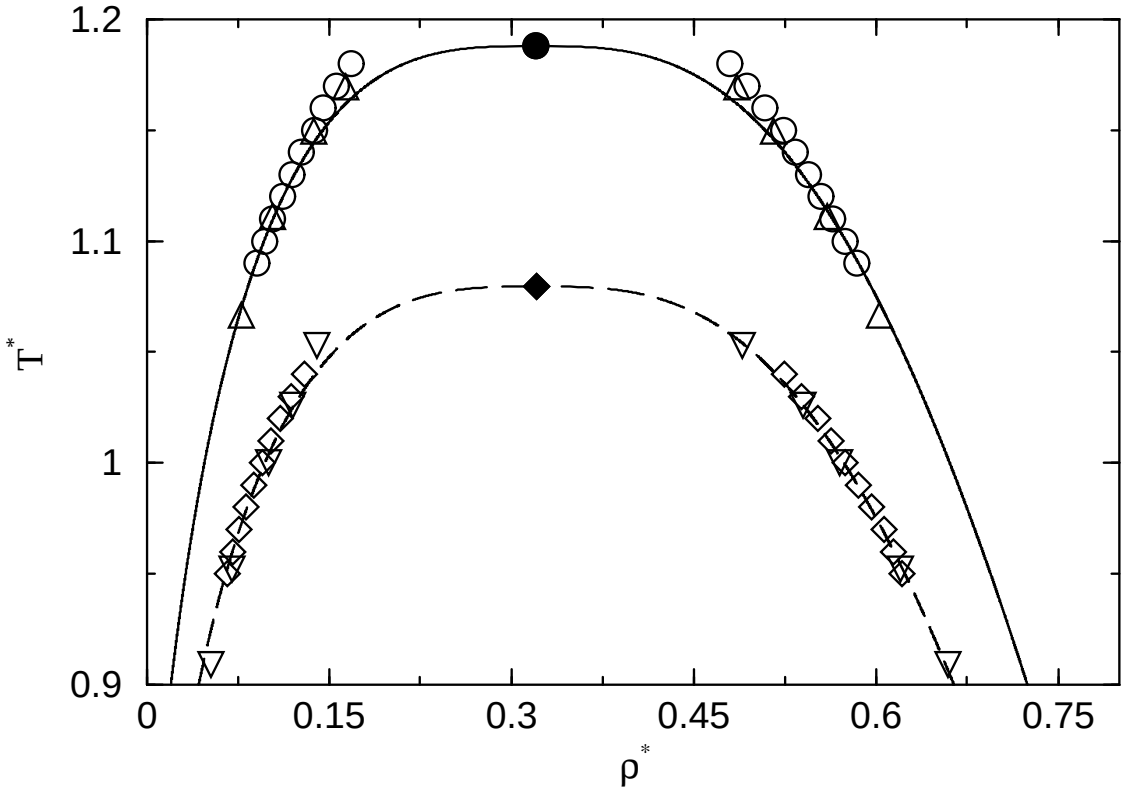

Figure 2.11: The phase diagrams for the TR and TS fluids with $r_c^* = 2.5$ and $V^* = 729$. The open circles (TR) and diamonds (TS) are computed from Hill's method. The filled symbols are the critical constants extrapolated from finite-size scaling. The lines are fits to the low temperature data and the critical points according to Eq. (2-23). The coexistence data for the TR fluid from Wilding[20] ($\triangle$) and the TS fluid from Smit[54] ($\bigtriangledown$) are included for comparison.

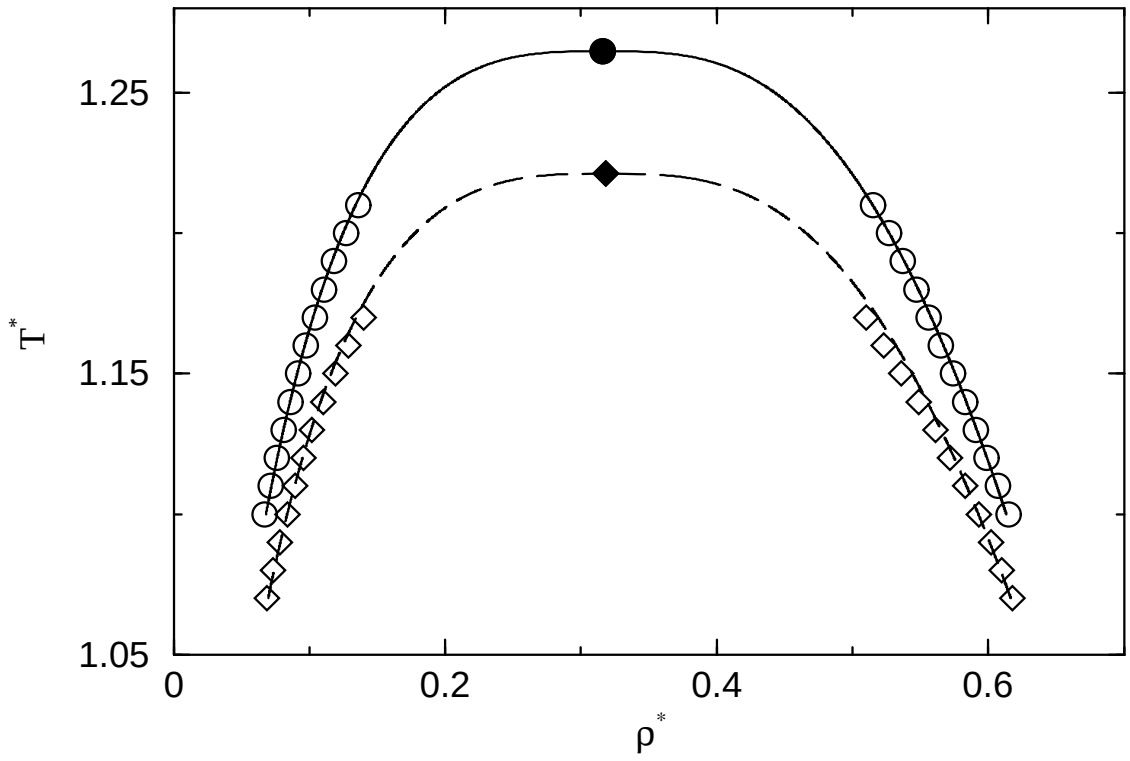

Figure 2.12: The phase diagrams for the TR and TS fluids with a cutoff of $r_c^* = 3.5$ and a volume of $V^* = 729$. The data for the TR fluid are shown as open circles, and the data for the TS fluid are denoted by the open diamonds. The infinite volume critical constants are shown as filled symbols. The lines are fits of the critical constants and VLE data away from criticality to Eq. (2-23).

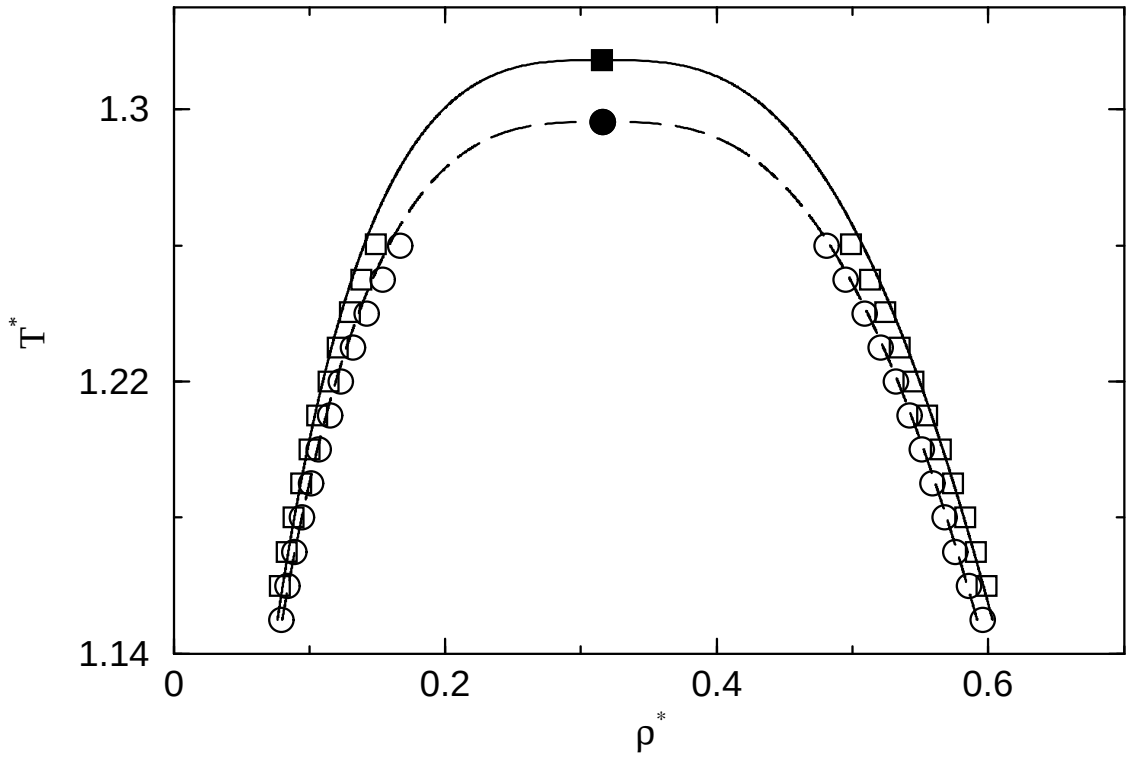

Figure 2.13: The phase diagrams for the LRC (open squares) and TR (open circles) fluids with $r_c^* = 5.0$ and $V^* = 1331$. The finite-size scaling corrected critical constants are shown as filled symbols. The lines are fits of the critical constants and VLE data away from criticality to Eq. (2-23).

3.0 PHASE TRANSITIONS OF ADSORBED FLUIDS COMPUTED FROM MULTIPLE HISTOGRAM REWEIGHTING [1]

3.1 Introduction

Confined fluids are known to exhibit a rich variety of phase transitions that are absent in bulk fluids[6,70,71]. Perhaps three of the most interesting phenomena are capillary condensation, prewetting transitions, and layering transitions. Each of these transitions have previously been studied in some detail through the use of a variety of computer simulation techniques. Different simulation methods are often required to characterize these different phenomena; for example grand potential or Gibbs ensemble calculations are needed to locate capillary condensation[72–74]. Prewetting transitions are often located by plotting the isotherms and density profiles from grand canonical Monte Carlo or isothermal-isobaric Monte Carlo simulations[75,76]. Layering transitions have been observed from grand canonical Monte Carlo simulations coupled with grand potential calculations. [73].

In this paper we demonstrate that multiple histogram reweighting (MHR)[11–13] can be an accurate and efficient tool for studying phase transitions in confined fluids. The MHR method has been shown to be useful for studying the phase behavior of bulk fluids[4,5,77,78], but has not been widely used for studying the properties of confined fluids.

Gelb and Gubbins have applied the histogram reweighting technique to study the phase diagram of a simple binary liquid mixture in the semi-grand canonical ensemble[79]. They used single histogram reweighting to estimate the biasing potential needed for barrier crossing. Escobedo and de Pablo have studied the secondary transition for a 12-6 Lennard-Jones fluid in a composite large-sphere matrix with histogram reweighting analysis[80]. Recently, Potoff and Siepmann have calculated the effect of branching on the fluid phase behavior of alkane monolayers using histogram reweighting with the finite-size scaling technique[81].

[1] This chapter is reprinted from reference[45]

Capillary condensation occurs when a fluid is strongly adsorbed in a micropore below the capillary condensation critical temperature. The transition is characterized by a gas condensing to a liquid-like state that entirely fills the pore space at a bulk pressure less than the saturation value[6,82]. Grand canonical Monte Carlo (GCMC) simulations are typically used to construct the adsorption isotherms for the prediction of capillary condensation. Peterson and Gubbins[72] calculated the grand potential through integration of isotherms and paths of constant chemical potential in order to compute the equilibrium chemical potential for capillary condensation. In a completely different approach, Heffelfinger *et al.*[7] used quenched molecular dynamics to study capillary condensation in cylindrical pores. The chemical potentials of the gas-like and liquid-like regions were computed from the potential distribution theorem for inhomogeneous fluids. Some prior knowledge of the phase behavior is required to implement this approach, because the overall density must be chosen such that the system is in the unstable region when quenched. Panagiotopoulos extended the Gibbs ensemble Monte Carlo method for the prediction of adsorption and capillary condensation[74]. The coexistence densities of gas-like and liquid-like phases in equilibrium inside a pore can be obtained through a single pore-pore calculation. However, a series of pore-fluid calculations are then needed to construct the isotherm.

The existence of wetting transitions was first predicted in 1977 independently by Cahn[83] and Ebner and Saam[84]. It was predicted that a gas that weakly adsorbs onto a solid surface will exhibit nonwetting behavior at low temperature and may undergo a first order transition to wetting behavior at a higher temperature T_w. By nonwetting we mean that the thickness of a film adsorbed on a surface remains finite at all pressures below the saturation vapor pressure; by wetting we mean that the film thickness diverges as the saturation pressure is approached. Prewetting occurs when there is a first order transition from a thin-film to a thick-film adsorbed on the surface. The prewetting transition terminates at the critical prewetting temperature[70,85]. Finn and Monson were the first to observe the existence of a prewetting transition through molecular simulation. [76] They used isothermal-isobaric Monte Carlo to identify the prewetting transition by observing the jump in adsorption on an isotherm associated with the thin- to thick-film transition[76]. Large

fluctuations in the coverage typically accompany prewetting transitions, making precise location of the transition a difficult task. For this reason, later work by Fan and Monson[86] utilized calculation of the surface tensions in the thin- and thick-films in order to locate the prewetting transition more precisely. Experiments and simulations by Mistura *et al.*[87] recently demonstrated that Ar on solid CO_2 actually exhibits triple-point wetting rather than prewetting as predicted by Monson and coworkers. The reason for this discrepancy is that the potential models used in the simulations [76,86] do not accurately represent the potential surface of the real Ar-CO_2 system. More realistic solid-fluid potential models[87] are more strongly attractive than the potential used by Monson *et al.* We note that grand canonical Monte Carlo simulations have been used to study prewetting transitions for a variety of other systems[88,89].

Thick films adsorbing on a substrate can either grow continuously or in a stepwise fashion. If the growth is stepwise, then each layer grows by a succession of first-order layering transitions at pressures lower than the bulk saturation pressure[90]. Layering transitions of simple fluids and lower alkanes on graphite have been studied extensively through experimental techniques[91]. Iwamatsu has shown that layering transitions can be expected to occur for systems that exhibit both incomplete and complete wetting[92]. For wetting growth the thickness of the film increases to infinity as the bulk saturation pressure is approached. If the wetting is incomplete then a transition from incomplete wetting to wetting will occur as the temperature is increased. Layering transitions will persist to T_w if $T_w < T_R$ where T_R is the bulk roughening transition[93]. If $T_w > T_R$ then a thin-film to thick-film prewetting transition precedes divergence of the film thickness. Each of the layers terminates at a layer critical point temperature, $T_c(m)$, where m is the number of layers in the film. It has been found that $T_c(m)$ can approach the triple point either from above[93] or below[94] with increasing m.

In this paper we demonstrate that MHR can be applied accurately and efficiently to compute capillary condensation, prewetting transitions, and layering transitions. Histograms for a given system can be combined in order to compute isotherms at any of the conditions spanned by the simulations. The location of phase transitions can be accurately computed through the equal area

criterion[44] without resorting to computation of the grand potential[72,73]. The precision of MHR allows us to observe crossover in the critical exponents for capillary condensation. This is difficult to accomplish through a series of isolated simulations. In this paper, we use MHR to construct estimates for the capillary condensation, wetting temperature and prewetting critical temperatures, and to find layering transition pressures for propane on graphite.

3.2 Theory and Methods

The basic idea of MHR is that histograms collected from a number of independent simulations may be combined to construct an estimate for the partition function[11–13]. The multiple histogram reweighting technique can be used to accurately calculate phase diagrams of bulk fluids[4,5,44,77,78]. This method allows the calculation of equilibrium properties over a range of conditions from a relatively small number of state points. The phase diagrams from histogram reweighting can be very accurate[4]. The coexistence densities and saturation chemical potential can be calculated through the use of the equal area criterion and Hill's method[44].

Sufficient overlap between histograms of adjacent state points is necessary in order to implement the MHR technique. We here describe one method for checking for the extent of overlap between pairs of state points. The grand canonical partition function can be written as

$$\begin{aligned} \Xi(\mu, V, T) &= \sum_N \sum_{U_N} \exp[N\beta\mu - \beta U_N]\Omega(N, V, U_N) \\ &= \sum_N \sum_{U_N} CH(U_N, N), \end{aligned} \tag{3-1}$$

where $\beta = 1/kT$, k is the Boltzmann constant, T is the absolute temperature, $\Omega\,(N, V, U_N)$ is the microcanonical partition function, C is a simulation-specific constant, and $H(U_N, N)$ is the two dimensional histogram of configurational energy, U_N, and number of molecules, N, collected during the simulation. The configurational chemical potential, μ, is defined by

$$\mu = \mu^f - kT \ln \Lambda^3 + kT \ln(q_{\text{int}}), \tag{3-2}$$

where μ^f is the full chemical potential, Λ is the thermal de Broglie wavelength, and q_{int} is the intramolecular partition function, accounting for density independent terms such as rotational and vibrational Hamiltonians. The grand canonical partition function for a different state point with configurational chemical potential μ', and temperature T' can be estimated by single histogram reweighting

$$\begin{aligned}\Xi(\mu', V, T') &= \sum_N \sum_{U_N} \exp[N\beta'\mu' - \beta' U_N]\Omega(N, V, U_N) \\ &= \sum_N \sum_{U_N} \exp[N(\beta'\mu' - \beta\mu) - (\beta' - \beta)U_N] H_{\mu,V,T}(U_N, N) C, \end{aligned} \tag{3-3}$$

where $H_{\mu,V,T}(U_N, N)$ is the histogram collected at (μ, V, T). The ratio of the grand canonical partition functions between these two state points based on the histogram collected at (μ, V, T) is computed through

$$\frac{\Xi(\mu', V, T')}{\Xi(\mu, V, T)} = \frac{\sum_N \sum_{U_N} \exp[N(\beta'\mu' - \beta\mu) - (\beta' - \beta)U_N] H_{\mu,V,T}(N, U_N)}{\sum_N \sum_{U_N} H_{\mu,V,T}(U_N, N)}. \tag{3-4}$$

Likewise, one may collect histogram data at the state point defined by (μ', V, T') and extrapolate to (μ, V, T). The ratio of these two partition functions can be expressed by interchanging μ with μ' and T with T' in Eq. (3-4). In the thermodynamic limit the following equation must be satisfied,

$$\frac{\Xi(\mu', V, T')}{\Xi(\mu, V, T)} \times \frac{\Xi(\mu, V, T)}{\Xi(\mu', V, T')} = 1. \tag{3-5}$$

We use Eq. (3-5) to check the extent of overlap between histograms by performing relatively short GCMC simulations at each state point. Not all of the fluctuations in energy and particle number accessible to the state points in the thermodynamic limit can be observed in a finite simulation. Consequently, Eq. (3-5) will not be exactly satisfied for state points extrapolated from histogram reweighting, but should be approximately satisfied within some tolerance

$$\left.\frac{\Xi(\mu', V, T')}{\Xi(\mu, V, T)}\right|_{\text{HR}} \times \left.\frac{\Xi(\mu, V, T)}{\Xi(\mu', V, T')}\right|_{\text{HR}} = 1 \pm \delta, \tag{3-6}$$

where the subscript HR indicates that the partition function in the numerator has been extrapolated from histogram reweighting. We have found that $\delta = 0.65$, that is, values of the left hand side of Eq. (3-6) between 0.35 and 1.65, indicate sufficient overlap of the two state points. We have

used this method to select the state points to simulate in longer production runs. We denote this procedure to check the overlap as the single histogram reweighting method (SHR). Note that Eq. (3-6) is not symmetric with respect to inversion because we stipulate that the extrapolated partition functions are always in the numerator.

Details of our implementation of the multiple histogram reweighting technique are described elsewhere[44]. The ratios of the Ξs for several state points were obtained from multiple histogram reweighting and compared with the values calculated from Eq. (3-4) in order to verify that the degree of overlap between adjacent state points was sufficient. Single histogram reweighting from Eq. (3-6) and MHR were used to analyze the histograms. The results are presented in Table 3.1. The values computed from MHR are based on a combination of 30 histograms. The values of the ratios Ξ_2/Ξ_1 between 10 pairs of state points as calculated from SHR and MHR are tabulated in Table 3.1. The good agreement between the two methods indicates that a value of $\delta \leq 0.65$ in Eq. (3-6) is indicative of histograms with sufficient overlap.

3.3 Capillary Condensation

In this section we present results of MHR for capillary condensation. The potential model used to investigate capillary condensation is the same as that used by Jiang *et al.*[73], namely, methane adsorbing in a graphite slit-like pore of width $H = 5\sigma$, where σ is the Lennard-Jones (LJ) diameter of a methane molecule. The fluid particles in the slit pore interact with each other via the truncated and shifted (TS) LJ potential

$$\phi_{\mathrm{TS}}(r) = \begin{cases} \phi(r) - \phi(r_c) & r \leq r_c \\ 0 & r > r_c \end{cases} , \tag{3-7}$$

where $\phi(r)$ is the full LJ potential given by

$$\phi(r) = 4\epsilon \left[\left(\frac{\sigma}{r}\right)^{12} - \left(\frac{\sigma}{r}\right)^{6} \right], \tag{3-8}$$

where ϵ is the well depth and σ is the molecular diameter. The value of the cutoff was 2.5σ as used in ref.[73]. The solid-fluid interactions are represented by the 10-4-3 solid-fluid potential[95,96]

$$\phi_{\rm sf}(z) = 2\pi\rho_{\rm s}\epsilon_{\rm sf}\sigma_{\rm sf}^2\Delta\left[\frac{2}{5}\left(\frac{\sigma_{\rm sf}}{z}\right)^{10} - \left(\frac{\sigma_{\rm sf}}{z}\right)^{4} - \left(\frac{\sigma_{\rm sf}^4}{3\Delta\left(0.61\Delta + z\right)^3}\right)\right], \tag{3-9}$$

where z is the distance between a fluid particle and a solid surface, Δ is the separation between the individual graphene planes, and $\rho_{\rm s}$ is the solid density. The cross-parameters $\sigma_{\rm sf}$ and $\epsilon_{\rm sf}$ were calculated from the Lorentz-Berthelot combining rules. The parameters were taken from refs.[95,96]. They are $\sigma_{\rm ff} = 0.381$ nm, $\epsilon_{\rm ff}/k = 148.1$ K, $\sigma_{\rm ss} = 0.340$ nm, $\epsilon_{\rm ss}/k = 28.0$ K, $\Delta = 0.335$ nm, and $\rho_{\rm s} = 114$ nm^{-3}. For a given slit pore of width H, the external potential experienced by a fluid molecule at z is given by $\phi_{\rm ext}(z) = \phi_{\rm sf}(z) + \phi_{\rm sf}(H - z)$.

The volume of the unit cell was fixed at $900\sigma^3$ with a separation of 5σ between the two opposite adsorbent surfaces. The lateral dimensions of the box were equal in the x and y directions. Periodic boundary conditions in the x and y directions were employed. We used 7×10^7 trials to achieve equilibrium and 7×10^7 moves for data collection. Histograms were collected every 14 moves. Standard reduced units were used with the reduced temperature given by $T^* = kT/\epsilon$ and the reduced density $\rho^* = \rho\sigma^3$. The reduced chemical potential is $\mu^* = \mu/\epsilon$.

We combined 30 histograms in the reduced temperature region from 0.6 to 0.9. Two representative isotherms are plotted in Fig. 3.1. As a general test of the accuracy of the MHR isotherms we have also plotted state points calculated directly from GCMC simulations in Fig. 3.1. We show data from simulations that were included in generating MHR isotherms and also data from state points that were not used to construct the histograms in the MHR. The differences between densities obtained from multiple histogram reweighting and those from GCMC simulations are small. The average densities obtained from 19 GCMC simulations not included in multiple histogram reweighting, were compared with densities from multiple histogram reweighting. The isotherms examined were $T^* = 0.9$, 0.85, 0.825, 0.8, 0.7, and 0.6. The average absolute error in the densities between GCMC and MHR is 3×10^{-3}. The maximum and minimum absolute errors are 7×10^{-3}

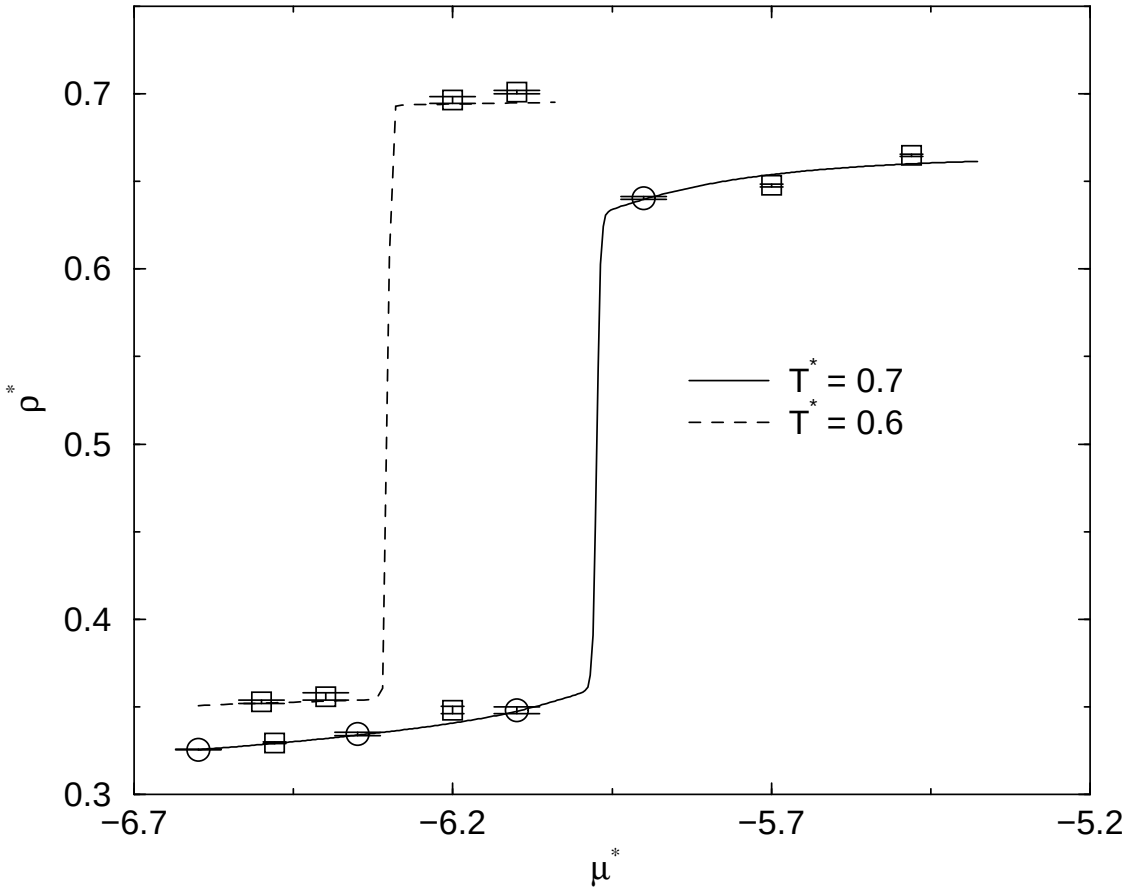

Figure 3.1: Isotherms for $T^* = 0.7$ (solid line) and 0.6 (dashed line) from multiple histogram reweighting for methane adsorption in a graphitic slit pore of width 5σ. Data from individual GCMC simulations that were ($\circ$) and were not ($\square$) included in the MHR calculations are shown.

and 2×10^{-4}, respectively. Many of the values from MHR agree with those from the simulations within the uncertainty of the simulations.

For $T^* = 0.7$, the values of the coexistence densities computed from MHR are 0.358 and 0.631 for the vapor-like and liquid-like branches, respectively, and the capillary condensation coexistence chemical potential μ^*_{cc} is -5.978. These data are in excellent agreement with the values from Jiang *et al.*[73], who reported densities of 0.36 and 0.627 for the vapor-like and liquid-like branches, respectively, and $\mu^*_{cc} = -5.93$. Jiang *et al.* located the coexistence points by calculating the grand potentials in each branch. The equilibrium transition occurs when the grand potentials in each phase are equal[72], whereas adsorption and desorption isotherms are plagued by metastability-induced hysteresis.

The lowest temperatures where histograms were collected were 0.6 and 0.65 for the vapor-like and liquid-like sides, respectively. The $T^* = 0.6$ isotherm was generated by extrapolating the histograms at higher temperatures and lower densities in order to generate the liquid-like branch of the isotherms. This is possible because fluctuations recorded at higher temperatures and lower densities sample some of the microstates important at lower temperatures and higher densities, giving a physically realistic extrapolation. The reliability of the extrapolation is confirmed by the agreement between the MHR isotherm and the two simulation points (not included in the histograms) on the liquid-like branch shown in Figure 3.1. The values of coexistence densities from MHR are 0.360 and 0.692 for the vapor-like and liquid-like branches, respectively. These values are very close to those of 0.36 and 0.68 from Jiang *et al.*[73]. The MHR isotherm gives $\mu^*_{cc} = -6.309$, which is in good agreement with the value computed from grand potential calculations of -6.32[73].

The coexistence densities in the reduced temperature region from 0.68 to 0.76 were fitted to the scaling law and rectilinear law[54].

$$\frac{\rho_l^* + \rho_v^*}{2} = \rho_c^* + A(T^* - T_c^*) \tag{3-10}$$

$$\rho_l^* - \rho_v^* = B(T_c^* - T^*)^{\beta_c} \tag{3-11}$$

where ρ_l^* and ρ_v^* are the reduced coexistence densities for the liquid-like and vapor-like branches, respectively, T_c^* and ρ_c^* are the reduced critical temperature and density, β_c is the critical exponent, A and B are fitting parameters. Regression of the MHR equilibrium data to Eqns. (3-10) and (3-11) gave $T_c^* = 0.77$, $\rho_c^* = 0.482$, and $\beta_c = 0.119$. The fitted value of β_c is reasonably close to the value of 0.125 (1/8) for the 2-D Ising university class[97]. The data calculated from MHR and the fitting are shown in Figure 3.2.

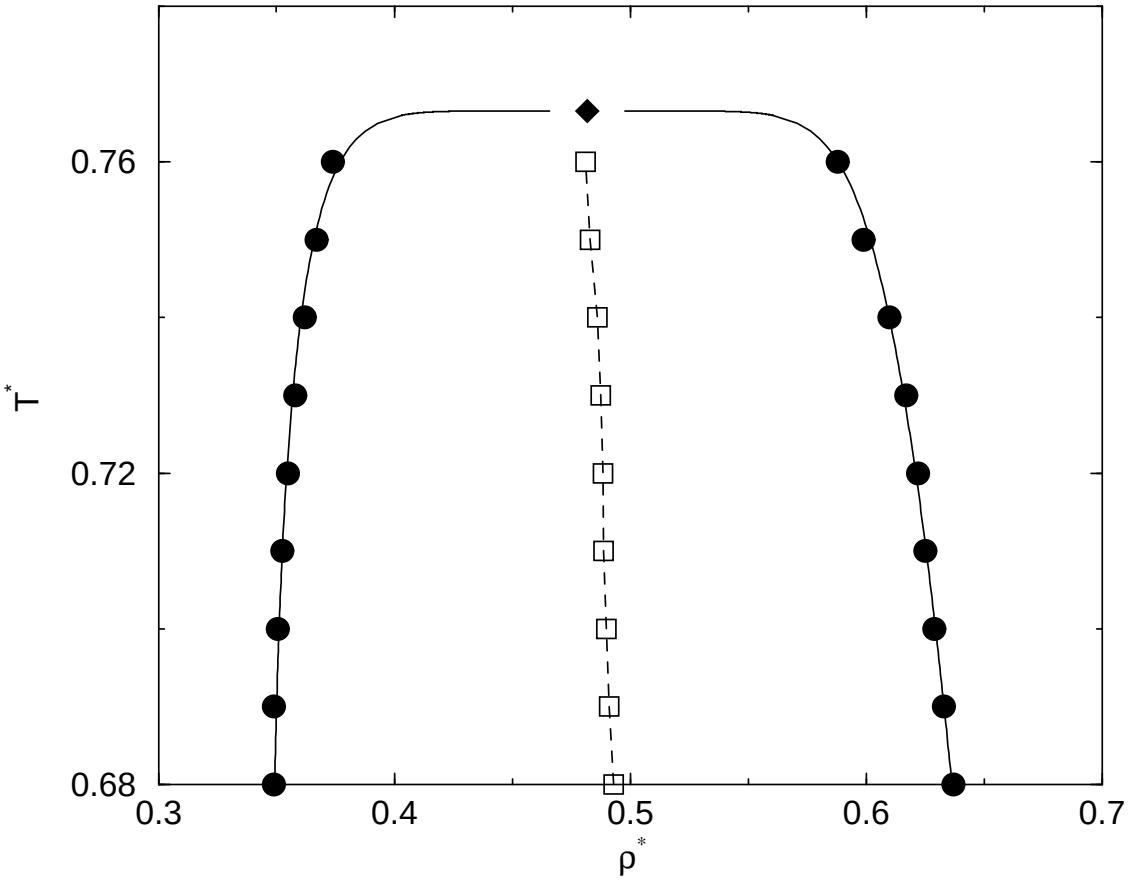

Figure 3.2: The T^*–ρ^* phase diagram for capillary condensation of methane in a graphitic slit pore. The filled circles are the coexistence data calculated from the equal area criterion. The filled diamond is the critical point estimated from fitting the coexistence data to the rectilinear and scaling laws, Eqns. (3-10)-(3-11). The solid line is the fit to the data. The squares are the rectilinear diameters. The dashed line is shown as a guide to the eye.

The crossover of the effective exponent from 2-D Ising-like (1/8) away from the critical point to the mean-field value (1/2) in the immediate vicinity of the critical point can be observed clearly in Figure 3.3. These results reveal the 2-D behavior of capillary condensation. As Mon and Binder

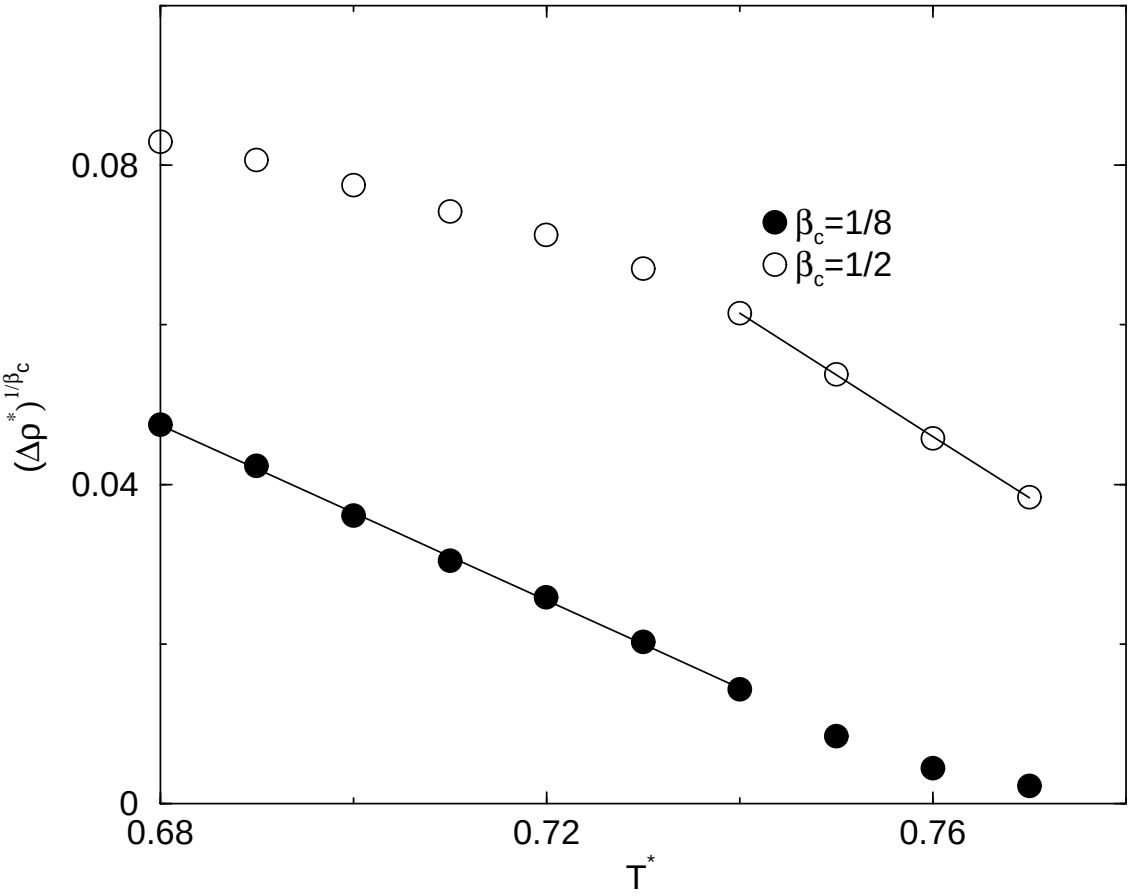

Figure 3.3: Scaled width of the coexistence data versus reduced temperatures for the capillary condensation of methane in a graphitic slit pore. The 2-D Ising exponent of $\beta_c = 1/8$ is shown as • and ∘ denotes the mean-field value of $\beta_c = 1/2$.

have pointed out[52], one expects the observed exponents to correspond to the correct universality class when the correlation length is much less than the simulation box length. This is indeed the case for low temperatures, corresponding to $T^* < 0.74$ for the system represented in Figure 3.3. At temperatures near the capillary condensation critical point the correlation length becomes large compared with the box length and the fluid then conforms to mean field behavior due to the suppression of critical fluctuations. Figure 3.3 is, to the best of our knowledge, the first observation of crossover for capillary condensation.

3.4 Prewetting

In this section we present details and results of our MHR calculations for a system that exhibits a prewetting transition. We have investigated the same system studied by Monson and coworkers, namely, Ar adsorbing on a solid CO_2 surface[76,86,98]. Their simulations were performed for a fluid interacting through the truncated LJ potential,

$$\phi_{\rm TR}(r) = \begin{cases} \phi(r) & r \le r_c \\ 0 & r > r_c \end{cases} , \tag{3-12}$$

where $\phi(r)$ is the full LJ potential given by Eq. (3-8) and r_c is 2.5σ. The fluid-solid interaction at the adsorbing wall is given by the LJ 9-3 potential,

$$\phi_{\rm w}(z) = \frac{2\pi}{3}\rho_{\rm w}\sigma_{\rm w}^3\epsilon_{\rm w}\left[\frac{2}{15}\left(\frac{\sigma_{\rm w}}{z}\right)^9 - \left(\frac{\sigma_{\rm w}}{z}\right)^3\right], \tag{3-13}$$

with $\sigma_{\rm w} = 0.3727$ nm, $\epsilon_{\rm w}/k = 153$ K, $\rho_{\rm w}\sigma_{\rm w}^3 = 0.988$, and z is the distance between the fluid and the adsorbing wall. The opposite wall was chosen to be reflecting. The parameters for the fluid-fluid interactions are $\epsilon/k = 119.8$ K, and $\sigma = 0.340$ nm.

Monson and coworkers[76,86,98] reported isotherms between $T^* = 0.83$ and 1.0 for pressures up to saturation. Their estimate for the reduced wetting temperature is $T_w^* = 0.84 \pm 0.01$ and the reduced prewetting critical temperature estimate is $T_{pwc}^* = 0.94 \pm 0.02$. They observed a prewetting

transition at $T^* = 0.88$ from their simulations, but no prewetting transitions at $T^* = 0.83$ and $T^* = 0.80$.

In this work we have chosen the volume of the unit cell for the Ar/CO_2 model system to be $1620\sigma^3$ with $H = 20\sigma$. Periodic boundary conditions were applied in the x and y directions. We used 10^7 steps for equilibration followed by an additional 10^8 steps for data collection. Histograms were collected at every step. We collected and combined 30 histograms in the temperature region from 0.8 to 1.05. We compute the total, not excess adsorption in this work. Note that the equal area criterion can be used with the total adsorption to find prewetting transitions. The bulk density term adds a constant to both the thin and thick films at a fixed T^* and μ^*. This constant cancels out when computing the difference between the areas of the probability density distributions. The ability to use total instead of excess adsorption isotherms is an advantage because the procedure for computing excess adsorption in a simulation is somewhat ambiguous[99–101]. Several isotherms computed from MHR are shown in Figure 3.4,

along with results from GCMC simulations. The differences between densities obtained from GCMC simulations and MHR are typically smaller than the errors in the simulations. Prewetting is associated with the first S-shaped rise in coverage in Figure 3.4 for $T^* = 0.83$ and 0.88. The second rise and plateau are associated with box filling close to the bulk saturation point. The prewetting transition exhibits considerable rounding due to finite-size effects[67]; hence it is difficult to tell if there is a first order transition from the shape of the isotherm. The coexistence densities and chemical potentials were computed from the equal area criterion as for capillary condensation. Hill's method was used to get an initial estimate for the value of the coexistence chemical potential [44]. The existence of two distinct peaks with equal areas in the density probability is sufficient to identify the transition as first order. The density probability distribution at $T^* = 0.83$ and $\mu^* = -3.801$ is shown in Figure 3.5.

We also obtained a two peak equal area density distribution for $T^* = 0.80$. This is significant because Monson and coworkers did not observed prewetting transitions at these temperatures. At these low temperatures, the prewetting transition pressure is closer to the saturation pressure than

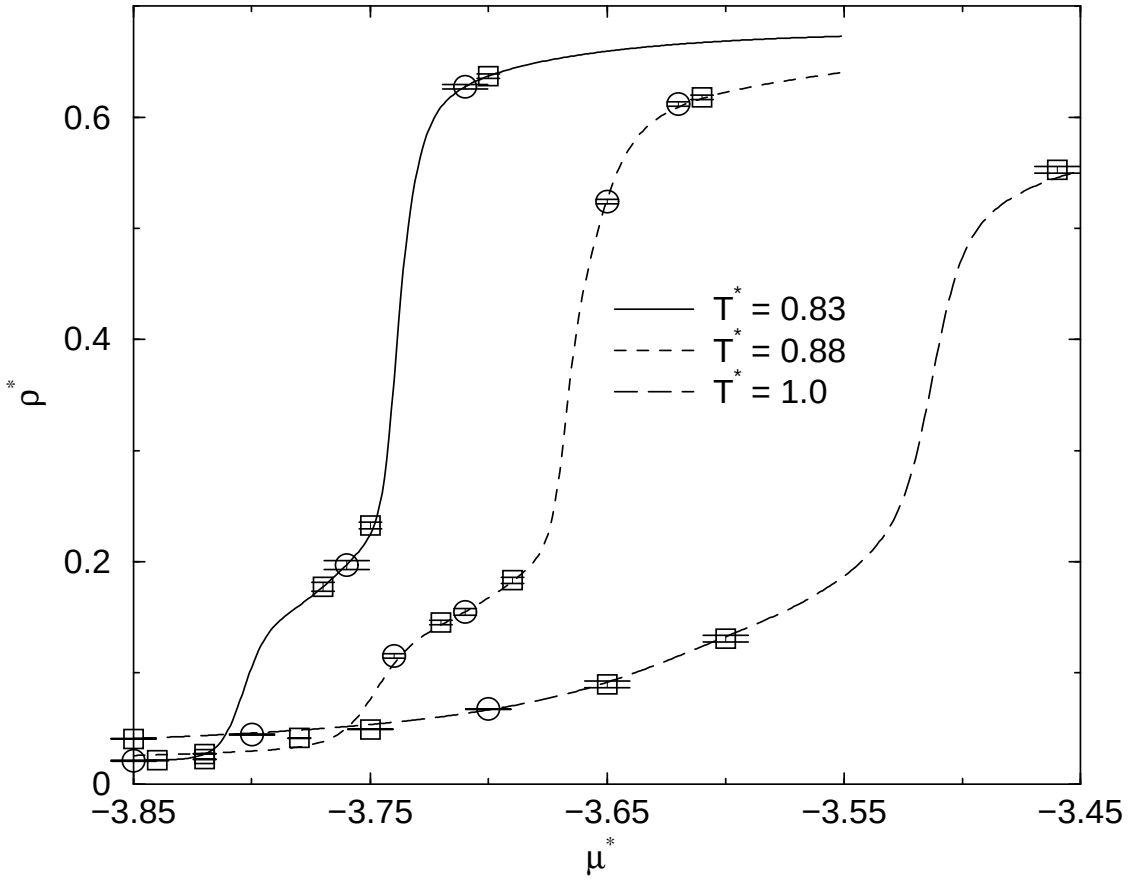

Figure 3.4: Isotherms for $T^* = 0.83$ (solid line), 0.88 (dashed line), and 1.0 (long dashed line) from multiple histogram reweighting for Ar adsorption on solid CO_2. Data from individual GCMC simulations that were ($\circ$) and were not ($\square$) included in the MHR calculations are shown.

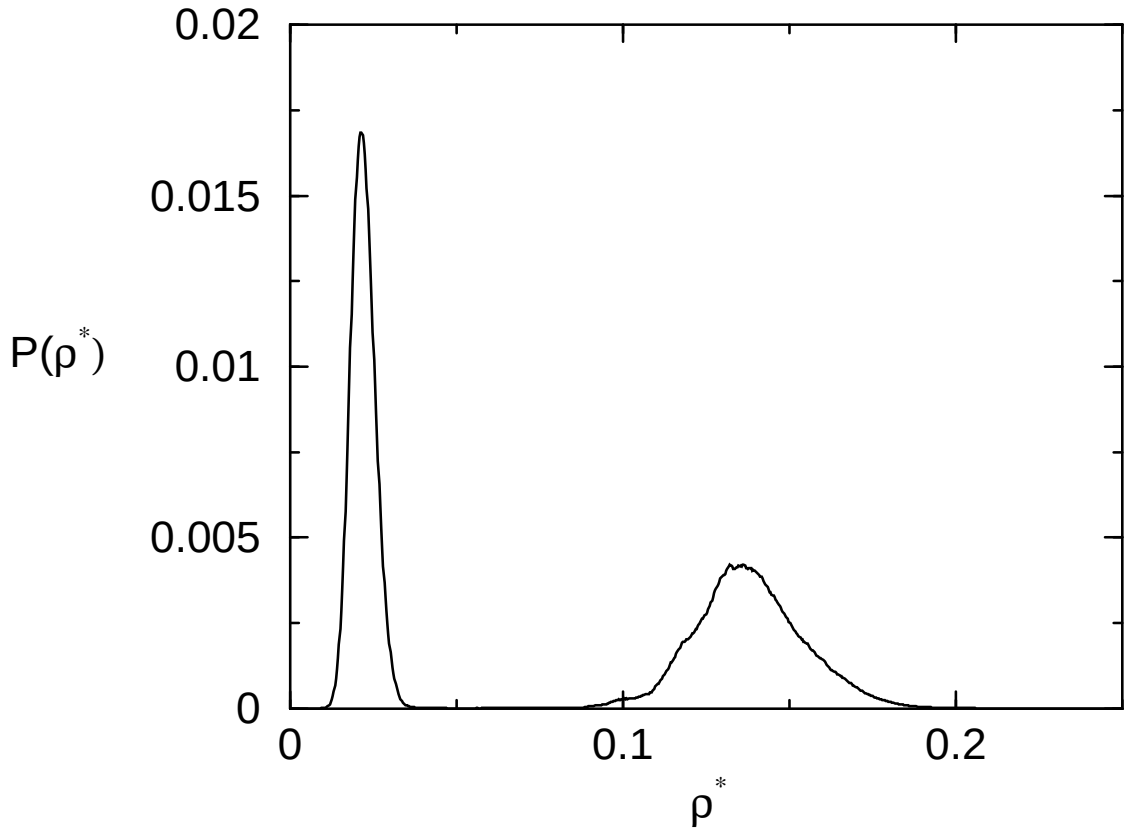

Figure 3.5: Density probability distribution for the same system as Figure 3.4 at $T^* = 0.83$ and $\mu^* = -3.801$.

at higher temperatures, making identification of the prewetting transition especially difficult from standard simulations. However, MHR allows relatively easy identification of prewetting transitions, even very near the saturation pressure.

The prewetting transitions seen on the $T^* = 0.83$ and 0.88 isotherms can also be characterized by the local density profiles, shown in Figs. 3.6 and 3.7. We note that density profiles cannot

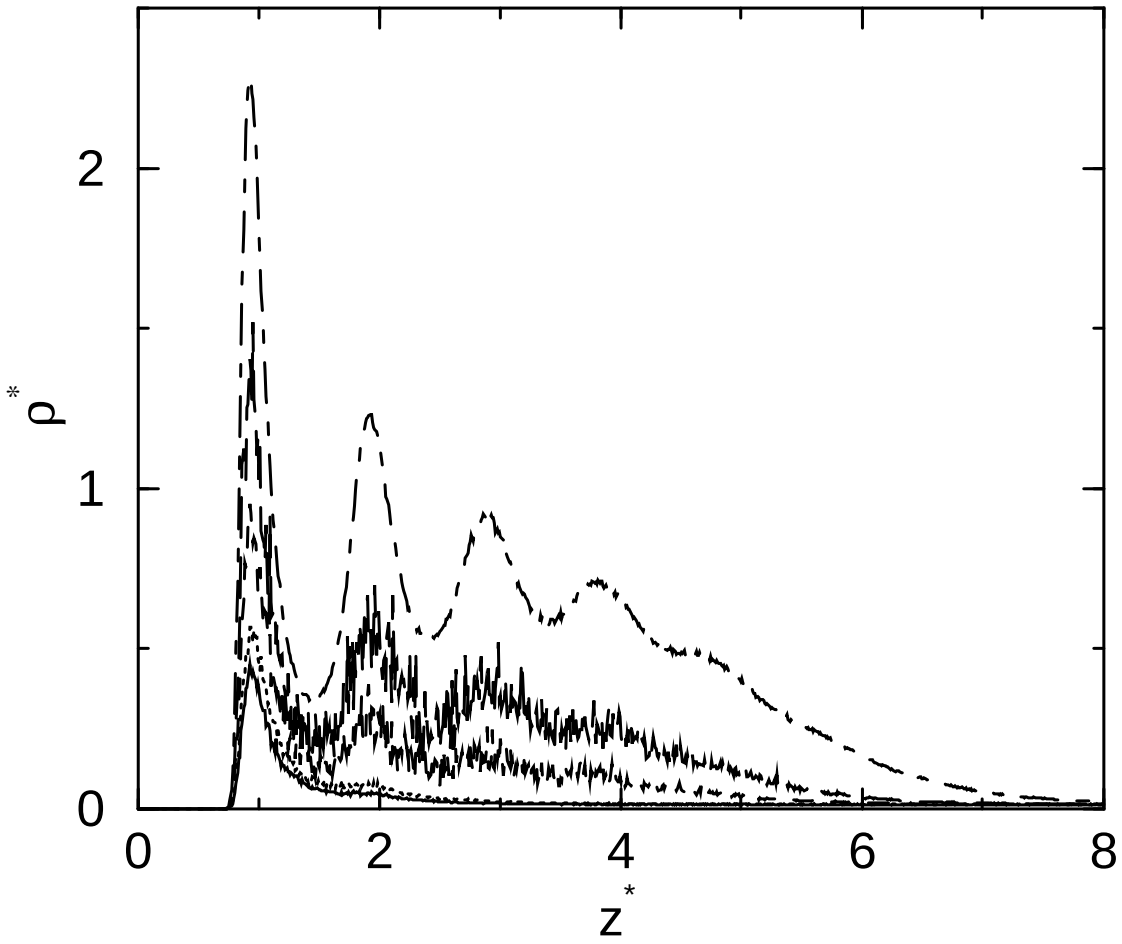

Figure 3.6: Local density profiles obtained from GCMC simulations for the same system as Figure 3.4. Profiles are for $\mu^* = -3.9$ (solid line), -3.81 (dotted line), -3.8 (dashed line), -3.78 (long dashed), and -3.77 (dot-dashed) at $T^* = 0.83$.

be computed from MHR because we have not collected histograms of $\rho(z)$ as a function of U_N, N. Referring to Figure 3.6, we observe that adsorption is limited to a thin layer on the surface for $\mu^* < -3.8$. For $\mu^* \geq -3.8$ the adsorption abruptly changes to multiple layers that appear to grow continuously as the chemical potential is increased. This behavior is indicative of a prewetting

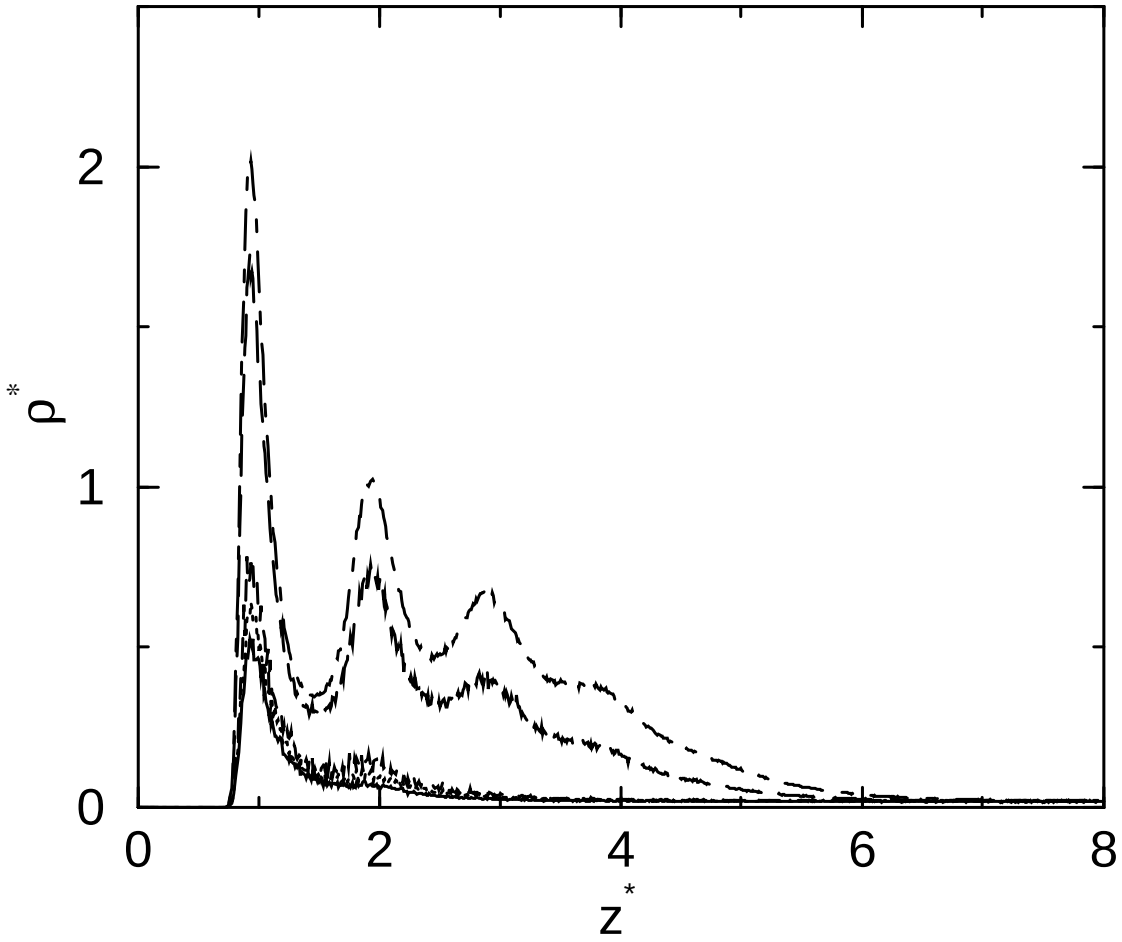

Figure 3.7: Local density profiles obtained from GCMC simulations for the same system as Figure 3.4. Profiles are for $\mu^* = -3.85$ (solid line), -3.8 (dotted line), -3.76 (dashed line), -3.75 (long dashed), and -3.73 (dot-dashed) at $T^* = 0.88$.

transition occurring. The coexistence chemical potential at this temperature calculated from the equal area criterion is -3.801, in agreement with the local density profiles in Figure 3.6. Similar behavior can be seen in Figure 3.7, where the thin- to thick-film transition occurs between $\mu^* = -3.76$ and -3.75. The coexistence chemical potential calculated from MHR is about -3.75, in agreement with the local density profiles.

We have computed the saturation chemical potential (μ^*_{sat}) for the bulk phase vapor-liquid transition from $T^* = 0.8$ up to the apparent critical point from MHR of the bulk fluid[44]. The values of the prewetting transition chemical potentials (μ^*_{pw}) were computed over $0.8 \leq T^* \leq 0.88$ from which $\Delta\mu^* = \mu^*_{sat} - \mu^*_{pw}$ was computed. The plot of $\Delta\mu^*$ vs. T^* is shown in Figure 3.8.

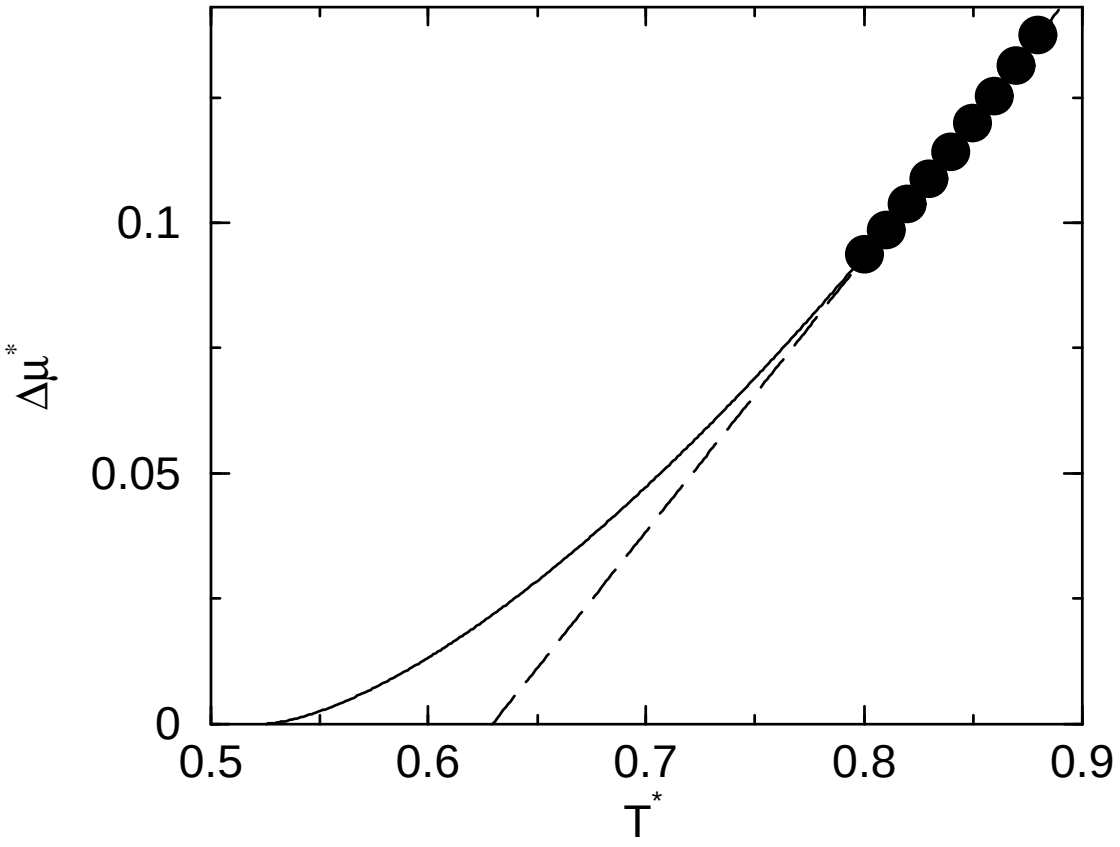

Figure 3.8: A plot of $\Delta\mu^* = \mu^*_{sat} - \mu^*_{pw}$ as a function of temperature for the same system as in Figure 3.4. Filled circles are computed from MHR. Also shown are the fits to the data to the power law form (solid line), and linear form (long dashed).

Theoretical predictions indicate that $\Delta\mu^* \propto (T^* - T_w^*)^{3/2}$ [102]. Hence, a plot of $\Delta\mu^*$ vs. T^* can be used to identify the wetting temperature by extrapolating the curve to $\Delta\mu^* = 0$ [103]. The solid line in Figure 3.8 is the result of a power law fit to the data using an exponent of 3/2. However, inspection of simulation data reveals that they lie on a straight line with a correlation coefficient of 0.9994. The estimates of T_w^* from the power law and linear fits are 0.53 and 0.623, respectively.

The prewetting line for this system was computed [104,105] in order to compare with data from ref. [76]. The density of the gas in equilibrium with the adsorbed phase at the prewetting point was computed by

$$\rho_{pw}^* = \rho_{sat}^* \exp\left(\frac{\mu_{pw}^* - \mu_{sat}^*}{T^*}\right), \tag{3-14}$$

where ρ_{pw}^* and ρ_{sat}^* are the reduced bulk densities for gas at the prewetting transition and vapor-liquid saturation, respectively. This assumes that the bulk gas is ideal in the calculation. The results are shown in Figure 3.9.

The prewetting transition densities at $T^* = 0.85$, 0.87 and 0.88 are 0.0146, 0.0170 and 0.0183, respectively. These results agree well with values reported by Finn and Monson [76]. We fitted the prewetting line and the saturated vapor line to two separate polynomials. The solid and long dashed lines are the results from the fitting. The value of T_w^* was estimated by extrapolating the two lines to where they intersect. This gave $T_w^* = 0.69$. We note that it has been predicted from theory that the prewetting and bulk saturation lines should meet tangentially [76,104–106]. Therefore, extrapolation of the two polynomials is not only unreliable, but also theoretically not justified. Nevertheless, the estimate of $T_w^* = 0.69$ is in reasonable agreement with $T_w^* = 0.62$ obtained from linear extrapolation of $\Delta\mu^*$ vs. T^*.

The reduced wetting and critical prewetting temperatures estimated for the Ar/CO_2 system or similar systems are given in Table 3.2. Note that many of the calculations employed density functional theory, which is not expected to give results identical to simulations given the approximations of the theory. From comparison with the previous estimates of T_w^* we conclude that the power law extrapolation of the $\Delta\mu^*$–T^* curve is not accurate. We believe that T_w^* for this system is probably

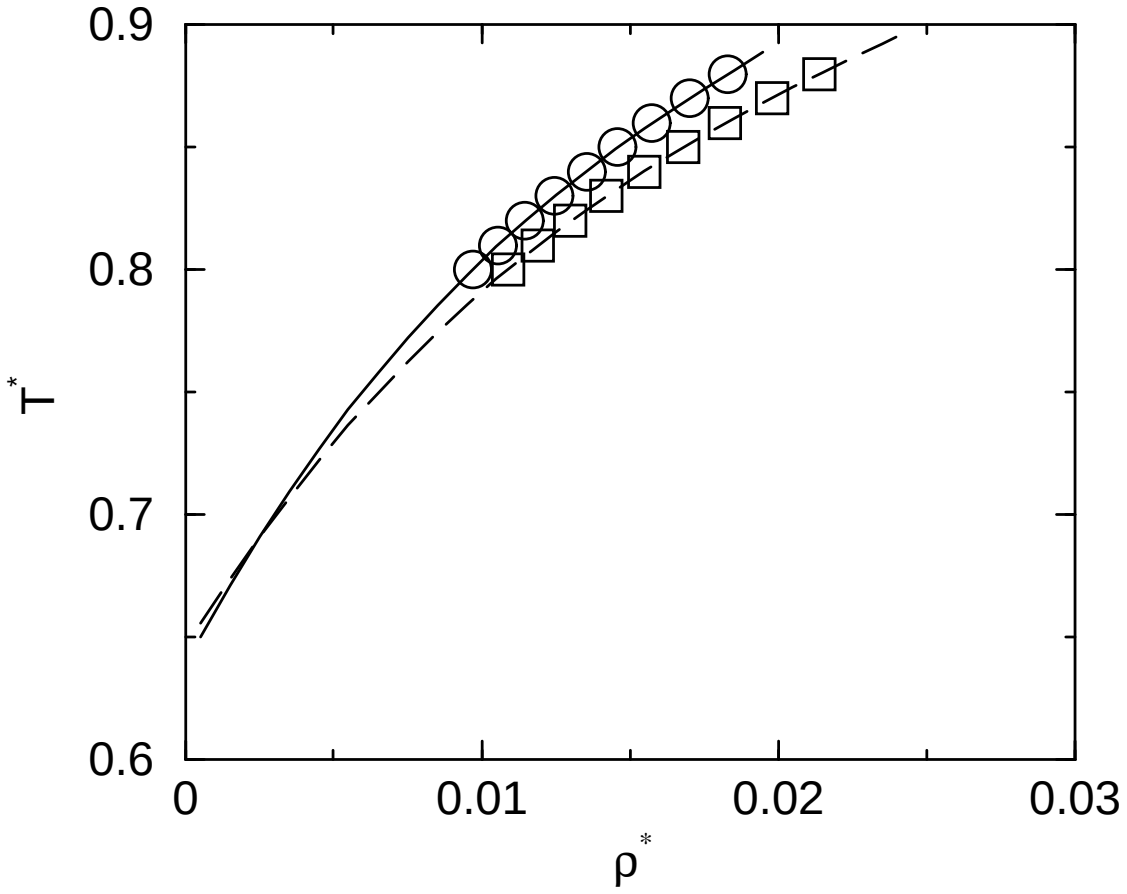

Figure 3.9: The temperature–density phase diagram for the same system as in Figure 3.4. The circles are the densities of the bulk gas in equilibrium with the adsorbed fluid at the prewetting transition points calculated from MHR. The squares are the vapor side of the bulk vapor-liquid phase diagram computed from MHR of the bulk fluid. The solid line and the dashed line are polynomial fits to the data. The two lines intersect at $T^* = 0.69$.

close to our estimates from linear $\Delta\mu^*$–T^* extrapolation and extrapolation of the prewetting line, $T_w^* \sim 0.69$. The estimate of Finn and Monson of $T_w^* = 0.84$ is undoubtedly too high given that we definitely observe a prewetting transition at $T^* = 0.8$.

The relative ratios, P_{wet}/P_{sat}, are plotted in Figure 3.10.

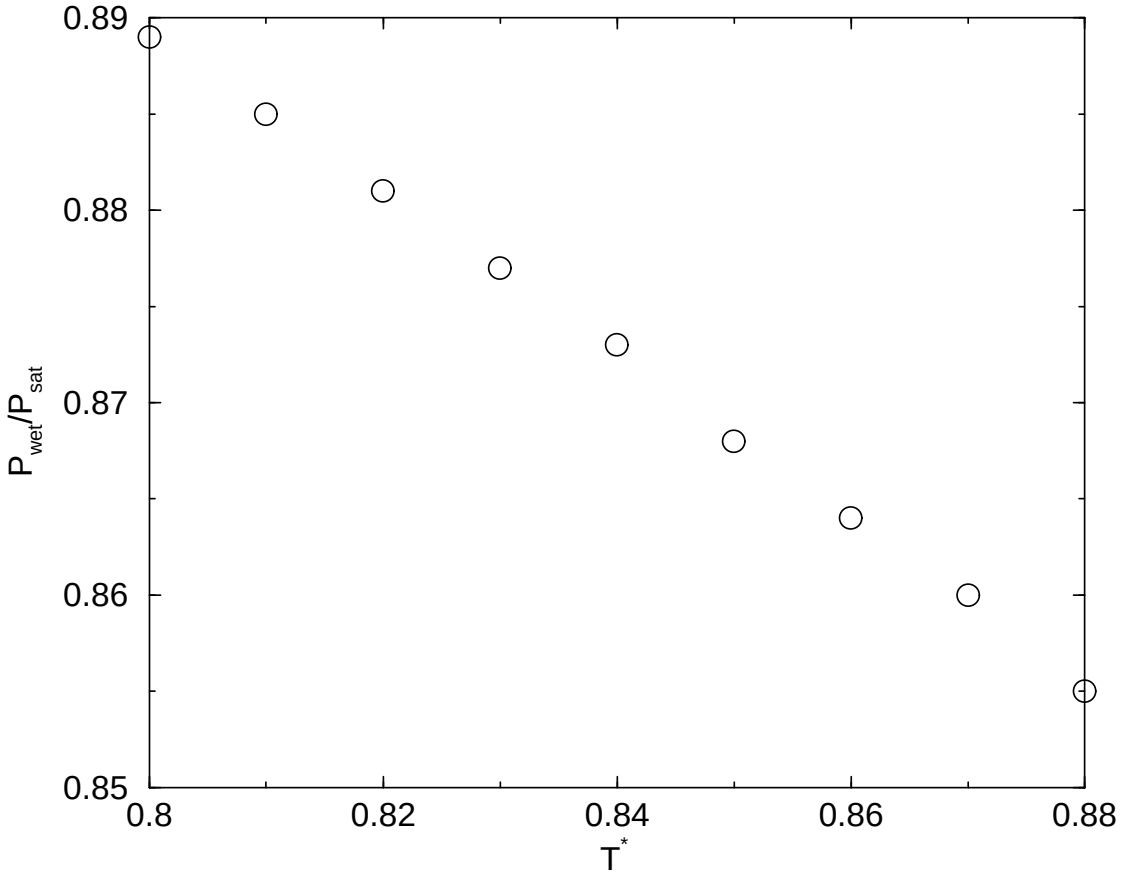

Figure 3.10: The ratio of the prewetting transition pressure to the saturation pressure for the same system as in Figure 3.4.

The ratio was computed from $P_{wet}/P_{sat} = \exp(\frac{\mu_{pw}^* - \mu_{sat}^*}{T^*})$, where P_{wet} and P_{sat} are the pressures at the prewetting transition and saturation, μ_{pw}^* and μ_{sat}^* are the reduced chemical potentials calculated from MHR the with the equal area criterion. Ideal gas behavior was assumed in the calculation. As expected, the ratio decreases with temperature. The value at $T = 0.88$ is 85.5%, close to 87.9% calculated by Finn and Monson[76].

The density probability distributions at $T^* = 0.92$ for $-3.72 \leq \mu^* \leq -3.66$ are shown in Figure 3.11(a). The isotherm is shown in Figure 3.11(b). It is difficult to tell from the isotherm

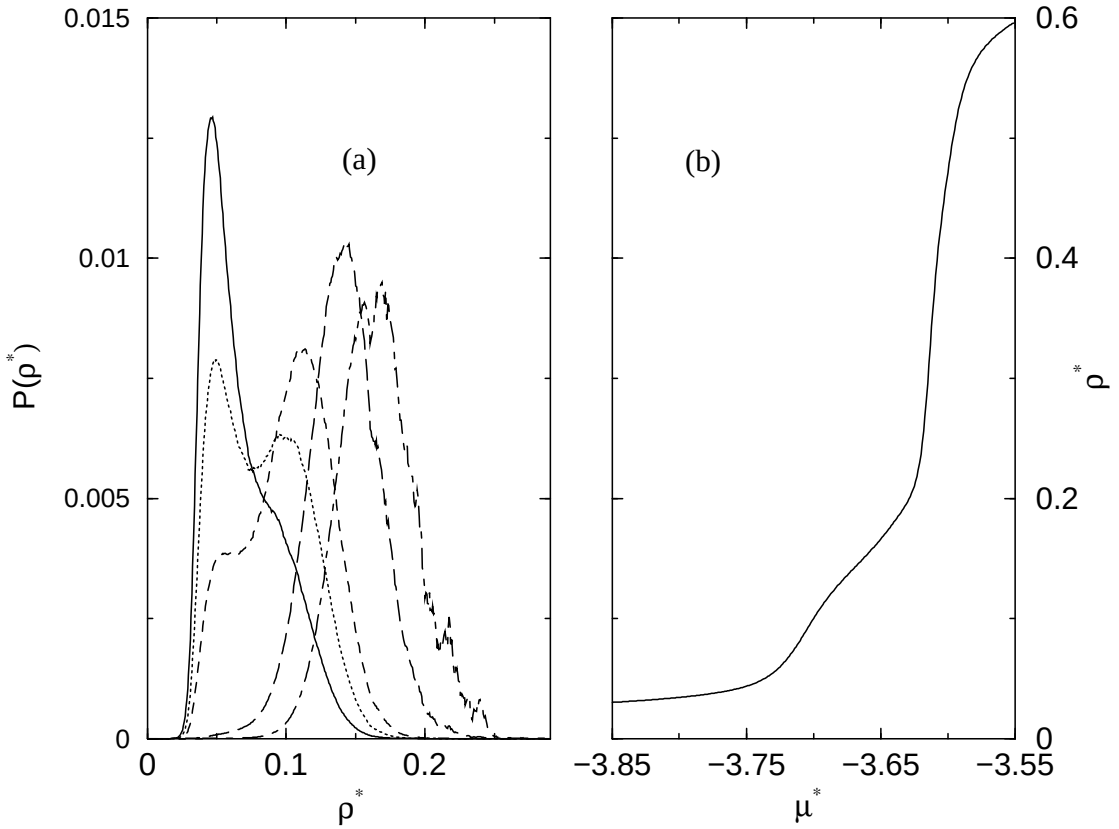

Figure 3.11: (a) The density probability distributions for the same system as in Figure 3.4 at $T^* = 0.92$. Distributions are for chemical potentials of $\mu^* = -3.72$ (solid line), -3.71 (dotted line), -3.7 (dashed line), -3.67 (long dashed) and -3.65 (dot-dashed). (b) The isotherm computed from MHR at $T^* = 0.92$.

whether or not their is a prewetting transition at this temperature (Figure 3.11(b)). However, the density probability distributions are definitive proof that $T^* = 0.92$ is above the prewetting critical point because the equal area criterion can not be satisfied for any choice of μ^* (Figure 3.11 (a)). Probability distributions at $T^* = 0.91$ and 0.9 are somewhat ambiguous. They show two peaks that are in the process of merging. From these observations we estimate that T^*_{pwc} is close to 0.92. This value is in reasonable agreement with other estimates (see Table 3.2). We note that an accurate estimate of T^*_{pwc} would require a finite-size scaling analysis, which is beyond the scope of this work.

3.5 Layering Transition

In this section we present our MHR predictions for the 1-2 layering transition of propane on the basal plane of graphite. Propane was modeled as a three site united atom molecule using the potential model of Lustig and Steele[107]. The potential parameters for this model are the LJ parameters ϵ and σ, the bond lengths of the isosceles triangular framework δ, and the bond angle θ. The values of the potential parameters are $\epsilon/k = 119.57$ K, $\sigma = 3.527$ Å, $\delta = 2.16$ Å, and $\theta = 90°$. We note that there are several united atom propane models available in the literature[108–111]. We adopted this model because of its accuracy in predicting the PVT properties and internal energies of pure propane and the good agreement between experimental and simulated adsorption isotherms for propane on graphite[112]. The graphite surface was modeled as a smooth basal plane using the 10-4-3 potential given by Eq. (3-9).

The volume of the simulation box for histogram collection calculations was set to $1000\sigma^3$. Periodic boundary conditions and minimum image conventions were applied in the x and y directions of the simulation box. The lateral dimensions of the simulation box were equal in x and y directions. One wall of the simulation box was chosen as the adsorbing surface and the opposite wall was chosen to be purely repulsive to keep the molecules in the box. The separation between the two walls was fixed at $H = 10\sigma$ so that the influence of the repulsive wall on the adsorption properties was negligible. The site-site interaction cutoff distance was 3.5σ and no long range corrections were applied. Each simulation was equilibrated for 5×10^7 moves, after which histogram data were collected for another 5×10^7 moves. We collected histograms spanning coverages ranging from a monolayer (5.9μmol m^{-2}) to a complete bilayer (14.2μmol m^{-2}) at a temperature of 130 K. We chose this temperature because it appears to be above the critical layering transition temperature, which allowed sampling of all coverages spanning the 1-2 layering transition. Additional histograms were collected at temperatures down to 100 K, but only sampling a few state points in the monolayer or bilayer regime. A total of 53 histograms from different state points were collected.

An independent series of GCMC simulations were performed (without collecting histograms) for a larger system size with a volume of $4250\sigma^3$ and $H = 20\sigma$ [112]. The isotherms predicted from MHR for the smaller volume are compared with GCMC simulations in Figs. 3.12 and 3.13.

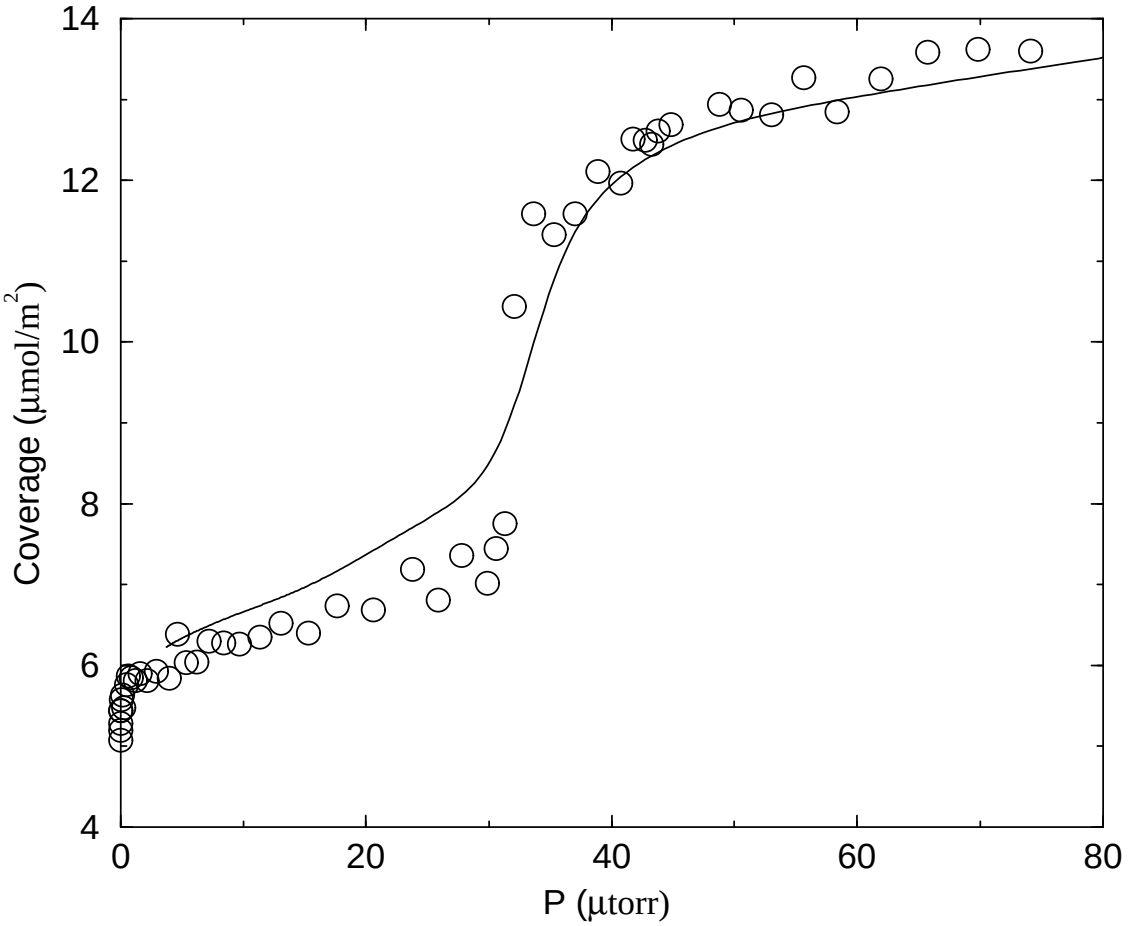

Figure 3.12: The $T = 100$ K isotherm (solid line) for propane adsorption on graphite predicted from MHR for a small system size (volume = $1000\sigma^3$) compared with GCMC simulations for a larger system volume of $4250\sigma^3$ (circles).

We observe that the MHR calculations on the small system size give a very reasonable representation of the behavior of the larger system size. The layering transitions occur at close to the same pressures, although there is some difference in the coverages, which may be due to finite size effects. The 1-2 layering transition observed from the GCMC simulations does not appear to be very sharp. In contrast to simple fluids like methane on graphite [113] that show very sharp layering transitions, the propane/graphite system is complicated by orientational changes of the propane in

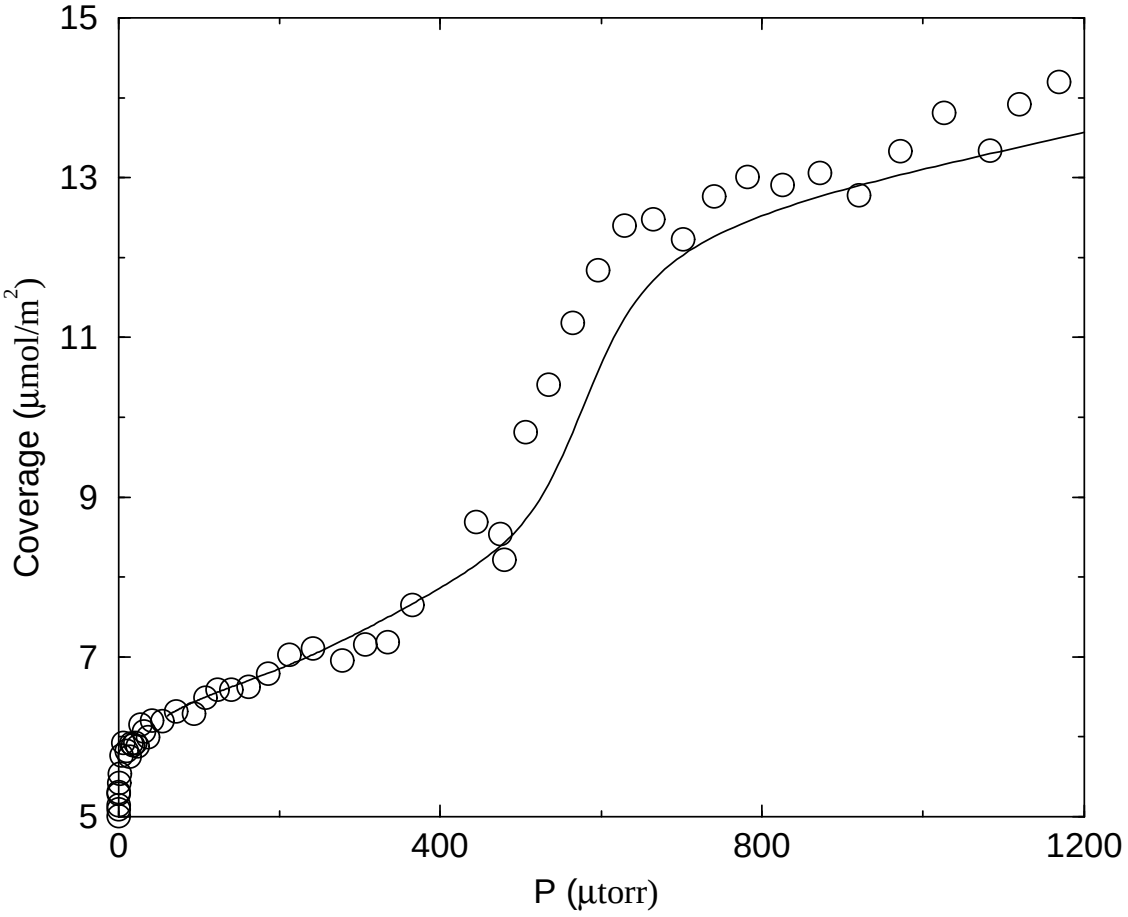

Figure 3.13: The $T = 110$ K isotherm (solid line) for propane adsorption on graphite predicted from MHR for a small system size (volume = $1000\sigma^3$) compared with GCMC simulations for a larger system volume of $4250\sigma^3$ (circles).

the first layer. The orientational changes allow an increase in coverage in the first layer after the monolayer is apparently "full" and also promotes adsorption in the second layer[112]. Density distributions from MHR at 100 K show two regions that are not well separated. This may be indicative of system size effects. We have previously observed that vapor-liquid density distributions for bulk fluids start to merge for subcritical temperatures, when the system size is small.

The value of the critical layering transition temperature is often of interest[91]. In principle, one can estimate the location of the critical layering transition temperature by the disappearance of two distinct peaks in the density distribution. However, the lack of distinct peaks is not a necessary condition for supercriticality, since two peaks in the density probability distribution may be observed for temperatures slightly greater than the apparent critical temperature[114]. A rigorous estimate of the critical layering transition temperature would require finite-size scaling analysis. An additional problem for this system is that the density distributions at subcritical temperatures are not well separated to begin with. Nevertheless, we have estimated $T_c(2)$ to be around 120 K for the propane/graphite system. This value is very close to the experimental result for ethane on graphite of $T_c(2) = 120.8 \pm 0.3$ K[115]. It is somewhat surprising that $T_c(2)$ is so similar for ethane and propane. This may be due to inaccuracies in the potential models used in these simulations or perhaps due to the orientational transitions in the propane monolayer. Additional simulations for ethane adsorption would be useful for understanding the similarities and differences in these systems.

3.6 Conclusion

The multiple histogram reweighting technique has been used to study capillary condensation, prewetting transitions, and layering transitions. The critical capillary condensation temperature and density are estimated to be $T_c^* = 0.77$ and $\rho_c^* = 0.482$ for methane adsorption in a graphitic slit pore of width $H = 5\sigma$. Crossover of the effective exponent value from 2-D Ising-like to mean-field

occurs for capillary condensation. To our knowledge, crossover for capillary condensation has not previously been observed. The precision and abundance of the coexistence data generated from MHR were crucial factors in the successful observation of crossover. Adsorption of Ar on solid CO_2 using the potential models of Finn and Monson shows prewetting transitions at temperatures lower than previously observed. The reduced wetting temperature is estimated to be around 0.69 from the extrapolation of the prewetting transition line and the saturated vapor line. The reduced critical prewetting temperature is about 0.92 as estimated from the disappearance of two distinct peaks in the density probability distribution. Layering transitions were computed from MHR for propane adsorbing on graphite. The transition pressures are in good agreement with previous simulations for larger system sizes, indicating that MHR calculations for small system sizes can be useful for predicting the behavior of larger systems. We estimate $T_c(2) \sim 120$ K based on the merging of the density probability distributions.

We have demonstrated that MHR can be a useful tool for computing the properties of adsorbed fluids, especially when one is interested in investigating phase transitions. There are, however, drawbacks to MHR that we should mention. Efficiency in collecting histograms decreases dramatically with decreasing temperature and increasing volume. It is advisable to use the smallest simulation box size that is possible when performing MHR. The reasons for this are two fold: (1) The overlap between neighboring states becomes smaller as the system size increases, necessitating a larger number of simulations to span the same temperature range. (2) Longer simulations are required to capture the increased number of microstates available in larger systems. We have used standard Metropolis Monte Carlo in our work. Efficiency gains could be made by implementing biasing methods that would increase the width of the density and energy distributions sampled in a single simulation. However, it is clear that MHR is not a very efficient method if large system sizes are needed. Another drawback of the MHR method is that there is no clear way to estimate the precise critical temperature for a transition without resorting to finite-size scaling methods. The disappearance of two peaks in the density distribution is a sufficient but not necessary condition for a system being in the supercritical region. The double peaked distribution is known to persist

to temperatures that are slightly supercritical[114], so that absence of the two peaks can only serve as an upper bound measure of the critical point.

Table 3.1: Ratios of the grand canonical partition function computed from single histogram reweighting (SHR) and multiple histogram reweighting (MHR). The calculation is for methane adsorption in graphitic slit pore.

T_1^*	μ_1^*	T_2^*	μ_2^*	SHR			MHR
				$\frac{\Xi_1}{\Xi_2}$	$\frac{\Xi_2}{\Xi_1}$	$\frac{\Xi_1}{\Xi_2} \times \frac{\Xi_2}{\Xi_1}$	$\frac{\Xi_2}{\Xi_1}$
0.9	−5.57	0.9	−5.50	7.5374×10^{-14}	1.5222×10^{13}	1.1473	1.4971×10^{13}
0.9	−5.50	0.9	−5.45	3.7830×10^{-11}	2.9184×10^{10}	1.1040	2.7088×10^{10}
0.9	−5.45	0.9	−5.40	6.9859×10^{-12}	1.352×10^{11}	0.9444	1.3634×10^{11}
0.85	−5.65	0.9	−5.57	7.5537×10^{27}	1.3189×10^{-28}	0.9962	1.2211×10^{-28}
0.75	−5.90	0.7	−6.10	2.5573×10^{-26}	1.6060×10^{25}	0.4107	3.3113×10^{25}
0.7	−6.6	0.7	−7.0	3.7151×10^{71}	2.7838×10^{-72}	1.0342	2.7188×10^{-72}
0.65	−7.2	0.6	−7.6	2.4925×10^{17}	4.0865×10^{-18}	1.0185	4.4315×10^{-18}
0.9	−5.0	0.85	−5.0	1.1024×10^{-65}	1.4597×10^{65}	1.6091	1.1898×10^{65}
0.725	−5.90	0.725	−5.8	1.8069×10^{-34}	8.9568×10^{33}	1.6184	6.8511×10^{33}
0.7	−5.9	0.685	−6.02	1.8520×10^{14}	4.9617×10^{-15}	0.9189	4.5241×10^{-15}

Table 3.2: Reduced wetting temperature (T_w^*) and reduced prewetting critical temperature (T_{pwc}^*) for Ar on CO_2 and Ne on Mg.

Source	T_w^*	T_{pwc}^*
Ebner and Saam[84]	0.77	0.92
Tarazona and Evans[116]	0.957	0.988
Meister and Kroll[117]	0.90	...
Finn and Monson[76]	0.84 ± 0.01	0.94 ± 0.02
Sokołowski and Fischer[118]	0.975 ± 0.025	...
Bojan *et al.*[119]	0.65	0.88 ± 0.03
This work	0.69	0.92

4.0 MULTIPLE HISTOGRAM REWEIGHTING APPLIED TO PATH INTEGRAL FLUIDS

4.1 Introduction

It is well known that the thermophysical properties of light molecules at low temperatures can be dramatically altered by quantum mechanical effects. These effects have their origin in the wave-particle duality of mater and are manifest when the thermal de Broglie wavelength is similar to the spacing between molecules. An example of quantum effects on the thermodynamic properties of fluids can be seen by comparing the critical temperatures of H_2 with "classical" H_2, i.e., a hypothetical hydrogen with the exact same intermolecular potential, but with a high mass so that no quantum effects are manifest. Real H_2 has a critical temperature of about 33 K, while "classical" H_2 has a critical temperature of about 44 K,[120] showing that quantum effects are profound for phase equilibrium properties.

Until recently, no simulation methods existed for directly computing the phase equilibrium properties of strongly quantum fluids. By strongly quantum, we mean fluids for which the Wigner-Kirkwood expansion does not converge within the first two terms. Such fluids are most commonly simulated using the path integral formalism of Feynman.[121] Wang and coworkers developed the first direct method for computing phase equilibria within the path integral formalism by extending the Gibbs ensemble method.[120,122] They also developed an extension of the grand canonical Monte Carlo technique for path integral fluids.[123] Nevertheless, until multiple histogram reweighting (MHR)[11–13] has not been applied to path integral fluids. This is because the MHR technique cannot be directly applied to the Hamiltonian used in the path integral formalism. The MHR technique is very efficient and accurate for computing phase transitions of classical fluids[4,5,44,45,77,78,81] and is especially useful in cases where it is important to locate the coexistence point with high precision. An example of such a case is the study of prewetting and wetting transitions. For H_2 adsorbing on Rb the prewetting transition occurs at about 99.2% of the saturation pressure at

19.91 K[103]. The uncertainties in the saturation chemical potential computed from Gibbs Ensemble simulations of quantum fluids give rise to errors in the saturation pressures of several percent. In contrast, the saturation pressure for classical fluids can be computed from MHR to within a fraction of a percent.[44].

In this study, we have successfully extended the MHR technique to path integral fluids and have calculated phase diagrams of hydrogen isotopes. We have used the Silvera-Goldman potential [124] to compute properties of H_2 and D_2 with different potential cutoffs. The saturation chemical potentials have been used to study the wetting behavior of H_2 on Rb with MHR. The importance of this work is that the method of dealing with the microcanonical partition function can be extended to other kinds of Hamiltonians. The key is to split the Hamiltonian in a suitable way such that the microcanonical partition function is indepdendent of temperature.

4.2 Theory

The basic equation for the MHR method applied to classical fluids is that the microcanonical partition function, Ω_c, is independent of temperature. I.e.,

$$\Omega_c(N, V, U^{\text{tot}}, T_i) = \Omega_c(N, V, U^{\text{tot}}, T_j) \neq f(T), \tag{4-1}$$

where N is the number of the particles, V is the volume of the simulation cell, U^{tot} is the total configurational potential energy, T_i and T_j are two different temperatures. Obviously, Ω_c with indices of N, and U^{tot} will be constant if the volume is the same for different state points. However, this is not true for path integral fluids, i.e,

$$\Omega(N, V, U^{\text{tot}}, T_i) \neq \Omega(N, V, U^{\text{tot}}, T_j). \tag{4-2}$$

For path integral fluids, the total potential energy is given by

$$U^{\text{tot}} = U^{\text{ext}} + U^{\text{int}}. \tag{4-3}$$

The external potential is given by

$$U^{\text{ext}} = \frac{1}{P}\sum_{\alpha=1}^{P}\sum_{i<j}^{N} V(r_{ij}^{\alpha}), \tag{4-4}$$

where P is the number of beads in the polymer, N is the total number of molecules, $V(r_{ij}^{\alpha})$ is the pair potential between bead α on molecule i and bead α on molecule j. Note that $V(r_{ij}^{\alpha})$ only depends on the positions of the molecules and therefore U^{ext} is independent of temperature. U^{int} is in the form of a harmonic potential given by

$$U^{\text{int}} = \frac{Pm}{2\beta^2}\sum_{\alpha=1}^{P}\sum_{i=1}^{N}(r_i^{\alpha} - r_i^{\alpha+1})^2, \tag{4-5}$$

where r_i^{α} is the position of bead α on ring i, m is the mass of the quantum molecule, β is $1/kT$, k is the Boltzmann constant. When $\alpha = P$, $\alpha + 1 = 1$ as required for a ring polymer. Note that U^{int} depends on temperature and hence U^{tot} is a function of temperature and positions of the beads. This implies that the microcanonical partition function, $\Omega(N, V, U^{\text{tot}})$, is an implicit function of temperature.

It is clear that new indices for the microcanonical partition function, Ω, are needed in order to obtain a temperature independent Ω. The new indices are chosen to be N, V, U_1, U_2, where U_1 and U_2 are given by

$$U_1 = U^{\text{ext}}, \tag{4-6}$$

and

$$\begin{aligned} U_2 &= U^{\text{int}}\beta^2 \\ &= \frac{Pm}{2}\sum_{\alpha=1}^{P}\sum_{i=1}^{N}(r_i^{\alpha} - r_i^{\alpha+1})^2. \end{aligned} \tag{4-7}$$

The microcanonical partition function will be temperature independent provided that the number of beads, P, is constant. The Ω described by the new indices can be written as

$$\Omega(N, V, U_1, U_2) \neq f(T). \tag{4-8}$$

The grand canonical partition function for path integral fluids in the context of the new indices is given by

$$\Xi(\mu, V, T) = \sum_{N}\sum_{U_1}\sum_{U_2}\Omega(N, V, U_1, U_2)\frac{\exp\left[-\beta U^{\text{tot}} + N\beta\mu\right]}{\Lambda^{3N(P-1)}}, \tag{4-9}$$

where $\Xi(\mu, V, T)$ is the grand canonical partition function at μ and T, μ is the configurational chemical potential defined by $\mu = \mu^f - kT \ln \Lambda^3$, Λ is the thermal de Broglie wavelength, μ^f is the full chemical potential and U^{tot} is the total potential energy given by Eq. (4-3).

Using the same procedure for the derivation of multiple histogram reweighting for classical fluids [11–13,44], we obtained the formula for multiple histogram reweighting for path integral fluids. The microcanonical partition function is given by

$$\Omega(N, U_1, U_2) = \frac{\sum_j H_j(N, U_1, U_2)}{\sum_j \mathcal{N}_j \exp\left(-\beta_j U_j^{\text{tot}} + \beta_j \mu_j N\right) / (\Xi_j \Lambda_j^{3N(P-1)})}, \tag{4-10}$$

where j denotes the j th state points at temperature T_j, and chemical potential μ_j. $H_j(N, V, U_1, U_2)$ is the histogram collected at the j th state point in terms of N, U_1, and U_2, and

$$\mathcal{N}_j = \sum_N \sum_{U_1} \sum_{U_2} H_j(N, V, U_1, U_2). \tag{4-11}$$

The grand canonical partition function at μ and T is given by Eq. (4-9). The ensemble average of any property X at μ, V and T is given by

$$\langle X \rangle_{\mu,V,T} = \frac{\sum_N \sum_{U_1} \sum_{U_2} \Omega(N, V, U_1, U_2) X(N, U_1, U_2) \exp\left[-\beta U^{\text{tot}} + N\beta\mu\right] / \Lambda^{3N(P-1)}}{\Xi(\mu, V, T)}. \tag{4-12}$$

The extension of the above MHR technique for pure path integral fluids to path integral mixtures is very simple. All that needs to be changed are the indices for the microcanonical partition function. For a binary mixture, the indices for the microcanonical partition function are N_1, N_2, U_{21}, U_{22}, U_1, and U_2, where N_1 and N_2 are the number of species 1 and 2, respectively, U_{21} and U_{22} are the internal energies divided by temperature given by Eq. (4-7) of the species 1 and 2, U_1 and U_2 are the total external energies given by Eq. (4-6) for the species 1 and 2.

To test the above algorithm, we have run three sets of NVT simulations with $N = 108$, the reduced volume, $V = 222$ and temperatures of 45 K, 50 K, and 55 K. The number of beads P is set to be 10. The number of histogram observations is 6.25×10^6. The histograms at these three temperatures are combined and used to predict the thermodynamical properties at 47 K. The total potential energy of Eq. (4-3) and the internal energy of Eq. (4-5) per particle are 16.31 and 19.05,

respectively, as predicted from the MHR technique. A simulation was run at 47 K giving values of the total and internal energies per particle of 16.32 ± 0.02 and 19.07 ± 0.02, respectively. The results from the MHR calculation agree with those from direct simulation. This agreement between the simulation and the MHR calculation verifies the algorithm.

4.3 Simulation Details

Molecular simulations were performed using path integral grand canonical Monte Carlo[123]. The fluid interactions were modeled with the Silvera-Goldman potential[124], which is accurate for both H_2 and D_2[120,123]. The number of beads was set to 40 for H_2 and 20 for D_2 in the simulations. For H_2, the cutoff for both the long-ranged corrected (LRC) and truncated (TR) potentials was set to 15 Å. The volumes are chosen to be 27.1 nm^3. We used 6×10^5 steps to collect the data with 2×10^5 steps for equilibration. For LRC H_2, 57 state points in the temperature range between 25 K and 36 K both on the gas and liquid sides were chosen. For TR H_2, 84 state points covering the temperature range of 19 K and 36 K were used. The cutoff for LRC D_2 was chosen to be 9 $Å^3$. The volume of the simulation is chosen to be 19 nm^3. The number of steps is 3.2×10^5 to collect the data following 2×10^5 steps for equilibration. Fifty five state points between 31 K and 41 K were performed. Some liquid state points had to be as close as 0.25 K in temperatures to obtain good overlap between the neighboring state points.

We also studied the adsorption of H_2 on the Rb surface using MHR. The truncated potential was used for the adsorbate-adsorbate interaction. The adsorbate-adsorbent interaction was calculated with the empirical 9-3 potential[125],

$$V(z) = \frac{4C_3^3}{27D^2z^9} - \frac{C_3}{z^3}, \tag{4-13}$$

The parameters of C_3 and D are 2420 K$Å^3$ and 44 K, respectively. The simulation cell was a cube with a volume of 27.1 nm^3. A total of 33 state points were run to cover temperature range from 28 K to 32 K.

Since the microcanonical partition function is described by three indices, the histograms are collected in a table list. The instantaneous values of N, U_1, and U_2 are recorded in the table during the production run. The raw data in the table were then sorted in terms of N followed by concatenation of the table with the same indices of N, U_1, and U_2. The table was first sorted because it is very time consuming to concatenate the table list. Our calculation showed that sorting of the table saved a good deal of time. After the histograms were processed as specified as above, they were combined to estimate the grand canonical partition function from Eq. (4-9).

The isotherms were calculated from Eq. (4-12). The saturation chemical potential was estimated from Hill's method[44,67]. The equal area criterion was applied to calculate the coexistence chemical potential and coexistence densities by constructing the density probability distribution[44,45].

4.4 Results

The coexistence densities for the LRC and TR H_2 potentials are shown in Figure 4.1. The coexistence densities for the TR H_2 were fitted to the scaling law and rectilinear law. The critical temperature and critical density from the fitting are about 32.5 K and 32.2 kg/m^3, respectively. These values are close to the experimental values of 32.976 K and 31.4285 kg/m^3 for para-hydrogen, 33.180 K and 31.4285 kg/m^3 for normal hydrogen[126]. The coexistence densities for LRC H_2 are close to those for TR H_2. The difference in the coexistence densities between TR and LRC is small. The average absolute deviation (ADD) for the coexistence densities was calculated as

$$AAD\% = \frac{\sum_{i=1}^{N} \left| \frac{\rho_i^{TR} - \rho_i^{LTC}}{\rho_i^{LRC}} \right|}{N}, \tag{4-14}$$

where N is the number of points for comparison, and ρ^{TR}, ρ^{LRC} denote the coexistence densities for TR and LRC H_2, respectively. The values for AAD between LRC and TR H_2 of the vapor and liquid sides are 6.9% and 1.1%, respectively. The values for ADD between TR and LRC classical Lennard-Jones (LJ) fluids both with a cutoff of 5σ are 0.8% and 1% for the vapor and

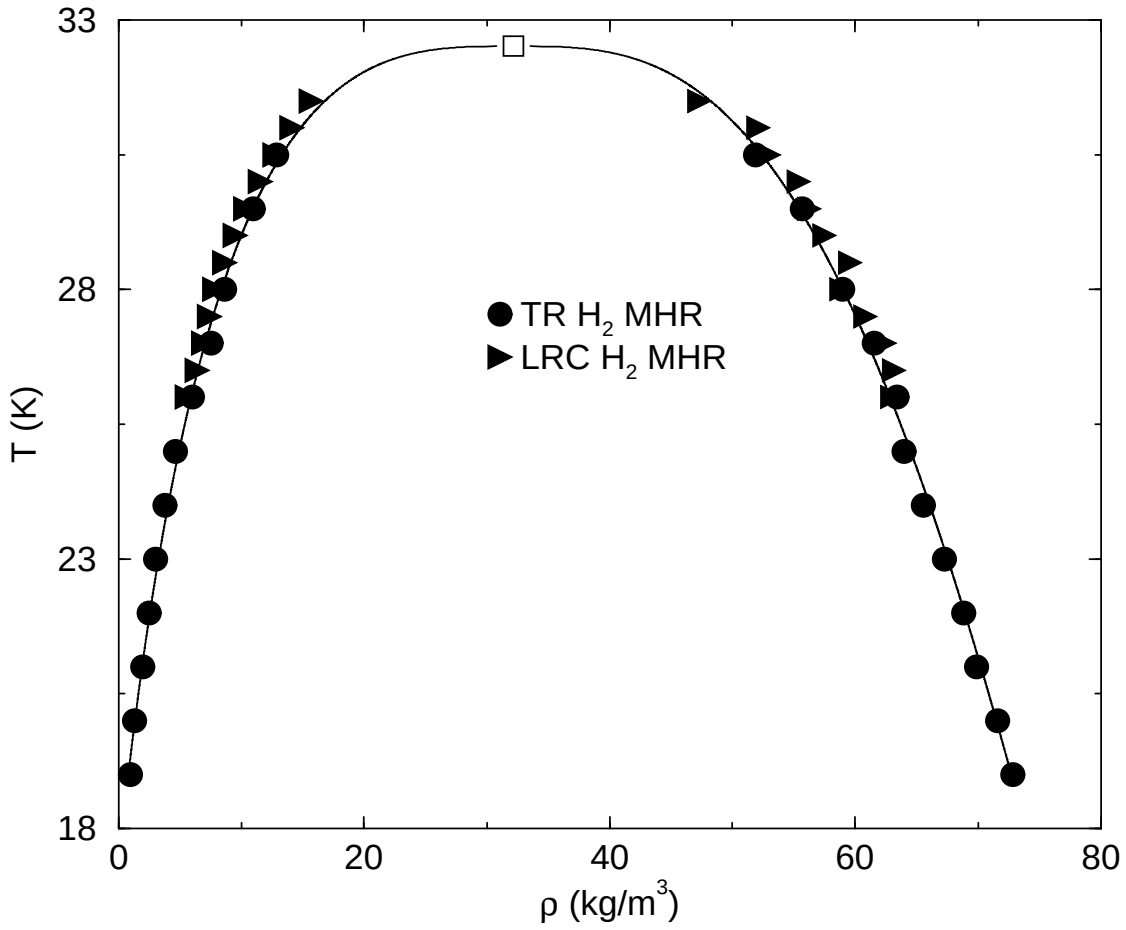

Figure 4.1: The T–ρ phase diagram for the TR H_2 with a cutoff of 15 Å calculated from multiple histogram reweighting (MHR). The line is a fit of the data to the scaling law and rectilinear law. The open square is an estimate of the the critical point based on the fit. Also shown are the coexistence data (filled right triangles) of the long range corrected H_2 with a cutoff of 15 Å calculated from MHR.

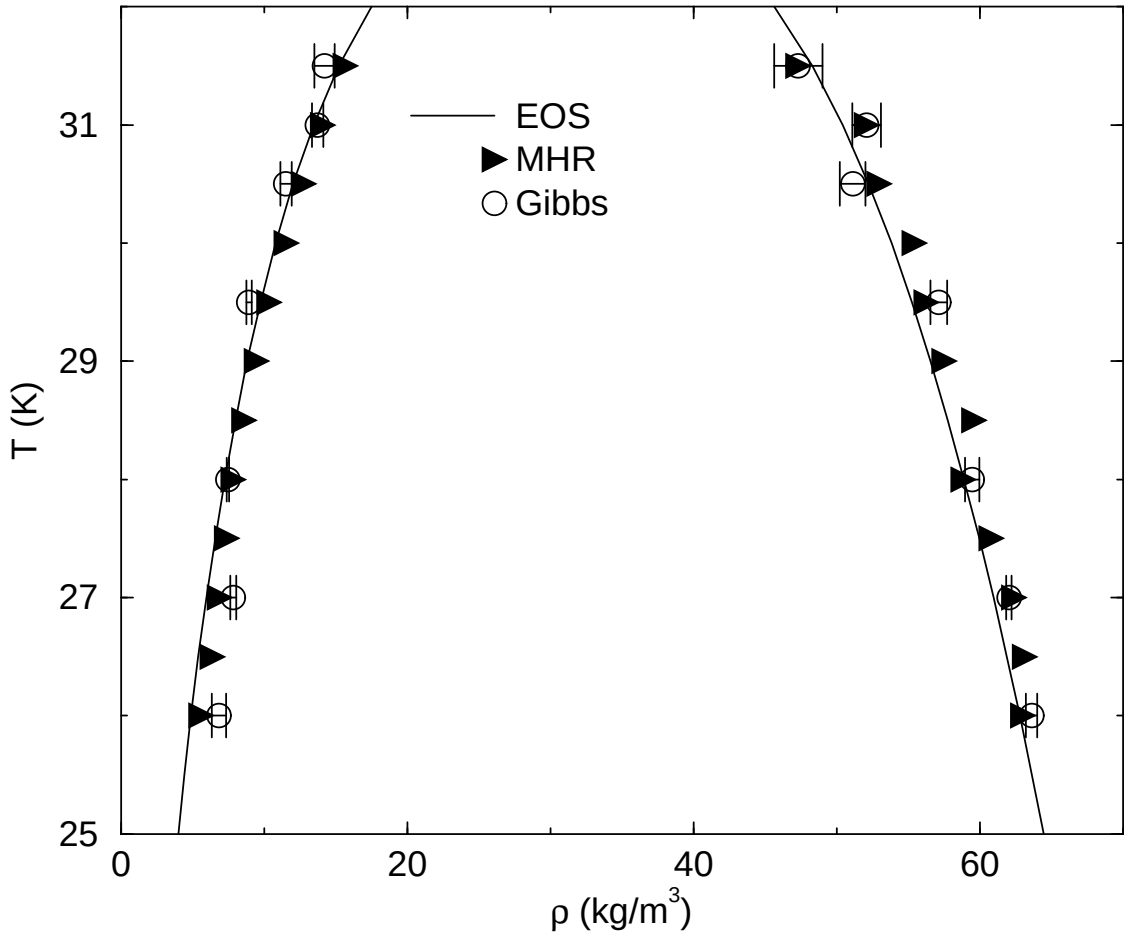

Figure 4.2: The T–ρ phase diagram of long range corrected H_2 with a cutoff of 15 Å computed from multiple histogram reweighting. The filled right triangles are the coexistence data. The solid lines are calculated from the equation of state. The circles are Gibbs ensemble data from [127].

liquid branches, respectively[44]. The coexistence densities for LRC H_2 are shown in Figure 4.2. The results from MHR calculation agree very well with those from equation of state and Gibbs ensemble calculations. Note that the results from the MHR calculations are not smooth on the liquid side. This is also the case for the TR H_2 phase diagram calculated from MHR shown in Figure 4.1. We attribute this to runs that are not sufficiently long to collect accurate histograms for liquid-like state points. Runs that are too short will result in density distributions that are not smooth, as shown in Figure 4.3. These rough density distributions give rise to uncertainty in the coexistence densities and hence scatter in the phase envelop.

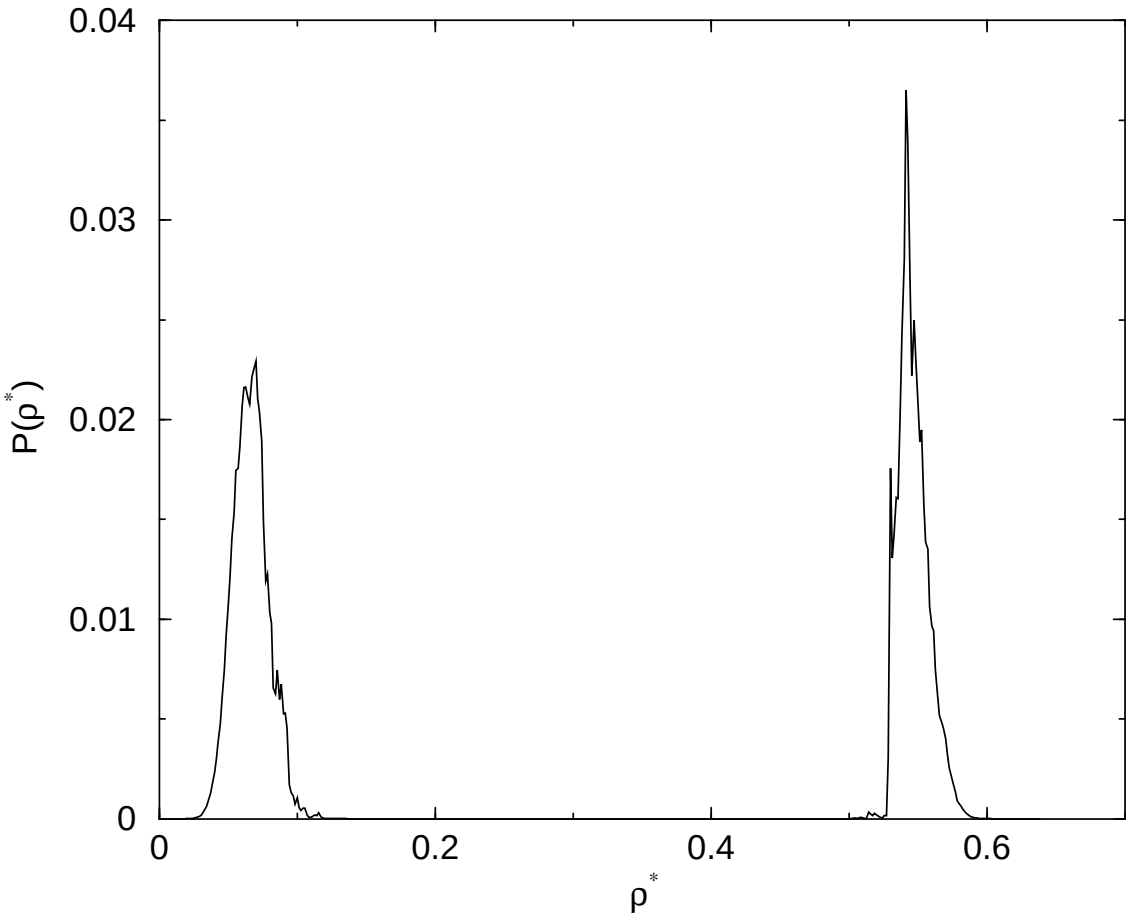

Figure 4.3: The density distribution with equal area under two peaks. This is for D_2 with a cutoff of 9 Å at 33 K.

A plot of $\mu_{\rm sat}/T$ versus $1/T$ is shown in Figure 4.4. The data are very close to being linear, with correlation coefficients of x and y for the TR and LRC potentials to be very close to 1.0. The

linearity of the data make it possible to interpolate and even extrapolate (over a limited range) μ_{sat} with a high degree of confidence.

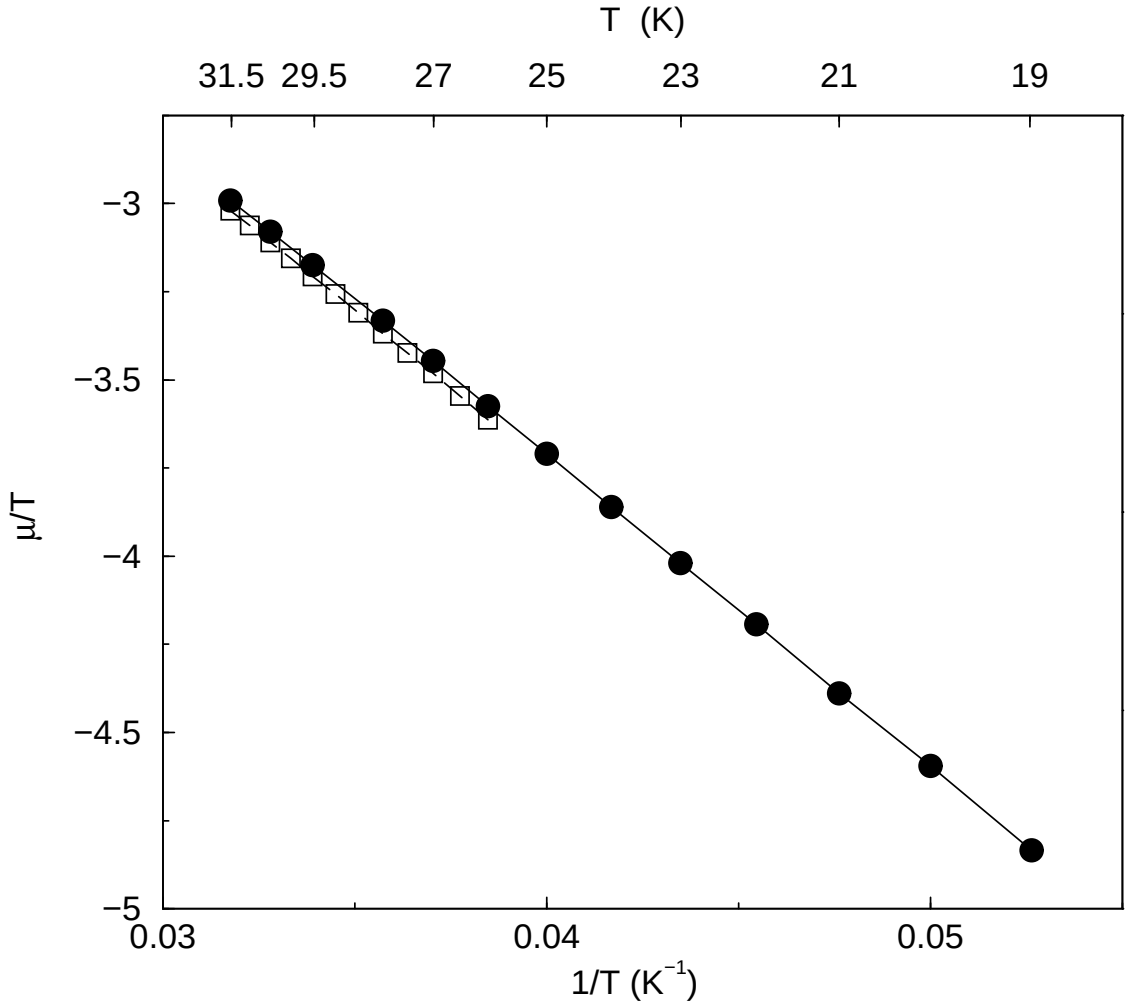

Figure 4.4: The T–μ/T phase diagrams of the truncated and long range corrected H_2 both with cutoffs of 15 Å. The filled circles corresponds to truncated H_2. The open squares corresponds to long range corrected H_2. The lines are the linear fitting to the data.

The coexistence densities for LRC D_2 with a cutoff of 9 Å are shown in Figure 4.5. The coexistence densities are are fitted to the scaling law and rectilinear law. The critical temperature and density from the fitting are about 37.9 K and 71.1 kg/m^3, respectively. The value of critical temperature for D_2 from the experiment is 38.2 K, close to that from the calculation. The coexistence densities computed from MHR agree with those from experiments[126] and Gibbs ensemble simulations[127]. The AAD between MHR and Gibbs ensemble for the vapor and liquid branches are

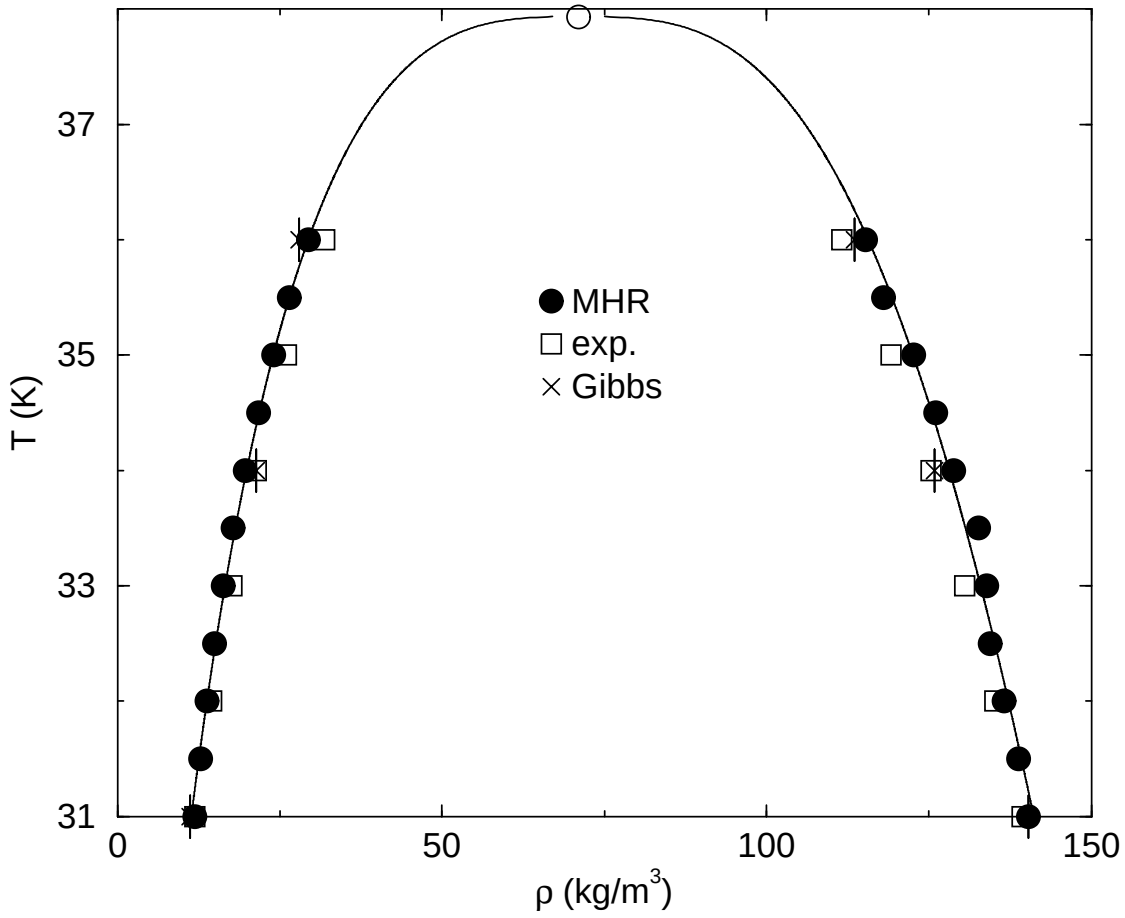

Figure 4.5: The T–ρ phase diagram of long range corrected D_2 with 9 Å. The filled circles are calculated from multiple histogram reweighting (MHR). The solid line is the fitting of the coexistence data computed from MHR to the scaling law and rectilinear law. The unfilled circle denotes the critical point from the fitting. The squares are from the experiment [126]. Also shown are the results (crosses) calculated from Gibbs ensemble simulations.

5.2% and 1.6%, respectively. It is common within Gibbs ensemble simulation to allow the potential cutoffs in the two boxes to fluctuate in response to volume moves during the simulation. For example, at 32 K, the average cutoffs are 12 Å and 16.5 Å for the liquid and vapor branches, respectively. The results from MHR calculation are for 9 Å. This may attribute slightly to the difference in the coexistence densities between MHR and Gibbs ensemble. The values of ADD between MHR and the experiment are 6% and 2% for the vapor and liquid branches, respectively.

An additional 50 sets of simulations were run for LRC D_2 to estimate the uncertainty from MHR. Histograms were collected for 3.2×10^5 steps, with simulations starting from different initial configurations for the previous set of 55 state points. There are 19 state points out of the 50 sets different from all of the 55 sets. The left 31 state points out of the 50 sets have the same temperature and chemical potential as those of 55 sets do. The uncertainties of the coexistence densities computed from the two sets of data are in the third decimal places for both the liquid and vapor densities. The uncertainties of the saturation chemical potentials are also typically in the third decimal places.

We have previously shown that MHR can be used to accurately identify wetting transitions in classical simulations[45]. Here we present similar calculations for quantum fluids. The isotherms for H_2 adsorption on the Rb surface are shown in Figure 4.6. The isotherms at 28 K and 29 K clearly indicate nonwetting since the amount adsorbed is finite even past the saturation chemical potential. The isotherms at 31 K and 32 K are continuous, indicating complete wetting. A jump on the isotherm at 30 K can be observed when the chemical potential is close to that of the saturation chemical potential. A density distribution of Figure 4.7 shows two peaks. Although the curves are not smooth and the two peaks are not well separated, the equal area construction does indicate a first order phase transition between a thin and thick film. The roughness of the density distribution may be attributed to insufficiently long runs for collecting histograms. The fact that the peaks are not well separated is attributed to the temperature being close to the bulk critical temperature. The jump in the isotherm corresponds to a prewetting transition. The wetting temperature is hence estimated to be 29.5 K. This value is much higher than the wetting temperature of 20 K computed

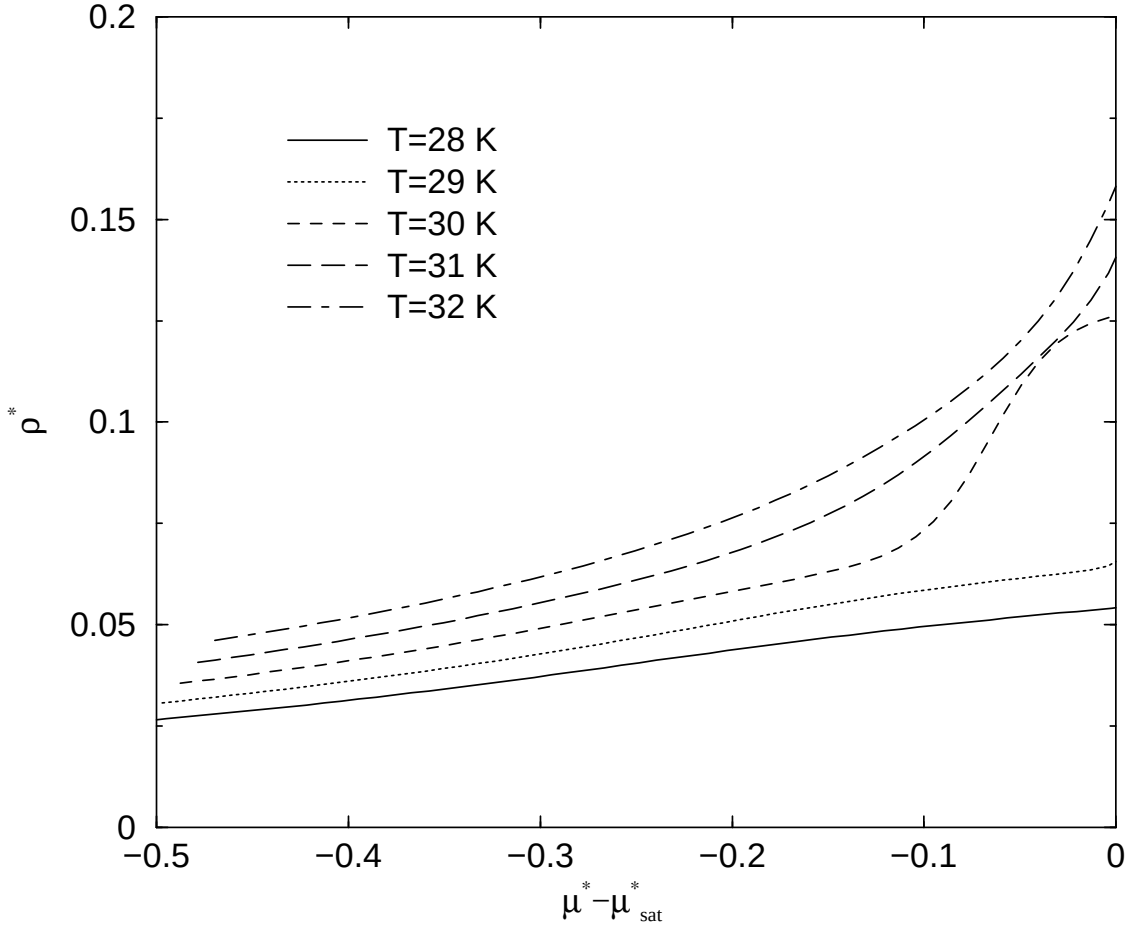

Figure 4.6: The isotherms calculated from multiple histogram reweighting calculations for the 9-3 potential.

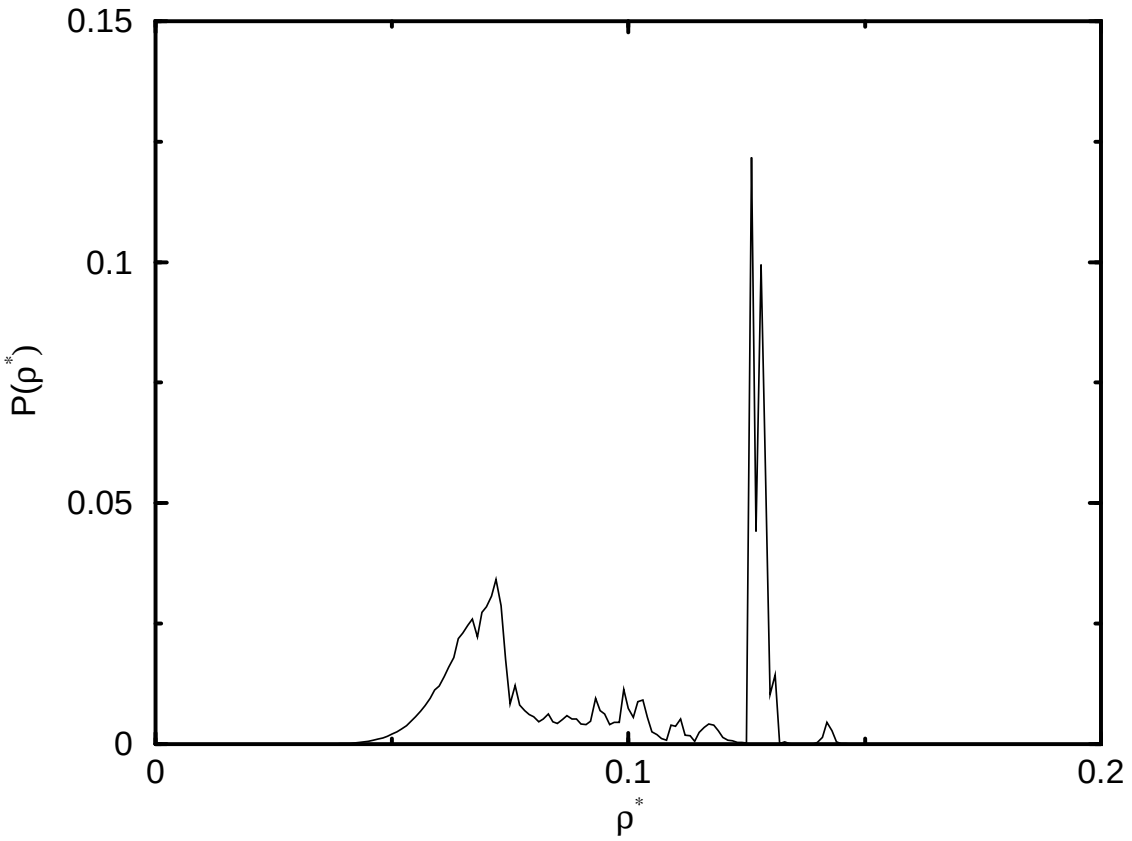

Figure 4.7: The number density distribution at 30 K. Note that we can see two peaks although the two peaks are not well separated.

from the simple theory[125]. The critical prewetting critical temperature is estimated to be 31 K. The wetting temperature from experiment is 19.10 K[103]. The discrepancy between experiments and simulations can be attributed to errors in the solid-fluid potential, as discussed in the next chapter.

4.5 Conclusions

We have extended the multiple histogram reweighting technique to path integral fluids for both bulk and inhomogeneous fluids. The phase diagrams of both TR and LRC H_2 with a cutoff of 15 Å, LRC D_2 with a cutoff of 9 Å were calculated. The average absolute deviations for the the coexistence density between LRC and TR H_2 are 6.9% and 1.1%, respectively, for the vapor and liquid branches. This is considerably larger than for classical fluids. The wetting temperature for H_2 adsorption onto Rb surface with the 9-3 model potential is estimated to be 29.5 K,

The disadvantage of MHR technique for path integral fluids is that many more state points are needed compared with classical fluids. This is due to the number of beads needed to accurately describe H_2 and D_2, making the overlap in U_1 and U_2 rather poor. The number of state points may be reduced by employing the multicanonical ensemble technique[128].

5.0 WETTING TRANSITIONS OF HYDROGEN AND DEUTERIUM ON THE SURFACE OF ALKALI METALS

5.1 Introduction

Consider a fluid near a solid surface at pressure P and temperature T (below the liquid-vapor critical temperature T_c). When P is equal to the saturated vapor pressure ($P_{\rm svp}$), an adsorbed liquid film may exhibit either one of two possible behaviors: spreading across the surface or beading up to form a droplet. These possibilities are called wetting (or complete wetting) and nonwetting (or incomplete wetting), respectively. This distinction is compatible with Young's equation for the contact angle (which vanishes in the wetting case) and thus the behavior of a given system can, in principle, be derived from the T-dependence of three surface tensions (gas-solid, liquid-solid and gas-liquid). Some 25 years ago, scenarios of thermodynamic transitions between wetting and nonwetting were predicted by Cahn[83] and Ebner and Saam[84]. Subsequently, such wetting transitions have been observed experimentally for both isotopes of He and for hydrogen on Rb and Cs, for Ne on Rb, and for Hg on sapphire and Ta. Similar transitions have been predicted to occur for other adsorption systems (e.g. Ne/Mg and Ar, Kr and Xe on alkali metal surfaces)[103,129–138]. The common feature of all of these systems is the existence of a very weakly attractive adsorption potential; the well-depth (D) of the gas-surface interaction $V(z)$ is less than, or of the order of, the well-depth (ϵ) of the intermolecular potential of the adsorbing fluid.

These wetting transitions have been studied by a variety of general theoretical models, including lattice-gas, density functionals, and classical Monte Carlo simulations[76,102,139–142]. To date, remarkably, there has been no quantum simulation exhibiting a wetting transition[143], even though the quantum fluids He and H_2 are paradigms of this transition[144]. Moreover, the only classical simulation study pertinent to *any* experimentally observed wetting transition (Ne/Rb) is difficult to compare with the data because of uncertainties arising from the proximity (within 1%) of the wetting transition temperature T_w to T_c[131,140] and neglect of quantum effects in the simulations[120].

This lack of theoretical analysis for systems studied in the laboratory leaves open many questions, e.g., how reliable are the adsorption potentials and theoretical models used to predict the transition? What is the detailed nature of the thin-to-thick film wetting transition? Can simulations accurately predict other systems which will exhibit prewetting transitions?

In the absence of exact calculations for experimentally relevant systems, an alternative approach to predicting T_w has been posited, a so-called "simple model" [141]. In that model, the thin-to-thick film transition is predicted to occur when the surface tension "price" of forming two interfaces becomes equal to the free energy reduction due to the integrated fluid-surface attraction. Estimates of these terms lead to an implicit relation for the wetting temperature:

$$\sigma_{lg} = -\frac{1}{2}\rho_0 \int_{z_{min}}^{\infty} V(z)dz, \tag{5-1}$$

where σ_{lg} is the bulk liquid-vapor surface tension and ρ_0 is the bulk fluid number density, both at T_w, and the integral extends from the minimum of the potential to infinity. Some evidence implies that this model works surprisingly well in predicting T_w of classical gases, except in cases of the least attractive interactions [142]. However, no comparison between "exact" calculations, this model, and experimental data has ever been made. Such calculations are therefore needed in order to further test this model and theoretical calculations of the adsorption potential. This paper presents evidence relevant to these open questions by comparing wetting transition data with results of path integral grand canonical Monte Carlo simulations for the hydrogen isotopes. This simulation method is exact, in principle, assuming that the interaction potentials are correct.

5.2 Theory and Simulation Details

Molecular simulations were performed using path integral grand canonical Monte Carlo [123,145]. The fluid interactions were modeled with the Silvera-Goldman potential [124], which is accurate for

both H_2 and D_2 [120,123,146]. The saturation properties of the bulk fluids were computed from multiple histogram reweighting (MHR) [11,12] adapted for path integral Hamiltonians [146].

A number of different potentials for for H_2/Rb were considered, four of which appear in Figure 5.1. The *ab initio* potential of Chizmeshya *et al.* (CCZ) [137] was derived from a Hartee-Fock

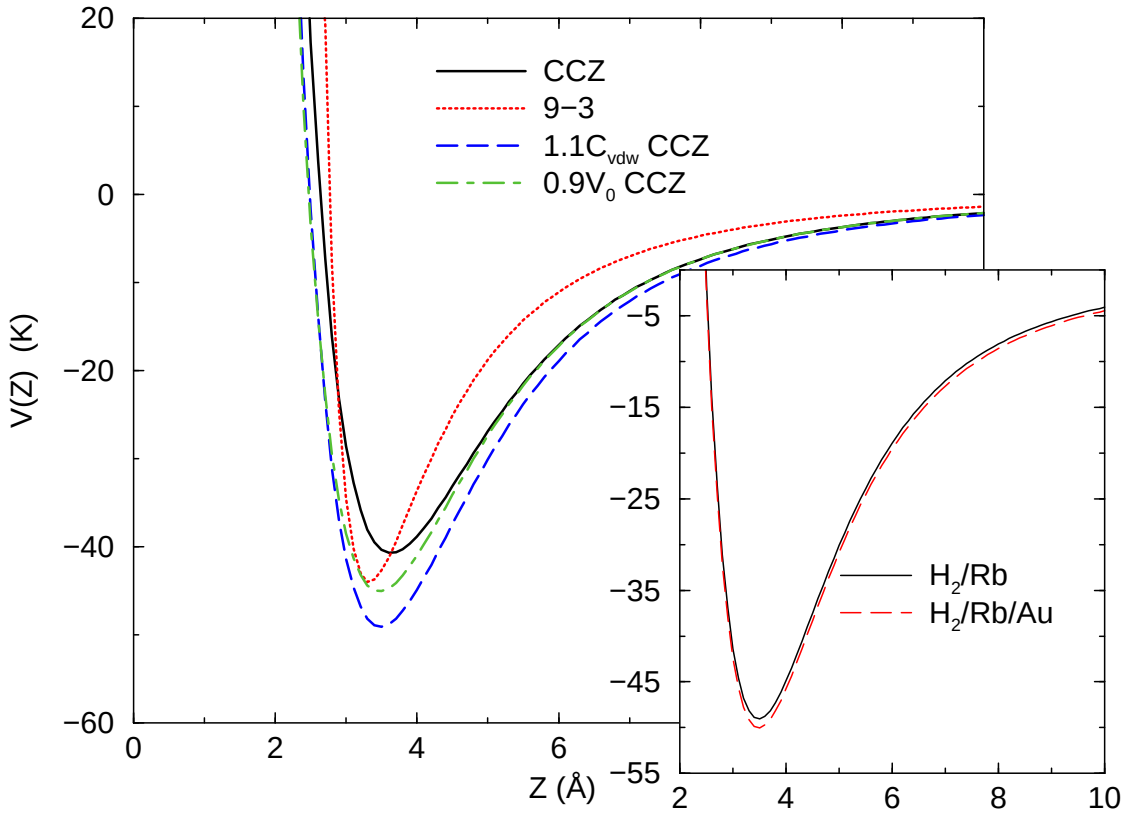

Figure 5.1: (Color online) The original CCZ [137] and the 9-3 potentials [125] for H_2 on Rb. Also shown are two modified potentials obtained by varying the $C_{\rm vdw}$ and V_0 parameters in the CCZ potential. The inset shows a comparison of the $1.1C_{\rm vdw}$ H_2/Rb potential (solid line) and the corresponding potential for a 15 Å thick film of Rb on Au (dashed line).

repulsion and a damped van der Waals (vdw) dispersion term [147]. The resulting potential was found to fit the following expression:

$$V(z) = V_0(1+\alpha z)e^{-\alpha z} - f_2(\beta(z)(z-z_{\rm vdw}))\frac{C_{\rm vdw}}{(z-z_{\rm vdw})^3}, \tag{5-2}$$

where z is the distance between the adsorbate the jellium boundary of the metal, f_2 is a damping function given by $f_2(x) = 1 - e^{-x}(1+x+x^2/2)$, $\beta(z)$ is given as $\beta(z) = \alpha^2 z/(1+\alpha z)$, V_0, α, $C_{\rm vdw}$ and $z_{\rm vdw}$ are the four parameters of the potential. We have also used an empirical 9-3 potential,

which was used by Cheng *et al.*[125] to compute the wetting temperature for H_2 on Rb from the simple model.

The CCZ parameters for H_2/Rb are $V_0 = 0.274$ eV, $\alpha = 1.769$ Å^{-1}, $C_{\rm vdw} = 0.297$ eV Å^3, and $z_{\rm vdw} = 0.246$ Å. This potential is characterized by a well-depth ratio $D/\epsilon \sim 1.26$.

5.3 Results

The simple model predicts a T_w of 22.7 K[137] for the CCZ potential and a value of 22 K for the 9-3 potential. The simulations discussed below indicate that $T_w = 25.5 \pm 0.5$ K for the CCZ potential and 29.5±0.5 K for the 9-3 potential. This finding was unexpected because the 9-3 potential has a substantially larger well depth than the CCZ potential, which would be expected to result in a *lower* T_w. This is reflected in the predictions from the "simple model" (see Table 5.1). However, the simulations show that the broader potential well of the CCZ potential more than compensates for the smaller value of D compared with the 9-3 potential. This sensitivity to the shape of the potential does not appear to be adequately captured in the "simple model". Figure 5.2 presents simulation results for the film density, obtained with the CCZ potential, at 25 K and 26 K. At 25 K, only a thin film forms at all $P < P_{\rm svp}$, indicating nonwetting. Note that due to metastability the adsorption is very small even at a pressure a little higher than $P_{\rm svp}$. The thermodynamic excess coverage (the integrated excess of the film density relative to the vapor density) is minuscule, about ∼15% of

Table 5.1: Well depths, wetting temperatures, and prewetting critical points (T_{pwc}) for H_2 on Rb computed from the 9-3 potential[125], the original CCZ potential[137], and several variants obtained with altered parameters. The values of T_w in parentheses are determined from the simple model while the other values are from simulations (with uncertainty ±0.5 K). The experimental values are $T_w = 19.1$ K and $T_{pwc} \sim 23$ K[103].

Potential Model	D (K)	T_w (K)	T_{pwc} (K)
9-3	44	29.5 (22)	31
CCZ	41	25.5 (22.7)	30
0.9 V_0	45	22.5 (20.3)	28
1.1 $C_{\rm vdw}$	49	18.5 (19)	25.5
0.9 V_0, 1.08 $C_{\rm vdw}$	53	17.5 (18.6)	24.5

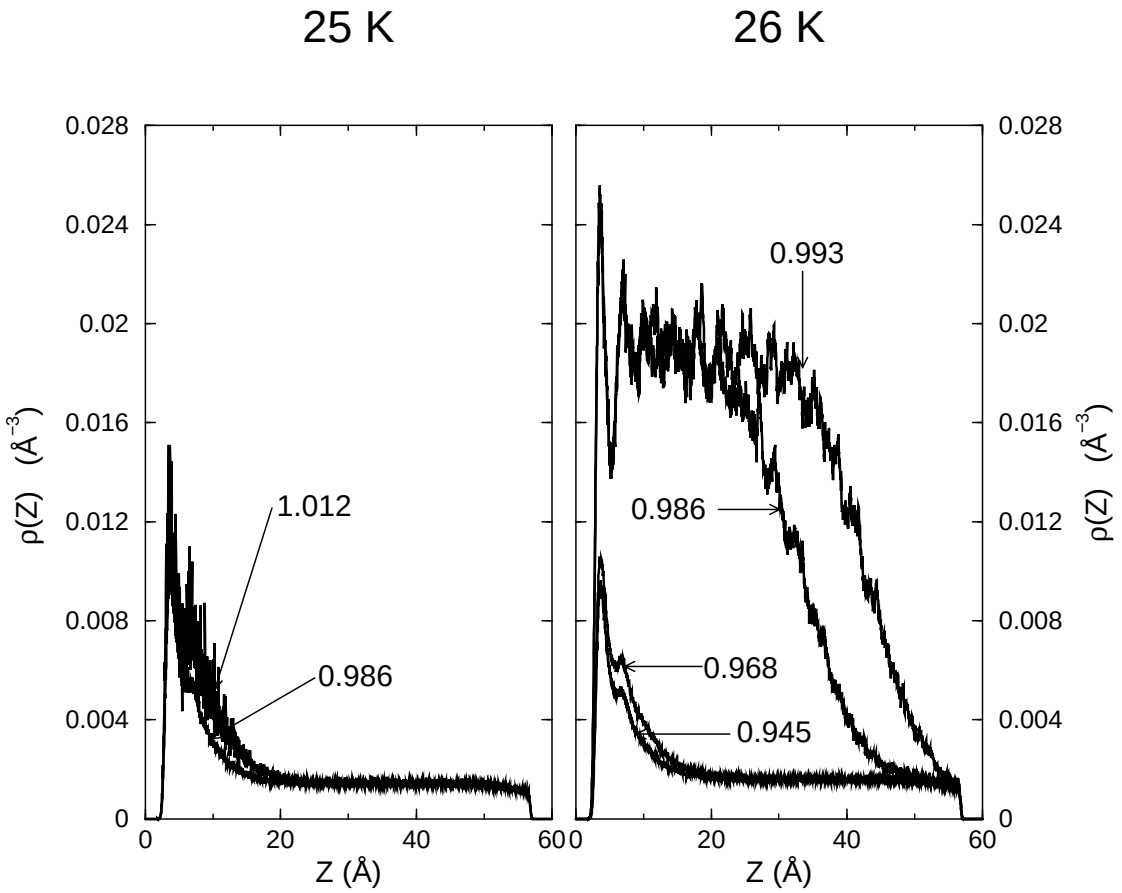

Figure 5.2: The local density profiles for the original CCZ potential[137] at 25 and 26 K. The relative pressure, $P/P_{\rm svp}$, at which the calculations were performed are indicated by the numbers on the graph.

the close-packed monolayer coverage. The simulation results for the film at 26 K manifest quite different behavior, characteristic of a prewetting transition. Below 98% of $P_{\rm svp}$, a thin film forms. At $P/P_{\rm svp} = 0.98$, however, there is a factor of 8 jump in the excess coverage. Further increases in P toward $P_{\rm svp}$ yield an ever thickening film, i.e, wetting behavior. Thus, the CCZ potential yields a first order wetting transition, with a wetting temperature somewhere between these two values of T, i.e., $T_w = 25.5 \pm 0.5$ K. This value is significantly higher than the experimentally measured value of $T_w = 19.10 \pm 0.06$ K[103]. The discrepancy implies that the assumed $V(z)$ is too weakly attractive, which we address below. We have empirically adjusted $V(z)$ to bring the T_w prediction into agreement with experiment by making changes to $C_{\rm vdw}$ and V_0. Some results are shown in Table 5.1.

These results (and others, not tabulated) indicate the sensitivity of the wetting behavior to the potential parameters, especially the vdw coefficient. For example, for H_2 on Rb a 10% increase in $C_{\rm vdw}$ ($1.1C_{\rm vdw}$) leads to a 27% decrease in T_w, whereas a 10% decrease in V_0 ($0.9V_0$) gives a 12% decrease in T_w. Of the potentials we have examined, $1.1C_{\rm vdw}$ gives the best agreement with experiments. The simple model consistently underestimates the wetting temperature by a few Kelvin, or about 10% for most of the potentials in Table 5.1. This finding is consistent with that obtained from classical simulations[142], which show a similar systematic discrepancy. This semiquantitative consistency is better than what might be expected with such a primitive model!

Comparison of calculated and experimental T_w values implies that the CCZ potential is not sufficiently attractive to explain the H_2/Rb data. We have made additional comparisons to test the generality of this conclusion. One comparison involves the adsorption of D_2 on Rb. This is a fairly stringent test of the new potential and its relation to the experiments, which were carried out in the same laboratory in which the H_2/Rb data were taken. We have used the potential in best agreement with H_2/Rb experimental data, i.e., $1.1C_{\rm vdw}$, for these simulations. The result is that the simulation yields $T_w = 29 \pm 0.5$ K, in excellent agreement with the experimental value of 28.9 ± 0.3 K[103]. This agreement improves our confidence in the new potential, which should be virtually identical for the two isotopes (differing only in very small effects of the 1% difference in

the isotopes' polarizabilities). We have also studied H_2 wetting on a similar system, H_2/Cs. The potential well-depth for H_2/Cs was found by Chizmeshya *et al.*[137] to be some 5% smaller than that for H_2/Rb. The simple model predicts a T_w ∼23 K, which is higher than the experimental value of 20.57 ± 0.05 K of Ross *et al.*[148]. We have simulated this system with the $1.1C_{\rm vdw}$ potential, assuming that the error in the *ab initio* potential is systematic. The resulting wetting temperature for this system is 19.5 ± 0.5 K which is slightly lower than the experimental result. The agreement for the three relevant systems that have been studied experimentally encourages our confidence in the both the revised potential and the experiments. The comparison is particularly meaningful because the experiments were performed in different laboratories, using quite distinct methods of surface preparation.

We have computed T_w of H_2 on Au coated with Rb, a system not yet studied experimentally. The potential for this system is given by $V_{\rm Rb/Au}(z) = V(z) - \frac{\delta c}{(z+d)^3}$, where $\delta c = 474$ meV Å^3 is the difference of the $C_{\rm vdw}$ between Au and Rb, d is the film thickness of Rb, set to 15 Å in this case, and $V(z)$ is given by Eq. (5-2) with the parameter for H_2/Rb using $1.1C_{\rm vdw}$. The potentials for H_2 interacting with a pure Rb surface and a 15 Å film of Rb on Au are plotted in the inset of Figure 5.1. Note that the potentials are nearly identical, with the Rb/Au potential being about 1 K deeper at the minimum. T_w for H_2 on a 15 Å film of Rb on Au is 17.5 ± 0.5 K, about 1 K lower than the pure Rb case. The lowering of T_w has been observed for ^{4}He on Cs films of various thicknesses[149]. At 20 K the relative prewetting transition pressure, $P_w/P_{\rm svp}$, is 0.93 for the Rb on Au substrate, while for the pure Rb substrate $P_w/P_{\rm svp} = 0.97$, a decrease of about 4%. The $P_w/P_{\rm svp}$ at 21 K also differ by about 4%. These differences in T_w and $P_w/P_{\rm svp}$ should be large enough to detect experimentally. The simple theory predicts that the wetting temperature shifts in proportion to δc, with a resulting shift of 0.9 K for a Rb film thickness of 15 Å[150]. This is consistent with the simulation result. The surprisingly large shift is indicative of the extreme sensitivity of the wetting transition behavior to the long range interaction, as implied by Eq. (5-1). It is possible to experimentally construct such a film of Rb on Au and to measure the wetting properties to test these predictions[149].

5.4 Discussion and Conclusion

We address briefly the intriguing question: why does the theoretical CCZ potential underestimate the gas-surface attraction by $\sim 10\%$? Possible explanations include the contribution of the H_2 quadrupole interaction with its image (omitted from CCZ), uncertainty about the image plane's position, the form of the damping function, and the need for a more careful treatment of the electron gas, including hybridization with the adsorbate states[151]. Here, we consider the contributions of two independent quadrupole-related terms. The first is the permanent quadrupole moment's orientation-dependent interaction with its image, which has been evaluated elsewhere for similar problems[152]. The resulting energy is small: just 0.2 K (compared to a well depth of 41 K). The other term is the fluctuating quadrupole moment of the molecule interacting with its image in the metal. Using the theory of Jiang et al. to evaluate this quantity, we obtain an attractive energy of 2.0 K for an H_2 molecule at its equilibrium position on Rb[153]. This represents a 5% contribution to the well depth, too small to explain the discrepancy manifested in T_w. Thus, the adsorption potential remains an open problem.

Finally, we comment on the decade-long evolution of our understanding of this problem. A theoretical potential was proposed in 1993, from which the simple model predicted a wetting temperature $\sim$22 K for H_2/Rb, close to the experimental value of 19 K[125]. This agreement was a fortuitous consequence, we now believe, of a systematic error inherent in the simple model (explained above) and a systematic error in the potential used at that time. These two errors shifted the prediction of T_w in opposite directions, so that their effects approximately canceled, resulting in nominal agreement with experiment. In that initial study, the uncertainty in the well depth of the potential was reported to be 40%. The more recent CCZ potential employs better justified methods and approximations than the 1993 study and has a smaller estimated uncertainty, $\sim$25%. However, the good agreement of 1993 between experiment and theory has been lost, leaving unanswered questions about the origin of the remaining discrepancy. The present study indicates how wetting transition data can be utilized to test and refine theoretical adsorption potentials. Com-

plementary experimental investigations, such as gas-surface scattering measurements and a test of the predicted shift in T_w for the Rb/Au compound substrate, would provide additional assessments of predictions based on these new potentials.

6.0 CHEMICAL ACTIVATION OF SINGLE-WALLED CARBON NANOTUBES FOR HYDROGEN ADSORPTION [1]

In this chapter, we report the isotherms of hydrogen adsorption onto single carnon nanotube bundles. The data have been compared with the experiments. All the experimental work are done by M. R. Smith, Jr., E. W. Bittner, and B. C. Bockrath.

6.1 Introduction

The unique porosity of single walled carbon nanotubes (SWNTs) has prompted considerable interest in their gas adsorption properties. The present need for better materials for hydrogen storage has led to much of the interest in this direction. Several reviews of this rapidly growing area have appeared.[21,154,155] Among the various reports are claims that significant amounts of hydrogen are taken up by SWNTs. Claims of high values of hydrogen adsorption have been made in reports of investigations at low temperature,[22] room temperature[23,24] and even higher temperatures.[28] In contrast, most theoretical calculations of hydrogen adsorption have given considerably lower estimates.[156–166] These results may indicate that physisorption on pure nanotubes may not be an effective method of storing hydrogen. Other experimental studies have found very limited uptake of hydrogen,[25–27] in agreement with simulations. However, variations in the experiments may be due to differences in the way the SWNT samples were prepared or pretreated.

Chemical activation is one option for improving adsorption characteristics. Although it has a long history of application in carbon chemistry, its potential for use with the recently synthesized carbon nano-structures is just beginning to become evident.[167,168] It has been shown that Xe adsorption on SWNTs is dramatically affected by the pretreatment procedure.[169] Eklund and coworkers have shown that the hydrogen uptake on nanotubes at low temperatures can be increased radically by activation of the nanotube samples.[168]

[1] This chapter is reprinted from reference[46]

In the work described below, we have used a tapered element oscillating mass analyzer (TEOM) to obtain isotherms for hydrogen adsorption on SWNTs at 25 °C over the range of pressure from one to 48 bar. This instrumental method is based on measurement of the weight change observed as a function of the applied hydrogen pressure in a flow-through system. The application of this instrument to determine adsorption isotherms has been recently demonstrated in the case of light alkanes (methane – butane) on silicalite.[170] In the work reported below, samples of SWNTs were used as-received and after various pretreatments. The most remarkable results were obtained using a simple activation procedure based on partial oxidation using carbon dioxide at 600 °C. The adsorption of excess hydrogen increased markedly after SWNTs were activated by this procedure. Activated samples were found to adsorb 1.2 wt% hydrogen at 48 bar and 25 °C. Details of the activation procedure are described in a recent paper.[171] Characterization of the surfaces of the same raw and purified nanotubes as used in this work has been made by a pulse adsorption technique using the TEOM.[172]

We also present molecular simulations as a means of identifying possible reasons for the observed increase in adsorption in the samples that have been activated by CO_2 oxidation. Theoretical calculations of hydrogen adsorption on SWNTs have been performed using various methods.[156–166] With few exceptions, these studies indicate only modest uptake of hydrogen at room temperature and moderate pressures. *Ab initio* simulations that indicate the potential for higher uptake are subject to substantial error because the description of the H_2-nanotube interaction within the tight-binding or density functional approximations is not expected to be accurate for physisorption.[173–177]

All of the theoretical studies performed so far have been carried out on SWNT samples that are, by necessity, idealized in some ways. Some of the studies consider only single isolated nanotubes. Other studies assume idealized nanotube bundles composed of perfect hexagonal or square arrays of identical nanotubes, all of the same diameter and chirality. In reality, experimentally produced SWNT bundles are composed of nanotubes of different diameters and chiralities.[178–182] While nanotubes pack into a hexagonal array, the packing is not expected to be perfect because of the

distribution of nanotube diameters in a bundle. At least some nanotube samples have a significant number of defects that may contain carbonyl or other oxygenated groups.[183] Nanotube bundles are also not perfectly straight. There is curvature over length scales of hundreds of nanometers, allowing nanotube bundles to cross one another, leading to complex secondary structures. The external surfaces of the SWNT bundles are also complicated by the presence of amorphous carbon and catalytic metals. All of these factors make exact modeling of real SWNT bundles a very difficult task. In addition, the exact form of the nanotube-hydrogen potential is unknown and could only be computed accurately from very high-level electronic structure methods that include electron correlation (e.g., coupled cluster or configuration interaction); such calculations are impractical for SWNTs because of the large number of atoms involved. It is also not known exactly how the presence of defects changes the interaction potential. Activation processes, such as the one used in this study to improve hydrogen uptake, further complicate the description of the nanotube samples by adding unknown chemical and topological changes to the underlying structure. Previous simulations have accounted for defects in an approximate way by including point dipoles or point charges.[184] Size heterogeneity in different bundles has been modeled by picking nanotube diameters randomly from a given size distribution.[185] In this study we examine the effect of the nanotube diameter distribution and packing on hydrogen uptake. We also vary the nanotube-hydrogen interaction potential by arbitrarily increasing the potential well depth to mimic the effect of chemical activation.

6.2 Experimental Methods

A block diagram of the experimental apparatus including the TEOM Series 1500 Pulse Mass Analyzer (Rupprecht and Patashnick Co.) is given in Figure 6.1.

The TEOM Series 1500 is a flow-through microbalance that detects mass changes by an inertial system. It was initially used to study coke deposition on zeolite catalysts,[186] and has since found general application for following mass changes in a variety of chemical systems including a recent study of the adsorption isotherms of light hydrocarbons on zeolites.[170] It employs a tapered glass element to measure mass changes. The element consists of a hollow glass tube that leads the gas stream through a cylindrical sample bed, diameter 4 mm, height 6 mm, located at its lower end. Samples were packed into the bed between "Astro quartz" wool plugs and retained there by a ventilated, gold-plated metal cap. Gas streams were controlled using a manifold that included mass flow controllers and a back-pressure regulator. Instrument control and data recording were managed through a PC. The control system allowed the programmed selection of the gases, their flow rates, system pressure and temperature, and other functions. Two gas streams were supplied to the instrument; one passes through the sample in the packed bed (reactive gas) and the other sweeps the volume outside the sample bed (purge gas). The tapered-element was enclosed within a heated stainless steel pressure vessel. The instrument is capable of operating from ambient temperature to 700 °C and from ambient pressure to 48 bar. The combined flow of both gas streams is sampled at the exit port by a capillary tube that serves as a transfer line to a quadrupole mass spectrometer.

The operating principle of the instrument is based on the relationship between changes in the mass of the sample bed to changes in the frequency of oscillation of the tapered element. The element is stimulated to vibrate at its natural frequency by a mechanical system. The frequency of oscillation is measured by an optical system through two ports in the pressure vessel. Mass changes are determined by the following equation:

$$\Delta m = \frac{k}{\frac{1}{f_1^2} - \frac{1}{f_2^2}}, \tag{6-1}$$

where f_1 and f_2 represent the frequencies observed at two different loadings, and k is an empirically determined constant. The instrument was equilibrated at the isotherm temperature and flow conditions in order to determine the value of k. The frequency of the empty reactor was measured without the retaining cap in place, then the procedure was repeated with the cap in place. The constant was calculated using the known mass of the cap.

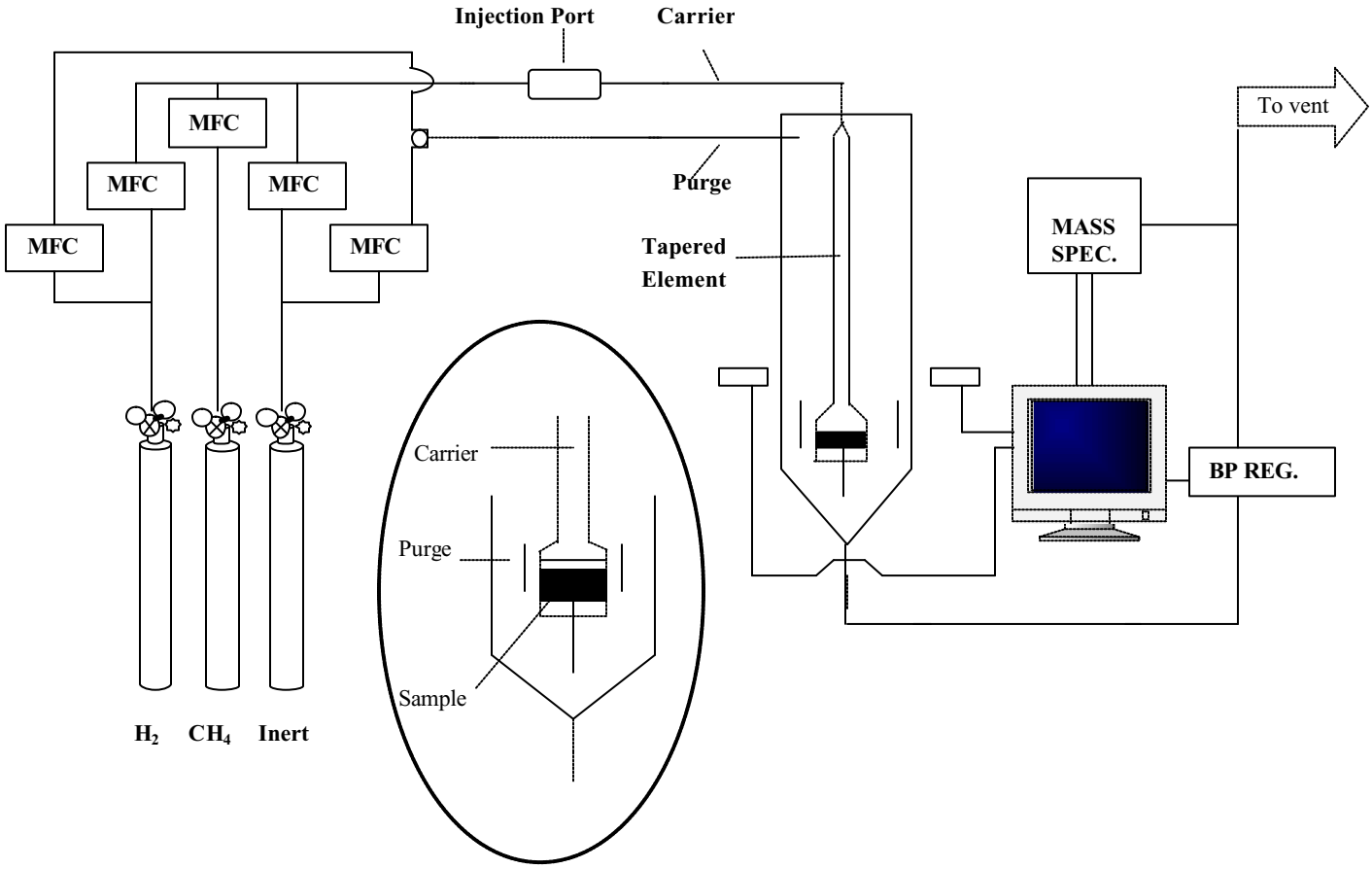
Injection Port
Carrier
To vent
MFC
MFC
MFC
MFC
MFC
Purge
Tapered
Element
MASS
SPEC.
BP REG.
Carrier
Purge
Sample
H2
CH4
Inert

The mass changes observed in the instrument as the pressure is varied result from both changes in density of the free gas within the oscillating element and the change in the amount of gas adsorbed by the sample. To obtain the isotherm of the excess adsorbed gas, the amount due to the change in density of the free gas must be subtracted from the total. The values due to the free gas density changes were obtained from experiments with the reactor empty. In this case, the observed mass change increased in a nearly linear fashion with pressure. Measurements were then taken with a sample in place under exactly the same conditions. Isotherms were generated by subtracting the mass change found with the empty reactor from the corresponding value found with the packed reactor for each step in pressure. A correction was applied to the empty reactor data to account for the volume occupied by the sample (see calculations below).

In a typical experiment, a sample of 30-50 mg was packed into the bed between 20-40 mg of quartz wool used as plugs. The bed was flushed with dry helium or nitrogen, then heated to 200 °C for at least two hours. After the signal from the mass spectrometer indicated that the release of small amounts of water and oxygen was complete, the sample was cooled to 25 °C and both reactant and purge gases were switched to hydrogen at a flow rate from 10-50 cc/min. Hydrogen was used as both purge and reactant gas in all experiments reported here to eliminate possible instrumental artifacts that may arise due to back-mixing of a dissimilar purge gas into the packed bed.

The pressure program was only begun after all of the inert gas had been swept from the reactor by hydrogen as indicated by the response of the mass spectrometer sampling the exit stream. Then the pressure was taken from ambient to 48 bar in seven steps. It was held constant for 10–20 minutes after each increment. At the end of the ascending program the pressure was returned to ambient using 1.4 bar decrements to avoid expelling the sample from the bed. The entire program was then repeated several times. Note that in these experiments, the origin of the pressure/mass change data is ambient pressure. Thus, isotherms refer to the increment in hydrogen adsorption above that already taken up at one atmosphere.

As noted above, a correction was applied to account for the portion of the free gas volume in the packed bed that is occupied by the sample and quartz wool. The correction was made by multiplying the mass changes for the empty reactor by the ratio of the free volume for the packed to that of the empty reactor. The total free volume sensed by the oscillating element was determined by applying the ideal gas law to the variation of the measured mass of the empty reactor when the hydrogen pressure was increased from ambient to 48 bar. The error in the specific volume from assuming ideal gas behavior at 48 bar and room temperature is about 3%. The volume of the sample was calculated from the mass of carbon in the sample and the theoretical density. The correction factor found using these values had a relatively small effect on the calculated amount of adsorbed hydrogen because the measured free volume of the reactor element is roughly an order of magnitude larger than the volume occupied by the sample. The mass change assigned to excess hydrogen was expressed as weight percent of gas adsorbed based on the total mass of carbon in the sample. The later was determined by thermal gravimetric analysis (TGA). Atomic adsorption spectroscopy was used to verify the identity of the residual catalytic metals recovered after the TGA analysis.

The weight percent of excess H_2 adsorbed is given by

$$wt\% = 100\frac{\Delta m_s - V_{\text{corr}}\Delta m_E}{f_c m_{\text{ads}} - \Delta m_{\text{ads}}}, \tag{6-2}$$

where Δm_s is the mass change for the packed bed after change to pressure P_i, V_{corr} is the volume correction factor ($\sim$0.977) to account for the volume occupied by the sample, Δm_E is the corresponding mass change in the empty reactor on reaching P_i, f_c is the fraction of SWNT sample that is carbon, m_{ads} is the mass of the SWNT sample, and Δm_{ads} is the weight lost after pyrolysis at either 200 or 700 °C.

The values used for each mass change were averages of from 80 to 160 data points taken over the 10-20 minute interval after a plateau was reached following each pressure step. Points in the isotherms are averages of 2-13 individual determinations of excess hydrogen for each pressure. The most extensively measured sample was calculated from 7 cycles of pressure up and down made

over 12 days. Data were taken from the 20 min plateaus at each step of the seven programs up in pressure and the 10 min plateaus of six programs down. The last depressurization failed and was not included. Sample standard deviations for the average of the 13 values for each point in the isotherm were between 0.03 and 0.11 wt%, being smaller at lower pressures. No trends were apparent over time nor differences noted for pressurizing or depressurizing sequences. One set of values for wt% H_2 (reaching 1.54 wt% at 48 bar) was tested for rejection using updated values for Dixon's Q test. The resulting $Q_{\mathrm{EXP}} = 0.72$ indicated rejection at the 99% confidence interval and this set was therefore not incorporated in the isotherm in Figure 6.2. The remaining set of 12 values for each pressure has standard deviations between 0.02-0.03 wt% for each point.

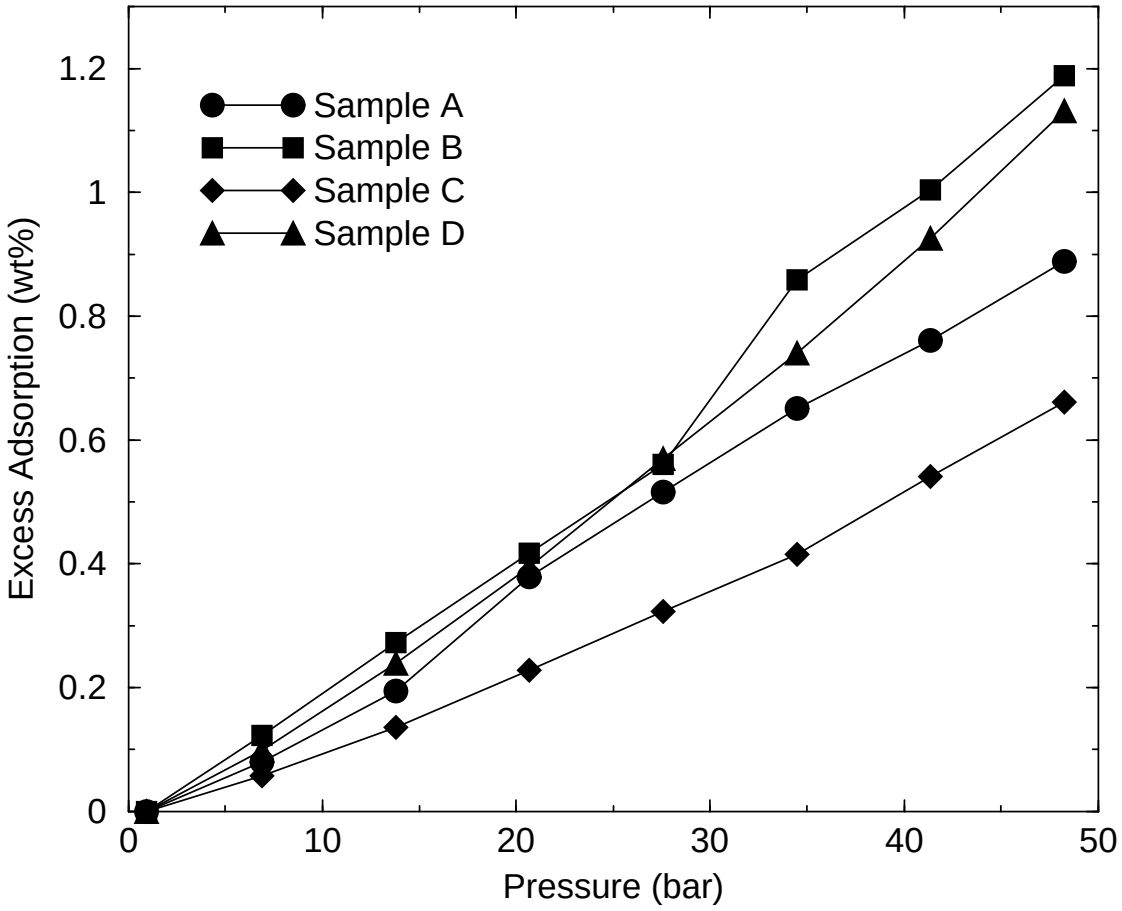

Figure 6.2: Adsorption isotherms for hydrogen on "Raw Material" Rice SWNTs after CO_2 oxidation (sample A). Sample B is derived from A after heating at 700 °C in H_2. Sample C consists of "Purified" Rice nanotubes after CO_2 Oxidation. Sample D is sample C after heating at 700 °C in He. The lines are drawn to guide the eye.

Nanotubes were purchased from Tubes@Rice in two grades. "Raw Material Grade" was obtained as a solid, fibrous, mat. It was subjected to light grinding to make it easier to load into the sample cell. Grinding was performed by agitation for 4-8 min. in a small agate ball mill (Wiggle Bug, Brinkman Instruments). "Purified Grade" was purchased as a suspension in toluene. Typically 10-15 mL of the suspension was withdrawn from the bulk sample and evaporated in a stream of dry nitrogen at ambient temperature. When toluene was no longer evident, the sample was further dried at 140 °C for up to a week. Activated nanotubes were prepared by partial oxidation in a tube furnace held at 600 °C using a stream of CO_2 and argon at about a 50/50 ratio. Details are given in another paper.[171] A sample of activated carbon (G-32 H, 4 × 10 mesh, Süd Chemie Inc.) was used to compare with the nanotube samples. The hydrogen, nitrogen, and carbon dioxide isotherms of this sample have been determined independently at this laboratory by a volumetric technique.[187] Hydrogen was "Extra Dry" grade (> 99.9%) from Matheson Tri-Gas. Helium and nitrogen were Matheson Tri-Gas UHP grade. The gases were further dried by passage through a Matheson Gas Purifier Cartridge Type 452 (4A molecular sieve).

6.3 Simulation Methods

Adsorption isotherms were computed from grand canonical Monte Carlo (GCMC) simulations.[2] The Silvera-Goldman potential[124] was used to describe the H_2-H_2 interactions. This potential has been shown to be accurate for computing equilibrium bulk properties over a very wide range of temperatures and pressures.[120] The H_2-nanotube interaction was taken as a pair-wise summation over H_2-C interactions computed from the Crowell-Brown potential.[188] This type of potential has been shown to reproduce experimental H_2-graphite adsorption isotherms and isosteric heats at low temperatures.[189] The solid-fluid potential used in the simulations is actually an integrated potential form so that a single polynomial function was fitted to the H_2-exohedral (outside) nanotube interactions and a second polynomial was used for the H_2-endohedral (inside) nanotube interactions.

Thus, each type of nanotube was described by two polynomial functions.[160] We have constructed several different types of SWNT bundles in order to study the effects of diameter heterogeneity and packing effects on hydrogen uptake. We have constructed bundles by choosing nanotubes of various diameters from a given diameter distribution to mimic experimental distributions.[181] We have also developed bundles based on an arbitrary diameter distribution for comparison with results from the experimental distributions. The bundles were packed by placing the first nanotube in the bundle at the center of the cell. The next nanotube was placed at a random position far enough away so as to ensure no overlap with the existing nanotube. The nanotube was then brought in a straight line toward the center of the box until the van der Waals (vdW) gap between the first and second nanotubes achieved some pre-specified value. The vdW gap is defined as the shortest distance between the walls of adjacent nanotubes, as measured from atom-center to atom-center. Subsequent nanotubes were added in a similar fashion to the second, except that the tube is brought in until its vdW gap with any other tube in the bundle reaches the specified value. The simulation box is a rectangular parallelepiped with a height (z-direction) of 34 Å and equal x and y dimensions. Periodic boundary conditions were applied in all three directions. The x and y dimensions were large enough to eliminate nearest neighbor interactions with tubes or hydrogen in the periodic images in order to mimic isolated SWNT bundles. Typical values of the width of the simulations box were between 100 Å and 250 Å, depending on the size of the bundle. A sample nanotube bundle is shown in Figure 6.3. The bundle contains 45 nanotubes and corresponds to bundle type a in Table 6.1. Typical GCMC moves[2] were attempted randomly with probabilities of 0.4 for displacements and

Table 6.1: Classes of nanotube bundles studied in the molecular simulations in this work.

Bundle ID	Num. of tubes	(8,8)	(9,9)	(10,10)	(11,11)	(12,12)	Average diameter (Å)
a	45	10	25	5	5	0	12.35
b	100	6	29	35	28	2	13.44
c	50	3	14	18	14	1	13.45
d	20	0	4	14	2	0	13.42
e	50	0	10	35	5	0	13.42

0.3 each for creation and deletion. The systems were first equilibrated for 5×10^6 steps, followed by 10^7 steps for data collection. Adsorption isotherms were computed for five different classes of

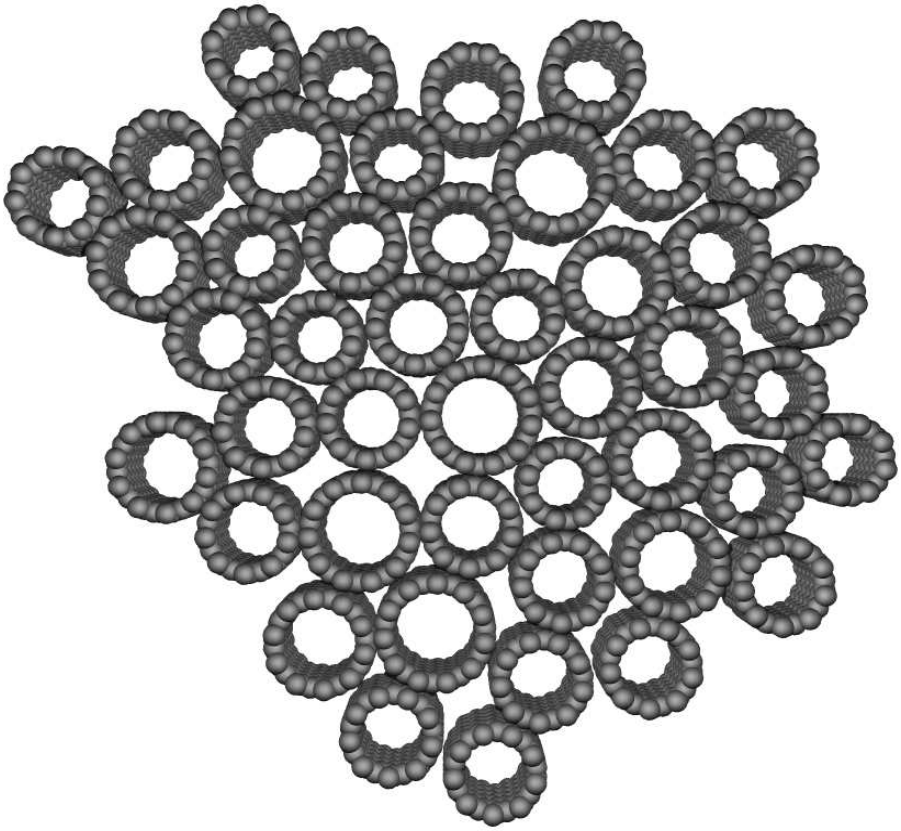

Figure 6.3: Sample nanotube bundle used in the molecular simulation. This bundle contains 45 nanotubes with diameters drawn randomly from a distribution similar to that observed in experiments (sample a in Table 6.1).

nanotube bundles shown in Table 6.1. The bundles contain from 20 to 100 nanotubes. Samples a – c are constructed to mimic two different diameter distributions observed in the experiment.[181] Samples d and e were constructed from an arbitrary diameter distribution. Samples b and c have almost the same diameter distribution. Sample c contains half as many nanotubes as sample b. Samples d and e have exactly the same diameter distribution, with sample e having 2.5 times as many nanotubes as sample b.

From two to ten different realizations of each bundle were constructed by starting the construction procedure outlined above with different random number seeds. Adsorption isotherms were computed for each of the realizations and the averages were reported. The differences in adsorption on different bundle realizations for a specified diameter distribution were typically on the order of the uncertainties in the simulations. To be consistent with the experiment, the excess adsorption is calculated as

$$wt\% = 100\frac{(N_{\mathrm{H}_2,P} - N^{\mathrm{rep}}_{\mathrm{H}_2,P}) - (N_{\mathrm{H}_2,1} - N^{\mathrm{rep}}_{\mathrm{H}_2,1})}{6N_{\mathrm{C}}}, \tag{6-3}$$

where $N_{\mathrm{H}_2,P}$ is the number of adsorbed H_2 molecules in the simulation cell at pressure P, $N^{\mathrm{rep}}_{\mathrm{H}_2,P}$ is the number of H_2 molecules at pressure P in the cell when the attractive part of the potential between H_2 and nanotube is turned off, $N_{\mathrm{H}_2,1}$ and $N^{\mathrm{rep}}_{\mathrm{H}_2,1}$ are the corresponding values at the reference pressure, i.e., 1 atm, N_{C} is the number of carbon atoms in the simulation cell. The excess adsorption defined in Eq. (6-3) is directly comparable to those from the experiments defined in Eq. (6-2). Note that this definition of the excess adsorption is different from that typically used because of the reference to one atmosphere rather than to vacuum.

6.4 Results and Discussion

Figure 6.4 contains the mass data used as a basis for the hydrogen isotherms described below. Curve A is the record of the mass changes for the packed reactor, and curve B is that for the empty reactor. Both mass curves closely follow the pressure curves (not shown). The initial spike found

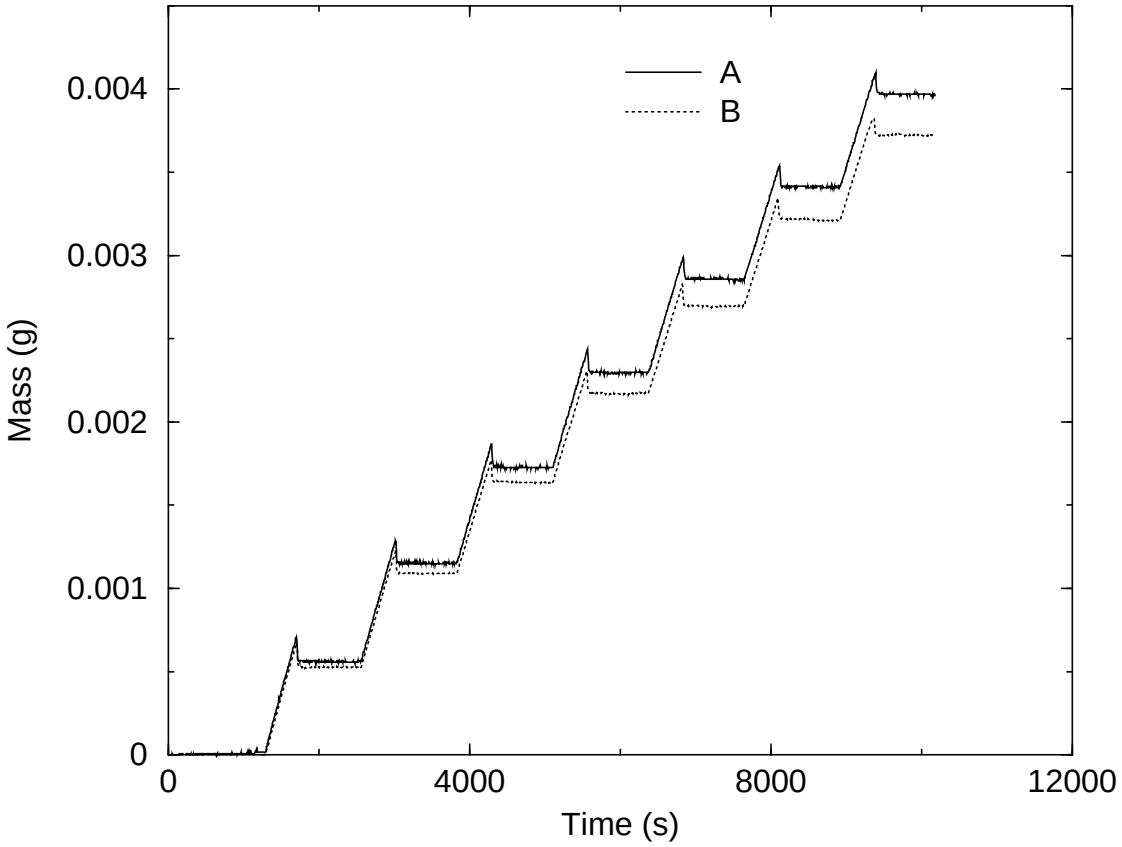

Figure 6.4: Mass versus time as the H_2 pressure increases in steps of about 7 bar from one to 48 bar. Curve A is a 29 mg sample of purified Rice nanotubes after CO_2 oxidation and B is for the empty reactor.

at the leading edge of each pressure step is due to an overrun of the set point by the back-pressure regulator. The mass change curve for the packed reactor reaches a new plateau after each pressure change and remains constant. This behavior is consistent with a physisorption process without a significant kinetic barrier. Separate experiments were made to test whether slow adsorption might take place over time scales much longer than the 20 min intervals used here. No measurable mass changes were found even when the initially formed plateau was extended for 28 hours at 48 bar. A very similar pattern was found for the depressurization data. These results for the kinetics of hydrogen adsorption and those reported on a different set of SWNTs of somewhat larger diameter [23] are distinctly different. In the later case, six hours was required for the pressure to equilibrate during the volumetric measurement made at room temperature, indicative of a significant kinetic barrier. No such barrier was found in any of the adsorption results given here.

The adsorption isotherm for hydrogen on an activated carbon is given in Figure 6.5 curve A. The isotherm is nearly linear up to the limit of pressure for these measurements, reaching a value of 0.66 wt% at 48 bar. Isotherms for hydrogen and other gases up to about 19 bar have recently been determined by a volumetric technique on this same lot of activated carbon.[187] Comparison of the two sets of data reveals the value measured volumetrically at room temperature and 14 bar is 1.2 moles/kg, while the corresponding point from the TEOM at 25 °C is 1.04 moles/kg. There is reasonable agreement between the values obtained by the two different techniques. Note that the TEOM and volumetric methods have different reference points. The TEOM technique measures the increment in hydrogen adsorbed above 1 atmosphere [see Eq. (6-2)], while the volumetric technique begins the measurement of excess adsorption after the sample chamber has been evacuated. Given that the amount adsorbed at 1 atm is only about 0.01 wt%, the observed differences between the TEOM and the volumetric method cannot be attributed to the difference in reference points.

Two isotherms for a sample of "Raw Material" SWNTs from Rice are also shown in Fig 6.5. Curve B was taken after the sample had been heated *in situ* to 200 °C under a flow of helium, then cooled before the isotherm experiment was begun. Curve C was obtained in a subsequent experiment after the sample had been heated in a similar manner but to 700 °C. Pyrolysis at

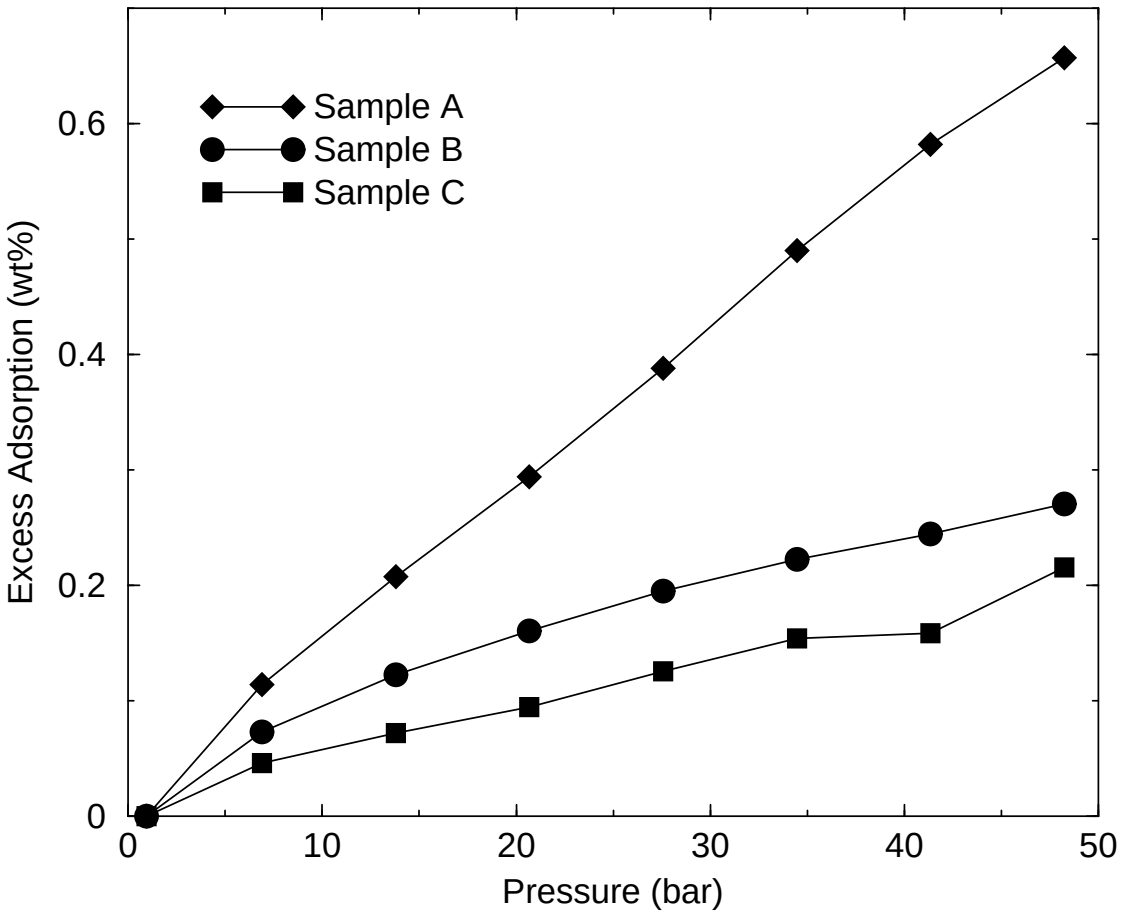

Figure 6.5: Hydrogen isotherms for activated carbon (A) and "Raw Material" as-produced Rice nanotubes after treatment at 200 °C (B) and 700 °C (C) in flowing helium. The lines are drawn to guide the eye.

700 °C reduced the affinity of the sample for hydrogen by a significant amount. (The apparently anomalous value at 41 bar for curve C was due to the influence of one of only two values determined under these conditions for this sample.)

Evidence that the pyrolysis of the raw material resulted in considerable loss of functional groups was provided by the in-line mass spectrometer used to monitor the exit gases throughout the course of heating to 700 °C. Hydrogen, methane, and carbon oxides were detected as the temperature increased. After the sample had returned to 25 °C, the TEOM measured a weight loss of 13.2 mg, or 23.2% of the sample weight. Data in Figure 6.5 are based on total mass of non-metals and have been corrected for loss of mass to allow direct comparison of the samples.

In comparison to the sample of activated carbon (curve A), the "Raw Material" nanotube samples have at best roughly one half the storage capacity under the same pressure. Again, the saturation loading of either the fresh or the pyrolyzed samples has not been reached at the highest pressure used here, although curve B seems to show some curvature not apparent in curve A.

Adsorption isotherms on "Purified" nanotubes obtained from Tubes@Rice are shown in Figure 6.6. These tubes have undergone oxidation by reflux in 2.6 M nitric acid for 12 hours.[181] The oxidation is reported to selectively remove amorphous carbon, leaving behind a greater proportion of nanotubes in the sample.[181] The samples were represented as containing greater than 90% SWNT. The relative amount of the residual metal catalyst left in the sample increases as well. Presumably an overlay of graphitic carbon protects these particles from removal by oxidation. The metal content of the sample used here was determined by complete combustion using TGA in combination with atomic adsorption spectroscopy of residual oxides. The metals content was 8.8 wt% and the spectroscopy confirmed the presence of nickel and cobalt. The isotherms given in Figure 6.6 were normalized on the basis of total carbon content to obtain a more useful comparison, but were not adjusted for the fraction purported to be SWNT.

Isotherms A and B in Figure 6.6 were taken sequentially using the same protocol as employed for raw material above. To a first approximation, the amounts of hydrogen adsorbed by the purified

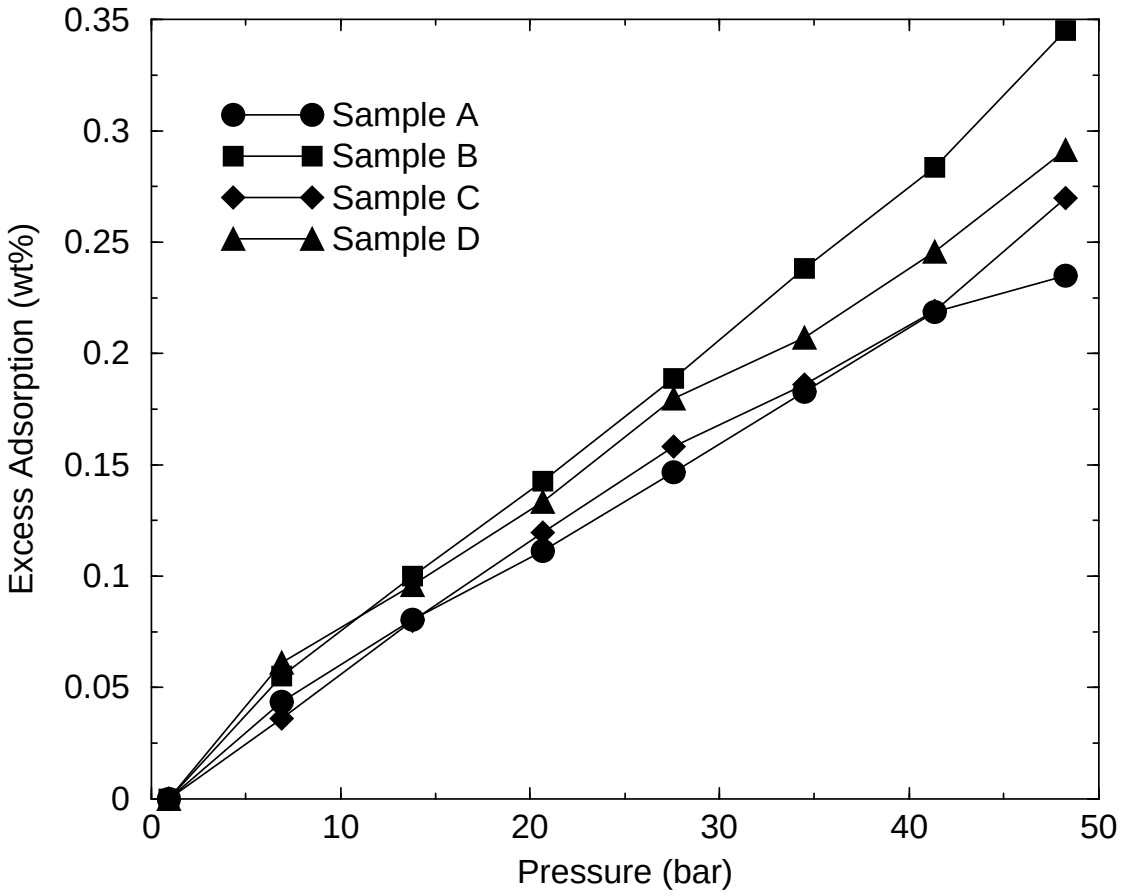

Figure 6.6: Comparison of adsorption isotherms of hydrogen on "Purified" Rice tubes: Sample A was heated at 200 °C in He. Sample B is sample A heated at 700 °C in He. Sample C is sample B after removal and milling in air. Sample D is sample C treated at 700 °C in H_2. The lines are drawn to guide the eye.

nanotubes and the raw material are similar. This result is contrary to the simple expectation that the purified material should adsorb a greater amount of hydrogen per sample weight because of its higher nanotube content. Heating to 700 °C in flowing He led to a modest increase in hydrogen adsorption as shown by comparing curves A and B. Perhaps it is more significant that the slope over this nearly linear region of the isotherm has increased after pyrolysis. Thus, the difference between the two may well increase at hydrogen pressures above those used here.

The mass spectra of the gases produced during pyrolysis were similar to those seen with the raw material and consistent with the loss of carboxyl and other oxygen containing functionalities. The mass loss following pyrolysis was 12.7% and may be compared with the value of 23.2 wt% found with the raw material. The functional groups responsible for this weight loss were likely introduced during the oxidative purification with nitric acid. Further evidence of their connection to the adsorption properties of the SWNTs was provided by a separate experiment in which another sample was carried through five cycles of pyrolysis at 700 °C over several days. The isotherms found before and after the first pyrolysis are nearly identical to A and B given in Figure 6.6. However, repetition of the initial pyrolysis had little further effect on the storage capacity or the slope of the isotherms. The relative amounts of the products from pyrolysis detected by the mass spectrometer were much reduced after the first cycle. Thus, the sample is chemically stable to 700 °C after the first pyrolysis cycle and no evidence for further annealing of the physical structure is found in the isotherms.

As mentioned in the Experimental section, these nanotube samples are difficult to pack into a small bed because their fibrous nature resists compaction. A mild mechanical milling procedure renders them much more amenable to packing. To determine whether this procedure has an effect on the adsorption properties, the sample was removed after isotherm B in Figure 6.6 was completed, milled by agitation in a small ball mill, and repacked in the bed. Milling the sample in air in this way decreased its adsorption capacity slightly (curve C). This loss was mostly restored (curve D) when the sample was again pyrolyzed, this time in flowing H_2. Thus, the effects seem more related to the oxidative consequences of milling in air rather than the milling itself. Mild ball milling in air

introduces oxygen containing functional groups into the nanotubes as evident from the evolution of CO and CO_2 observed in the mass spectrum on heating to 700 °C. In view of the small change, the issue was not pursued further.

Activation of the nanotube samples took place in two steps. The first step was conducted by partial oxidation of a roughly 200 mg sample of nanotubes in a tube furnace under a stream of CO_2 at about 600 °C. Burn out during the initial oxidative procedure removed about 37 wt% of the purified nanotube sample. In the case of the raw material, about 21% of the weight was removed during CO_2 oxidation. TEM images taken before and after the reaction with CO_2 show that in the case of the purified grade material the rope-like structures are left intact.[171] It is unexpected that a larger fraction of the purified sample would oxidize in the CO_2 treatment than for the raw material. This may be a result of the damage done to the nanotubes during the purification procedure.[190]

A marked improvement in the amount of hydrogen adsorbed was obtained for both the raw material and the purified tubes (Figure 6.2, curves A and C) after the first step. The amount adsorbed at 48 bar has increased from 0.29 to 0.89 wt% for the raw material and from 0.23 to 0.64 wt% for the purified material. The second step of activation was accomplished in the TEOM by heating the oxidized tubes to 700 °C in a flow of He or H_2. This induced further weight loss. For example, the oxidized raw material lost an additional 20% when pyrolyzed under H_2 at 700 °C. The pyrolysis lead to a further increase in hydrogen adsorption. The cumulative effect of the two steps is a significant increase in hydrogen storage capacity (Figure 6.2, curves B and D). Values of 1.16 wt% ("Purified") and 1.2 wt% ("Raw Material") were reached at 48 bar.

The data in hand do not permit an assignment of hydrogen adsorption capacity to particular fractions of carbon such as those identified by TGA for example. Thus, if the material removed by CO_2 oxidation had been relatively inert toward hydrogen adsorption the remaining material would show a corresponding increase in percent adsorption. Removal of this dilution effect could account for increases of 16% for the raw material and 59% for the purified material, but that is far short of the more than three-fold increase actually found. Instead, the large magnitude of the increase points toward a form of chemical activation.

It is reasonable to assume that this activation for adsorption may occur by opening the internal surfaces of tubular structures by oxidative destruction of part of the tube wall. In fact, evidence has been presented for thinning and opening of multi-walled tubes by partial oxidation with CO_2 at 850 °C, a somewhat higher temperature than used here.[167] The potential benefit created by removing tube end-caps and thus enhancing gas storage properties through the use of this method has been claimed in a patent, although no adsorption data were given.[191] Another study has demonstrated that opening the sidewalls of SWNTs by a combined cycle of oxidation and pyrolysis enhances the kinetics of xenon adsorption.[184] In this case, oxidation was accomplished with ozone, and the pyrolytic removal of the carboxylic groups so created was performed at the same temperature as used here, 700 °C. The maximum in the observed rate of xenon adsorption was found after a considerable percentage of the carbon had been etched away.

Parallels exist with the result reported here. The activation by CO_2 is likewise an oxidation. Because it is carried out at 600 °C it is simultaneously a pyrolysis, thus combining oxidation/pyrolysis cycle in one step. It also removes a considerable fraction of the carbon in the sample. The adsorption isotherms measure a thermodynamic property and we are unable to detect evidence for kinetic limitations in any case. However, TPD experiments described in the xenon adsorption work show that the majority of the sites that are more accessible after oxidation also desorb xenon at higher temperatures, implying deeper potential wells.[184] On the other hand, comparison of our data with computer simulation results (see below) indicate that in this case the increase in adsorption cannot be ascribed to opening of entry ports to the nanotubes alone.

It should be noted that pyrolysis of purified tubes results in a modest increase in hydrogen storage (Figure 6.6), but in the case of "Raw Material" SWNTs it results in a decrease of smaller magnitude (Figure 6.5). This result is puzzling, but we note that in the first case an oxidation using nitric acid was done to generate purified material before the pyrolysis was carried out. In the later case, pyrolysis was applied without prior oxidation. Annealing of the rope-like structures of nanotubes at elevated temperatures has been reported and must be considered as another potential side effect of pyrolysis. Annealing may reduce the amount of interstitial volume in bundles of the

raw material. The differences seen in Figure 6.5 are rather small, and would be in concert with the expectation that the relative amount of hydrogen taken up in the interstitial spaces is a small part of the total. Thus, the contradictory trends in adsorption may be the result of the dominance of an annealing effect in the case of raw nanotubes and the opening of additional porosity in the case of the purified nanotubes.

6.5 Simulation Results

We have computed H_2 adsorption isotherms on each of the nanotube bundles listed in Table 6.1. The isotherms on the different bundles are in quantitative agreement with one another. This is an important result because it indicates that the simulation results are not strongly dependent on the details of the bundle geometry or even the nanotube size distribution within the bundle. This insensitivity to the details of the geometry was unexpected. The excess adsorption isotherms are plotted in Figure 6.7. Results from simulations on bundle samples b, c, and e from Table 6.1 are plotted along with experimental data for purified nanotubes before being subjected to CO_2 oxidation (curve B from Figure 6.6). Adsorption isotherms from simulations on other bundles are very similar and are not shown for the sake of clarity. The agreement between the simulation and experimental isotherms is striking. Assuming that the solid-fluid interaction potential is accurate, the remarkable agreement between simulations and experiments indicates that the samples before CO_2 oxidation can be considered to be mainly composed of nanotube bundles (once the weight of the metal has been subtracted) and that amorphous carbon present in the sample and pore blocking functional groups do not severely inhibit hydrogen adsorption. On the other hand, it could be that the assumed H_2-nanotube interaction potential is too weak and that the adsorption is attenuated in the experiment due to pore blocking or unopened nanotubes to a degree that gives fortuitous agreement with simulations. Given the insensitivity of the computed adsorption isotherms to the

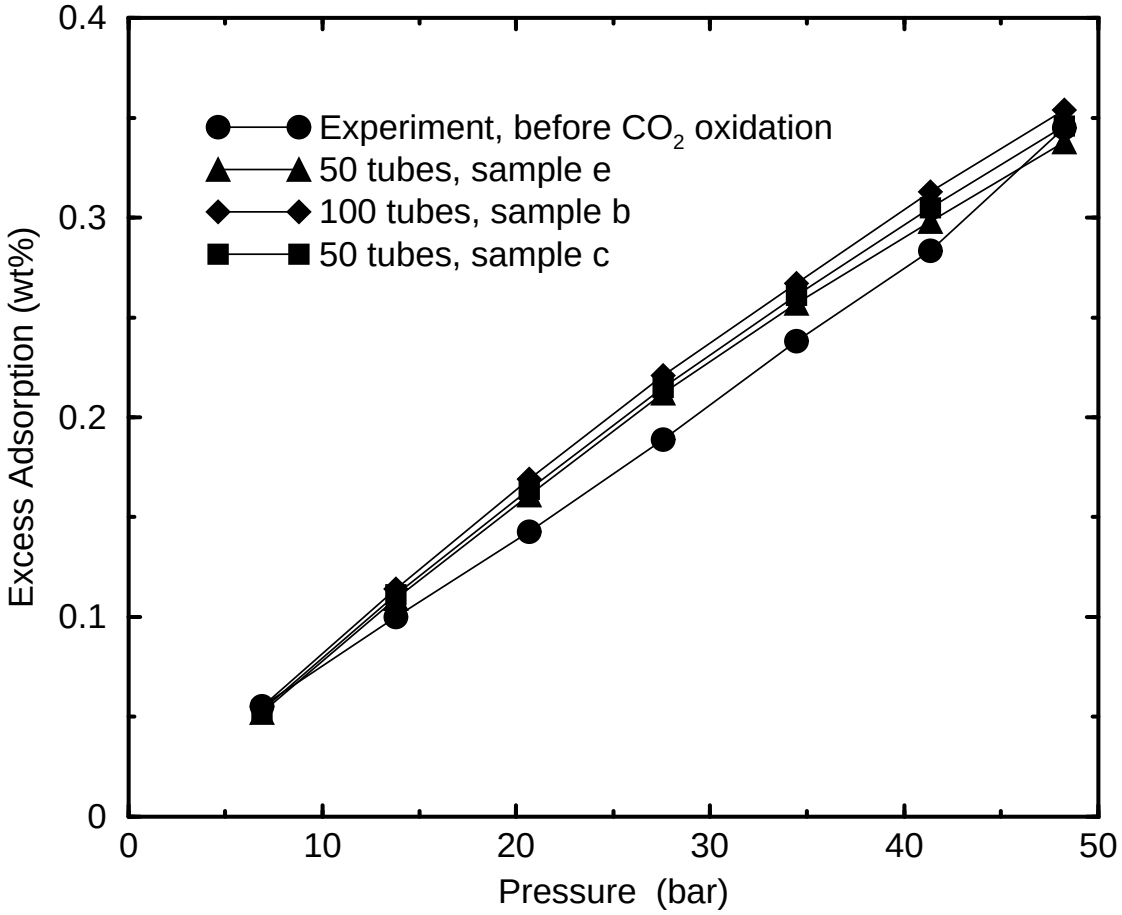

Figure 6.7: Adsorption isotherms computed from simulations for several of the bundles listed in Table 6.1. The experimental data for a sample of purified nanotubes heat treated to 700 °C, (sample B from Figure 6.6) are shown for comparison. The lines are drawn to guide the eye.

bundle size and nanotube diameter distribution, we cannot deduce anything about the experimental nanotube bundle geometry from the agreement between the simulations and experiments.

We next examine the possible causes for the dramatic increase in adsorption observed after CO_2 oxidation and subsequent heat treatment. The oxidation treatment will likely etch holes in the nanotubes and deposit oxygen-containing functional groups at these defect sties. We therefore hypothesize that the increase in adsorption capacity may be due to an enhancement of the solid-fluid potential (as a result of the introduction of polar functional groups), or due to an increase in the available volume (from holes etched in the tubes), or to a combination of these. We test this hypothesis by arbitrarily increasing the gap between the nanotubes, or increasing the strength of the solid-fluid potential, or a combination of both increasing the gap and the strength of the interaction potential. This procedure is only a first order approach to modeling the effects of CO_2 oxidation. Simulations of nanotubes with side-wall holes and explicit functional groups will be part of a future study. The optimal vdW gap for a perfect SWNT array is about 6.4 Å for maximizing the excess volume adsorbed at moderate pressures.[160] This is double the experimentally measured gap in as-produced nanotube bundles. Our simulations (not shown) indicate that increasing the vdW gap alone is not sufficient to reproduce the magnitude of the increase in adsorption observed after CO_2 oxidation and subsequent heat treatment of the nanotube samples. The solid-fluid potential V_{sf} was increased by simply multiplying the potential by an arbitrary factor. Thus, $1.5V_{sf}$ means that the potential has been increased by 50%. Isotherms computed from bundles with various values of the vdW gap and V_{sf} multipliers are shown in Figure 6.8. The experimental data for H_2 adsorption on the CO_2 oxidized and heat treated purified nanotubes (sample D from Figure 6.2) are plotted as circles in Figure 6.8. Simulations show that increasing the interaction potential while holding the vdW gap fixed at 3.2 Å produces a curve that is substantially concave downward and hence cannot match both the low and high pressure regions of the experimental data, which are approximately linear in pressure. This indicates that the mechanism for increasing the adsorption in experiments cannot be described by a simple increase in the solid-fluid potential. An adsorption isotherm on a bundle with a vdW gap of 6.4 Å and a potential of 1.3 V_{sf} is represented by the up

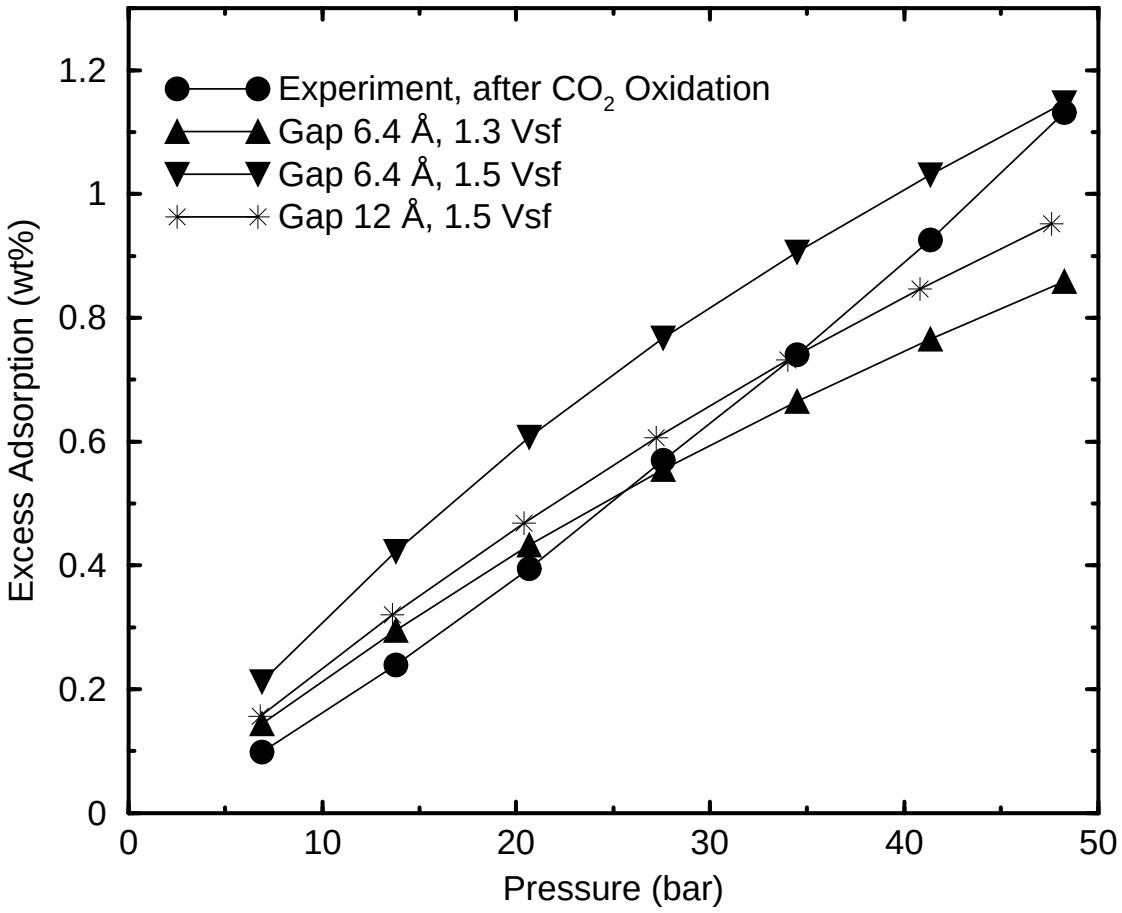

Figure 6.8: Adsorption isotherms computed from simulations with increased gap spacing and enhanced solid-fluid attractive potentials. All the simulations are for bundles containing 45 nanotubes with a diameter distribution given by sample a, from Table 6.1. Experimental data from Figure 6.2 sample D are shown as circles. The up triangles denote the results for a bundle with the vdW gap increased to 6.4 Å and the solid-fluid potential increased by 30%. The down triangles represent data for a bundle with a vdW gap of 6.4 Å and the potential increased by 50%. The stars are for a vdW gap of 12 Å and a potential increased by 50%. The lines are drawn to guide the eye.

triangles in Figure 6.8. These simulation data agree well with the experiments at low pressures but under-predict the amount adsorbed at high pressures. If a potential of $1.5V_{\mathrm{sf}}$ is used with a gap of 6.4 Å (down triangles) then the simulations and experiments agree at high pressure but not at low pressure. If we increase the vdW gap further the curvature of the simulation data decreases. The simulations for a vdW gap of 12 Å and 1.5 V_{sf} are shown as stars in Figure 6.8. This value of the vdW gap is unrealistically large and yet still gives an isotherm that is slightly concave downward. This indicates that no physically reasonable values of the vdW gap and interaction potential can be found that can accurately reproduce the shape of the experimental isotherms observed on samples that have been oxidized with CO_2. The simulated isotherms are all curved and tend to approach a plateau region at higher pressures, while the experimental isotherms are all approximately linear or concave upward in coverage at all pressures studied. However, reasonable qualitative agreement between experiments and simulations is achieved for 1.5 V_{sf} and a vdW of 12 Å. All of the isotherms shown in Figure 6.8 were computed from nanotube bundles of type a from Table 6.1. Calculations for nanotube bundles from sample b are similar to those shown for sample a and are not shown for clarity.

6.6 Conclusions

The hydrogen adsorption properties of SWNTs have been investigated using a TEOM to determine mass changes on exposure of the samples of up to 48 bar pressure. The rates of adsorption and desorption are apparently fast and indicative of physisorption. The isotherms are still ascending at the upper pressure limit of the instrument and it is clear that the saturation loading of these materials is not defined by these experiments. The raw and purified SWNTs samples do not adsorb as much hydrogen as a typical sample of activated carbon under similar conditions. Most importantly, we have shown that a simple, controlled oxidation with CO_2 activates SWNTs for adsorption of hydrogen. A roughly three-fold increase in the amount of hydrogen adsorbed

is observed at the highest pressures. Up to 1.2 wt% hydrogen was observed in the best case. Molecular simulations have been performed to compute the adsorption isotherms of hydrogen on finite size nanotube bundles that are composed of nanotubes of various diameters. The size of the bundles studied ranged from 20 to 100 tubes drawn from three different diameter distributions. Adsorption isotherms from simulations on the various bundles are all in relatively good agreement with one another. The amount of hydrogen adsorbed at these conditions does not appear to be a strong function of the size of the bundle or the diameter distribution for the samples studied here. Remarkably good agreement is seen between the simulations and experimental isotherms on nanotube samples before activation. This implies that the solid-fluid potential for the nanotubes before activation is fairly accurate and that the endohedral sites are available for adsorption on these samples. It is also possible that the agreement between simulations and experiments is fortuitous and that the unactivated samples do not adsorb H_2 inside the nanotubes, although this scenario seems unlikely. Adsorption isotherms on nanotube bundles with larger free volumes and stronger solid-fluid attractive potentials were computed to evaluate if these factors could explain the observed increase in H_2 uptake capacity after activation. It was found that a bundle with a vdW gap of 12 Å and a potential increased by 50% agrees fairly well with the experimental data, although the shape of the simulated and experimental isotherms differs. Given that the size of the vdW gap and the increase in the potential are both too large to be physically reasonable we conclude that the increase in adsorption upon activation is not solely due to increased free volume and solid-fluid potential enhancement. Hence, standard physisorption potentials do not adequately describe the activated nanotube samples. However, chemisorption cannot make a significant contribution to the experimental isotherms because the process is completely reversible and adsorption and desorption kinetics are too fast to be described by chemisorption.

This work shows that activation of SWNT samples can profoundly impact the adsorption of H_2. Understanding the process will ultimately help optimize the activation, further enhancing the adsorption capacity.

7.0 GAS ADSORPTION ON HETEROGENEOUS SINGLE-WALLED CARBON NANOTUBE BUNDLES

7.1 Introduction

The adsorption of gases on single-walled carbon nanotubes (SWNTs) has been of great interest for the past several years due to the unique structural properties of SWNTs. There are four types of adsorption sites on SWNT bundles: inside the nanotubes (endohedral), interstitial channels (where three or more tubes meet), external groove sites (where two tubes meet on the surface of the bundle), and the external surface of individual tubes.[163,192] One-dimensional (1-d) and quasi-1-d phases are possible for gases adsorbed on SWNT bundles.[32,33,193–195] As-prepared SWNTs are capped, making endohedral adsorption unlikely to occur to any significant extent. Many careful experimental studies of gas adsorption on closed SWNT bundles have been performed, yielding adsorption isotherms, binding energies, and isosteric heats of adsorption ($q_{\rm st}$).[29–42,196–199] Several of these studies have focused on determining where gases are adsorbed on SWNT bundles. The theoretical analysis of the data assumed SWNT bundles composed of homogeneous (all the same diameter) nanotubes, perfectly aligned on a 2-d hexagonal lattice. This is also the case for almost all simulations of adsorption on SWNTs.[156,160,162–164,192,200–202] Interpretation of the experimental data in terms of this idealized model of SWNT bundles has lead to the conclusion that gases do not adsorb in the interstitial channels (ICs) of bundles.[35] Theory, based on homogeneous bundles, predicts that small molecules such as H_2, He, and Ne will adsorb in the ICs, but that larger molecules, such as CH_4, Ar, and Xe, are too large to enter the ICs.[192] In reality, nanotube bundles are not homogeneous; they contain a distribution of different nanotube diameters (heterogeneous).[178–182] Here we present molecular simulations of adsorption on both heterogeneous and homogeneous SWNT bundles. We compare our simulations to previous experimental $q_{\rm st}$ data for adsorption of CH_4,[30,31,34,37], Xe [31,36,39,42] and Ar[36,40] onto SWNT bundles. These data are found to be in excellent agreement when the coverage dependence of $q_{\rm st}$ is considered. We show, for the first time, that low coverage

q_{st} values from experiments strongly indicate that gases as large as Xe can easily adsorb in the interstitial channels formed by packing defects in heterogeneous bundles.

7.2 Simulation Details

We have generated both homogeneous and heterogeneous SWNT bundles containing from 45 to 100 tubes. The tube diameters in the heterogeneous bundles were chosen to resemble the diameter distributions measured in experiments.[181] Homogeneous bundles were constructed of (10,10) SWNTs. The initial positions of the nanotubes were chosen randomly with the constraint that none of the tubes overlap.[46] The tubes were held rigid and geometries were optimized using the basin-hopping method.[203–205] Sample optimized homogeneous and heterogeneous bundles, each containing 45 nanotubes, are shown in Figure 7.1. Optimization of homogeneous bundles results in packing of the tubes into perfect 2-d hexagonal lattices, while optimized heterogeneous bundles *always* contain multiple packing defects that give comparatively large ICs. This is a key result. It shows that the basin-hopping method is capable of finding near-global minima for tube packing, as is evident from the hexagonal packing of homogeneous bundles. It also indicates that heterogeneous bundles, such as those produced in current experiments, must contain a number of packing defects that give rise to relatively large ICs. The heterogeneous bundle in Figure 7.1 contains 10 (8,8), 25 (9,9), 5 (10,10), and 5 (11,11) nanotubes. This gives an average diameter of 12.4 Å and a standard deviation of 1.2 Å, which is much smaller than the 2 Å standard deviation calculated from detailed analysis of the types of SWNT bundles used in the experiments.[178] We therefore expect our models to exhibit fewer defects than real SWNT bundles.

We have performed grand canonical Monte Carlo (GCMC) simulations[2] to study the adsorption of CH_4, Xe, and Ar onto bundles of closed-ended SWNTs. The Lennard-Jones (LJ) potential was used to model fluid-fluid and solid-fluid interactions. The parameters are σ_x =3.4, 3.81, 3.4, 4.1 Å and ϵ_x = 28, 148.1, 120, 221 K, for x = C, CH_4, Ar, and Xe, respectively. Lorentz-

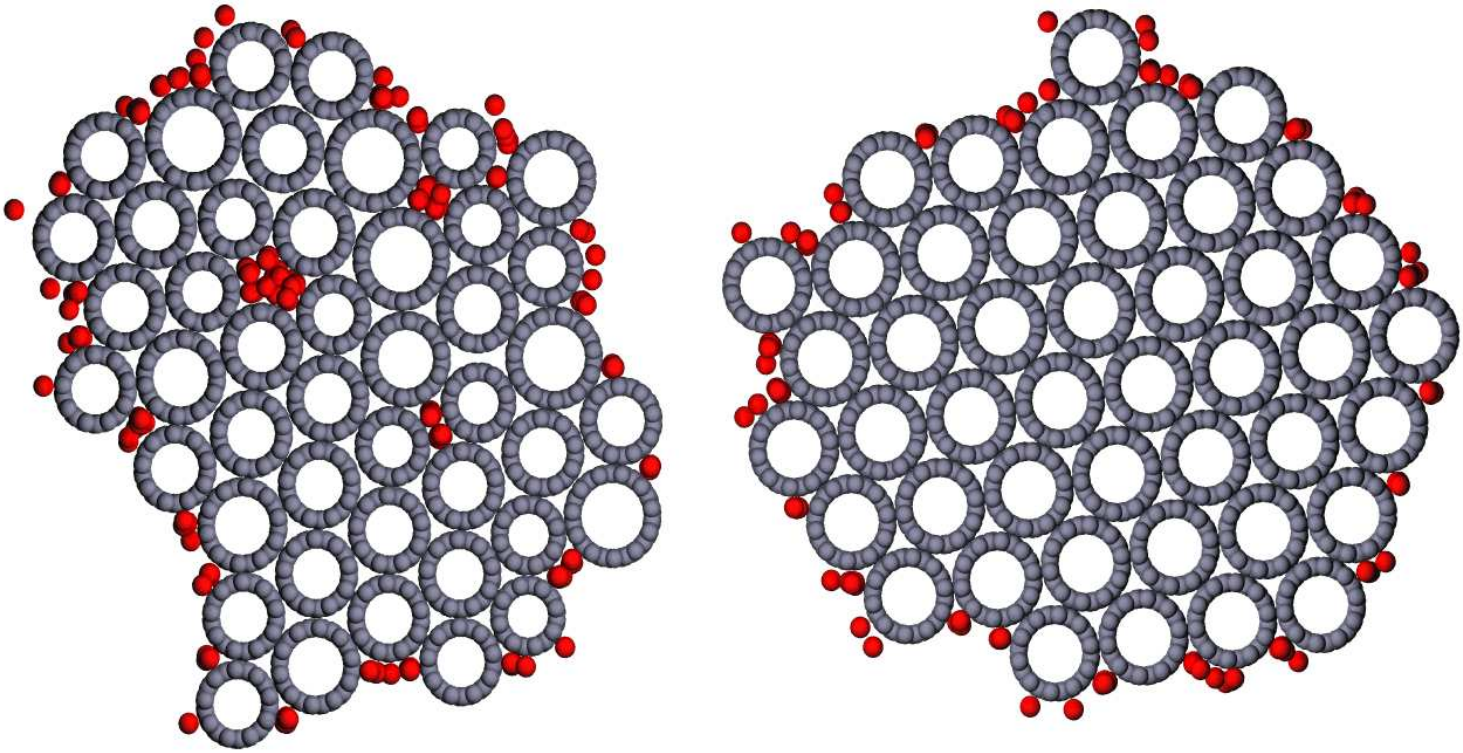

Figure 7.1: Sample of heterogeneous (left) and homogeneous (right) bundles optimized by the basin-hopping technique.[203–205] The blue spheres represent CH_4 adsorbed in equilibrium with a bulk phase at 159.88 K and 0.05 bar.

Berthelot combining rules were applied and the parameter values were taken from the literature.[95,192,206] Binding energies for the gases on graphite from the potentials (experiments) are 11.4 (12.2), 9.1 (9.2), and 15.2 (15.6) kJ mol^{-1} for CH_4, Ar, and Xe, respectively. The experimental data were reported by Vidali *et al.*.[207] The excellent agreement between the potential models and the experimental data indicate that these parameters are a good first approximation to the fluid-nanotube interaction potential. Our molecular simulations confirm the assumption that CH_4, Ar, and Xe do not adsorb into the ICs of homogeneous bundles (see Figure 7.1). Simulations also show that all heterogeneous bundles we have constructed contain large ICs at packing defect sites that do allow adsorption of all three probe molecules. For example, CH_4 is shown to adsorb in four interstitial defect sites in the left hand panel of Figure 7.1, while no interstitial adsorption is found for the homogeneous bundle on the right hand side.

7.3 Results

Experimental[34,37] and simulation q_{st} data for CH_4 are plotted in Figure 7.2. The coverage (mol CH_4/mol C) was computed from the known weight of the sorbent and an estimated purity of 60%.[39,208] The inset shows the low coverage region. This low coverage region has been assigned to adsorption into the groove sites of SWNT bundles.[35,37] The simulation data show that groove site adsorption on homogeneous tubes (squares in Figure 7.2) gives q_{st} about 40% lower than values from experiments. In contrast, q_{st} for simulations on heterogeneous bundles are in good qualitative and quantitative agreement with experiments. The diamonds in Figure 7.2 are for a heterogeneous bundle containing 45 nanotubes that has a larger number of packing defects than the bundle shown in Figure 7.1. The more defective bundle was generated by making only a few optimization steps in the basin-hopping method. Simulations for a number of different heterogeneous nanotube bundles all have q_{st} values at low coverage that agree quite well with the experimental data. The low coverage isosteric heats result from adsorption in the interstitial defect channels of the bundles, where the

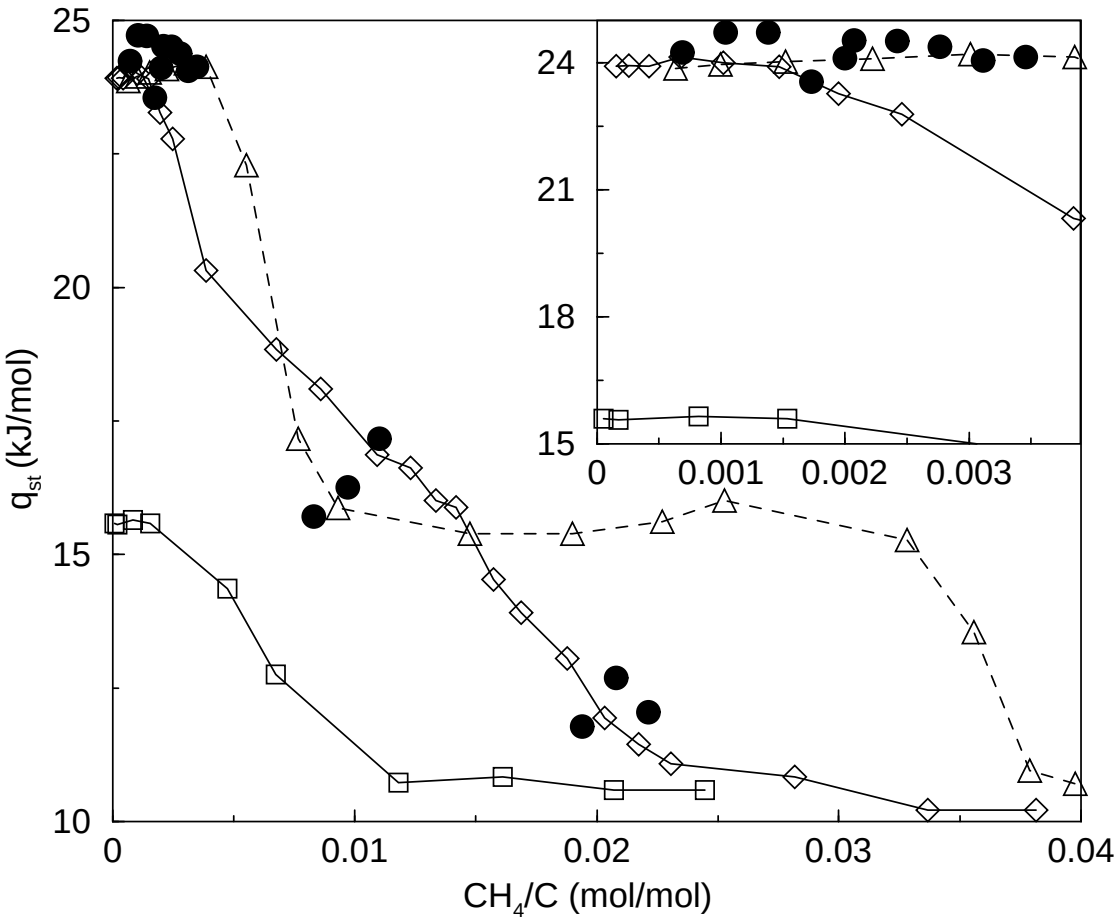

Figure 7.2: Isosteric heats of adsorption for CH_4 from experiments[34,37] (circles) and simulations. The diamonds (squares) are for adsorption onto heterogeneous (homogeneous) bundles. The triangles are for a homogeneous bundle with the solid-fluid potential increased by 45%. All bundles contain 45 nanotubes. The simulations were performed at 159.88 K. The inset shows $q_{\rm st}$ at low coverage. The lines are drawn as a guide to the eye. The estimated error bars are about the size of the symbols.

adsorption potential is the highest. More highly optimized bundles contain fewer such defects per bundle, resulting in a narrower low coverage plateau region than observed in experiments. We also observe a large low-coverage plateau region for larger bundles. Simulations on heterogeneous bundles containing 100 nanotubes give similarly good quantitative agreement with the experimental q_{st} values. This indicates that either the bundles in the SWNTs used in the experiments contain more tubes than previously estimated [31,178] or more defects than our highly optimized bundles. The larger number of defects in real bundles may be due to the larger standard deviation of nanotube diameters observed in real bundles. [178]

One might argue that the nanotube-gas (solid-fluid) interaction potential is not accurately known and that q_{st} for homogeneous bundles could be brought into agreement with experimental data by adjusting the solid-fluid potential. We have manually increased the solid-fluid potential to bring the low coverage q_{st} from simulations on homogeneous bundles into agreement with experiment. We found that the magnitude of the potential must be increased by 45% to match experiments in the low coverage region. Isosteric heat data for this system are shown as triangles in Figure 7.2. As can be seen from the inset, the agreement at low coverage is excellent. However, at high coverage, corresponding to complete monolayer formation on the external surface of the nanotubes, the simulated q_{st} values are at least 25% too high compared with experiments. Only when the coverage reaches the multilayer do q_{st} values from these simulations agree with the monolayer values from experiments. In contrast, the monolayer heats from both homogeneous and heterogeneous bundles are in fairly good agreement with experiments, although the simulations are consistently lower than experiments. This analysis suggests that the assumed solid-fluid potential is relatively accurate and that only adsorption onto heterogeneous bundles, including interstitial adsorption, is consistent with experimental data.

The plot of q_{st} versus coverage for heterogeneous bundles shows a plateau region at low coverage corresponding to adsorption in ICs and some groove sites. At high coverage another plateau is observed that corresponds to adsorption on external surface sites, near monolayer completion. This is in qualitative agreement with the experimental data from Migone *et al.*, [34,37] although more

experimental data are needed to identify these regions with certainty. Muris *et al.*[30] identify two steps in experimental isotherms of CH_4 adsorption on closed nanotubes, one corresponding to low coverage and another to high coverage. They estimate $q_{st} = 18.3 \pm 1$ and 11.2 ± 0.5 kJ mol^{-1} for low and high coverage, respectively. Talapatra and Migone[37] point out that the low coverage data from Muris *et al.* corresponds to the intermediate coverage range of their data, or around 0.01 CH_4/C (mol/mol) in Figure 7.2. Thus, these data are in reasonable agreement with both the experimental data of Talapatra and Migone[37] and also our simulation data. The high coverage datum from Muris and coworkers is likewise in good agreement with the highest coverage region in Figure 7.2 for simulations on heterogeneous bundles and experimental data. Thus, q_{st} values computed from adsorption on heterogeneous bundles are in good agreement with all available experimental data, while simulations on homogeneous nanotubes are not consistent with the data.

The simulation data in Figure 7.2 were calculated at a temperature of 159.88 K, corresponding to one of the isotherms used in the experiments. While q_{st} is usually assumed to be independent of temperature,[209] our simulations show that q_{st} values computed at 110 K are typically about 5-10% larger than at 159.88 K. Data from both temperatures are in reasonably good agreement with experimental values, which were derived from isotherms over a range of temperatures.

q_{st} for Ar on closed SWNT bundles has been reported by Wilson et al. over a range of coverages.[40] No purity is given for the nanotubes used in this experiment. We have assumed a purity of 60%, the same as in the studies of Migone *et al.*,[39,208] because the nanotubes in each of these studies were obtained from the same source. The isosteric heats for Ar from simulations and experiments[40] are plotted in Figure 7.3. The experimental data (circles) were derived from isotherms at average temperatures around 90 K. The simulation data were collected at 90 K. We see from Figure 7.3 that the data for heterogeneous bundles (diamonds) are in qualitative agreement with experiments. The experimental data are shifted to larger abscissa values compared with the simulation results; if the experimental x values are multiplied by a factor of 0.6 then nearly perfect agreement results between experiment and simulation. The values of q_{st} from simulations on homogeneous bundles (squares) are not in good agreement with the experimental data. However, experimental data for much lower

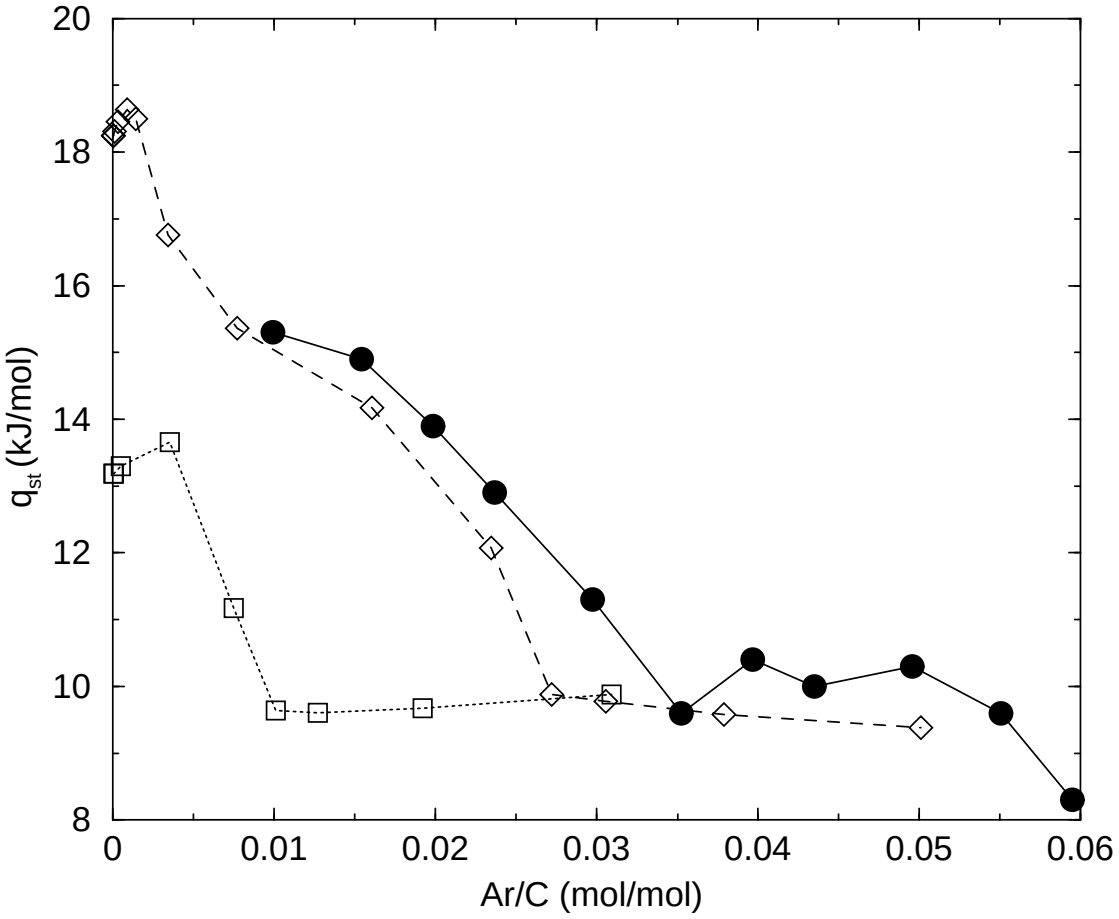

Figure 7.3: Experimental[40] and simulated q_{st} for Ar on SWNT bundles. Symbols have the same meaning as in Figure 7.2.

coverages (near zero loading) are needed to unambiguously resolve the major difference between homogeneous and heterogeneous bundles. The simulations on heterogeneous bundles predict that the isosteric heat increases dramatically at the lowest coverage due to adsorption into defect ICs. This should be observable in experiments at higher temperatures where it is possible to achieve lower coverages.

Ar adsorption adsorption isotherms between 60 and 87 K have been measured by Talapatra and Migone.[36] They report q_{st} = 13.2 kJ mol^{-1} for the groove phase, which is about 2 kJ mol^{-1} lower than the lowest coverage data of Wilson et al. in Figure 7.3, but in exellent agreement with a coverage of about 0.025 mol Ar/mol C and also in good agreement with the simulation data corresponding to filling of the groove phase, which occurs at about 0.005 and 0.015 for homogeneous and heterogeneous tubes, respectively.

The heat of adsorption or binding energy of Xe on closed SWNT bundles has been determined experimentally by at least three different groups.[31,35,39,42] Only one of these groups reported q_{st} as a function of coverage.[39] These data are plotted in Figure 7.4 along with simulation results. The main graph contains data from simulations on homogeneous (squares) and heterogeneous (diamonds) bundles. These data were collected at 110.6 K at coverages up to complete monolayer formation on the external surface of the tubes. The experimental data (circles) are from isotherms over a range of temperatures from 210 to 295 K at very low coverage. The inset is for the low coverage range and includes simulations for heterogeneous nanotubes at 210 K. Note that the high temperature simulation data are qualitatively different from the low temperature data, although the two sets only differ by about 10%. At low temperatures the Xe molecules are much more likely to become trapped in the lowest energy sites, which at this loading are the defect ICs, giving a larger variance in q_{st} as high energy sites fill first, followed by lower energy sites. At the higher temperature, adsorbates tend to sample many different sites, averaging out the energy differences between the sites. Note that this gives better agreement with the experimental data, which were collected at higher temperatures. Other studies report binding energies at low coverage[35,42] and q_{st} at high coverage.[31] Talapatra *et al.*[35] report a binding energy of -27 kJ mol^{-1} based on isotherms

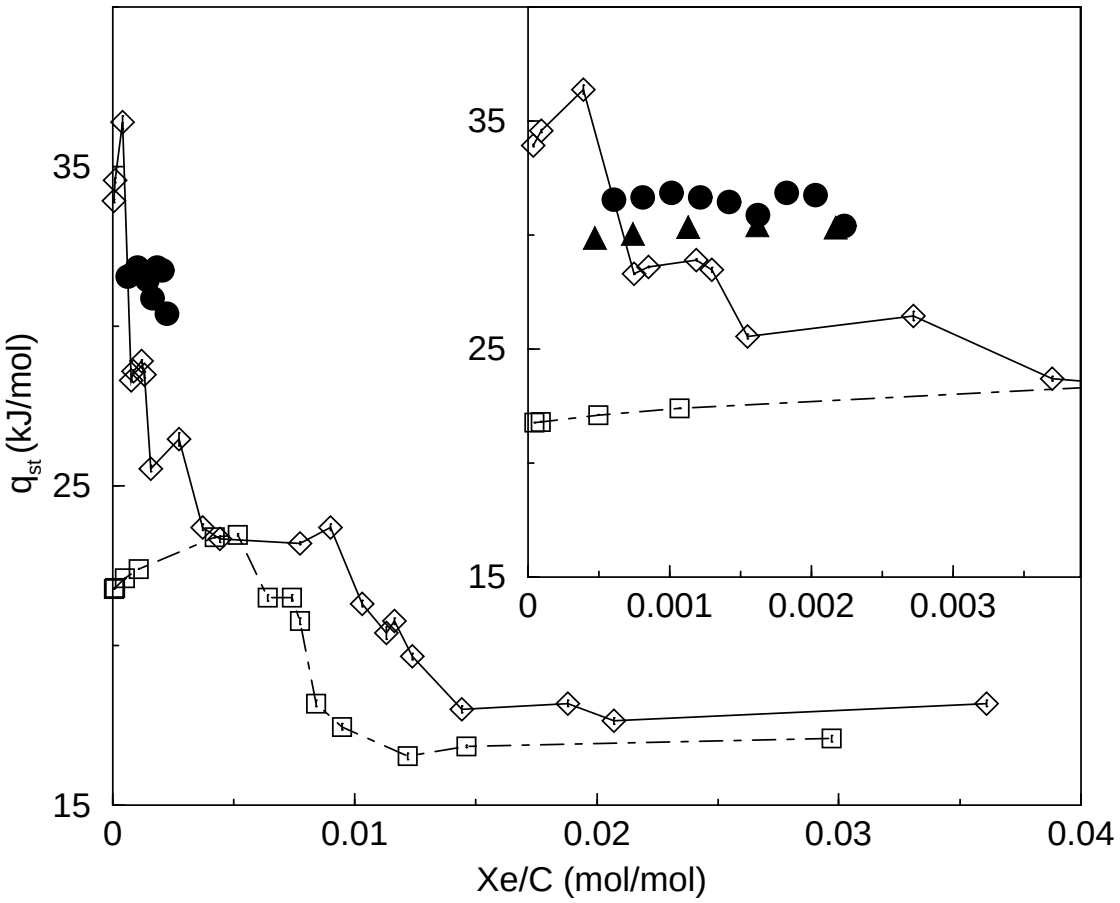

Figure 7.4: Xenon q_{st} from experiments[39] (circles) and simulations on homogeneous (squares) and heterogeneous (diamonds) bundles at 110.6 K. The inset shows the low coverage region along with simulations on a heterogeneous bundle at 210 K (triangles).

from 220 to 295 K. This is in excellent agreement with the binding energy measured from thermal desorption spectroscopy of 27 kJ mol^{-1} at around 100 K.[42] Using the formula $q_{\rm st} = -\epsilon + \alpha kT$ where ϵ is the binding energy, $\alpha = 0.5$ for 2-d systems and 2 for 1-d systems,[40] we find $q_{\rm st} = 29$ and 30.5 kJ mol^{-1} at 110.6 and 210 K, respectively. These values are in very good agreement with our low coverage simulation data for heterogeneous bundles. Note that the simulations for homogeneous bundles give values of $q_{\rm st}$ that are too low compared with experiments by about 25-30%. Muris and coworkers measured $q_{\rm st}$ =15.7 kJ mol^{-1} and Talapatra and Migone[36] reported $q_{\rm st}$ =16.6 kJ mol^{-1} for coverages corresponding to full monolayer completion. These values are in reasonably good agreement with simulations on both the homogeneous and heterogeneous bundles near monolayer completion. This is to be expected, since the external surface of the nanotubes are not sensitive to the diameter distribution or packing defects in the bundles.

7.4 Conclusions

In summary, $q_{\rm st}$ for CH_4 and Xe on closed SWNT bundles from different experimental groups [30,31,34,37,39,42] are shown to be in remarkable agreement with each other when the coverage dependence of $q_{\rm st}$ is considered. These data, along with data for Ar,[40] agree very well with simulation data of adsorption on heterogeneous nanotube bundles over the entire range of coverage. The low coverage region is dominated by adsorption in the interstitial channels of heterogeneous bundles, whereas homogeneous bundles do not allow adsorption of these gases into the ICs. The overall agreement between simulations and experiments clearly indicates that gases do adsorb in the ICs that result from packing defects in real nanotube bundles.

8.0 ADSORPTION ONTO CLOSED NANOTUBE BUNDLES: THEORETICAL CALCULATIONS AND COMPARISON WITH THE EXPERIMEN

8.1 Introduction

There has been a great deal of recent interest in adsorption of gases on single walled carbon nanotubes (SWNTs) both experimentally[22–28,30–43,46,169,197–199,210] and theoretically.[46,156,160,162–164,192,200–202] Many of these studies have focused on identifying potential adsorption sites. Experimentally produced SWNTs are known to form bundles containing 10s to 100s of individual tubes.[178–182] The bundles contain tubes with a distribution of diameters, depending on the methods used to produce the SWNTs. The tubes are observed to pack into hexagonal lattices when they form bundles, with gaps between the tubes of about 3.2 Å,[211] slightly smaller than the gap between layers of graphite. There is little direct experimental evidence that the nanotube diameter heterogeneity causes packing defects in the bundles. Most of the theoretical calculations to date have assumed that nanotubes in the bundles have identical diameters (homogeneous) and are packed in perfect 2-d hexagonal arrays.[156,160,162–164,192,200–202] This simple model is also invoked by many experimentalists to interpret experimental data.[36,38,40,42] We have shown in our previous paper[47] that SWNT bundles composed of heterogeneous nanotubes with diameter distributions similar to those observed in experiments always exhibit packing defects. Moreover, these defects result in large interstitial channels that allow adsorption of gases as large as Xe, and perhaps larger gases. This finding contradicts the interpretation of previous experimental data, reportedly showing that gases do not adsorb in interstices of SWNT bundles.[36,37] We have shown that experimental isosteric heat of adsorption at low coverage is a very sensitive indicator of interstitial adsorption and that these data are very consistent with adsorption into interstices of heterogeneous bundles.[47]

In our modeling we assume that nanotubes are straight, rigid, and parallel to each other. Dilation of the bundle induced by adsorption into the ICs[212] and thermal vibrations of tubes

themselves[213] are ignored. We also ignore the atomic corrugation of the nanotubes by integrating over the individual atoms in the nanotube to produce a smooth potential.[46,160] This is a reasonable assumption given that the corrugation in the solid-fluid potential is only a few Kelvin.[214]

8.2 Theorical Calculations

The interaction potentials between tubes are required to construct realistic models of nanotube bundles. By considering the periodicity of the tube, The averaged smoothed potential between two parallel tubes with indices (n_{1p},n_{1p}) and (n_{2p},n_{2p}) is given by

$$\begin{aligned}\langle u(r)\rangle &= \frac{\int_0^{\theta_{1max}} d\theta_1 \int_0^{\theta_{2max}} d\theta_2 \int_0^{Z_{uc}} dz_1 \int_0^{Z_{uc}} dz_2 \; u(r,\theta_1,\theta_2,z_1,z_2)}{\theta_{1max}\theta_{2max}Z_{uc}Z_{uc}} \\ &= \frac{\int_0^{\theta_{1max}} d\theta_1 \int_0^{\theta_{2max}} d\theta_2 \int_0^{Z_{uc}} dz_2 \; u(r,\theta_1,\theta_2,z_2)}{\theta_{1max}\theta_{2max}Z_{uc}}, \end{aligned} \tag{8-1}$$

where r is the distance between the centers of the two tubes, $\theta_{1max} = 2\pi/n_{1p}$, $\theta_{2max} = 2\pi/n_{2p}$, θ_1 and θ_2 are the rotational angles of tube 1 and tube 2 around their respective z axes, z_2 is the displacement in z direction of tube 2, Z_{uc} is the length for the unit cell of the tubes, $u(r,\theta_1,\theta_2,z_2)$ is the interaction between the two tubes. The interaction energy depends on the length of the two tubes. In our calculations, tube 1 is one unit cell in length, and tube 2 contains an effective infinite number of unit cells. Equation (8-1) is derived from the following related equations,

$$\begin{aligned}\int_0^{Z_{uc}} dz_2 \int_0^{\theta_{1max}} d\theta_1 \int_0^{\theta_{2max}} d\theta_2 \; u(r,\theta_1,\theta_2,z_1=0,z_2) &= \\ \int_z^{z+Z_{uc}} dz_2 \int_0^{\theta_{1max}} d\theta_1 \int_0^{\theta_{2max}} d\theta_2 \; u(r,\theta_1,\theta_2,z_1=z,z_2) &= \\ \int_0^{Z_{uc}} dz_2 \int_0^{\theta_{1max}} d\theta_1 \int_0^{\theta_{2max}} d\theta_2 \; u(r,\theta_1,\theta_2,z_1=z,z_2). \end{aligned} \tag{8-2}$$

The pair-wise summation over all carbon-carbon atoms in the system is represented by $u(r,\theta_1,\theta_2,z_2)$. The Lennard-Jones (LJ) potential for carbon is used. In the computation, tube 2 is set to 20 unit cells in height. This height is found to be large enough such that the contribution to the interaction energy due to carbon atoms beyond 20 unit cells is negligible . Tube 1 with one unit cell is fixed

to be in the center of a cubic box as a reference tube. The minimum image convention is used in z direction when the interaction between carbon atoms in tube 1 and tube 2 is calculated. Gaussian numerical integration is used. The values of $\langle u(r) \rangle$ are fitted to a polynomial with 15 terms. The fitting procedure has been described elsewhere.[46,160] The effective values of σ and ϵ/k for carbon atom are set to be 3.47 Å and 28 K. The equilibrium distance between two closest carbon atoms in two neighboring tubes is calculated as $d_{\rm eq} = r_{\rm eq} - R(1) - R(2)$, where $r_{\rm eq}$ corresponds to the well depth of $\langle u(r) \rangle$ between the two tubes, $R(1)$ and $R(2)$ are the tube radius of tube 1 and tube 2, respectively. The values of $d_{\rm eq}$ for 15 sets of combinations between (8,8) tube and (12,12) tube have been computed. Those values are between 3.199 and 3.205 Å, very close to 3.2 Å, a value observed from the experiment.[211] Note that the effective value of 3.47 Å was chosen to match the value of 3.2 Å for $d_{\rm eq}$. When the interaction between nanotube and adsorbate is calculated, the values of σ and ϵ/k for carbon are set to be 3.4 Å and 28 K. The adsorbate-nanotube interaction was taken as a pair-wise summation over adsorbate-carbon interactions. The parameters and the calculations have been described elsewhere.[46,47]

The final smoothed nanotube potential should be independent of which tube is chosen as the reference. This is indeed the case for the interaction potential given by Eq. (8-1) when the potential is expressed on a per length basis. We have calculated the interaction potential between (8,8) and (12,12) tubes with the (8,8) and (12,12) tubes to be the reference tube, respectively. The differences in all the potential energies are negligibly small.

The basin-hopping method[203–205] was used to construct both the heterogeneous and homogeneous bundles once the tube-tube interaction is obtained. This technique can be applied to locate the global minimum energy with a high probability as well as many local minimum energy structures for difficult clusters. The algorithm is outlined as below:

1. The initial configuration for all the tube centers is generated. This is done by randomly choosing the (x, y) coordinates of each tube center in a square box such that their is no overlap between the tubes. The size of the box in the calculation is typically set to be

between 150 Å and 300 Å depending on the size of bundle. The box is used to prevent the evaporation of the tubes from the bundle. Note that two neighboring tubes should not be too close. The van der Waals gap between two neighboring tube is set to be between 4 to 6 Å in the initial configuration.

2. Find the local minimum starting with the configuration from Step 1. This is done by the BFGS method.[68]

3. Randomly move the centers of all tubes in both x and y directions. Periodic boundary conditions are used in both x and y directions.

4. Find the local minimum of this new configuration as in Step 2.

5. Accept the new structure with probability of $min[1, \exp(-\beta\delta U)]$. The value for δU is the difference in energy between Step 4 and Step 2. The value of T is chosen to be about 0.8 of the value of the potential well depth in the calculation.

During the calculation, the maximum displacement of a single tube used in Step 3 is adjusted such that 50% of the trial configurations are accepted. Note that in conventional Monte Carlo, the step size is adjusted only during equilibration. During the production run, the maximum displacement is fixed to satisfy detailed balance. However, their is no such constraint in the basin-hopping method. We have checked the code by performing optimization of three dimensional Lennard-Jones clusters. We obtained exactly the same results as reported in reference.[203] The number of step to implement the basin-hopping calculation for the nanotube bundle was set to 4×10^5. The lowest energy in every run was typically found in several thousands steps. Note that this lowest energy may be not the true lowest energy, but a local minimum energy.

Once the nanotube bundle structure with a local minimum energy for both the homogeneous and heterogeneous bundles were constructed, isotherms and isosteric heat of adsorption were computed from grand canonical Monte Carlo (GCMC) simulations[2] on these bundles. The calculation details were described elsewhere.[46,47] The height of the simulation box was typically set to 10 σ, where σ

is the Lennard-Jones parameter for the gases. When the coverage was small at low pressures, the height of the box was increased to between 100 and 5000 σ such that the amount adsorbed had a magnitude of tens of gas atoms to make the calculations statistically reasonable. The length and the width of the simulation box were set to be equal to each other. The values were between 150 and 250 Å. To improve the efficiency of the simulation, the corrected volume in the calculation was defined as $V_{\text{box}} - V_{\text{tubes}}$, where V_{box} and V_{tubes} are the volumes of the simulation box and the summation of all tubes in the bundle, respectively. We have verified that this works. When an attempt is made to create a particle in a box, it is repeated until the position for the particle is found to be outside of all the tubes in the bundle. The number of attempted steps are set to 10^8 and 10^7 for the production and equilibration runs, respectively.

8.3 Results

We have constructed homogeneous bundles with 25, 45, 70, and 100 (10,10) tubes, and heterogeneous bundles with 45 and 100 tubes. The diameter distributions in the heterogeneous bundles were chosen to resemble those measured from the experiment.[181] The heterogeneous bundles with 45 tubes contain 10 (8,8), 25 (9,9), 5 (10,10), and 5 (11,11) tubes. The average of the diameter and the diameter standard deviation for this heterogeneous bundle is 12.36 Å and 1.18 Å, respectively. The heterogeneous bundle with 100 tubes contains 6 (8,8), 29 (9,9), 35 (10,10), 28 (11,11), and 2 (12,12) tubes. The average of the diameter and the diameter stand deviation for this bundle is 13.44 Å and 1.28 Å, respectively. Note that the values for the diameter standard deviation of the above two samples we chose are far less than the experimental value of 2 Å.[178] The nanotube materials with a standard deviation of 2 Å[178] have been used by many experimental groups.[30,40] This implies that the heterogeneous bundles in our calculations will have fewer ICs than the real bundles.

We have optimized every bundle starting from 10 different initial configurations. For the homogeneous bundles with 25 tubes, we got the same "lowest" minimum energy from two different initial configurations. These two "lowest" minimum energies converged to the eighth decimal place. The structures corresponding to these two "lowest" minimum energies look identical. This strongly indicates that the true "global" minimum has been found for this homogeneous bundle. For the homogeneous bundles containing 45, 70, and 100 tubes, we have not found the same "lowest" minimum energy from 10 sets of optimizations. For the 45 and 70 homogeneous bundles, Optimization *always* resulted in packing of the tubes into perfect 2-d hexagonal lattices. For the 100 tube bundles, Four sets of optimization gave perfect 2-d packing, the other six sets presented imperfect packing with packing defects inside the bundle. A single (10,10) tube can be fitted into the defects. This means that these six geometries are not close to the global minimum energy point. For the heterogeneous bundles with 45 and 100 tubes, we *always* obtained imperfect packing with defects inside the bundles. Some interstitial channels (ICs) (defects) are large enough to accommodate gas adsorption. Two examples of heterogeneous bundles are shown in Figure 8.1. The left bundle is obtained during 1000 steps of optimization. The right one is optimized only with one step. The left one seems to be more structured and has fewer ICs than the right one does. The interaction potential energy for the left is about 8% less than that for the right.

The nearest distance between two neighboring carbon atoms on the two neighboring tubes was computed for many of the optimized homogeneous and the heterogeneous bundles. For the homogeneous bundles, all the nearest neighbor distance were found to be between 3.2015 and 3.2027 Å, close to the equilibrium value of 3.2 Å. For the heterogeneous bundles, many of the nearest neighbor distance were less than 3.2 Å. For example, the right one in Figure 8.1 has 52 sets of neighboring tubes with the nearest distances between 3.05 and 3.2 Å. The right one has about 90 sets of neighboring tubes totally.

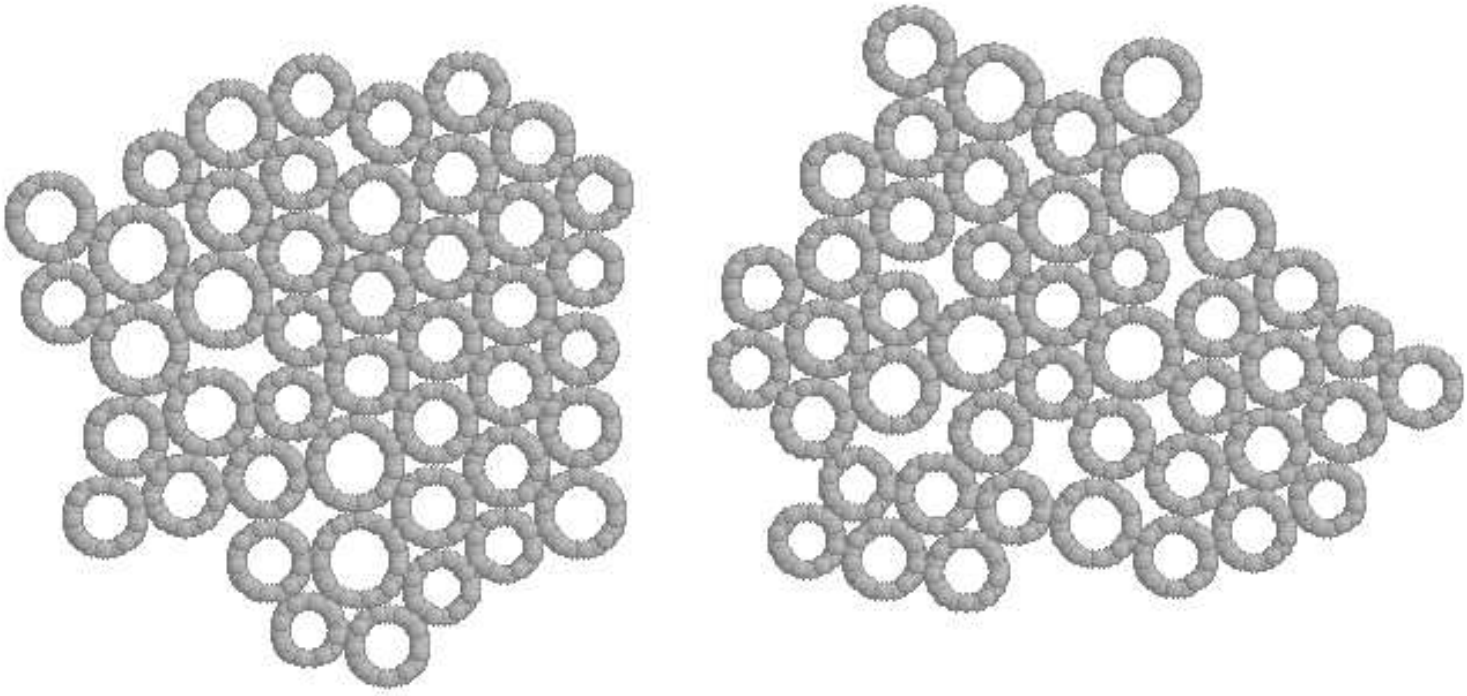

Figure 8.1: Figure for two heterogeneous bundles both with 45 tubes.

8.3.1 Results for CH_4

Isotherms from simulations and the experiment at 159.88 K are shown in Figure 8.2. This is the

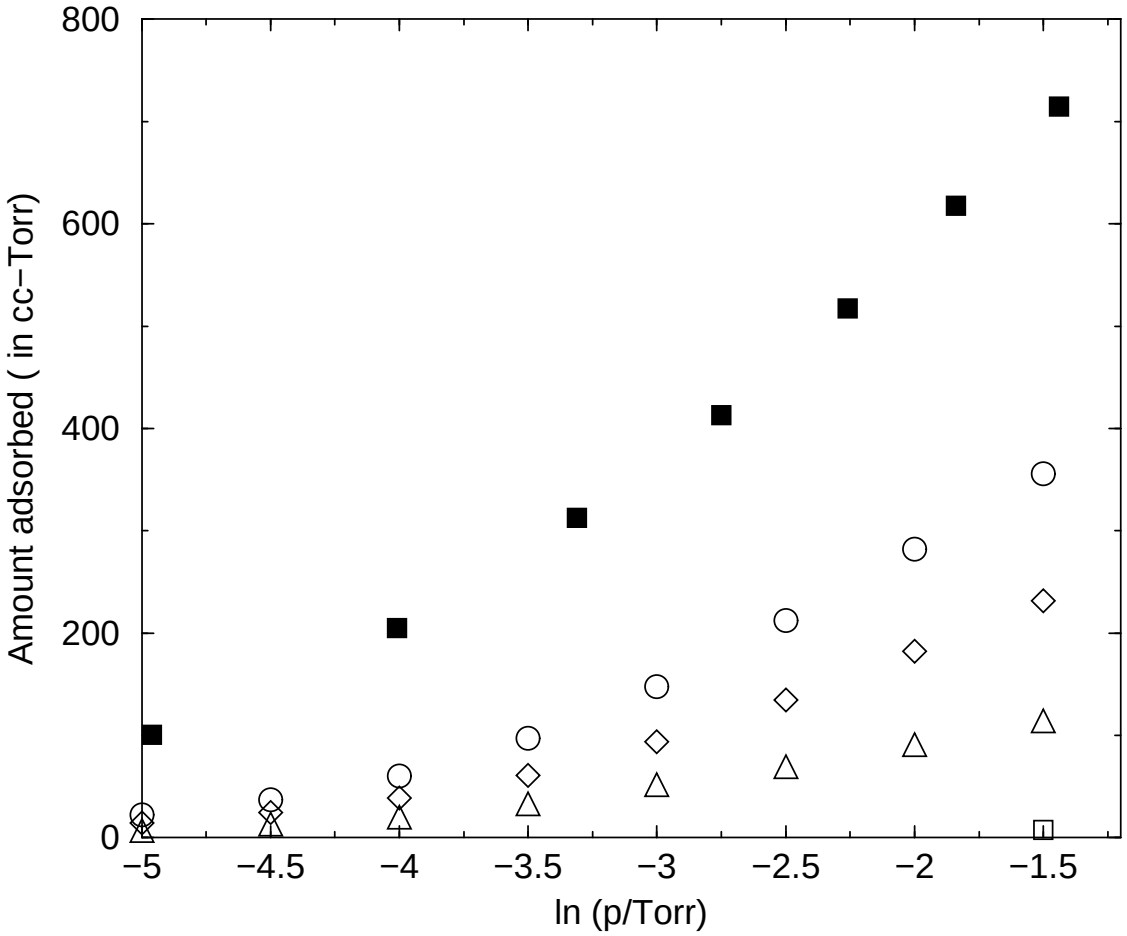

Figure 8.2: Isotherms from simulations and experiment for CH_4 at 159.88 K. Both the circles and triangles correspond to heterogeneous bundles with 45 tubes. The bundle (circles) has been less optimized than that (triangles). The diamonds are for a heterogeneous bundle with 100 tubes. The filled squares are from the experiment.[34] Also shown are open squares for a homogeneous bundle with 45 (10,10) tubes.

low coverage region used in the experiment[34] to compute the binding energy. The snap shots from simulations on the heterogeneous bundles in this region indicate that most of the gas molecules are adsorbed into the ICs region with only very few molecules adsorbed on the groove sites. Not all of the groove sites of the homogeneous bundle have gas adsorbed molecules in this low coverage region. The difference in the amount adsorbed between the homogeneous and heterogeneous bundles can be

seen clearly at this low coverage region. The amount adsorbed reported in the experiment is about 100 times larger than that on the homogeneous bundle. In contrast, the amount is only about 2 to 6 times of that onto the heterogeneous bundles for most of the pressures. The less optimized bundle with 45 tubes (circles), corresponding to the the bundle on the right in Figure 8.1, gives the highest adsorption capacity. We expect that realistic bundles with larger diameter standard deviation will exhibit higher adsorption capacity than the heterogeneous bundles used here. Isotherms at 194.68 K (not shown) also show the same behavior. The amount adsorbed from the experiment is about 6 times higher than those on the heterogeneous bundles, 50 times higher than those on the homogeneous bundles. It can thus be concluded that the heterogeneous bundles give isotherms more close to the experiment than the homogeneous bundles do for CH_4.

Isotherms in the temperature range between 69 and 195 K have been measured in the experiment to calculate the isosteric heats at low, intermediate, and monolayer coverage regions.[34,37] Three temperatures of 110, 159.88, and 194.68 K have been chosen to study the temperature effect on the isosteric heat of adsorption. The results are shown in Figure 8.3. The isosteric heat at 110K clearly shows a wide plateau region with a adsorption between 0.00264 and 0.00907 mol(CH_4)/mol(C). This region roughly corresponds to filling of the groove sites. It is interesting to note that the isosteric heat (q_{st}) at point "a" at 110 K is about 18% higher than that at point "b" at 159.88 K. The amount adsorbed at these two points are very close to each other. The amount adsorbed for "a" is 0.00907, a little higher than the value of 0.00889 for point "b". The difference in q_{st} is partially due to the sites where the gases are adsorbed. A snap shot for "a" shows that the ICs and the groove sites have almost been filled. Almost no adsorption occurs on the outside surface of the bundle. In contrast, about 20 out of 218 gas molecules are adsorbed onto the outside surface of the bundle for point "b". The outside surface is less attractive than the groove sites and the ICs. This gives a corresponding lower q_{st} value. This results in the overall q_{st} for point "b" being smaller than point "a". In both the low and the high coverage regions, the variance in q_{st} is typically less than 10% for different temperatures. The snap shots in the low coverage region for 110 K show that the adsorption occurs only in two strong ICs when the amount adsorbed is less than

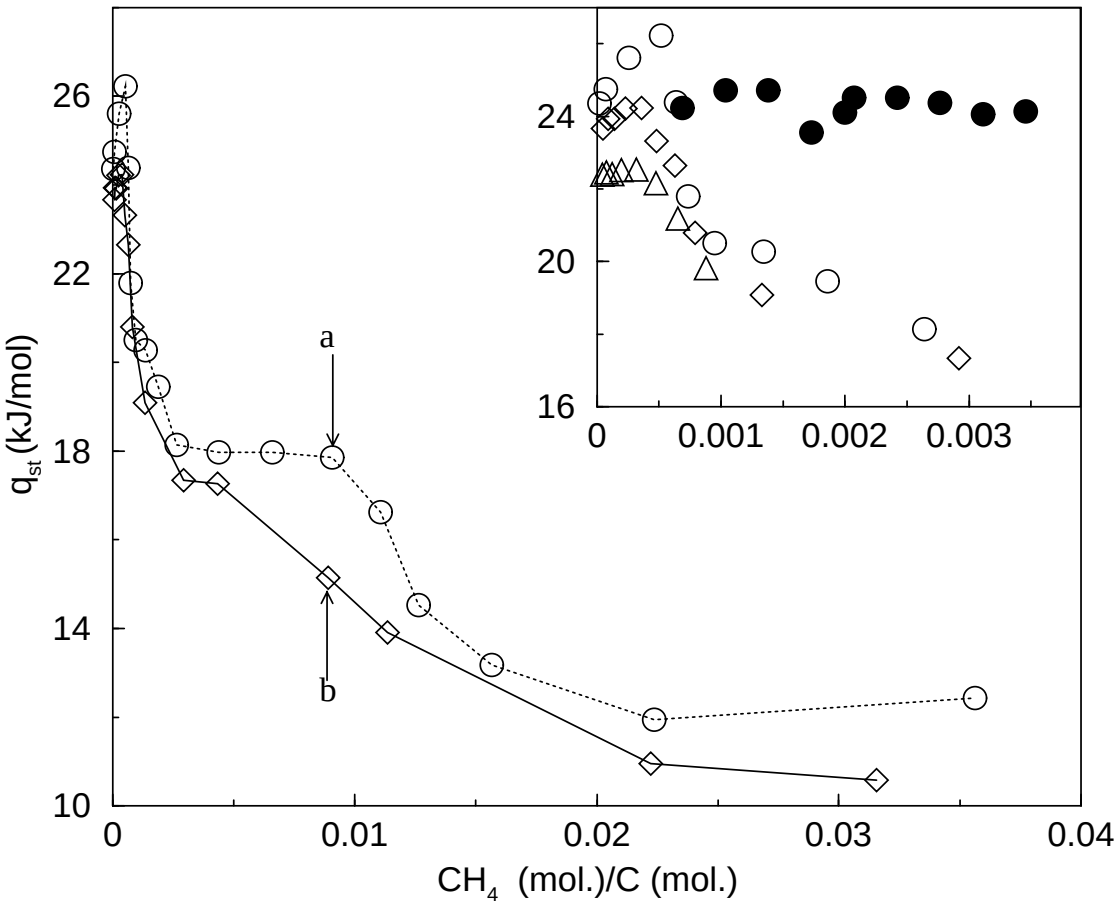

Figure 8.3: The temperature effect on isosteric heat for CH_4. All the simulations are performed on the same highly optimized heterogeneous bundle with 45 tubes. The diamonds and the open circles are for 159.88 K and 110 K, respectively. Also shown in the inset is the experimental data (filled circles)[37] and results from simulations at 194.68 K (triangles) at low coverages. The lines are drawn as a guide to the eye.

0.000516. Actually, the adsorption mainly occurs in only one IC. The linear density is increased in this IC when chemical potential (pressure) is increased. The isosteric heat is hence increased due to the interaction between adsorbate molecules. When the pressure is increased further beyond the amount adsorbed of 0.000516, the snap shots show that gas molecules will be adsorbed into ICs with smaller binding energies. This leads to a decrease in q_{st}. The isosteric heat for 194.68 K at low coverage show qualitatively different behavior from that for 110 K. This is because the temperature of 194.68 K is high enough to allow molecules to sample many different binding energy sites, such as different ICs and groove sites, even at low coverages. The temperature effect on the isosteric heat for the homogeneous bundle (not shown here) at low coverage is also studied. The difference in q_{st} is about 9% between 159.88 and 194.68 K. Note that the heterogeneous bundle in Figure 8.3 is highly optimized and hence it shows small plateau region at low coverage.

The effect of bundles of different sizes and different structures on the q_{st} is shown in Fig 8.4. The difference in q_{st} on the heterogeneous bundles at the low and the outside surface regions is typically less than 10%. The bundles with a larger number of tubes that are less optimized give results that are closer to the experimental results over the whole region. At low coverage, the less optimized and larger bundles show wider plateau region than the smaller, highly optimized bundles. This is due to the larger number of defects in those bundles.

One may wonder if their is a substantial difference between groove sites on homogeneous and heterogeneous bundles. The difference in adsorption capacity on the groove sites and the outside surface between the homogeneous and heterogeneous bundles has been studied. For a heterogeneous bundle (the left one in Figure 8.1), four ICs inside the bundle and one channel on the outside of the bundle enclosed by three neighboring tubes (the low left side) are excluded for adsorption. The isosteric heat and isotherms are shown in Figure 8.5 and Figure 8.6, respectively. The results on the homogeneous and heterogeneous bundles are very close to each other if the ICs for the heterogeneous bundles are excluded for adsorption. At the highest coverage, the difference between homogeneous and heterogeneous bundles is 6% for q_{st}, and at the highest pressure the difference in coverage is 2%. This strongly indicates that the adsorption capacity for groove sites and the outside surface

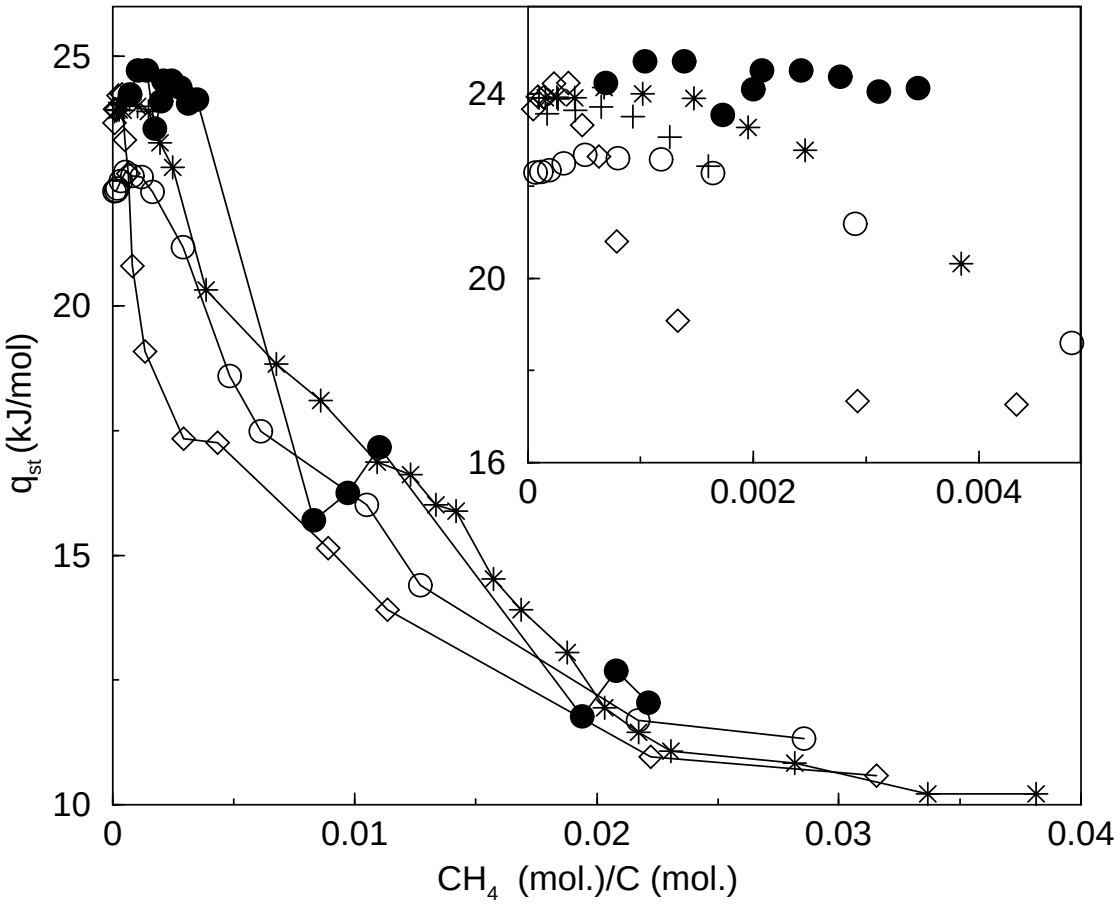

Figure 8.4: The bundle effect on isosteric heat of adsorption for CH_4. All the simulations are performed at 159.88 K. The diamonds are for a bundle highly optimized than that for stars. Both these two heterogeneous bundles have 45 tubes. The open circles and the pluses (shown in inset) both are heterogeneous bundles with 100 tubes. The circles are for a bundle a little highly optimized than that for the pluses. Also shown are the experimental data (filled circles).[34,37] The lines are shown as a guide to the eye.

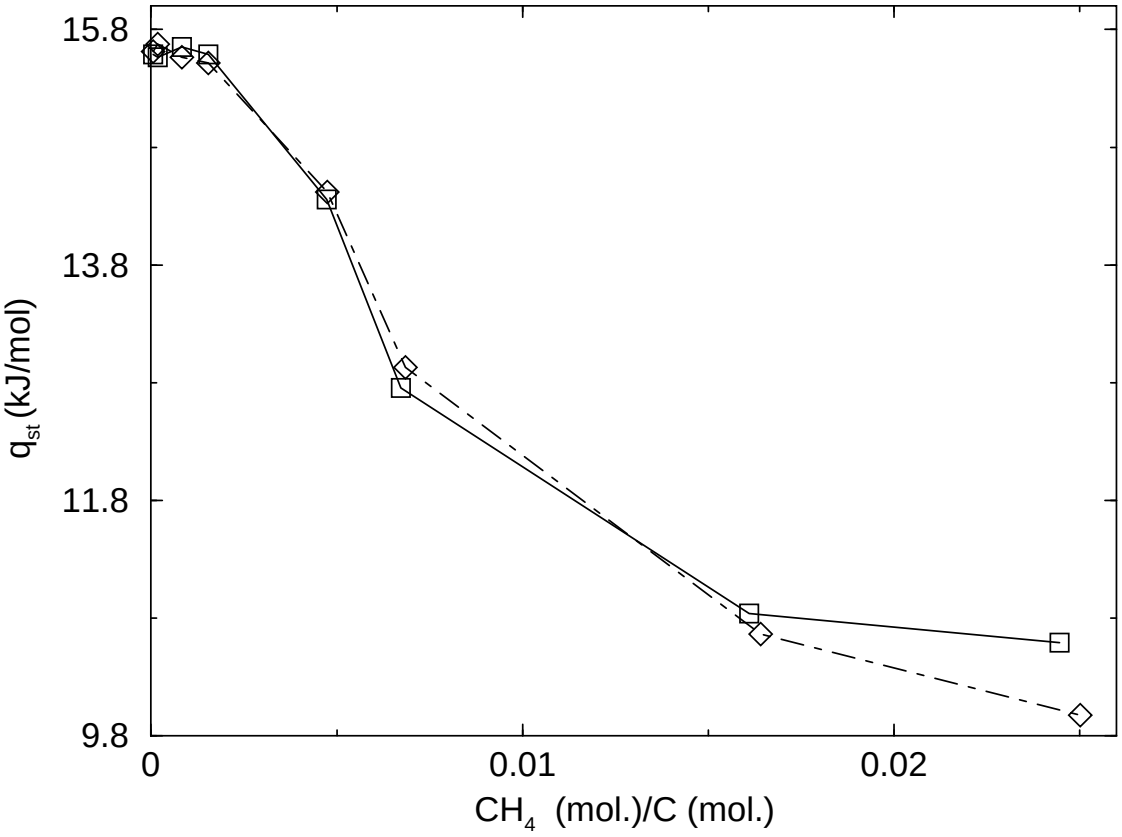

Figure 8.5: The isosteric heats at 159.88 K for CH_4 on the homogeneous and heterogeneous bundles excluding ICs adsorption. The diamonds are for a heterogeneous bundle with four ICs inside the bundle and one channel outside of the bundle excluded from adsorption. The squares are for a homogeneous bundle. The lines are drawn as a guide to the eye.

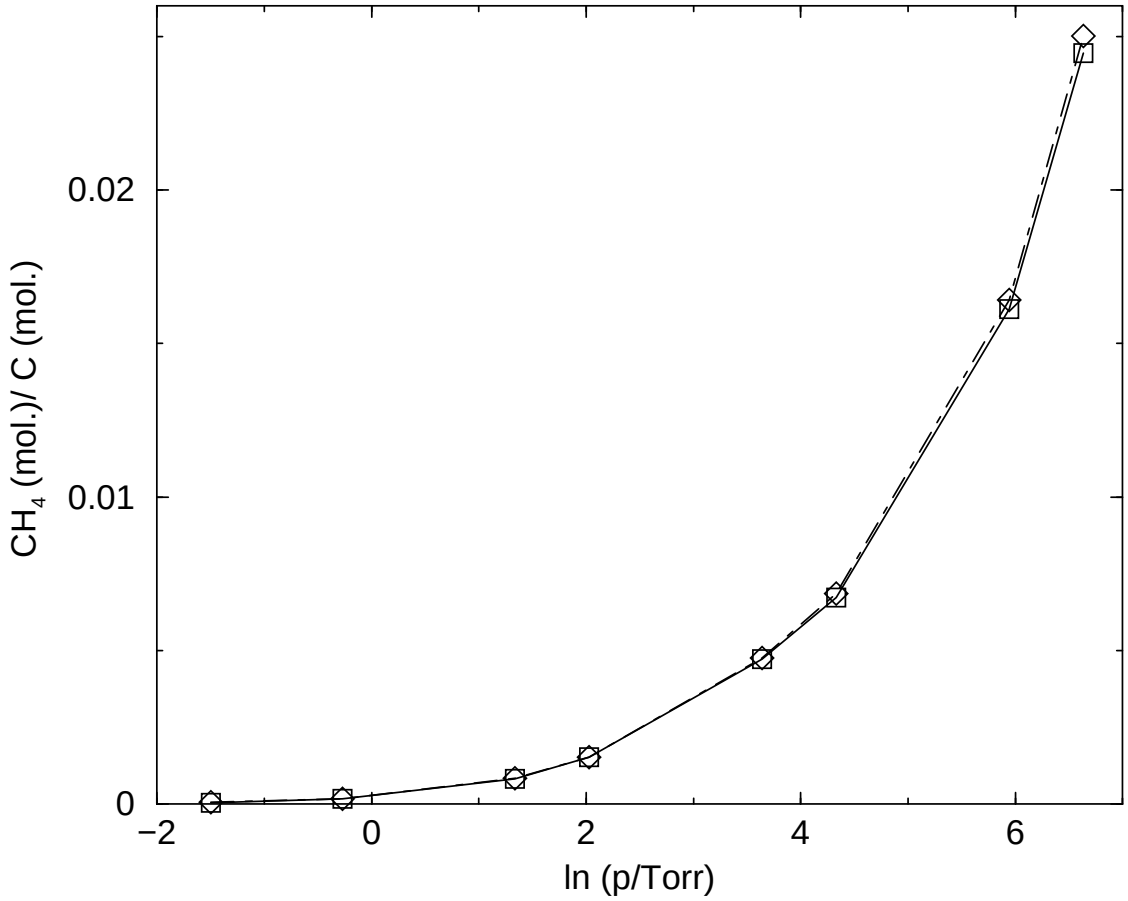

Figure 8.6: The isotherms at 159.88 K for CH_4 on the homogeneous and heterogeneous bundles excluding ICs adsorption. The diamonds and the squares have the same meaning as in Fig. 8.5. The lines are drawn as a guide to the eye.

is fairly insensitive to the size heterogeneity of the tubes in the bundles. Many simulations have been performed for CH_4 onto homogeneous 45 tube bundles with different optimized structures, homogeneous bundles with 25 and 70, and 100 tubes. At low coverage, the amount adsorbed per groove sites, and the isosteric heat are almost the same onto all those homogeneous bundles. This is expected since the adsorption capacity of the groove sites are insensitive to the detailed structure of the bundles.

8.3.2 Results for Ar

The effect of different bundles on the isosteric heat for Ar is shown in Figure 8.7. The difference in the isosteric heat on different heterogeneous bundles at low and the monolayer coverage regions is less that 10%. The experimental values are consistent with each other on the outside surfaces. However, their are some differences in the intermediate coverage region. This is in part due to Ar adsorbing on different sites even at the same coverage.

8.3.3 Results for Xe

Isotherms at 250 K for Xe are shown in Figure 8.8. Note that this temperature of 250 K and pressure range correspond to the low coverage region. Isotherms are measured in this low coverage range to calculate the isosteric heat of adsorption and the binding energy from the experiment. [39] The simulation onto a heterogeneous bundle shows that the gas molecules are adsorbed mainly into the ICs with only a few molecules on the groove sites in this low coverage region. For the homogeneous bundle, only a few groove sites hold a small number of molecules. The rest of groove sites are empty. The amount adsorbed at this low coverage region clearly shows the difference in amount adsorbed between the homogeneous and heterogeneous bundles. The results on the heterogeneous bundle are very close to the experiment. In contrast, the homogeneous bundle gives amount about 30 times less than that from the experiment. Two other sets of isotherms at 210

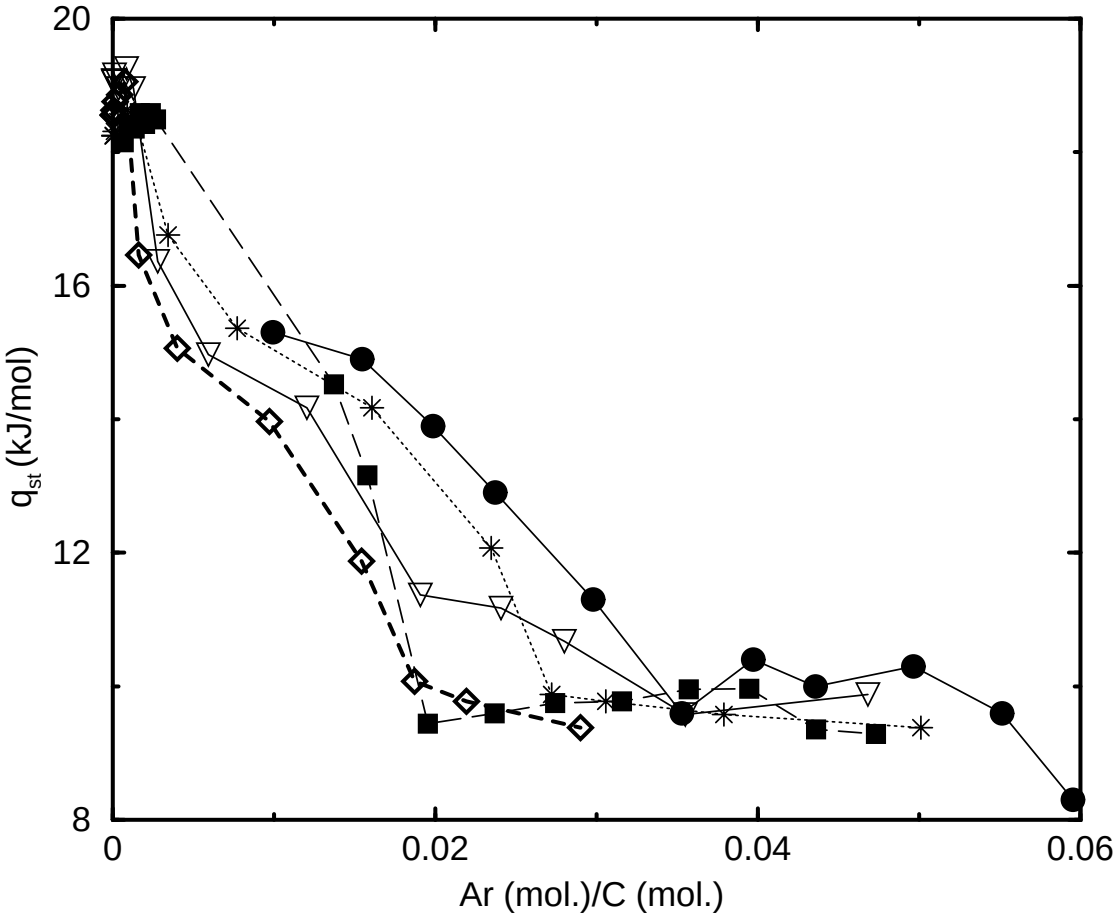

Figure 8.7: The effect of different bundles on isosteric heat for Ar. All the simulations were performed at 90 K. The stars are for a bundle less optimized than that corresponds to the diamonds. Both the stars and the diamonds are for heterogeneous bundles with 45 tubes. The triangles are for a heterogeneous bundle with 100 tubes. Also shown are the experimental results from two different groups (circles–[40] squares–[43]). The lines are drawn as a guide to the eye.

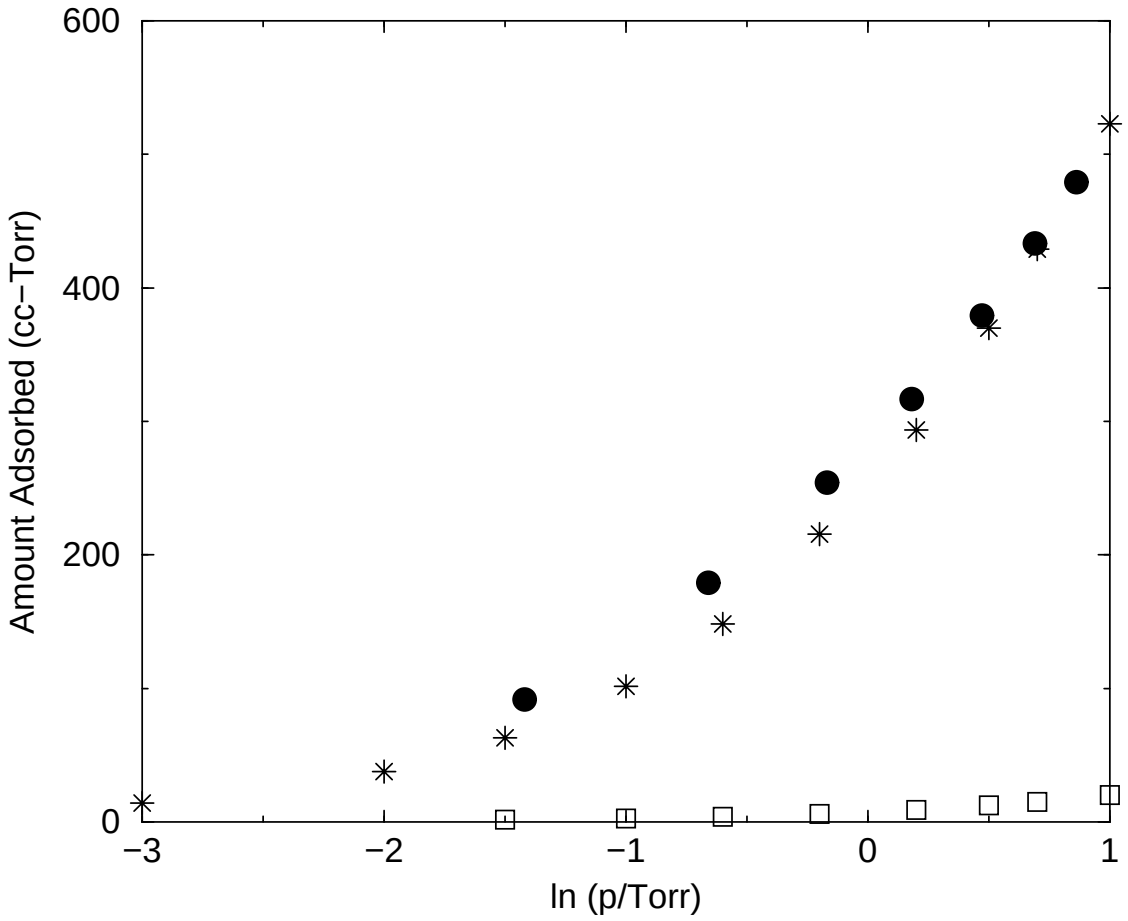

Figure 8.8: Isotherms at 250 K for Xe. The stars are for a heterogeneous bundle with 45 tubes, corresponding to the right bundle in Figure 8.1. The squares are for a homogeneous bundle with 45 tubes. Also shown are the experimental data from[39] (filled circles).

K and 295 K (not shown here) also show the same behavior. The heterogeneous bundle typically gives amounts adsorbed about 50 % less than experiments. However, the amount adsorbed on the homogeneous bundle is typically 10 to 30 times less than that from the experiments. The isotherms at these three temperatures verify again that the heterogeneous bundles give better agreement with the experiments than the homogeneous bundles do in the amount adsorbed.

Isotherms at 150 K are shown in Figure 8.9. Note that in the pressure region of the experiment,

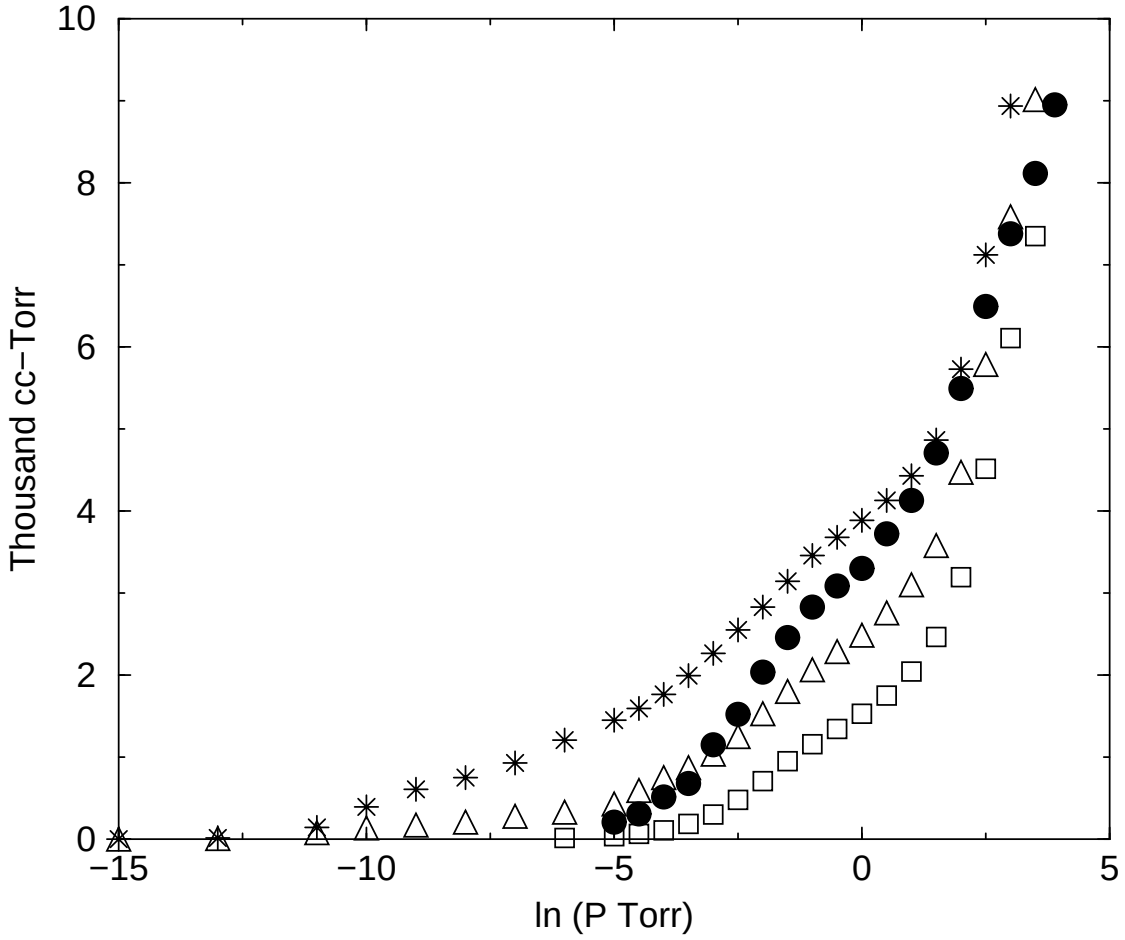

Figure 8.9: Isotherms at 150 K for Xe. The stars are for a heterogeneous bundle with 45 tubes corresponding to the right one in Figure 8.1. The triangles are for an heterogeneous bundle with 45 tubes more highly optimized than that for the stars. The squares are for a homogeneous bundle with 45 tubes. Also shown are the experimental data (filled circles) from[39].

Xe molecules have already filled all the accessible ICs region of the heterogeneous bundles. The two steps observed from the experiment corresponding to the groove site and outside surface filling

can not be resolved very clearly from the isotherms on both the heterogeneous and homogeneous bundles. The step corresponding to filling of the ICs can not be resolved. This is partially due to the small number of defects in the heterogeneous bundles. The experimental data lie between two heterogeneous bundles. The amount adsorbed onto the homogeneous bundle is systematically smaller than the experiment.

Migone and coworkers[39] have concluded that Xe can not adsorb into ICs by calculating the ratio of the heights for the two steps. One significant drawback in their argument is that they count all the ICs region in a bundle when they assume that ICs can adsorb Xe. This assumption is not correct. Only a few ICs in the bundle are accessible for adsorption of Xe.

The temperature effect on q_{st} for both the homogeneous and heterogeneous bundles up to monolayer coverage region is shown in Figure 8.10 for Xe. The temperature range between 112 and 150 K has been used in the experiment[36] to measure the isosteric heat for the outside surface of the bundle and the second layer. The difference in q_{st} is typically less than 10% for both the homogeneous and heterogeneous bundles at the low and monolayer coverage regions. The isosteric heat for the monolayer region from the experiment[36] is 16.5 kJ/mol, consistent with the values from the simulations on both the heterogeneous and homogeneous bundles. This is expected since the adsorption capacities of the outside surface of the homogeneous and heterogeneous bundles are very close to each other as has been shown for CH_4 (see Figure 8.5). Simulations have also been performed onto a heterogeneous bundle with a different detailed structure at 110.6 K (not shown here). The isosteric heats in the low and outside surface regions are close to the values in Figure 8.10 for the heterogeneous bundles. The difference is typically less than 6%. The isosteric heat of adsorption at low coverage is calculated from isotherms at temperatures between 210 K and 295 K.[39]

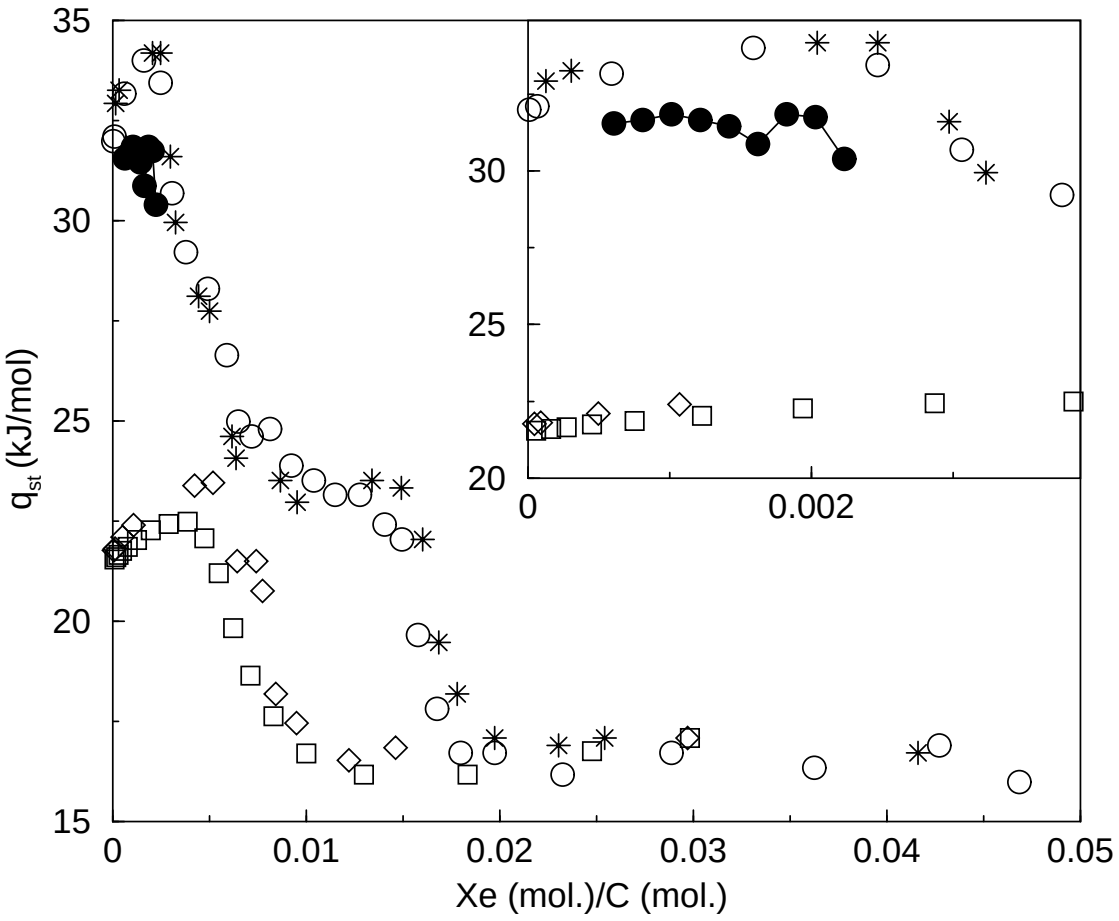

Figure 8.10: The temperature effect on isosteric heat for Xe. All the bundles have 45 tubes. The squares and the diamonds are for the same homogeneous bundle. The diamonds correspond to a temperature of 110.6 K. While, the squares are for 150 K. The open circles and the stars are for the same heterogeneous bundle. The open circles are for 150 K. While, the stars are for 110.6 K. Also shown are the isosteric heats from the experiments at low coverage (filled circles).[39] The inset shows the data at low coverage.

8.4 Conclusion

Isotherms at low coverage region onto heterogeneous bundles are typically about 2–6 times less than those from the experiment for CH_4 and close to the eperimental value for Xe at all the temperatures. In contrast, the amount adsorbed from the experiment are typically 30-50 times larger than those on homogeneous bundles. The isotherms at low coverage indicate that adsorption into ICs of heterogeneous bundle does occur. In the high coverage region, the isotherms from both the heterogeneous and homogeneous bundles are very similar although the isotherms onto homogeneous bundles are systematically less than those onto heterogeneous bundles. This is due to the small number of accessible ICs in the heterogeneous bundle.

The adsorption capacity for the groove sites and outside surfaces of heterogeneous bundles are very close to those of the homogeneous ones. This implies that the adsorption capacity for these two kinds of adsorption sites are comparatively insensitive to the detailed bundle structures.

Temperature effects for isosteric heat of adsorption have been studied for Ar, Xe, and CH_4. The difference in the low and high coverage is typically less than 10%. The large difference in isosteric heat at the intermediate coverage region is due to adsorbates occupying different binding energy sites at different temperatures.

The binding energy sites for heterogeneous bundles can roughly be divided into three parts, i.e., the IC's, the groove sites, and the outside surface. The isosteric heats for CH_4 are $\sim$ 25 kJ/mol, 16 kJ/mol, and 11 kJ/mol, respectively for the ICs, groove sites, and outside surface. The values of $q_{\rm st}$ for Ar are $\sim$ 19 kJ/mol, 13 kJ/mol, and 10 kJ/mol respectively; for Xe are 32 kJ/mol, 21 kJ/mol, and 17 kJ/mol, respectively.

9.0 FUTURE WORK

9.1 Future Work

We have shown some results in chapters s 7 and 8. Some future work for these two chapters is proposed.

1. Migone and coworkers have identified the steps on the isotherms by computing the isothermal compressibility of dN/dP, where N and P are the amount adsorbed and the pressure, respectively[29,36,39]. These steps correspond to the binding sites with almost the same binding energies. The peaks on the curve of dN/dP versus P or N correspond to the jumps on the isotherm. It is difficult to directly observe a jump from the isotherms since the transition regions are somewhat rounded (See Figure 8.9). Note that the isothermal compressibility is closely related with $dN/d\mu = \frac{(<N^2>-<N>^2)}{kT}$, where μ is the chemical potential and T is the temperature. The transitions will be able to be located from simulations by computing these statistical fluctuations. However, many simulations have to be implemented in order to locate the transition accurately since one has to find a peak on a curve of $dN/d\mu$ versus μ or N. This problem can be alleviated by using multiple histogram reweighting. Only several simulations are needed to generate the full curve. The multiple histogram reweighting can also be used to calculate the heat capacity.

2. Some tubes may be open even in the claimed closed nanotube bundles[42]. Several initial calculations have been performed onto open homogeneous (10,10) tube bundles. It is shown that methane is first adsorbed inside the tubes at low pressures (low coverages). The isosteric heat at low coverage is 17.87 kJ mol^{-1}. This value is about 15% higher than the value of 15.6 kJ mol^{-1} for the groove site, 26% lower than the experimental value of 24 kJ mol^{-1} [215]. This implies that only the interstitial adsorption can interpret the high isosteric heat at low coverages from the experiment. However, it is still important to know the effect of open

tubes in the claimed closed bundles on the isosteric heats of adsorption and the isotherms. For example, how is the isosteric heat curve being changed by the open tubes in the bundles, especially at low coverage. The amount adsorbed will be increased after some tubes are open. An interesting question is how the transition steps on the isotherm is changed. This will affect the transition pressure, which has been measured from the experiments, for example by Muris *et al.*[30,31].

3. Several kind of gases, such as He, Ne, H_2, and D_2 have been studied in nanotube bundles [32,35,40,216]. These light molecules will exhibit quantum effects at low temperatures typically used in the experiment. Path integral calculations are needed to compare with experiments.

   The specific surface area of nanotube bundle is fundamental for it to be used as gas adsorbents. Migone and coworkers have reported that the surface areas measured from Ne and Xe for a sample of closed nanotube bundle are very close to each other. Both values are about 40 m^2/g. The specific surface area may be computed from the simulations and compared with the experiments. Several simulations have been reported to calculate the BET surface area [217–219].

BIBLIOGRAPHY

[1] J. M. Prausnitz, R. N. Lichtenthaler, and E. G. and de Azevedo. *Molecular Thermodynamics of Fluid Phase Equilibria 3rd edn.* Prentice-Hall, New York, 1999.

[2] M. P. Allen and D. J. Tildesley. *Computer Simulation of Liquids.* Clarendon, Oxford, 1987.

[3] D. Frenkel and B. Smit. *Understanding Molecular Simulation.* Academic Press, San Diego, 1996.

[4] A. Z. Panagiotopoulos. *J. Phys.: Condens. Matter.* , 12:R25, 2000.

[5] J. J. de Pablo, Q. Yan, and F. A. Escobedo. Simulation of phase transitions in fluids. *Annu. Rev. Phys. Chem.*, 50:377–411, 1999. and references therein.

[6] L. D. Gelb, K. E. Gubbins, R. Radhakrishnan, and M. Sliwinska-Bartkowiak. Phase separation in confined systems. *Rep. Prog. Phys.*, 62:1573–1659, 1999.

[7] G. S. Heffelfinger, F. van Swol, and K. E. Gubbins. *Mol. Phys.* , 61:1381, 1987.

[8] A. Z. Panagiotopoulos. *Mol. Phys.*, 61:813–826, 1987.

[9] A. Z. Panagiotopoulos, M. Stapleton, and D. J. Tildesley. *Mol. Phys.*, 63:527–545, 1988.

[10] J. I. Siepmann. *Monte Carlo Methods Chem. Phys.*, 105:443–460, 1999. and references therein.

[11] A. M. Ferrenberg and R. H. Swendsen. *Phys. Rev. Lett.*, 61:2635–2638, 1988.

[12] A. M. Ferrenberg and R. H. Swendsen. *Phys. Rev. Lett.*, 63:1195–1198, 1989.

[13] A. M. Ferrenberg and R. H. Swendsen. *Comput. Phys.*, Sep/Oct:101–104, 1989.

[14] A. Lotfi, J. Vrabec, and J. Fischer. *Mol. Phys.*, 76:1319–1333, 1992.

[15] D. A. Kofke and E. D. Glandt. *Mol. Phys.*, 64:1105–31, 1988.

[16] R. Agrawal and D. A. Kofke. *Phys. Rev. Lett.*, 74:122–125, 1995.

[17] P. Bolhuis and D. Frenkel. *J. Chem. Phys.*, 106:666–687, 1997.

[18] Q. Yan and J. J. de Pablo. *J. Chem. Phys.*, 111:9509–9516, 1999.

[19] N. B. Wilding and A. D. Bruce. *J. Phys.: Condense. Matter*, 4:3087–3108, 1992.

[20] N. B. Wilding. *Phys. Rev. E.*, 52:602–611, 1995.

[21] A. Dillon and M. J. Heben. Hydrogen storage using carbon adsorbents: past, present and future. *Appl. Phys. A*, 72:133–142, 2001.

[22] Y. Ye, C. C. Ahn, C. Witham, B. Fultz, J. Liu, A. G. Rinzler, D. Colbert, K. A. Smith, and R. E. Smalley. Hydrogen adsorption and cohesive energy of single-walled carbon nanotubes. *Appl. Phys. Lett.*, 74:2307–2309, 1999.

[23] C. Liu, Y. Y. Fan, M. Liu, H. T. Cong, H. M. Cheng, and M. S. Dresselhaus. Hydrogen storage in single-walled carbon nanotubes at room temperature. *Science*, 286:1127–1129, 1999.

[24] A. C. Dillon, K. M. Jones, T. A. Bekkedahl, C. H. Kiang, D. S. Bethune, and M. J. Heben. Storage of hydrogen in single-walled carbon nanotubes. *Nature*, 386:377–379, 1997.

[25] R. T. Yang. *Carbon*, 38:623–626, 2000.

[26] G. G. Tibbetts, G. P. Meisner, and C. H. Olk. Hydrogen storage capacity of carbon nanotubes, filaments, and vapor-grown fibers. *Carbon*, 39:2291–2301, 2001.

[27] P. E. Pinkerton, B. G. Wicke, C. H. Olk, G. G. Tibbetts, G. P. Meisner, M. S. Meyer, and J. F. Herbst. Thermogravimetric measurement of hydrogen absorption in alkali-modified carbon materials. *J. Phys. Chem. B*, 104:9460–9467, 2000.

[28] P. Chen, X. Wu, J. Lin, and K. L. Tan. High hydrogen uptake by alkali-doped carbon nanotubes under ambient pressure and moderate temperatures. *Science*, 285:91–93, 1999.

[29] S. Talapatra, V. Krungleviciute, and A. D. Migone. Higher coverage gas adsorption on the surface of carbon nanotubes: Evidence for a possible new phase in the second layer. *Phys. Rev. Lett.*, 89:246106, 2002.

[30] M. Muris, N. Dufau, M. Bienfait, N. D. Pavlovsky, Y. Grillet, and J. P. Palmari. Methane and krypton adsorption on single-walled carbon nanotubes. *Langmuir*, 16:7019–7022, 2000.

[31] M. Muris, N. D. Pavlovsky, M. Bienfait, and P. Zeppenfeld. Where are the molecules adsorbed on single-walled nanotubes? *Surf. Sci.*, 492:67–74, 2001.

[32] W. Teizer, R. B. Hallock, E. Dujardin, and T. W. Ebbesen. (4)helium desorption from single wall carbon nanotube bundles: A one-dimensional adsorbate. *Phys. Rev. Lett.* , 82:5305–5308, 1999.

[33] W. Teizer, R. B. Hallock, E. Dujardin, and T. W. Ebbesen. Erratum: (4)helium desorption from single wall carbon nanotube bundles: A one-dimensional adsorbate. *Phys. Rev. Lett.* , 84:1844–1845, 2000.

[34] S. E. Weber, S. Talapatra, C. Journet, A. Z. Zambano, and A. D. Migone. Determination of the binding energy of methane on single-walled carbon nanotube bundles. *Phys. Rev. B* , 61: 13150–13154, 2000.

[35] S. Talapatra, A. Z. Zambano, S. E. Weber, and A. D. Migone. Gases do not adsorb on the interstitial channels of closed-ended single-walled carbon nanotube bundles. *Phys. Rev. Lett.* , 85:138–141, 2000.

[36] S. Talapatra and A. D. Migone. Existence of novel quasi-one-dimensional phases of atoms adsorbed on the exterior surface of close-ended single wall nanotube bundles. *Phys. Rev. Lett.* , 87:206106, 2001.

[37] S. Talapatra and A. D. Migone. Adsorption of methane on bundles of closed-ended single-wall carbon nanotubes. *Phys. Rev. B* , 65:045416, 2002.

[38] A. Fujiwara, K. Ishii, H. Suematsu, H. Kataura, Y. Maniwa, S. Suzuki, and Y. Achiba. Gas adsorption in the inside and outside of single-walled carbon nanotubes. *Chem. Phys. Lett.*, 336:205–211, 2001.

[39] A. Z. Zambano, S. Talapatra, and A. D. Migone. Binding energy and monolayer capacity of xe on single-wall carbon nanotube bundles. *Phys. Rev. B* , 64:075415, 2001.

[40] T. Wilson, A. Tyburski, M. R. DePies, O. E. Vilches, D. Becquet, and M. Bienfait. Adsorption of hydrogen and deuterium on carbon nanotube bundles. *J. Low Temp. Phys.*, 126:403–408, 2002.

[41] H. Ulbricht, G. Moos, and T. Hertel. Physisorption of molecular oxygen on single-wall carbon nanotube bundles and graphite. *Phys. Rev. B* , 66:075404, 2002.

[42] H. Ulbricht, J. Kriebel, G. Moos, and T. Hertel. Desorption kinetics and interaction of xe with single-wall carbon nanotube bundles. *Chem. Phys. Lett.*, 363:252–260, 2002.

[43] S. Talapatra, D. S. Rawat, and A. D. Migone. Possible existence of a higher coverage quasi-one- dimensional phase of argon adsorbed on bundles of single-walled carbon, nanotubes. *J. Nanosci. Nanotechno.*, 2:467–470, 2002.

[44] W. Shi and J. K. Johnson. Histogram reweighting and finite size scaling study of the lennard-jones fluids. *Fluid Phase Equilibria*, 187-188:171–191, 2001.

[45] W. Shi, X. C. Zhao, and J. K. Johnson. Phase transitions of adsorbed fluids computed from multiple histogram reighting. *Mol. Phys.* , 100:2139–2150, 2002.

[46] M. R. Smith, Jr., E. W. Bittner, W. Shi, J. Karl Johnson, and B. C. Bockrath. Chemical activation of single-walled carbon nanotubes for hydrogen adsorption. *J. Phys. Chem. B*, 107: 3752–3760, 2003.

[47] W. Shi and J. K. Johnson. 2003. submitted.

[48] J. A. Barker. *Mol. Phys.*, 80:815–820, 1993.

[49] M. Mecke, J. Winkelmann, and J. Fischer. *J. Chem. Phys.*, 107:9264–9270, 1997.

[50] M. Blokhuis, D. Bedeaux, C. D. Holcomb, and J. A. Zolweg. *Mol. Phys.*, 85:665–674, 1995.

[51] J. J. Nicolas, K. E. Gubbins, W. B. Streett, and D. J. Tildesley. *Mol. Phys.*, 37:1429–1454, 1979.

[52] K. K. Mon and K. Binder. *J. Chem. Phys.* , 96:6989–6995, 1992.

[53] A. Z. Panagiotopoulos. *Int. J. Thermophys.*, 15:1057–1072, 1994.

[54] B. Smit. *J. Chem. Phys.*, 96:8639–8640, 1992.

[55] J. M. Caillol. *J. Chem. Phys.*, 109:4885–4893, 1998.

[56] J. J. Potoff and A. Z. Panagiotopoulos. *J. Chem. Phys.*, 109:10914–10920, 1998.

[57] H. P. Deutsch. *J. Stat. Phys.*, 67:1039–1082, 1992.

[58] K. Kiyohara, K. E. Gubbins, and A. Z. Panagiotopoulos. *J. Chem. Phys.*, 106:3338–3347, 1996.

[59] K. Kiyohara, K. E. Gubbins, and A. Z. Panagiotopoulos. *Mol. Phys.*, 94:803–808, 1998.

[60] P. B. Conrad and J. J. de Pablo. *Fluid Phase Equilibria*, 150-151:51–61, 1998.

[61] J. J. Potoff, J. R. Errington, and A. Z. Panagiotopoulos. *Mol. Phys.*, 97:1073–1083, 1999.

[62] J. J. Potoff and A. Z. Panagiotopoulos. *J. Chem. Phys.*, 112:6411–6415, 2000.

[63] N. B. Wilding, M. Müller, and K. Binder. *J. Chem. Phys.*, 105:802–809, 1996.

[64] N. B. Wilding. *J. Phys. Condens. Matter*, 9:585–612, 1997.

[65] H. Frauenkron and P. Grassberger. *J. Chem. Phys.*, 107:9599–9608, 1997.

[66] A. Z. Panagiotopoulos, V. Wong, and M. A. Floriano. *Macromolecules*, 31:912–918, 1998.

[67] T. L. Hill. *Thermodynamics of Small Systems, Part I.* Benjamin, New York, 1963.

[68] J. E. Dennis, Jr. *Numerical Methods for Unconstrained optimization and Nonlinear Equations.* Prentice-Hall, New Jersey, 1983.

[69] W. H. Press, B. P. Flannery, S. A. Teukolsky, and W. T. Vetterling. *Numerical Recipes.* Cambridge University Press, Cambridge, 1986.

[70] M. Schick. Introduction to wetting phenomena. In J. Charvolin, J. F. Joanny, and J. Zinn Justin, editors, *Liquids at interfaces*, pages 415–498, Amsterdam, 1988. North Holland.

[71] H. Taub, G. Torzo, H. J. Lauter, and S. C. Fain, Jr., editors. *Phase transitions in Surface Films 2.* Plenum Press, New York, 1991.

[72] B. K. Peterson and K. E. Gubbins. *Mol. Phys.* , 62:215, 1987.

[73] S. Y. Jiang, C. L. Rhykerd, and K. E. Gubbins. *Mol. Phys.* , 79:373, 1993.

[74] A. Z. Panagiotopoulos. *Mol. Phys.* , 62:701, 1987.

[75] S. Curtarolo, G. Stan, M. W. Cole, M. J. Bojan, and W. A. Steele. *Phys. Rev. E* , 59:4402, 1999.

[76] J. E. Finn and P. A. Monson. *Phys. Rev. A* , 39:6402, 1989.

[77] F. A. Escobedo. *J. Chem. Phys.* , 113:8444–8456, 2000.

[78] J. J. Potoff and J. Ilja Siepmann. *AICHE J.*, 47:1676–1682, 2001.

[79] L. D. Gelb and K. E. Gubbins. Studies of binary liquid mixtures in cylindrical pores: phase separation, wetting and finite-size effects from monte carlo simulations. *Physica A*, 244: 112–123, 1997.

[80] F. A. Escobedo and J. J. de Pablo. Molecular simulation of polymeric networks and gels: phase behavior and swelling. *Phys. Rep.*, 318:85–112, 1999.

[81] J. J. Potoff and J. Ilja Siepmann. *Phys. Rev. Lett.* , 85:3460, 2000.

[82] C. Lastoski and K. E. Gubbins. *Langmuir*, 9:2693, 1993.

[83] J. W. Cahn. *J. Chem. Phys.* , 66:3667, 1977.

[84] C. Ebner and W. F. Saam. *Phys. Rev. Lett.* , 38:1486, 1977.

[85] D. Bonn and D. Ross. Wetting transitions. *Rep. Prog. Phys.*, 64:1085–1163, 2001.

[86] Y. Fan and P. A. Monson. *J. Chem. Phys.* , 99:6897, 1993.

[87] G. Mistura, F. Ancilotto, L. Bruschi, and F. Toigo. *Phys. Rev. Lett.* , 82:795, 1999.

[88] M. W. Cole. *J. Low Temp. Phys.*, 101:25, 1995. and references therein.

[89] M. W. Cole. *Fluid Phase Equilibria*, 151:559–563, 1998. and references therein.

[90] H. S. Youn, X. F. Meng, and G. B. Hess. *Phys. Rev. B* , 48:14556, 1993.

[91] G. B. Hess. Multilayer physisorbed films on graphite. In H. Taub, G. Torzo, H. J. Lauter, and S. C. Fain, Jr., editors, *Phase transitions in Surface Films 2*, pages 357–389, New York, 1991. Plenum Press.

[92] M. Iwamatsu. A simple model of wetting, prewetting, and layering transitions of structured liquids. *J. Colloid Interface Sci.* , 199:177–186, 1998.

[93] Q. M. Zhang, Y. P. Feng, H. K. Kim, and M. H. W. Chan. *Phys. Rev. Lett.* , 57:1456, 1986.

[94] S. Ramesh, Q. Zhang, G. Torzo, and J. D. Maynard. *Phys. Rev. Lett.* , 52:2375–2378, 1984.

[95] W. A. Steele. The physical interaction of gases with crystalline solids, i. gas-solid energies and properties of isolated adsorbed atoms. *Surf. Sci.*, 36:317–352, 1973.

[96] W. A. Steele. *The Interaction of Gases with Solid Surfaces*. Pergamon Press, Oxford, 1974.

[97] O. Dillmann, W. Janke, M. Müller, and K. Binder. A monte carlo test of the fisher-nakanishi-scaling theory for the capillary condensation critical point. *J. Chem. Phys.* , 114:5853, 2001.

[98] J. E. Finn and P. A. Monson. *Phys. Rev. A* , 42:2458, 1990.

[99] A. V. Neimark and P. I. Ravikovitch. *Langmuir*, 13:5148, 1997.

[100] O. Talu and A. L. Myers. *AICHE J.*, 47:1160, 2001.

[101] S. Sircar. *AICHE J.*, 47:1169, 2001.

[102] F. Ancilotto and F. Toigo. Prewetting transitions of ar and ne on alkali-metal surfaces. *Phys. Rev. B* , 60:9019, 1999.

[103] G. Mistura, H. C. Lee, and M. H. W. Chan. Hydrogen adsorption on alkali metal surfaces: Wetting, prewetting and triple-point wetting. *J. Low Temp. Phys.*, 96:221, 1994.

[104] G. F. Teletzke, L. E. Scriven, and H. T. Davis. *J. Colloid Interface Sci.*, 87:550, 1982.

[105] P. Tarazona and R. Evans. *Mol. Phys.* , 48:799–831, 1983.

[106] E. H. Hauge and M. Schick. *Phys. Rev. B* , 27:4288, 1983.

[107] R. Lustig and W. A. Steele. *Mol. Phys.*, 65:475, 1988.

[108] W. L. Jorgensen, J. D. Madura, and C. J. Swenson. *J. Am. Chem. Soc.*, 106:813, 1984.

[109] M. G. Martin and J. I. Siepmann. *J. Phys. Chem. B*, 102:2569, 1998.

[110] S. K. Nath, F. A. Escobedo, and J. J. de Pablo. *J. Chem. Phys.* , 108:9905, 1998.

[111] J. I. Siepmann, S. Karaborni, and B. Smit. *Nature*, 365:330, 1993.

[112] X. Zhao, J. K. Johnson, S. Kwon, R. D. Vidic, and E. Borguet. *submitted*, 2001.

[113] S. Y. Jiang, J. A. Zollweg, and K. E. Gubbins. *Mol. Phys.* , 83:103, 1993.

[114] J. J. Potoff. (private communication).

[115] H. S. Nham and G. B. Hess. *Phys. Rev. B* , 38:5166, 1988.

[116] P. Tarazona and R. Evans. *Phys. Rev. A*, 28:1864, 1983.

[117] T. F. Meister and D. M. Kroll. *Phys. Rev. A*, 31:4055, 1985.

[118] S. Sokołowski and J. Fischer. *Phys. Rev. A*, 41:6866, 1990.

[119] M. J. Bojan, G. Stan, S. Curtarolo, W. A. Steele, and M. W. Cole. *Phys. Rev. E* , 59:864, 1999.

[120] Q. Y. Wang and J. K. Johnson. Phase equilibrium of quantum fluids from simulation: Hydrogen and neon. *Fluid Phase Equilibria*, 132:93–116, 1997.

[121] R. P. Feynman. Space-time approach to non-relativistic quantum mechanics. *Rev. Mod. Phys.*, 20:367–387, 1948.

[122] Q. Wang, J. K. Johnson, and J. Q. Broughton. Thermodynamic properties and phase equilibrium of fluid hydrogen from path integral simulations. *Mol. Phys.*, 89:1105–1119, 1996.

[123] Q. Y. Wang, J. K. Johnson, and J. Q. Broughton. Path integral grand canonical monte carlo. *J. Chem. Phys.* , 107:5108, 1997.

[124] I. F. Silvera and V. V. Goldman. The isotropic intermolecular potential for h2 and d2 in the solid and gas phases. *J. Chem. Phys.*, 69:4209–4213, 1978.

[125] E. Cheng, G. Mistura, H. C. Lee, M. H. W. Chan, M. W. Cole, C. Carraro, W. F. Saam, and F. Toigo. Wetting transitions of liquid hydrogen films. *Phys. Rev. Lett.* , 70:1854, 1993.

[126] R. D. McCarthy, J. Hord, and H. M. Roder. *Selected Properties of Hydrogen*. National Bureau of Standards, Ernest Ambler, 1981.

[127] S. Challa. Unpublished.

[128] U. H. E. Hansmann and Y. Okamoto. Comparative study of multicanonical and simulated annealing algorithms in the protein folding problem. *Physica A*, 212:415–437, 1994.

[129] J. E. Rutledge and P. Taborek. Prewetting phase diagram of he4 on cesium. *Phys. Rev. Lett.* , 69:937, 1992.

[130] K. S. Ketola, S. Wang, and R. B. Hallock. Anomalous wetting of helium on cesium. *Phys. Rev. Lett.* , 68:201, 1992.

[131] G. B. Hess, M. J. Sabatini, and M. H. W. Chan. Nonwetting of cesium by neon near its critical point. *Phys. Rev. Lett.* , 78:1739, 1997.

[132] D. Ross, J. A. Phillips, and P. Taborek. *J. Low Temp. Phys.*, 106:81, 1997.

[133] S. Herminghaus, J. Vorberg, H. Gau, R. Conradt, D. Reinelt, H. Ulmer, P. Leiderer, and M. Przyrembel. *Ann. Phys.-Leipzig*, 6:425, 1997.

[134] F. Hensel and M. Yao. *Eur. J. Sol. Stat. Inorg. Chem.*, 34:861, 1997.

[135] V. F. Kozhevnikov, D. I. Arnold, S. P. Naurzakov, and M. E. Fisher. Prewetting transitions in a near-critical metallic vapor. *Phys. Rev. Lett.* , 78:1735, 1997.

[136] E. Cheng, M. W. Cole, W. F. Saam, and J. Treiner. Wetting transitions of classical liquid films: A nearly universal trend. *Phys. Rev. B* , 48:18214, 1993.

[137] A. Chizmeshya, M. W. Cole, and E. Zaremba. Weak binding potentials and wetting transitions. *J. Low Temp. Phys.*, 110:677, 1998.

[138] F. Ancilotto, F. Faccin, and F. Toigo. Wetting transitions of he4 on alkali-metal surfaces from density-functional calculations. *Phys. Rev. B* , 62:17035, 2000.

[139] C. Ebner and W. F. Saam. Effect of long-range forces on wetting near bulk critical temperatures: An ising-model study. *Phys. Rev. B* , 35:1822, 1987.

[140] F. Ancilotto, S. Curtarolo, F. Toigo, and M. W. Cole. Evidence concerning drying behavior of ne near a cs surface. *Phys. Rev. Lett.* , 87:206103, 2001.

[141] E. Cheng, M. W. Cole, W. F. Saam, and J. Treiner. Helium prewetting and nonwetting on weak-binding substrates. *Phys. Rev. Lett.* , 67:1007, 1991.

[142] S. Curtarolo, G. Stan, M. J. Bojan, M. W. Cole, and W. A. Steele. Threshold criretia for wetting at the triple point. *Phys. Rev. E* , 61:1670, 2000.

[143] M. J. Bojan, M. W. Colei, J. K. Johnson, W. A. Steele, , and Q. Wang. Computer simulation studies of adsorption of simple gases on alkali metal surfaces. *J. Low Temp. Phys.*, 110:653, 1998.

[144] . We note that Faccin et al.[138] studied this transition with a finite T density functional method.

[145] . This method has previously been used in an attempt to locate a prewetting transition for H_2 on Rb but the results were inconclusive[143].

[146] W. Shi and J. K. Johnson. 2003. in preparation.

[147] E. Zaremba and W. Kohn. Theory of helium adsorption on simple and noble-metal surfaces. *Phys. Rev. B* , 15:1769, 1977.

[148] D. Ross, , P. Taborek, and J. E. Rutledge. Wetting bahavior of h2 on cesium. *Phys. Rev. B* , 58:R4274, 1998.

[149] P. Taborek and J. E. Rutledge. *Phys. Rev. Lett.*, 71:263, 1997.

[150] E. Cheng, M. W. Cole, W. F. Saam, and J. Treiner. *J. Low Temp. Phys.*, 89:739, 1992.

[151] J. F. Annett and R. Haydock. Hybridization interaction between helium and a metal surface. *Phys. Rev. B* , 34:6860, 1986.

[152] L. W. Bruch. Ground state energy and structure of physisorbed monolayers of linear molecules. *J. Chem. Phys.* , 79:3148–3156, 1983.

[153] X. P. Jiang, F. Toigo, and M. W. Cole. Quadrupole contribution to the physisorption interaction. *Chem. Phys. Lett.*, 101:159, 1983.

[154] M. S. Dresselhaus, K. A. Williams, and P. C. Eklund. Hydrogen adsorption in carbon materials. *MRS Bulletin*, November:45–50, 1999.

[155] H. M. Cheng, Q. H. Yang, and C. Liu. Hydrogen storage in carbon nanotubes. *Carbon*, 39: 1447–1454, 2001.

[156] G. Stan and M. W. Cole. Hydrogen adsorption in nanotubes. *J. Low Temp. Phys.*, 110: 539–544, 1998.

[157] M. Rzepka, P. Lamp, and M. A. de la Casa-Lillo. Physisorption of hydrogen on microporous carbon and carbon nanotubes. *J. Phys. Chem. B*, 102:10894–10898, 1998.

[158] F. Darkrim and D. Levesque. Monte carlo simulations of hydrogen adsorption in single-walled carbon nanotubes. *J. Chem. Phys.*, 109:4981–4984, 1998.

[159] Q. Wang and J. K. Johnson. Molecular simulation of hydrogen adsorption in single-walled carbon nanotubes and idealized carbon slit pores. *J. Chem. Phys.* , 110:577–586, 1999.

[160] Q. Y. Wang and J. K. Johnson. Optimization of carbon nanotube arrays for hydrogen adsorption. *J. Phys. Chem. B*, 103:4809–4813, 1999.

[161] V. V. Simonyan, P. Diep, and J. K. Johnson. Molecular simulation of hydrogen adsorption in charged single-walled carbon nanotubes. *J. Chem. Phys.*, 111:9778–9783, 1999.

[162] P. A. Gordon and R. B. Saeger. Molecular modeling of adsorptive energy storage: Hydrogen storage in single-walled carbon nanotubes. *Ind. Eng. Chem. Res.*, 38:4647–4655, 1999.

[163] K. A. Williams and P. C. Eklund. Monte carlo simulations of hydrogen physisorption in finite-diameter carbon nanotube ropes. *Chem. Phys. Lett.* , 320:352–358, 2000.

[164] F. Darkrim and D. Levesque. High adsorptive property of opened carbon nanotubes at 77 k. *J. Phys. Chem. B*, 104:6773–6776, 2000.

[165] S. M. Lee and Y. H. Lee. Hydrogen storage in single-walled carbon nanotubes. *Appl. Phys. Lett.*, 76:2877–2879, 2000.

[166] V. V. Simonyan and J. K. Johnson. *J. Alloys and Compounds*, 330-332:659–665, 2002.

[167] S. C. Tsang, Y. K. Chen, P. J. F. Harris, and M. L. H. Green. *Nature*, 372:159–162, 1994.

[168] B. K. Pradhan, A. R. Harutyunyan, D. Stojkovic, J. C. Grossman, P. Zhang, M. Cole, V. Crespi, H. Goto, J. Fujiwara, and P. C. Eklund. *J. Mater. Res.*, 17:2209–2216, 2002.

[169] A. Kuznetsova, D. B. Mawhinney, V. Naumenko, J. T. Yates, Jr., J. Liu, and R. E. Smalley. Enhancement of adsorption inside of single-walled nanotubes: opening the entry ports. *Chem. Phys. Lett.* , 321:292–296, 2000.

[170] W. Zhu, J. M. van de Graaf, L. J. P. van de Broeke, F. Kapteijn, and J. A. Moulijn. Teom: A unique technique for measuring adsorption properties. light alkanes in silicalite-1. *Ind. Eng. Chem. Res.*, 37:1934–1942, 1998.

[171] M. R. Smith, Jr., S. W. Hedges, R. LaCount, D. Kern, N. Shah, G. Huffman, and B. Bockrath. 2002. submitted.

[172] E. W. Bittner, M. R. Smith, Jr., and B. C. Bockrath. *Carbon*, 2002. submitted.

[173] T. van Mourik and R. J. Gdanitz. A critical note on density functional theory studies on rare-gas dimers. *J. Chem. Phys.*, 116:9620–9623, 2002.

[174] A. K. Rappé and E. R. Bernstein. Ab initio calculation of nonbonded interactions: Are we there yet? *J. Phys. Chem. A*, 104:6117–6128, 2000.

[175] A. J. Misquitta and K. Szalewicz. Intermolecular forces from asymptotically corrected density functional description of monomers. *Chem. Phys. Lett.*, 357:301–306, 2002.

[176] X. Wu, M. C. Vargas, S. Nayak, V. Lotrich, and G. Scoles. Towards extending the applicability of density functional theory to weakly bound systems. *J. Chem. Phys.*, 115:8748–8757, 2001.

[177] A. Milet, T. Korona, R. Moszynski, and E. Kochanski. Anisotropic intermolecular interactions in van der waals and hydrogen-bonded complexes: What can we get from density functional calculations? *J. Chem. Phys.*, 111:7727–7735, 1999.

[178] S. Rols, R. Almairac, L. Henrard, E. Anglaret, and J. E. Sauvajol. Diffraction by finite-size crystalline bundles of single wall nanotubes. *Eur. Phys. J. B*, 10:263–270, 1999.

[179] S. Bandow, S. Asaka, Y. Saito, A. M. Rao, L. Grigorian, E. Richter, and P. C. Eklund. Effect of the growth temperature on the diameter distribution and chirality of single-wall carbon nanotubes. *Phys. Rev. Lett.* , 80:3779–3782, 1998.

[180] A. M. Rao, E. Richter, S. Bandow, B. Chase, P. C. Eklund, K. A. Williams, S. Fang, K. R. Subbaswamy, M. Menon, A. Thess, R. E. Smalley, G. Dresselhaus, and M. S. Dresselhaus. Diameter-selective raman scattering from vibrational modes in carbon nanotubes. *Science*, 275:187–191, 1997.

[181] A. G. Rinzler, J. Liu, H. Dai, P. Nikolaev, C. B. Huffman, F. J. Rodríguez-Macías, P. J. Boul, A. H. Lu, D. Heymann, D. T. Colbert, R. S. Lee, J. E. Fischer, A. M. Rao, P. C. Eklund, and R. E. Smalley. Large-scale purification of single-wall carbon nanotubes: process, product, and characterization. *Appl. Phys. A*, 67:29–37, 1998.

[182] J. W. G. Wildoer, L. C. Venema, A. G. Rinzler, R. E. Smalley, and C. Dekker. Electronic structure of atomically resolved carbon nanotubes. *Nature*, 391:59–62, 1998.

[183] D. B. Mawhinney, V. Naumenko, A. Kuznetsova, J. T. Yates, Jr., J. Liu, and R. E. Smalley. Surface defect site density on single walled carbon nanotubes by titration. *Chem. Phys. Lett.* , 324:213–216, 2000.

[184] A. Kuznetsova, J. T. Yates, Jr., V. V. Simonyan, J. K. Johnson, C. B. Huffman, and R. E. Smalley. Optimization of xe adsorption kinetics in single walled carbon nanotubes. *J. Chem. Phys.*, 115:6691–6698, 2001.

[185] V. V. Simonyan and J. Karl Johnson. in preparation.

[186] F. Hershkowitz and P. D. Madiara. Simultaneous measurement of adsorption, reaction, and coke using a pulsed microbalance reactor. *Ind. & Eng. Chem. Res.*, 32:2969–2974, 1993.

[187] R. V. Siriwardane, M. S. Shen, E. P. Fisher, and J. A. Poston. Adsorption of co2 on molecular sieves and activated carbon. *Energy & Fuels*, 15:279–284, 2001.

[188] A. D. Crowell and J. S. Brown. *Surf. Sci.*, 123:296, 1982.

[189] Q. Wang and J. K. Johnson. Hydrogen adsorption on graphite and in carbon slit pores from path integral simulations. *Mol. Phys.*, 95:299–309, 1998.

[190] M. Monthioux, B. W. Smith, B. Burteaux, A. Claye, J. E. Fischer, and D. E. Luzzi. Sensitivity of single-wall carbon nanotubes to chemical processing: an electron microscopy investigation. *Carbon*, 39:1251–1272, 2001.

[191] U.S. Patent 5346683.

[192] G. Stan, M. J. Bojan, S. Curtarolo, S. M. Gatica, and M. W. Cole. Uptake of gases in bundles of carbon nanotubes. *Phys. Rev. B* , 62:2173–2180, 2000.

[193] A. M. Vidales, V. H. Crespi, and M. W. Cole. Heat capacity and vibrational spectra of monolayer films adsorbed in nanotubes. *Phys. Rev. B*, 58:R13426–R13429, 1999.

[194] M. W. Cole, V. H. Crespi, G. Stan, C. Ebner, J. M. Hartman, S. Moroni, and M Boninsegni. Condensation of helium in nanotube bundles. *Phys. Rev. Lett.*, 84:3883–3886, 2000.

[195] S. M. Gatica, M. J. Bojan, G. Stan, and M. W. Cole. Quasi-one and two-dimensional transitions of gases adsorbed on nanotube bundles. *J. Chem. Phys.*, 114:3765–3769, 2001.

[196] A. Kuznetsova, J. T. Yates, Jr., J. Liu, and R. E. Smalley. Physical adsorption of xenon in open single walled carbon nanotubes: Observation of a quasi-one-dimensional confined xe phase. *J. Chem. Phys.*, 112:9590–9598, 2000.

[197] D. H. Yoo, G. H. Rue, Y. H. Hwang, and H. K. Kim. Study of nitrogen adsorbed on single-walled carbon nanotube bundles. *J. Phys. Chem. B*, 106:3371–3374, 2002.

[198] D. H. Yoo, G. H. Rue, J. Y. Seo, Y. H. Hwang, M. H. W. Chan, and H. K. Kim. Study of argon adsorbed on open-ended carbon nanotube bundles. *J. Phys. Chem. B*, 106:9000–9003, 2002.

[199] C. M. Yang, H. Kanoh, K. Kaneko, M. Yudasaka, and S. Iijima. Adsorption behaviors of hipco single-walled carbon nanotube aggregates for alcohol vapors. *J. Phys. Chem. B*, 106: 8994–8999, 2002.

[200] V. V. Simonyan, J. Karl Johnson, A. Kuznetsova, and J. T. Yates, Jr. Molecular simulation of xenon adsorption on single-walled carbon nanotubes. *J. Chem. Phys.*, 114:4180–4185, 2001.

[201] M. M. Calbi, S. M. Gatica, M. J. Bojan, and M. W. Cole. Phases of neon, xenon, and methane adsorbed on nanotube bundles. *J. Chem. Phys.*, 115:9975–9981, 2001.

[202] M. M. Calbi, F. Toigo, and M. W. Cole. Dilation-induced phases of gases absorbed within a bundle of carbon nanotubes. *Phys. Rev. Lett.*, 86:5062–5065, 2001.

[203] D. J. Wales and J. P. K. Doye. Global optimization by basin-hopping and the lowest energy structures of lennard-jones clusters containing up to 110 atoms. *J. Phys. Chem. A*, 101: 5111–5116, 1997.

[204] J. P. K. Doye and D. J. Wales. Thermodynamics of global optimisaton. *Phys. Rev. Lett.* , 80:1357–1360, 1998.

[205] D. J. Wales and H. A. Scheraga. Global optimization of clusters, crystals, and biomolecules. *Science*, 285:1368–1372, 1999.

[206] S. Y. Jiang, K. E. Gubbins, and J. A. Zollweg. Adsorption, isosteric heat and commensurate-incommensurate transition of methane on graphite. *Mol. Phys.*, 80:103–116, 1993.

[207] G. Vidali, G. Ihm, H. Y. Kim, and M. W. Cole. Potentials of physical adsorption. *Surf. Sci. Rep.*, 12:133–181, 1991.

[208] A. D. Migone. (private communication).

[209] D. M. Ruthven. *Principles of adsorption and adsorption processes*. John Wiley & Sons, New York, 1984.

[210] A. Zuttel, P. Sudan, P. Mauron, T. Kiyobayashi, C. Emmenegger, and L. Schlapbach. Hydrogen storage in carbon nanostructures. *Int. J. Hydrogen Energ.*, 27:203–212, 2002.

[211] A. Thess, R. Lee, P. Nikolaey, H. Dai, P. Petit, J. Robert, C. Xu, Y.H. Lee, S.G. Kim, A.G. Rinzler, D.T. Colbert, G.E. Scuseria, D. Tomanek, J.E. Fischer, and R.E. Smalley. Crystilline ropes of metallic carbon nanotubes. *Science*, 273:483–487, 1996.

[212] M. M. Calbi, F. Toigo, and M. W. Cole. Dilation and intercalation of gases within carbon nanostructures. *J. low Temp. Phys.*, 126:179–186, 2002.

[213] K. Bolton and A. Rosén. Computational studies of gas-carbon nanotube collision dynamics. *Phys. Chem. Chem. Phys.*, 4:4481–4488, 2002.

[214] A. I. Skoulidas, D. M. Ackerman, J. Karl. Johnson, and D. S. Sholl. Rapid transport of gases in carbon nanotubes. *Phys. Rev. Lett.*, 89:185901, 2002.

[215] W. Shi and J. K. Johnson. 2003. in preparation.

[216] A. Siber. Adsorption of he atoms in external grooves of single-wall carbon nanotube bundles. *Phys. Rev. B*, 66:205406, 2002.

[217] L. D. Gelb and K. E. Gubbins. Characterization of porous glasses: Simulation models, adsorption isotherms, and the brunauer-emmett-teller analysis method. *Langmuir*, 14:2097–2111, 1998.

[218] N Setoyama, T Suzuki, and K Kaneko. Simulation study on the relationship between a high resolution alpha(s)-plot and the pore size distribution for activated carbon. *Carbon*, 36: 1459–1467, 1998.

[219] T Ohba and K Kaneko. Internal surface area evaluation of carbon nanotube with gcmc simulation-assisted n-2 adsorption. *J. Phys. Chem. B*, 106:7171–7176, 2002.